LIÈGE université Sciences

CIP CENTRE FOR PROTEIN ENGINEERING

Development and characterization of camelid antibody fragments (nanobodies) as theranostic agents against the β-lactamases TEM-1, NDM-1 and CMY-2

A thesis submitted in partial fulfillment of the requirements
for the degree of Doctor of Philosophy (PhD) in Science

by
Cawez Frédéric

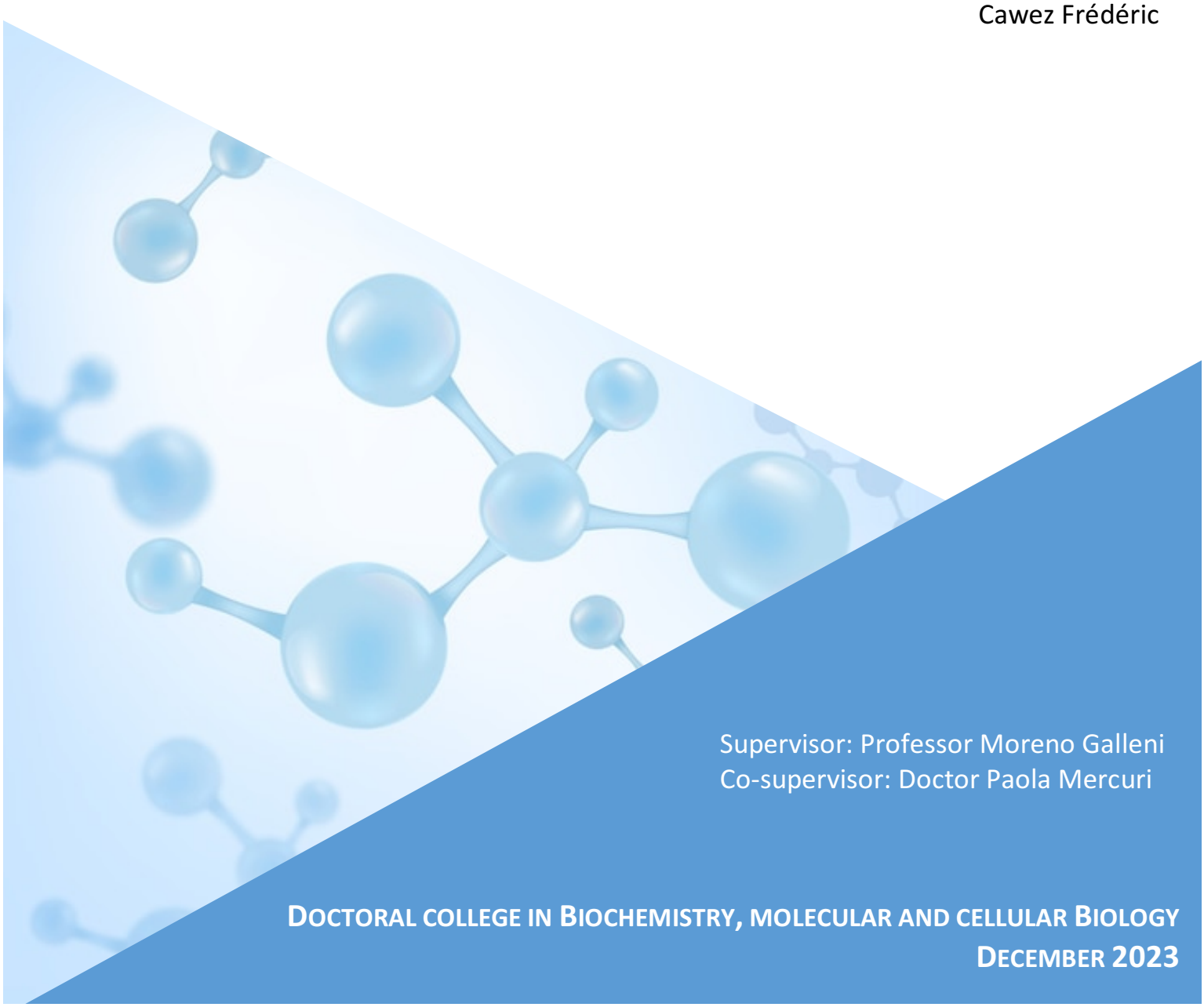

Supervisor: Professor Moreno Galleni
Co-supervisor: Doctor Paola Mercuri

DOCTORAL COLLEGE IN BIOCHEMISTRY, MOLECULAR AND CELLULAR BIOLOGY
DECEMBER 2023

Acknowledgement

Je tiens tout d'abord à remercier le professeur Moreno Galleni pour la confiance qu'il m'a accordée en me donnant l'opportunité de travailler sur ce projet de thèse financé par le SPF Santé Publique pendant trois ans et puis sur fonds propres pendant plus d'un an. Il a toujours cru en moi et m'a toujours encouragé et ce, malgré les deux malheureux échecs lors des défenses F.R.I.A. Je suis également reconnaissant des nombreuses discussions que nous avons pu avoir à la fois autour de la thèse, mais également sur la vie de tous les jours. Finalement, je pense que ce manuscrit n'aurait jamais vu le jour s'il n'y avait pas consacré une bonne partie de son temps.

Même si cela n'a pas abouti, je tiens à remercier personnellement Marylène Vandevenne pour tout son soutien et son investissement lors des deux préparations au F.R.I.A. Même si cela peut être démoralisant au début, on en retire finalement pas mal de leçons et c'est dans cette optique-là que je considère que ces échecs m'ont certainement rendu plus fort. Encore un énorme merci pour m'avoir donné goût aux sciences.

Je tiens à remercier toute l'équipe du CIP, je ne saurais les nommer tous, pour tous leurs conseils, les parties de cartes sur le temps de midi, les trappistes, les barbecues, les très longues soirées à manipuler et manger de la pizza, et pour bien d'autres raisons. Cette esprit d'équipe, finalement ces amitiés, ont rendu mon travail au quotidien bien plus agréable et enrichissante, même pendant cette fameuse période COVID.

Merci également à Virginie Guérin, Jacques Mainil, Damien Thiry de l'institut vétérinaire de l'université de Liège et Marc Saulmont de l'ARSIA dont la collaboration fut particulièrement fructueuse et m'as permis d'acquérir des connaissances dans le monde vétérinaire qui m'était totalement inconnu.

Je tiens à remercier et à féliciter toutes les personnes qui ont contribué à ce travail, car ce manuscrit n'est pas le simple reflet de mes efforts, il est aussi la preuve irréfutable de votre investissement et des nombreuses discussions qui en ont découlé. Dès lors j'aimerais

particulièrement dire merci à Christian Damblon, Marius, Frédéric Kerff, Mireille Dumoulin, Francisco, Maxi, Paola ainsi qu'à l'ensemble de mes étudiants à qui j'espère avoir laissé un bon souvenir.

Merci à tous mes proches et à ma famille pour avoir toujours cru en moi et pour avoir été là, même dans les moments difficiles. J'espère que ce manuscrit vous rendra fier de moi et vous montrera à quel point votre soutient fut important. Je tiens particulièrement à dire merci à Natalie et mon frère Arnaud pour la révision du manuscrit, à mes parents pour m'avoir rendu comme je suis et à ma compagne Pauline sans qui je ne serai rien. Quelle autre femme serait venu me rechercher au travail à des heures impossibles, l'aurai conduit au travail les week-ends, se serait occupée quasiment, j'ai bien dit quasiment, de tout à la maison pendant que son copain rédigeait, le soutiendrait même quand il voulait tout arrêter… Il n'y a que toi qui aurait pu le faire et qu'il l'a fait. C'est ce pourquoi je ne saurais jamais suffisamment te dire merci.

Summary

The intensive and misuse of β-lactam antibiotics selected a large number of resistant environmental and nosocomial strains. Nowadays, more than one million people per year die because of the antimicrobial resistance reflecting the lack of solutions to fight this phenomenon. A major factor of resistance consists in the expression of enzymes, called β-lactamases (BLAs), which are able to hydrolyze the β-lactam antibiotics. The apparition of Multi-Drug Resistance (MDR) bacteria able to express more than one β-lactamase scares the health society because of their non-susceptibility to all known clinically used antibiotics even the carbapenems. In this context, many groups develop new antibiotics or inhibitory peptides to fight the bacterial resistance. Others develop new technics in order to diagnose more rapidly the expression of the β-lactamases to avoid the misuse of antibiotics.

In this work, we selected and characterized camelid antibody fragments (nanobody, VHH) for the detection and the inhibition of the β-lactamases TEM-1, NDM-1 and CMY-2 widely spread in the animal and the human health.

A complete kinetic characterization showed nanobodies inhibited TEM-1 and CMY-2 following a non-competitive trend. Structural studies on the VHH/TEM-1 and VHH/CMY-2 complexes emphasized a binding area located near to the active site. Moreover, we demonstrated, by molecular dynamic simulations and relaxation experiments by NMR, that the VHH directed against TEM-1 disrupted the mobility of the protein with propagation in regions located far from the binding area, reflecting an interaction in an allosteric site of the enzyme. Interestingly, the kinetic characterization indicated the VHHs against NDM-1 acted as competitive inhibitors. In parallel, we developed a sandwich ELISA using both VHHs and rabbit polyclonal antibodies to detect specifically different members of the TEM family and of the CMY-2 sub-group. The utilization of the VHH in a bivalent form improved the sensitivity of the assay for the detection of CMY-2, without modifying the specificity of the ELISA.

To conclude, we demonstrated the VHH could be used as a powerful tool for either its capability to inhibit the activity of β-lactamases, and/or ensure their detection with a high specificity and sensitivity. The design of new constructs based on the VHH renders this antibody fragment particularly useful, as the development of peptides by peptidomimetics able to pass through the bacterial outer-membrane, or multivalent VHH to improve the sensitivity of detection assays.

Résumé

L'utilisation abusive d'antibiotiques à noyau β-lactame entraine la sélection d'un grand nombre de souches environnementales et nosocomiales résistantes. De nos jours, la résistance antimicrobienne entraine plus d'un million de décès par an dû au manque de solutions pour combattre la résistance bactérienne. Un des principaux facteurs de résistance consiste en la production d'enzymes (β-lactamases) capables d'hydrolyser ces antibiotiques. L'apparition de bactéries multi-résistantes qui produisent plusieurs β-lactamases effraie les soins de santé. En cause, l'inefficacité des antibiotiques utilisés en milieu clinique, même les carbapénèmes. Dès lors, de nombreux groupes développent de nouveaux antibiotiques et peptides inhibiteurs pour contrer la résistance bactérienne. D'autres groupes développent des alternatives pour un diagnostic plus rapide des facteurs de résistance afin d'assurer une meilleure utilisation des antibiotiques.

Dès lors, nous avons sélectionné et caractérisé des fragments d'anticorps de camélidé (nanobody, VHH) pour détecter et inhiber les β-lactamases TEM-1, NDM-1 et CMY-2 largement répandues en médecine humaine et vétérinaire.

La caractérisation cinétique des VHHs dirigés contre TEM-1 et CMY-2 a montré qu'ils agissaient en tant qu'inhibiteurs non-compétitifs. Les données structurales des complexes VHH/TEM-1 et VHH/CMY-2 ont mis en évidence un site d'interaction localisé autour du site actif de l'enzyme. De plus, des expériences de dynamique moléculaire et de relaxation par RMN ont montré que le VHH dirigé contre TEM-1 perturbait la dynamique de l'enzyme dû à un phénomène allostérique. A contrario, des premières données cinétiques semblent indiquées que les VHHs inhiberaient l'activité de NDM-1 selon un modèle compétitif. En parallèle, nous avons développé un test ELISA sandwich en utilisant les VHHs et des anticorps polyclonaux de lapin pour la détection spécifique des β-lactamases de la famille TEM et du sous-groupe CMY-2. L'utilisation d'un VHH bivalent améliora la sensibilité de détection de CMY-2, sans modifier la spécificité du test.

Pour conclure, le nanobody est un outil puissant pour sa capacité à inhiber l'activité d'enzymes, mais également pour assurer une détection spécifique et sensible des β-lactamases. Le développement de molécules sur base du VHH rend cet anticorps particulièrement utile comme le développement de peptides capables de passer au travers de la membrane externe des bactéries par peptidomimétique, ou un VHH multivalent qui a la capacité d'améliorer la sensibilité d'une méthode de détection.

Abbreviation list

AA	:	Amino Acid
ABR	:	Antibacterial Resistance
ACA	:	Aminocephalosporanic acid
AIC	:	Akaike Information Criteria
AMR	:	Antimicrobial Resistance
APA	:	Aminopenicillanic acid
ATP	:	Adenosine triphosphate
AVI	:	Avibactam
BCA	:	Bicinchoninic Acid Assay
BLA	:	β-lactamase
BLI	:	β-lactamase inhibitor
BLIP	:	β-lactamase inhibitor Protein
BSA	:	Bovine Serum Albumine
C	:	Carbone
cAmpC	:	Chromosomal AmpC
CD	:	Circular Dichroism
CDR	:	Complementary Determining Region
CPE	:	Carbapenemase Producing Enterobacterales
CTRL	:	Control
cUTI	:	Complicated urinary tract infection
cIAI	:	Complicated intra-abdominal infection
CV	:	Column Volume
DBO	:	Diazabicyclo[3.2.1]octanone
DNA	:	Deoxyribonucleic acid
DAP	:	Diaminopimelic acid
EDTA	:	Ethylenediaminetetraacetic acid
ELISA	:	Enzyme-Linked Immunosorbent Assay
ESBL	:	Extended-spectrum β-lactamase
FDA	:	Food and Drug Administration
FR	:	Framework
FT	:	Flow-Through
GT	:	Glycosyltransferase
HA	:	Hemagglutinin
H-bond	:	Hydrogen Bond
HCAb	:	Heavy Chain only Antibody
HER-2	:	Human Epidermal Receptor-2
HP	:	High Performance
HRP	:	Horseradish Peroxidase
HSQC	:	Heteronuclear Single Quantum Coherence
IgNAR	:	Immunoglobulin New Antigen Receptor
IMAC	:	Immobilized Metal Affinity Chromatography
IPTG	:	Isopropyl β-D-1-thiogalactopyranoside
IRT	:	Inhibitor Resistant TEM
KB	:	Kinetic Buffer

LB	:	Lysogeny Broth
LFA	:	Lateral Flow Assay
LOD	:	Limit of Detection
LPS	:	Lipopolysaccharide
LSBL	:	Limited Spectrum β-lactamase
MBL	:	Metallo-β-lactamase
MCS	:	Multiple Cloning Site
MD	:	Molecular Dynamic
MDR	:	Multi-drug resistance
Mg	:	Magnesium
MSSA	:	Methicillin-susceptible *Staphylococcus aureus*
N	:	Azote
Ni	:	Nickel
NMR	:	Nuclear Magnetic Resonance
NOE	:	Nuclear Overhauser effect
NTA	:	Nitrilotriacetic acid
OD	:	Optic Density
ON	:	Overnight
ori	:	Origin
PA	:	Phosphatase Alkaline
pAbs	:	Polyclonal Antibodies
pAmpC	:	Plasmid-mediated AmpC
PBC	:	Periodic boundary conditions
PBMC	:	Peripheral Blood Mononuclear Cell
PBP	:	Penicillin Binding Protein
PCR	:	Polymerase Chain Reaction
REL	:	Relebactam
RMSD	:	Root-mean-square deviation
RMSF	:	Root-mean-square fluctuation
RNA	:	Ribonucleic acid
RT	:	Room Temperature
SDS-PAGE	:	Sodium Dodecylsulfate Polyacrylamide Gel
TB	:	Terrific Broth
TEA	:	Triethanolamine
T_m	:	Thermal melt
TMB	:	3,3',5,5'-Tetramethylbenzidine
TP	:	Transpeptidase
TROSY	:	Transverse Relaxation-Optimized Spectroscopy
UDP	:	Uridine diphosphate
UV	:	Ultraviolet
VAB	:	Vaborbactam
VEGF	:	Vascular Endothelial Growth Factor
VHH	:	Variable heavy-chain domain of heavy-chain antibody
VNAR	:	Variable New Antigen Receptor
WT	:	Wide Type

Content

1. Introduction

1.1) The antimicrobial resistance, a global concern

Antimicrobial resistance (AMR) is a major risk to human health around the world, with a lot of organisms capable to resist bioactive molecules. In particular, the emergence of resistance factors commonly used by bacteria to fight the last antibiotics coming to market is a growing source of concern. A first review on AMR published in 2016 indicated that resistance kills around 700.000 people per year and could reach 10 million per year by 2050 (**O'Neill, 2016**). This forecast was largely criticized, but a more recent study published in 2022 estimated that 1.3 million deaths in 2019 in 204 countries were attributable to ABR with, at the top of the list, the following pathogens: *Escherichia coli*, *Staphylococcus aureus*, *Klebsiella pneumoniae*, *Streptococcus pneumoniae*, *Acinetobacter baumannii* and *Pseudomonas aeruginosa* (**Antimicrobial Resistance Collaborators, 2022**). Numbers may vary from one study to another. However, all studies demonstrate a dramatically elevated number of deaths associated to AMR, which is probably underestimated.

Consequently, the AMR increases considerably the public health cost as a result of more expensive antibiotics, the use of specialized equipment and longer hospital stays for patients. Moreover, it also indirectly impacts the economy by the loss of productivity of ill people (**World Bank Group, 2017**).

The antibiotic resistance occurs when microorganisms are exposed to antibiotic drugs. This creates a selective pressure killing the susceptible organisms, but where organisms naturally resistant or which acquire resistance genes can survive. The main factor contributing to the emergence of antibiotic resistance is the overuse of antibiotics, especially in developed countries, but also their inappropriate use often related to an inefficient diagnosis and/or a self-medication with an inappropriate use of antibiotics. Another source of resistance concerns the use of antibiotics in food-producing animals and aquaculture. Even though it was completely abolished in Europe, it is currently a common practice in the USA and Asia. Finally,

the environment is now recognized as a reservoir of antibiotic resistance genes with the transmission to humans caused by contaminated water or soils (**Prestinaci et al, 2015**).

Healthcare facilities, the food production and the environment (water, soil) represent the major sources of antibiotic resistance (**Woerther et al, 2013**). Then, the health of people is directly connected to the health of animals and the environment facilitating the spread of antibiotic resistance. It is well-known that toilets and sink drains are an important source of germs in healthcare facilities transmitting resistance genes between people, but also releasing resistance genes or traces of antibiotics in wastewater contaminating rivers and lakes. International travels drastically spread germs person to person resulting in some outbreaks or pandemic episodes worldwide. Finally, people may also be sick by the consumption of contaminated foods (animals and vegetables) (**CDC, 2019**). However, these statements must be qualified, as the transmission of resistant bacteria between human/environmental and animal reservoirs is not self-evident (**Miltgen et al, 2022**).

Mobile genetic elements contribute to the worldwide dissemination of genes rendering susceptible strains resistant to the antibiotic exposure. The selective pressure due to a high exposure to antibiotics lead to the random mutagenesis of resistance genes during the bacterial replication cycles allowing the survival of bacteria. Moreover, the transfer of resistance genes between bacteria is mainly conducted via plasmids. Those plasmids carry multiple resistance genes which are often a part of integron ensuring their expression. The resistance genes are generally carried by transposons for their transfer between plasmids or between a plasmid and the bacterial chromosome (**Bush & Bradford, 2020**).

1.2) The antibiotics and their mechanism of action

Fleming was the first to highlight the efficacy of an antibiotic in 1929 via the competition between *Penicillium notatum* and a *Staphylococcus* (**Fleming, 1929**). The penicillin was identified and developed in 1939 by *Florey and Chain* (**Chain et al, 1940**). It followed the discovery of a large number of other molecules throughout the 20th century, all active against prokaryotic organisms, but presenting a weak toxicity against eukaryotic cells, a significance advantage for a use in human medicine (**Fig 1.1**).

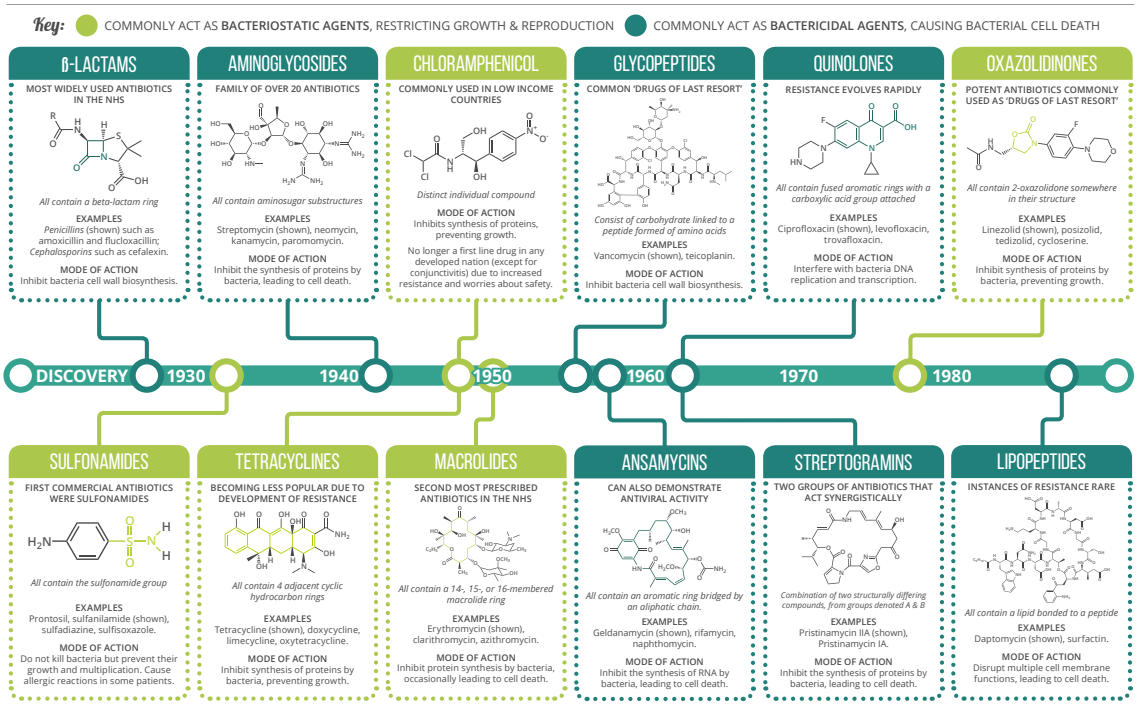

Fig 1.1. *Classification and introduction dates of the antibiotics (**https://www.compoundchem.com/2014/09/08/antibiotics/**).*

The antibiotics are classified following their mechanism of action, their chemical structure, the spectrum of action (bacterial type…) and their bacteriostatic or bactericide effect (**Fig 1.2**). Some antibiotics act directly on the cell wall as the β-lactam antibiotics inhibiting the Penicillin Binding Protein activity (**section 1.3**), the glycopeptides (e.g. vancomycin) preventing the bridging of the peptidoglycan and the polymyxins (e.g. colistin) binding the lipopolysaccharides (LPS) and disrupting the cell membrane. The antibiotics can also interfere with the synthesis of nucleic acids as the quinolones (e.g. nalidixic acid) and the fluoroquinolones targeting the DNA gyrase and the topoisomerases preventing the replication of the bacterial DNA, the rifampicin (e.g. rifampin) blocking the bacterial RNA polymerase and generally utilized to treat infections caused by *Mycobacterium tuberculosis* and finally, the sulfonamides interfering with the folate biosynthesis playing the role of cofactor for enzymes involved in the DNA and the RNA synthesis. A lot of antibiotics also prevent the protein synthesis by interaction with the ribosomal subunit 50S such as the macrolides (e.g. spiramycin) or the chloramphenicol used as topical for ocular infections (conjunctivitis, corneal ulcers), or with the subunit 30S as the tetracyclines or the aminoglycosides (e.g. streptomycin) (**Kohanski et al, 2010**).

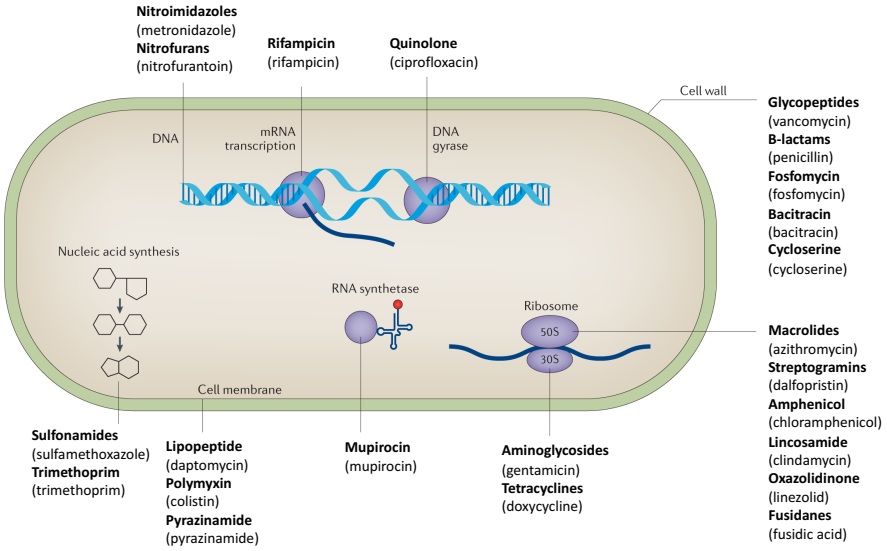

Fig 1.2. *Mechanisms of action of the antibiotics (**Boolchandani et al, 2019**).*

1.3) The β-lactam antibiotics

The D-D-transpeptidases are involved in the peptidoglycan biosynthesis and interacts via a conserved active-site serine with the extremity of the D-Ala-D-Ala peptide to form an acyl-enzyme. It is hydrolyzed by a water molecule to release the terminal D-Ala (carboxypeptidation reaction). It can also be attacked by the free NH_2 function of the diaminopimelic acid (DAP) (transpeptidation reaction) forming an interpeptidic bond to bridge two neo-synthesized glycan chains (**Fig 1.3 & 1.4B**).

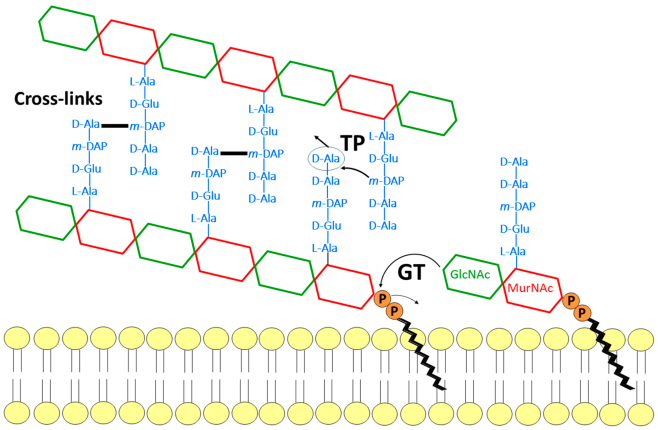

Fig 1.3. *Illustration of the glycosyltransferase (GT) and the transpeptidase (TP) activities catalyzed by the Penicillin Binding Proteins (PBP) in the peptidoglycan biosynthesis (**Sauvage & Terrak, 2016**).*

The β-lactam antibiotics are made of a four-piece ring (β-lactam ring) associated to a heterocycle and carrying lateral chains (R) chemically different in function of the antibiotic family. They act as suicide substrates towards the DD-transpeptidases (**Fig 1.4C**). Indeed, their structure mimics the structure of the D-Ala-D-Ala resulting in the formation of a highly stable acyl-enzyme complex (**Fig 1.4A**). Then, the transpeptidases are unable to ensure the peptidoglycan biosynthesis anymore, resulting in the bacterial lysis. The DD-transpeptidases are called Penicillin Binding Protein (PBP) for their ability to bind the penicillin (**Ghuysen, 1991**).

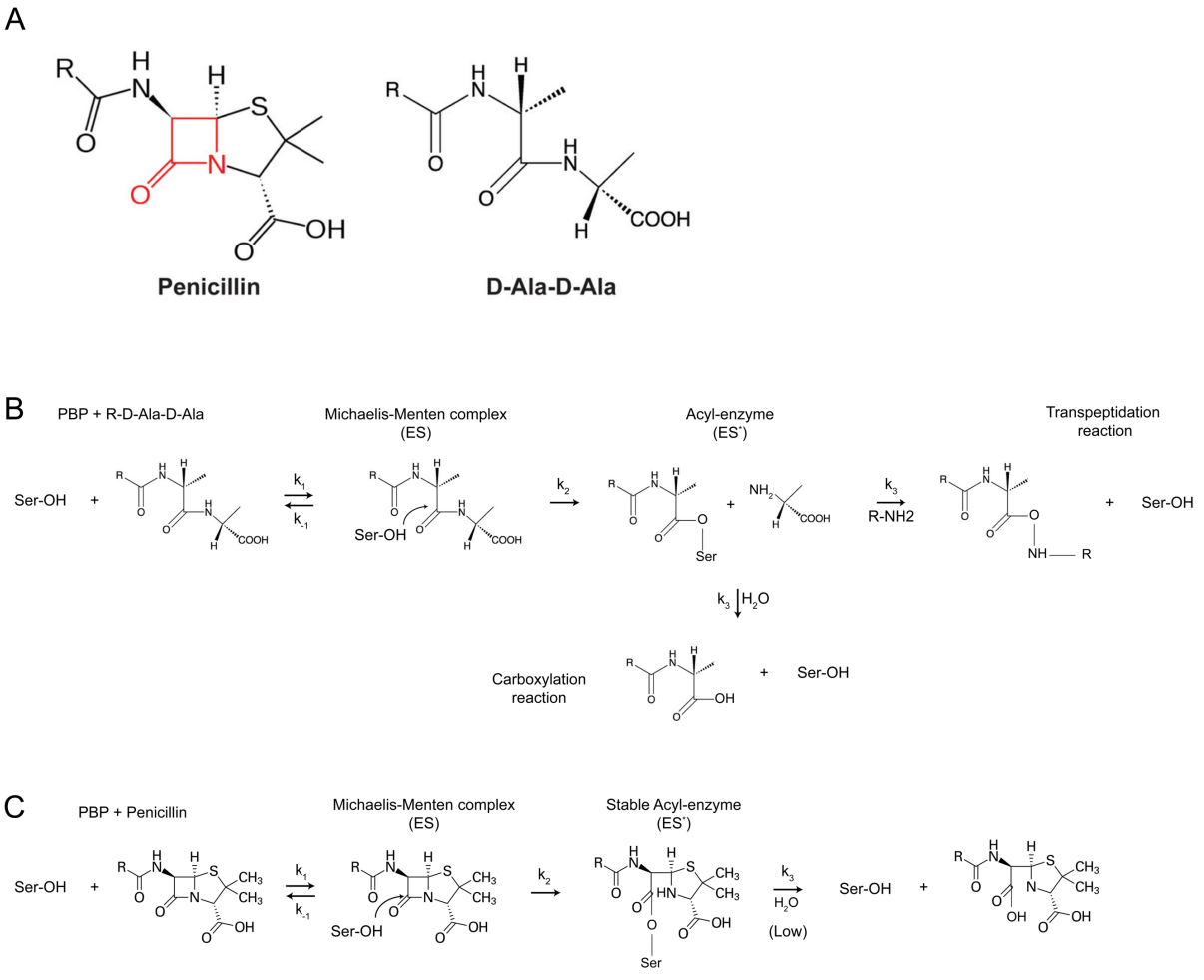

Fig 1.4. *General catalytic pathway of Penicillin Binding Proteins. (A) Structural mimicry between the penicillin antibiotic and the D-Ala-D-Ala peptide. (B) Transpeptidation and carboxylation reactions of the PBP for the D-Ala-D-Ala substrate. (C) Penicillin catalysis by the PBP. k_1 is the association constant between the enzyme and the substrate, while k_{-1} corresponds to the dissociation of the Michaelis-Menten complex (ES). k_2 and k_3 are the acylation and the deacylation constants of complexes ES and ES*, respectively (adapted from phD thesis of Patricia Lassaux).*

There are 4 families of β-lactam antibiotics: the penicillins, the cephalosporins, the monobactams and the carbapenems. They all present a common mode of action but differ by their spectrum of activity and their tolerance to the bacterial resistance (**Fig 1.5**) (**Bush & Bradford, 2016**).

The penicillins include all β-lactams carrying a 6-aminopenicillanic acid ring (6-APA). The first generation comprises natural (e.g. benzylpenicillin, penicillin V) and semi-synthetic (e.g. methicillin, oxacillin) penicillins largely utilized to threat infections caused by Gram-positive bacteria as *Streptococcus spp.* and *Staphylococcus aureus*. In the early 1970s, new penicillins were developed such as ampicillin, amoxicillin and piperacillin which are active against the *Enterobacterales* and *P. aeruginosa*. Nowadays, the increasing number of β-lactamases compromise the use of penicillins as monotherapy and some of them are combined to β-lactamase inhibitors (e.g. amoxicillin/clavulanate).

The cephalosporins were firstly isolated by Giuseppe Brotzu from *Cephalosporium acremonium* in 1948. Those cultures produced an active substance (cephalosporin C) against *Salmonella Typhi* causing the typhoid fever. It carries a 7-aminocephalosporanic acid ring (7-ACA) very similar to the penicillins, but formed by 6 atoms. The first (e.g. cephalexin, cefaclor) and the second (e.g. cefuroxime) generation of cephalosporins were introduced before the 80s and are mainly active against the Gram-positive cocci (e.g. *Streptococcus* and *Staphylococcus*). They are currently used to treat mild to moderate skin infections caused by the methicillin-susceptible *S. aureus* (MSSA) and respiratory infections such as sinusitis and bronchitis. However, they were rapidly rendered ineffective by the apparition of the TEM-1 penicillinase that rapidly spread in *Enterobacterales* after its first description in the 60's. Then, new agents were introduced in the 1980s such as the cefotaxime and the ceftazidime (class III), the cefepime (class IV) and the cefoxitin (cephamycin). They present a higher activity against Gram negative organisms but are less potent against staphylococci and enterococci. They are used for severe infections such as pneumonia and sepsis.

The carbapenems are natural or semi-synthetic and were developed from the thienamycin isolated for the first time in *Streptomyces cattleya* in 1976. They present a high affinity for PBPs, penetrate easily through the bacterial wall and resist to many β-lactamases.

They are employed to treat infections caused by Gram-positive and Gram-negative bacteria, sometimes in combination with inhibitors (e.g. imipenem/relebactam).

Finally, the monobactams (e.g. aztreonam) are only formed by one β-lactam ring. They are highly efficient against Gram-negative bacteria, but not against Gram-positive bacteria. The aztreonam combined to a β-lactamase inhibitor is probably a future option to treat infection caused by bacteria carrying multiple factors of resistance.

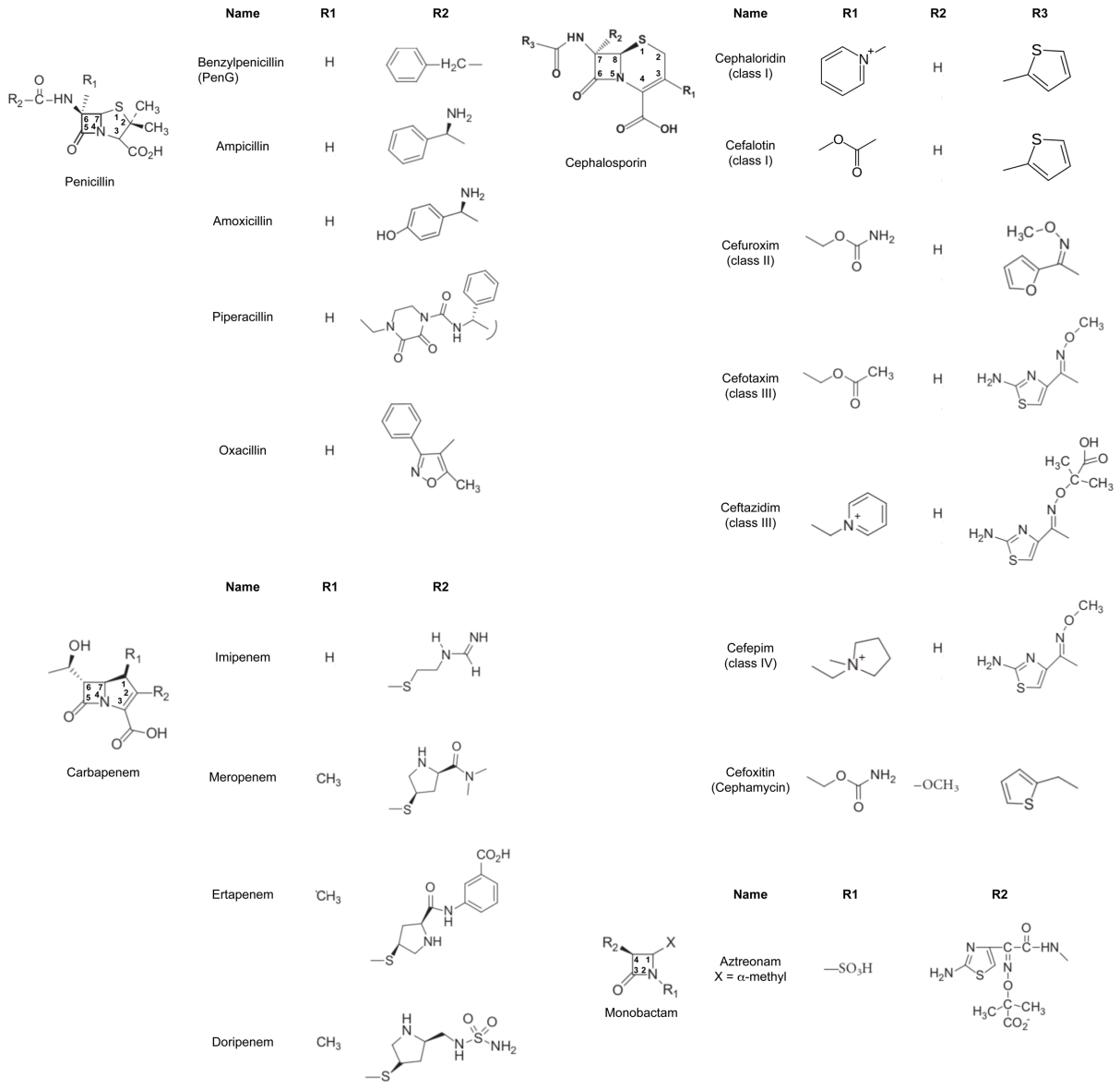

Fig 1.5. *Classification of the β-lactamines (adapted from Bush & Bradford, 2016).*

1.4) Resistance to β-lactam antibiotics

The intensive use of antibiotics lead to different mechanisms of resistance adopted by bacteria to abolish the efficacy of the β-lactam antibiotics.

The Gram-positive bacteria acquired the ability to produce PBPs presenting a reduced affinity for the β-lactam substrates, recovering their ability to play their transpeptidase function (**Lu et al, 2001**). It is notably the case of the PBP2a expressed by the methicillin-resistant *Staphylococcus aureus* where some structural constrains in the active site strongly decrease the formation of the acyl-PBP intermediate (**Lim & Strynadka, 2002**). A second strategy consists in the up-regulation of weakly expressed PBPs in order to compensate other PBPs inhibited by the β-lactams (e.g. PBP4 by *S. aureus*) (**Basuino et al, 2018**).

The Gram-negative bacteria carry an external membrane reducing the diffusion of the antibiotics into the periplasm. However, this membrane is composed by porins allowing a passive diffusion of small and charged molecules such as the β-lactam antibiotics. Then, the drug resistance is often associated to the decrease in porins expression or by mutations unfavorable for the permeation (**Vergalli et al, 2019**). Moreover, efflux pumps are employed to actively expel antibiotics or other toxic substances. They utilize either the hydrolysis of ATP or electrochemical gradient (Na^+, H^+) as energy supply, and can be overexpressed by regulatory systems activated by environmental signals such as the pH or the exposure to antibiotics (e.g. AraC, TetR). They are classified into MDR efflux pumps expelling a large range of substrates (e.g. Acr) or single-substrate efflux pumps generally conferring a high level of resistance for a specific substrate (e.g. macrolide-specific efflux pumps MacAB) (**Huang et al, 2022**).

Finally, the most commonly used mechanism of resistance, especially in Gram-negative bacteria, is the production of enzymes able to hydrolyze antibiotics carrying a β-lactam ring. They were firstly identified in 1940 by *Abraham and Chain* and were called penicillinase (**Abraham & Chain, 1940**). Few decades later, this family of enzymes was called β-lactamases. I will be mainly interested in this mode of resistance in the further part of this work.

1.5) The β-lactamases

1.5.1) Classification of β-lactamases

The increasing number of β-lactamases rendered their classification necessary (**Fig 1.6**). This classification largely evolved over time and is based on either the sequence identity (I) or the functionality of the enzyme (II). We will mainly use the sequence identity classification in the manuscript.

(I) The simplest classification is based on the protein sequence (**Ambler, 1980**). In 1980, Ambler determined two classes of β-lactamases from five known sequences. The class A gathered the active-site serine β-lactamases presenting a penicillinase activity, while the class B comprised the metallo-β-lactamases. In 1981, *Jaurin and Grundström* proposed a second class of serine β-lactamases, the class C. They present a low sequence identity with the class A and were originally considered as cephalosporinases (**Jaurin & Grundstrom, 1981**). Finally, *Dale* described a third class of active-site serine β-lactamases (class D) called oxacillinases due to their capability to hydrolyze the oxacillin (**Dale et al, 1985**).

(II) In 2009, *Karen Bush* updated the functional classification and regrouped all β-lactamases in three different groups (**Bush & Jacoby 2009**). The group 1 corresponds to cephalosporinases and belongs to class C. The majority are more active against the cephalosporins than penicillins and few of them hydrolyze oxymino-β-lactams (e.g. cefotaxime, ceftazidime) or cephamycins (cefoxitin). All resist to clavulanic acid and tazobactam. The group 2 comprises all active-site serine β-lactamases belonging to classes A and D and presenting a large range of activity profiles. Finally, the group 3 regroups the metallo-β-lactamases (class B) which present zinc ion(s) in their active site crucial for the hydrolysis of the carbapenems. They are not inhibited by clavulanic acid or tazobactam, but their activity drops dramatically in presence of EDTA chelating metal ions. This group is divided in three subclasses (B1, B2 and B3) which differ by the zinc ion(s) content and their activity profile.

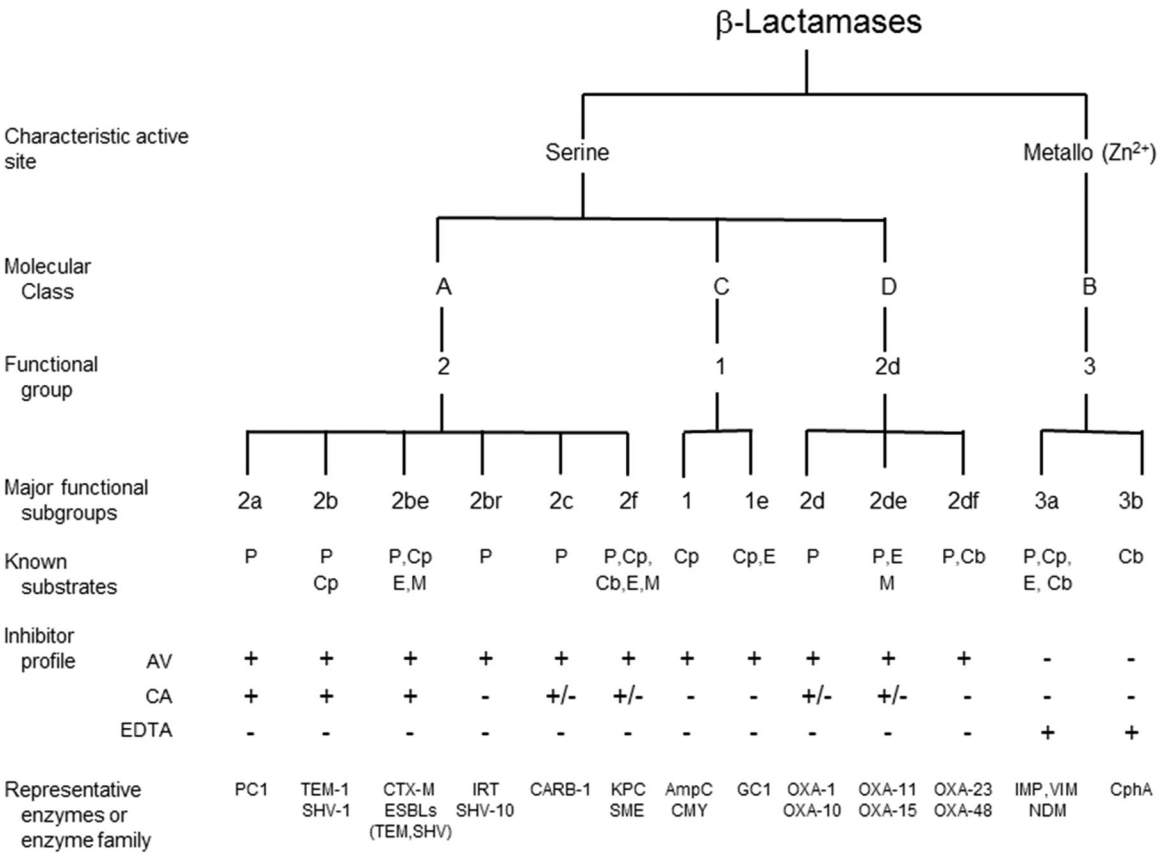

Fig 1.6. *Molecular and functional classifications of the β-lactamases (**Bush, 2018**). P: penicillin, Cp: cephalosporin, E: extended-spectrum cephalosporin, M: monobactam, Cb: carbapenem, AV: avibactam, CA: clavulanic acid.*

1.5.2) Active-site serine β-lactamases

Active-site serine β-lactamases and PBPs present a similar catalytic pathway (**Fig 1.4B & 1.7**). This mechanism starts with the formation of the non-covalent Michaelis-Menten complex (ES), followed by a covalent acyl-enzyme (ES*). Finally, a water molecule attacks the carbonyl carbon of the ester group to break the ester bond and to release the inactive product. As opposed to PBPs, the deacylation rate in β-lactamases is very fast (high k_3) resulting in a unstable complex (**Matagne et al, 1998**).

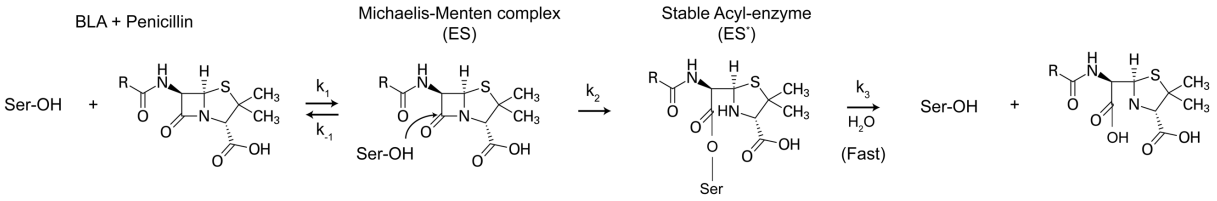

Fig 1.7. *Mechanism of hydrolysis of a β-lactam ring by a β-lactamase.*

The active-site serine β-lactamases are structurally similar to PBPs strengthening the idea whereby both enzymes diverged from a common ancestor. There are formed by two domains, one α and one α/β, between which is found the active site. Even though they present low sequence identities, some motifs are conserved and crucial for the catalytic activity of the enzymes and the binding of the substrate (**Table 1.1**). The next sections will describe in depth each class of β-lactamases.

β-lactamase	Motif 1	Motif 2	Motif 3	ω loop	General Base
A	***S**70**XXK**73	**R/K**234**T/S**235**G**236	**S**130**D**131**X**132	**164-179**	**E**166
C	***S**64**XXK**67	**K**315**T/S**316**G**317	**Y**150**D/A**151**N**152	**189-226**	**Y**150
D	***S**67**XXK**70	**K**205**T/S**206**G**207	**S**115**XV**117	**140-161**	**K**70 carbo

Table 1.1. *Conserved motifs and general base of serine active β-lactamases. *S active serine.*

1.5.3) Class A β-lactamases

1.5.3.1) Classification

Class A β-lactamases are mainly subdivided in 6 phylogenetic groups (A-F), five in the subclass A1 (B-F) and one group (A) belonging to the isolated subclass A2 (**Fig 1.8**). The subclass A2 consists in chromosomic-encoded β-lactamases and are species-specific (e.g. CfxA-*Bacteroides vulgatus*) (**Parker & Smith, 1993**). They hydrolyze cephalosporins and are also active against penicillins and monobactams. The five other groups include β-lactamases with different profiles of activity. Most β-lactamases of group C possess an activity LSBL (limited spectrum β-lactamase). They hydrolyze penicillins, first-generation cephalosporins and monobactams (e.g. TEM, SHV). The group D represents the largest diversity of enzymes encoded by Gram-positive bacteria (e.g. BlaZ). The group E includes ESBL clusters (extended-spectrum β-lactamase) active against the oxyminocephalosporins (e.g. CTX-M, BES-1), but also a CARBA cluster (carbapenemase) where the representatives hydrolyze the carbapenems (e.g. KPC). Finally, the group F mainly comprises enzymes identified in environmental species with a limited pathogenicity in humans. Some of them are carbapenemase such as BKC-1 and PAD-1 (**Philippon et al, 2019**).

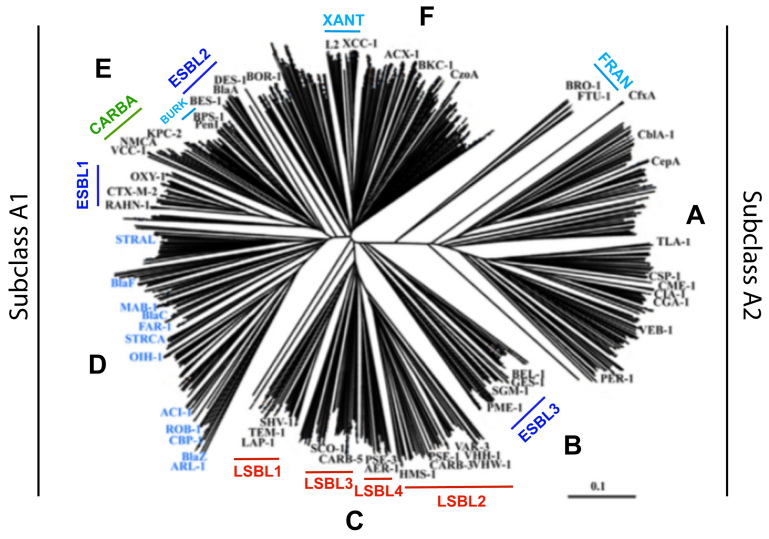

Fig 1.8. *Phylogram representing the diversity of 700 class A β-lactamases. LSBL (limited-spectrum β-lactamase); ESBL (extended-spectrum β-lactamase); CARBA (carbapenemase); BURK (Burkholderia); XANT (Xanthomonas); FRAN (Francisella); (**Philippon et al, 2019**).*

1.5.3.2) Structural characterization of class A β-lactamases

Despite a low sequence identity (**Fig 1.9**), class A β-lactamases share an important structural analogy (**Fig 1.10B**), reflecting a divergent evolution from a common ancestor.

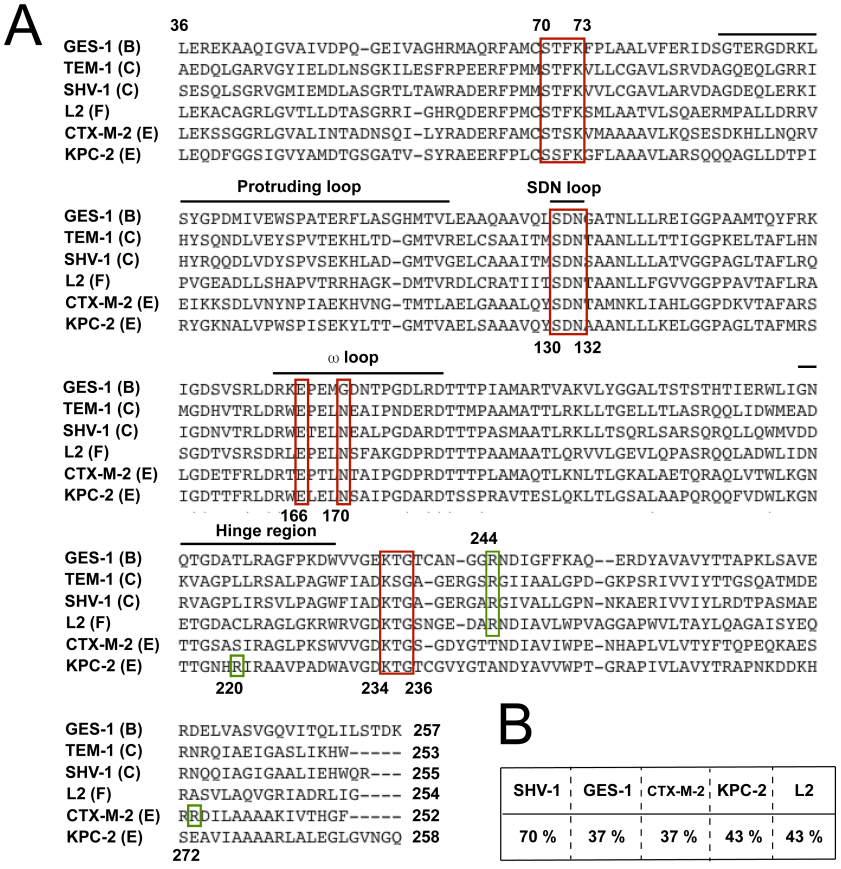

Fig 1.9. *Multiple sequence alignments of class A β-lactamases belonging to sub-groups B, C, E and F. (A) Strictly conserved motifs and the conserved arginine are surrounded in red and green, respectively. The main loops forming the active site are indicated by a black line. (B) Percentage sequence identities of class A members and TEM-1.*

Class A β-lactamases are made up of two domains: one domain only composed by α-helices (the α domain), and one domain with α-helices and β-strands (the α/β domain) (**Fig 1.10A**). The active site is located between the two domains and presents several conserved elements involved in the substrate recognition and the in catalytic activity of the enzyme (**Fig 1.10C**).

The active site is firstly composed by the N-terminal part of the first helix of the α domain carrying the first conserved motif (**S**70XX**K**73), with the active-site serine involved in the formation of the acyl-enzyme.

The second element (**S**130**D**131**N**132) is located on the short SDN loop. The S130 is involved in the hydrogen bond network, while the residue N132 plays a role in the transition-state stabilization via a H-bond with the O16 of the benzylpenicillin (**Jacob et al, 1990**).

The third conserved motif (**K**234**T**235**G**236) is located on a β-strand constituting the β-sheet from the α/β domain. The K234 forms a H-bond with the S130 and also belongs to the hydrogen bond network (**Brannigan et al, 1991**). Furthermore, the S235 makes a H-bond with the carboxylate group of the substrate (C3 for penicillin) and contributes to create the "carboxylic pocket" resulting in the correct positioning of the antibiotic and the stabilization of the acyl-enzyme.

The residue R244 (e.g. TEM-1) contributes to the "carboxylic pocket" since it directly interacts with the carboxylate group of the substrate and indirectly via a water molecule stabilized by the carbonyl group of the V216 (hinge region) and the side chain of the R244 (**Strynadka et al, 1992** & **Lamotte-Brasseur et al, 1991**). In class A β-lactamases, the guanidium function can be brought by the R244 such as TEM-1 and SHV-2, but also by another arginine like in CTX-M-2 (R272) and KPC-2 (R220) (**Marciano et al, 2009)**. The conservation of this positive charge highlighted its primordial role for the activity of almost all class A β-lactamases.

Importantly, the catalytic activity of class A β-lactamases induces the formation a tetrahedral intermediate where the carbonyl oxygen is negatively charged (**section 1.5.3.3**). This negative charge is stabilized by the main chain nitrogen of the S70 and the residue 237 (e.g. alanine for TEM-1) forming the oxyanion hole.

The last conserved element corresponds to the omega loop (residues 164 to 179 in TEM-1) which takes an "omega" shape via a salt bridge between the residues R164 and D179.

The N-terminal part of the ω loop contains the general base E166 and the residue N170 assuring the correct positioning of the catalytic water molecule located near to S70.

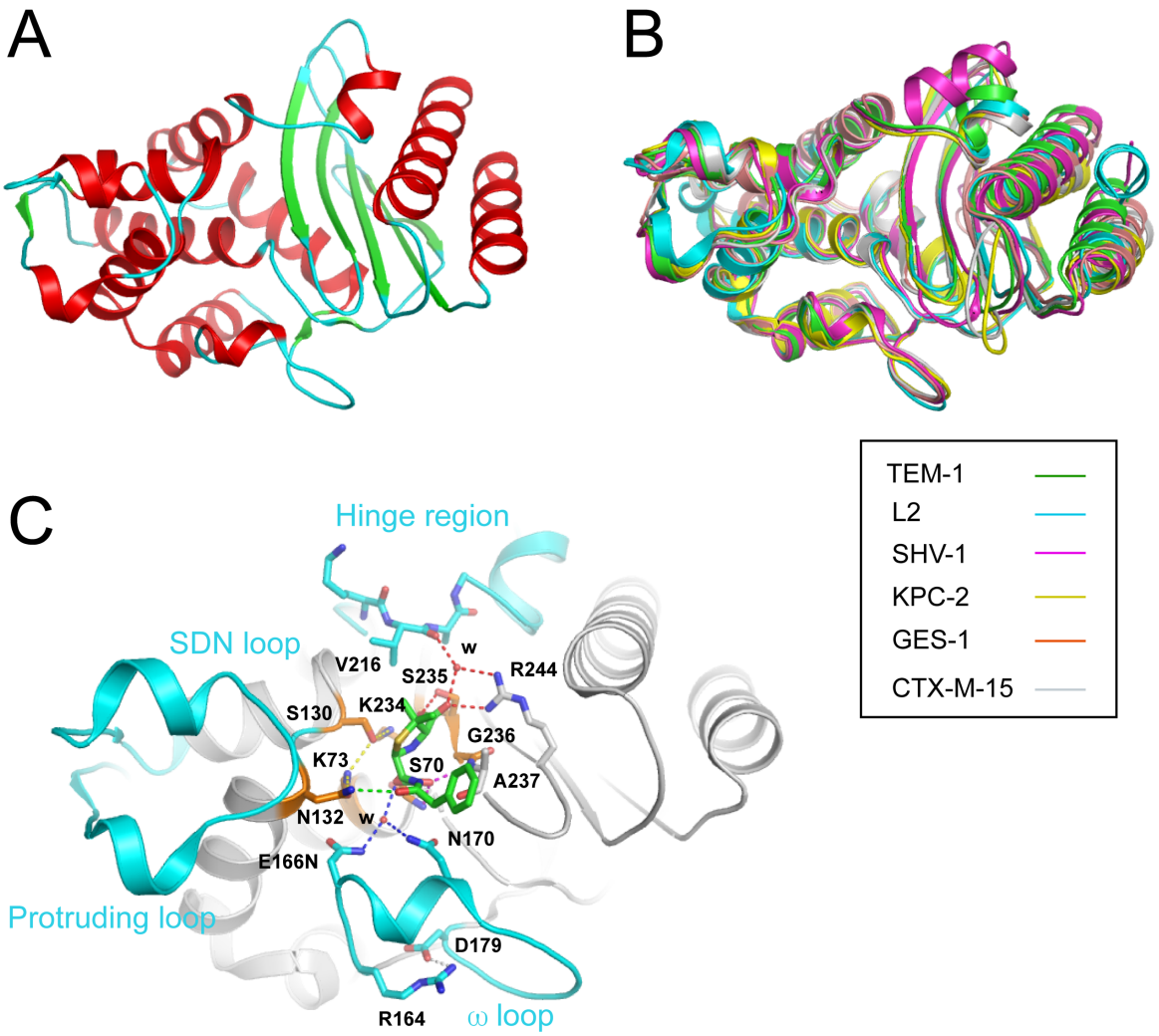

Fig 1.10. *Structural characterization of class A β-lactamases. (A) Overall representation of TEM-1 (PDB code 1m40) with helices, β-strands and loops colored in red, green and cyan, respectively. (B) Superposition of class A β-lactamases TEM-1 (PDB code 1m40), L2 (PDB code 1N4O), SHV-1 (PDB code 1ONG-3), KPC-2 (PDB code 2OV5), GES-1 (PDB code 2QPN) and CTX-M-15 (PDB code 4HBT-2). (C) Representation of the acyl-enzyme TEM-1 E166N with benzylpenicillin in green (PDB code 1FQG). Loops forming the active site are illustrated in cyan. Conserved motif 1 (**S**70XX**K**73), motif 2 (**S**130**D**131**N**132) and motif 3 (**K**234**T**235**G**236) residues are colored in orange. The H-bond network between residues K73, S130, K234 and N132 is represented by dotted yellow lines; The H-bond between the residue N132 and the substrate by a dotted green line; The H-bond networks involved in the "carboxylate pocket" and in the oxyanion hole are represented by dotted red and magenta lines, respectively.*

1.5.3.3) Catalytic mechanism of class A β-lactamases

Even though the accumulation of x-ray models, NMR studies, QM/MM studies… the acylation mechanism of class A β-lactamases remains controversial (**Fig 1.11**).

The first pathway implies the residue E166 acting as the general base to activate the S70 via a catalytic water molecule. The activated Oγ of the S70 attacks the β-lactam carbonyl group forming a tetrahedral intermediate where the carbonyl oxygen is negatively charged. Then, the residue S130 delivers back a proton to N4 of the thiazolidine group by the intermediate of the residue K73 (**Lamotte-Brasseur et al, 1991 & Hermann et al, 2005**).

However, the E166N mutant retains its long-lived acyl-enzyme (**Adachi et al, 1991**), resulting in an alternative acylation pathway where the residue K73 acts as a proton abstractor to activate the S70 (**Strynadka et al, 1992**). The K73A mutant strengthens this hypothesis since it completely abolishes the formation of a covalent acyl-enzyme (**Tremblay et al, 2010**). To be functional, K73 must be unprotonated and its location in an electrostatic environment (e.g. K234, N132) is favorable to attenuate its side chain pKa to 8.0-8.5 (**Golemi-Kotra et al, 2004**). This is debated with another publication where they measured the pKa of the K73 which was superior to 10 rendering this residue unable to accept a proton (**Damblon et al, 1996**). But this is insufficient at neutral pH and NMR titrations clearly demonstrated the protonated and unprotonated forms of the residues K73 and E166, respectively, in the apo-enzyme. The two residues are close to each other and it is conceivable that E166 becomes protonated in the non-covalent Michaelis complex, resulting in the unprotonated K73 able to activate the S70 (**Golemi-Kotra et al, 2004**). Nowadays, it was suggested a dual participation of the two pathways for the formation of the tetrahedral species via the S70 (**Meroueh et al, 2005**).

The mechanism of deacylation is widely accepted and corresponds to the hydrolysis of the covalent link between the β-lactam and the active serine. The catalytic water coordinated by both E166 and N170 is activated via the residue E166 and attacks upon the carbonyl carbon of the acyl-enzyme. This provokes the release of the cleaved β-lactam and the regeneration of the enzyme (**Lamotte-Brasseur et al, 1991**).

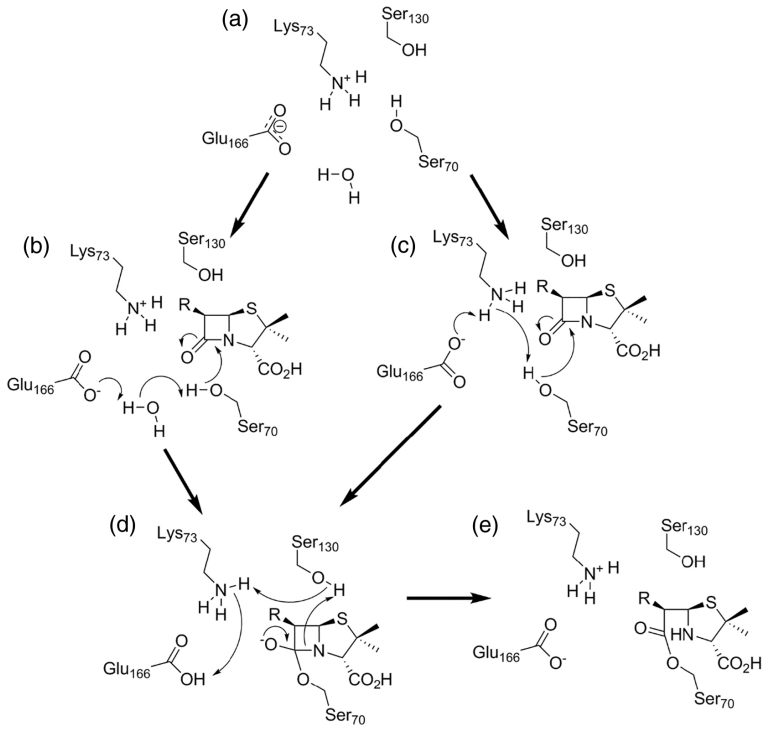

Fig 1.11. *Acylation mechanisms of class A β-lactamases. The E166 and K73 are deprotonated and protonated, respectively, in the apo-enzyme (a). The serine S70 is activated by the E166 via a water molecule (b), or by the K73 with the subtraction of one proton via the residue E166 (c), leading to a negatively charged tetrahedral intermediate (d) and followed by the protonation of the amide nitrogen from S130 to form the acyl-enzyme(e) (**Tooke et al, 2019a**).*

1.5.3.4) Extended-spectrum TEM family β-lactamases (TEM_{ESBL})

TEM-1 presents a high activity for penicillins and first and second-generation of cephalosporins. However, the oxymino-cephalosporins are poor substrates since their lateral chains hardly enter into the active site. Their massive use since the beginning of the 80s have led to mutations improving the efficacy of the enzyme for the oxymino-cephalosporins, with better affinities (lower K_m) and/or a more rapid turnover (higher k_{cat}) (**Palzkill, 2018**).

The G238S mutation is the best representative of the TEM extended spectrum β-lactamases (TEM_{ESBL}). The hydroxyl group of the serine forms a H-bond with the oxime group of the oxymino-cephalosporins increasing the affinity of the enzyme for the substrate (**Cantu & Palzkill, 1998**). Another study described the lateral chain of the serine creates a steric hindrance with the surrounding residues and the asparagine at position 170 provoking the motion of the β3-strand and the ω loop and expanding the active site (**Saves et al, 1995a**).

Then, the oxymino-cephalosporins are more easily accommodated in the active site. The G238S mutation can be co-expressed with other mutations as in TEM-52 (E104K/M182T/G238S). TEM-52 presents a more opened conformation of the active site due to the reorientation of the 238-243 loop out of the active site (**Orencia et al, 2001**) (**Fig 1.12A**).

The R164S mutant increases the activity for the oxymino-cephalosporins, but presents a decreased efficacy for penicillins and small cephalosporins. The residue R164 normally interacts with D179 in TEM-1 for the stabilization of the ω loop. The mutation R164S provokes the motion of the omega loop and the reorganization of some residues located on the α5-Helix (e.g. N132). It also displaces the residues 85-142 with a better access for large oxymino side chain cephalosporins (**Maveyraud et al, 1996**). This substitution in the triple mutant E104K/R164S/M182T (TEM-64) induces the flip of the residue N170 by almost 180° opening a large cavity in the active site (**Wang et al, 2002a**). (**Fig 1.12B**). More recently, the x-ray structure of the R164S mutant described the high heterogeneity of the ω loop allowing a better accommodation of the substrate in the active site (**Dellus-Gur et al, 2015**).

It was firstly suggested that the substitutions E104K and E240K established electrostatic interactions with the oxymino-cephalosporins (**Sowek et al, 1991**). However, advanced molecular dynamic studies highlighted the lysines were unable to directly bind the substrate meaning their respective roles are still unclear (**Singh & Dominy, 2012**).

Finally, the mutation M182T increases the stability of the enzyme. It is not directly involved in the ESBL behavior of the enzyme, but it compensates for the loss of stability due to ESBL mutations (e.g. G238S and R164S). The threonine in position 182 establishes a H-bond with the residue E63 by the intermediate of a water molecule strengthening the junction between the domains α and α/β. Moreover, it makes an additional H-bond with the nitrogen atom of A185 for the stabilization of the adjacent α-helix (**Wang et al, 2002a**) (**Fig 1.12C**).

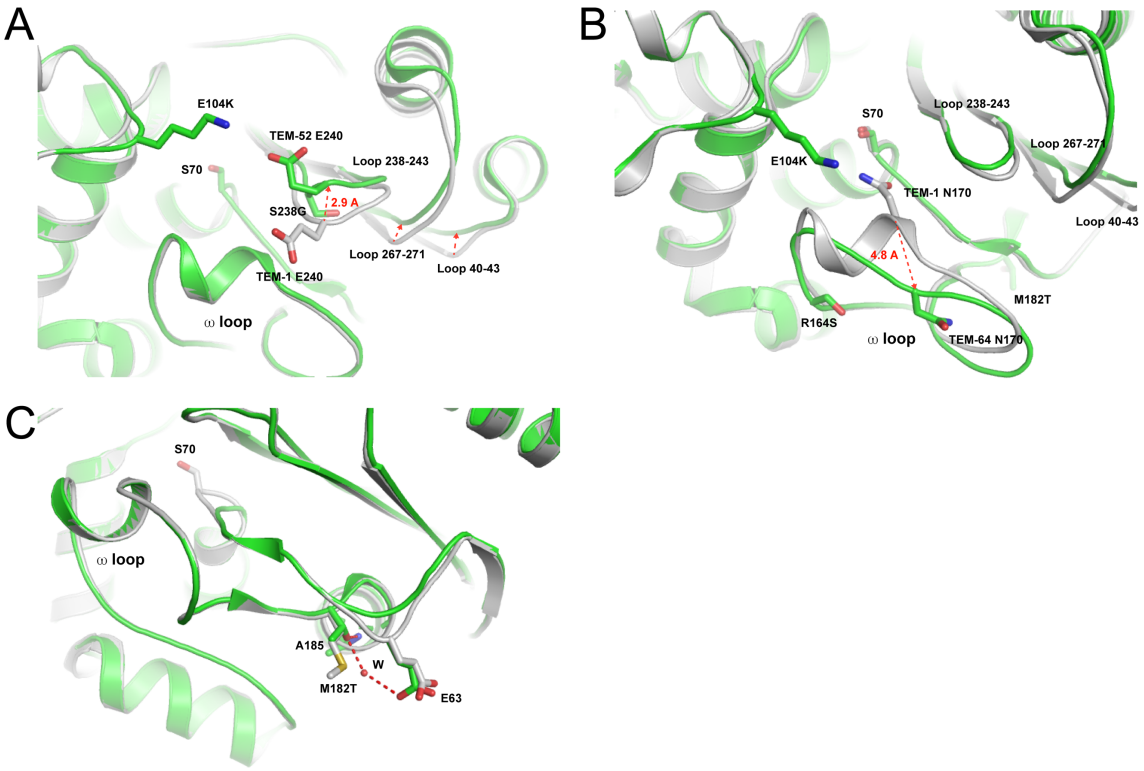

Fig 1.12. *Overlay views of TEM-1 (PDB code 1FQG) and TEM_{ESBL} represented in gray and green, respectively. (A) In TEM-52 (E104K/M182T/G238S) (PDB code 1HTZ), the mutation G238S displaces the E240 side chain by 2.9 Å from its original position and induces the movement of the adjacent 267-271 and 40-43 loops (illustration adapted from Orencia et al, 2001). (B) The mutation R164S in TEM-64 (E104K/R164S/M182T) (PDB code 1JWZ) disrupts the interaction of the residue with the D179 changing the configuration of the ω loop and consequently opening more space in the active site. (C) The mutation M182T (PDB code 1I7U) establishes new H-bonds with residues E63 and A185 increasing the stability of the enzyme.*

1.5.3.5) Inhibitor resistant TEM family β-lactamases (TEM_{IRT})

The intensive use of old-age inhibitors (**section 1.5.7.1**) resulted in the selection of a large panel of mutations abolishing the efficacy of the inhibitors but maintaining a sufficient activity for the enzyme against β-lactam substrates. (**Matagne et al, 1998**).

The residue R244 binds directly the carboxylate group of the inhibitor, as for the β-lactam antibiotic (**Ness et al, 2000**), while the water molecule is implicated in the inactivation mechanism by the clavulanic acid and the sulbactam (**Fig 1.13A**) (**Imtiaz et al, 1993 & Imtiaz et al, 1994**). Then, the substitution R244S (e.g. TEM-30) disrupts the H-bond for the

stabilization of the complex inhibitor/enzyme and the serine cannot coordinate the water molecule essential in the inactivation process by the clavulanic acid (**Fig 1.13B**) (**Wang et al, 2002b**).

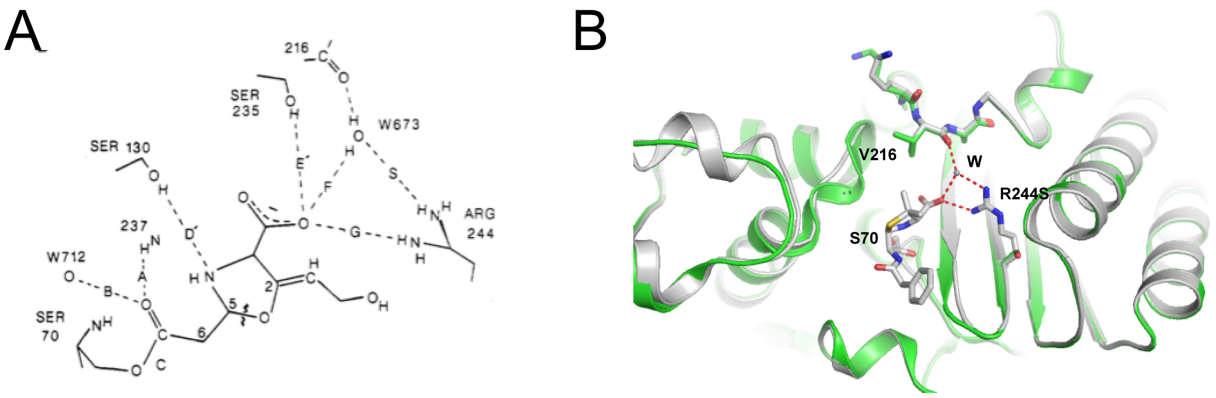

Fig 1.13. *(A) Open-ring acetylated complex of clavulanate with TEM-1 calculated by docking simulations (**Imtiaz et al, 1993**). (B) Superposition of the acyl-enzyme PenG/TEM-1 E166N (PDB code 1FQG) and TEM-30 (PDB code 1hly) represented in gray and green, respectively.*

The mutations M69I (TEM-32), M69L (TEM-33) and M69V (TEM-34) slightly modify the active site of the enzyme. As an example, the isoleucine at position 69 distorts the active-site serine S70 resulting in a dual configuration (e.g. TEM-32) (**Fig 1.14**). It was not clearly demonstrated that this flexibility may impact the formation of the acyl-enzyme. However, this effect is transmitted to the S130 which adopts a new conformation far from its original position, rendering the serine inefficient in the process of inactivation by the clavulanic acid (**section 1.5.7.1**) (**Wang et al, 2002b**). Moreover, the replacement of the methionine by a longer hydrophobic side chain alters the oxyanion hole and changes the positioning of the R244 located on the β4 strand (**Bonomo et al, 1995**).

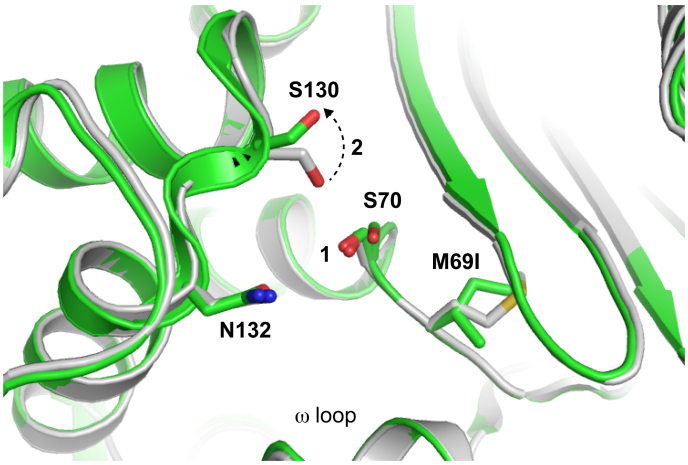

Fig 1.14. *Schematic representation of TEM-32 (M69I, M182T) active site (PDB code 1LI0, green) superimposed to the apo-enzyme TEM-1 (PDB code 1m40, gray). The isoleucine at position 69 induces a dual configuration of the S70 (1) and the rotation of the Oγ S130 64° away from the original configuration (2).*

The S130G substitution (e.g. TEM-76) is very rare, notably due to the importance of the S130 in the catalytic activity of the β-lactamase. Nevertheless, TEM-76 retains some activity against the β-lactam due to a new catalytic water molecule replacing the Oγ function of the S130 as proton donor for the hydrolysis of the substrate. This explains why the serine is exclusively changed in glycine to easily accommodate the water molecule (**Jacob et al, 1990**). As expected, the substitution S130G mainly confers the resistance to inhibitors due to the deletion of the cross-linking between the residues S70 and S130 essential in the inactivation process (**section 1.5.7.1**). Intriguingly, this mutation also brings subtle structural modifications observed in other IRTs mutants, as the disorder of the catalytic water molecule stabilized by the guanidium group of the R244 and the carbonyl function of the V216 (e.g. TEM-30 (R244S) and TEM-84 (N276D)) perturbing the inactivation process (**Fig 1.15**) (**Thomas et al, 2005**).

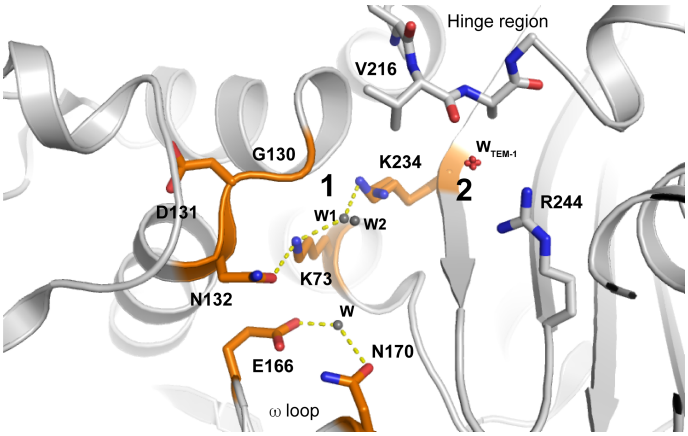

Fig 1.15. *Active site representation of TEM-76 (S130G) (PDB code 1YT4) with the water molecule (in a dual configuration (W1 and W2)) replacing the Oγ function of the S130 (1) and the absence of the water molecule stabilized by the R244 and the carbonyl function of the V216 (W_{TEM-1}) (2).*

One last mutation which accounts for the inhibitor-resistance behavior of TEM is the substitution N276D (e.g. TEM-84). The residue N276, located on the α12-helix, establishes one electrostatic interaction with the guanidium group of the residue R244 (**Olehnovics et al, 2021**). Interestingly, the mutant forms more interactions with the residue R244 decreasing the positive electrostatic potential of the arginine. Consequently, this disrupts its interaction with the carboxylate group of the substrate resulting in a lower affinity (**Saves et al, 1995b**). Moreover, the coordinated water molecule is absent in the crystallographic model of the mutant what totally affects the inactivation process (**Fig 1.16**) (**Swaren et al, 1999**).

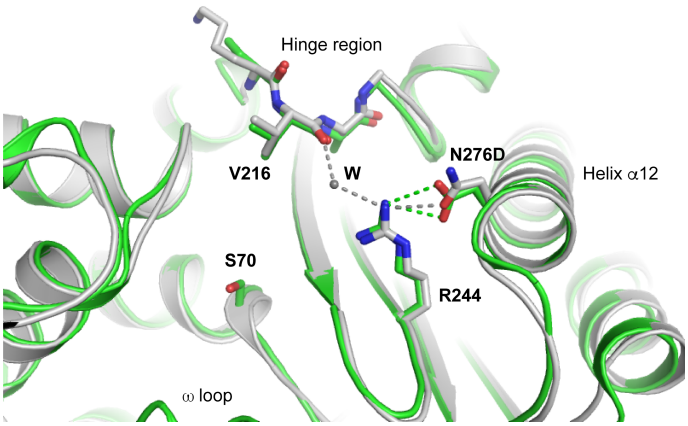

Fig 1.16. *Superposition of TEM-1 (PDB code 1BTL, gray) and TEM-84 (PDB code 1CK3, green). The water molecule involved in the inactivation process is lacking in TEM N276D.*

1.5.3.6) Carbapenemase activity of class A β-lactamases

Carbapenems (**Fig 1.5**) are generally utilized as last barrier to fight the bacterial resistance. They inactivate almost all class A β-lactamases such as TEM-1 (**Maveyraud et al, 1998**) or SHV-1 (**Nukaga et al, 2008**).

The structure of SHV-1 in complex with the meropenem (**Fig 1.17A**) emphasized the stabilization of the acyl-enzyme via the interaction of the carbapenem C3-carbonyl group with the α-amine functions of A237 and S70 (oxyanion hole). Moreover, the reorientation of the Oγ function of the S130 creates an interaction with K234 and disrupts the H-bound network with K73 amino group present in the apo-enzyme. In this conformation, S130 is not able to transfer the proton for the hydrolysis of the substrate anymore. Finally, the structure of the complex finally demonstrated that the 6-α-1-R-hydroxyethyl group of the carbapenem is the main determinant for the reduction of the deacylation rate. It firstly obligates the SDN loop to change its configuration to accommodate the hydroxyethyl group with the hydroxyl function interacting with the lateral chain of the residue N132. Furthermore, the structure revealed the catalytic water molecule interacts with the residues E166 and N170, but also with the hydroxyethyl substituent. This reduces the nucleophelicity of the deacylation water molecule and contributes to the acyl-enzyme stability. Intriguingly, the residue E166 is normally deprotonated to activate the water molecule. The general base presents a proton in the complex to optimize the hydrogen bond network around the deacylation water molecule contributing to decrease the deacylation rate of the enzyme for carbapenems (**Fig 1.17B**).

Serine carbapenemases such as KPC (*Klebsiella pneumoniae* carbapenemase) acquired the ability to hydrolyze carbapenems. The structure of KPC-2 in complex with the bicine molecule highlighted features in the active site, compared to classical class A β-lactamases, explaining its carbapenemase activity (**Ke et al, 2007**). The majority of residues in the KPC active site are identical to TEM-1 or SHV-1 excepted for residues T235, T237, R220 and H274 interacting with the carboxyl moiety of the bicine and probably of carbapenems (**Fig 1.17C**). The complex faropenem/KPC-2, compared to the complex imipenem/TEM-1, illustrated the shift of some residues which may explain the carbapenemase activity of KPC-2. Firstly, the S70 is positioned less deep in the active site creating more space to accommodate bulkier

substrates and avoiding steric clashes between the 6-α-1-R-hydroxyethyl group and the nearby residues. Moreover, the S130 returns to its original position ensuring the bridging with the residue K73. Finally, the reorientation of the residue N132 disrupts the H-bond established with the 6-α-1-R-hydroxyethyl group in non-carbapenemase class A β-lactamases and unfavorable for the carbapenem hydrolysis (**Fig 1.17D**) (**Pemberton et al, 2017**).

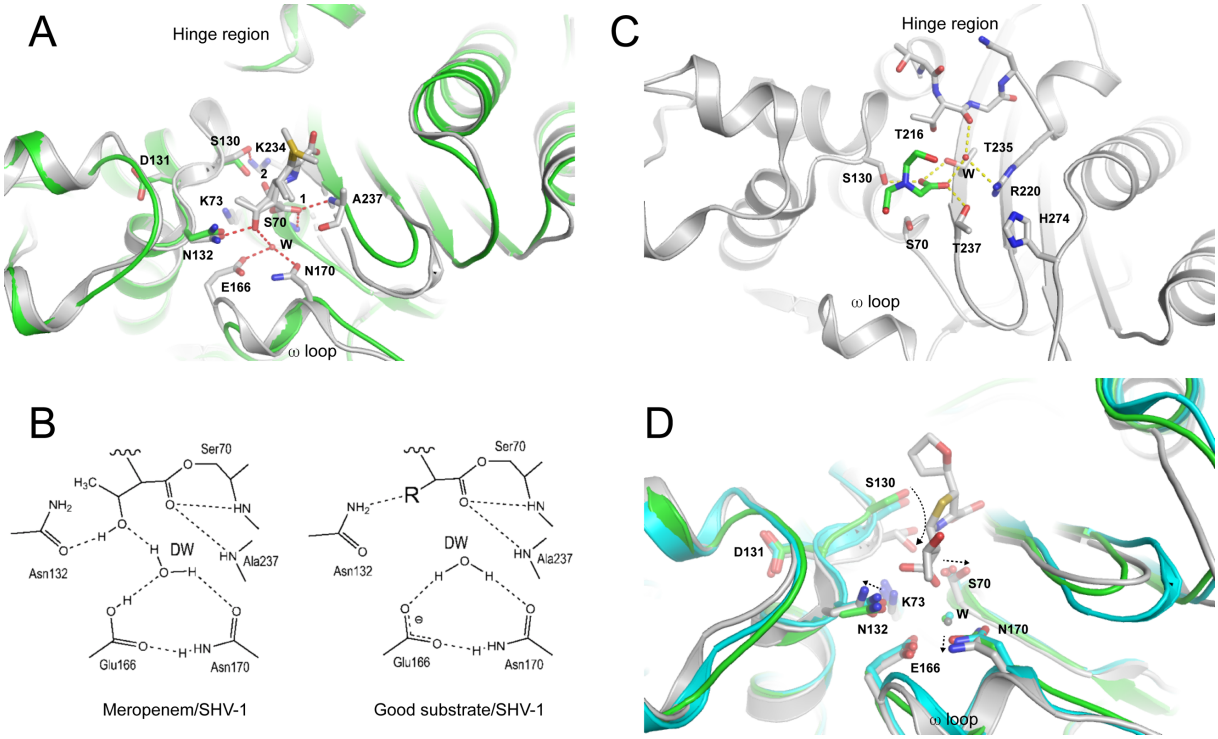

Fig 1.17. *Carbapenemase activity of class A β-lactamases. (A) Superposition of the apo-*enzyme *SHV-1 (green, PDB code 1SHV) and SHV-1 complexed to the meropenem (gray, PDB code 2ZD8). The meropenem takes two configurations with the carbonyl function into (1) or away (2) from the oxyanion hole. (B) H-bond network around the catalytic water molecule for the acyl-enzyme meropenem/SHV-1 and for the complex between SHV-1 and a good substrate (**Nukaga et al, 2008**). (C) Model of KPC-2 in complex with the bicine molecule (PDB code 2OV5) highlighting interactions applied in the carboxylate group stabilization. (D) Superposition of complexes faropenem/KPC-2 (PDB code 5UJ4, gray), imipenem/TEM-1 (PDB code 1BT5, green) and meropenem/SHV-1 (cyan). Both imipenem and meropenem were removed for more visibility. Shifts of crucial residues for the carbapenemase activity of KPC-2 are represented by black dotted lines.*

1.5.4) Class C β-lactamases

1.5.4.1) Structural generalities of class C β-lactamases

As for the class A β-lactamases, the class C β-lactamases (AmpCs) present an α-helical and an α/β domain, with the active site located in the center of the enzyme (**Fig 1.18A**). The active site is subdivided in two distinct domains formed by different loops: the R1 site accommodating the R1 side chain of the β-lactam via the ω loop, the c-loop and the P2 loop; the R2 site interacting with the R2 side chain via the R2 loop (**Fig 1.18B**). Their active site contains the three conserved motifs **S**64XX**K**67, **Y**150X**N**152 and **K**315XX**A**318 intervening in the catalytic activity of the enzyme. As opposed to class A β-lactamases, the active site of the AmpCs possesses a more open configuration, mainly due to the large number of loops, allowing the accommodation of cephalosporins with a bulkier side chain.

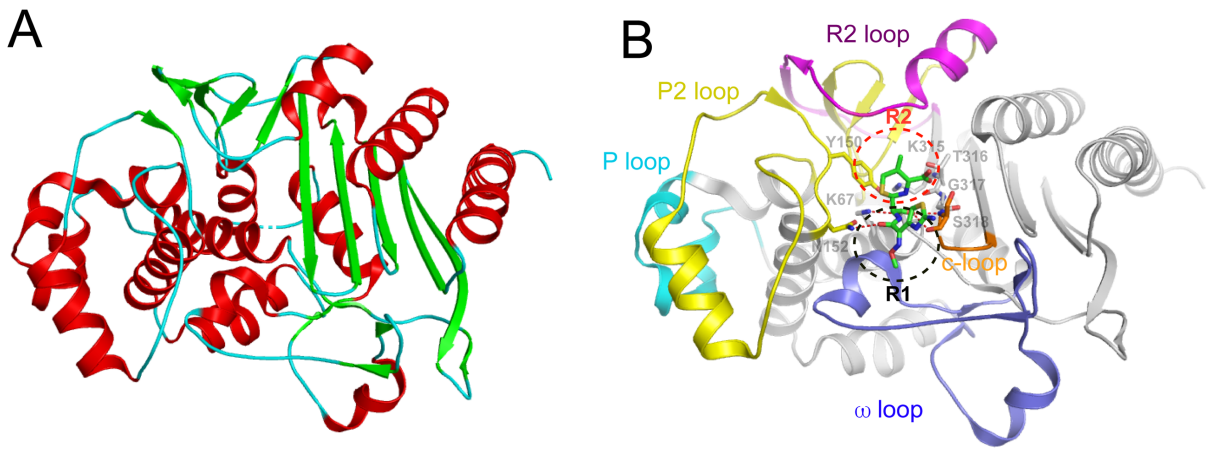

Fig 1.18. *Structural characterization of class C β-lactamases. (A) Global representation of ACC-1 (B) General overview of cefotaxime/ACC-1 acyl-enzyme (PDB code 6K9T) with the active site delimited by the ω loop (blue), the R2 loop (purple), the P2 loop (yellow), the P loop (cyan) and the c-loop (orange). The R1 and R2 binding sites are represented by black and red dotted circles, respectively.*

1.5.4.2) Kinetic properties of class C β-lactamases

The class C β-lactamases hydrolyze efficiently the penicillins and both first cephalosporin generations (e.g. cefalotin, cephaloridine). The oxyminocephalosporins (e.g.

ceftazidime, cefotaxime), the monobactams (e.g. aztreonam) and the penams (e.g. imipenem) generally constitute poor substrates. However, AmpCs bind nearly all β-lactams with a high affinity (low K_m values) representing an advantage in low substrate concentrations (**Galleni & Frère, 1988; Bauvois et al, 2005**). Unfortunately, AmpCs are not inhibited by β-lactamase's classical inhibitors such as the clavulanic acid (**Bush et al, 1993 & Endimiani et al, 2010**).

Some AmpCs possess an extended-spectrum cephalosporinase profile and are able to hydrolyze carbapenems. This activity was found for the chromosomal AmpC ADC-68 expressed by *A. baumannii* (**Jeon et al, 2015**) and the plasmid AmpC CMY-10 (**Kim et al, 2006**). Compared to classical AmpCs, the main alterations occur in the ω loop and in the R2 loop expanding the active site and decreasing the steric clashes between the active site residues and the bulkier lateral chain of oxymino-cephalosporins and carbapenems (**Fig 1.19**).

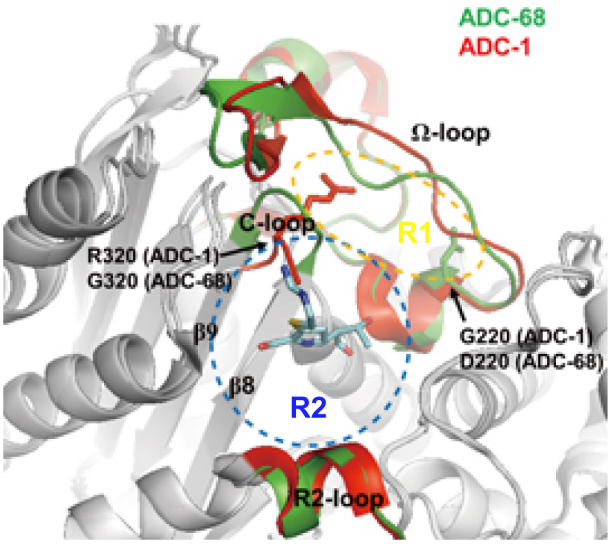

Fig 1.19. *Superposed models of imipenem (blue) with ADC-1 (red) and ADC-68 (green). The R1 and R2 binding sites are illustrated by a yellow and blue dotted circle, respectively. The mutated residues D220 and G320 in ADC-68 allow a more opened configuration of the R1 binding site for the accommodation of the R1 bulkier lateral chain of the cephalosporins and the carbapenems (**Jeon et al, 2015**).*

The AmpCs can also be involved in a carbapenem resistance profile when the reduction of the membrane permeability (mutations or under-expression of porins) is associated with over-expression of efflux pumps and the hyper-production of AmpCs (**Quale et al, 2006**).

1.5.4.3) Chromosomal AmpCs (cAmpCs)

Some *Enterobacterales* present an *ampC* gene located on their chromosome with the particularity to be expressed in a constitutive or an inducible manner (**Fig 1.20**). In the absence of inducible agent, the expression of the chromosomal AmpC (cAmpC) is maintained at a weak basal level. The cell wall is constantly recycled forming 1,6-anhydro-N-acetylmuramic acid oligopeptides (muropeptides) which reintegrate the cytosol via the AmpG transporter. AmpD (N-acetyl-muramyl-L-alanine-amidase) regulates the concentration of the muropeptides by cleaving the stem peptides from 1,6-anhydro-N-acetymuramic acid peptides which are recycled in UDP-N-acetylmuramic acid peptide utilized in the peptidoglycan biosynthesis. This peptide binds to the transcriptional regulator AmpR repressing the expression of the *ampC* gene (**Bugg et al, 2011**).

The presence of a β-lactam inhibiting the activity of the PBPs leads to the instability of the cell wall with an increase in peptidoglycan degradation products (muropeptides). As a consequence, the AmpD is saturated and the accumulation of muropeptides displace the UDP-N-acetylmuramic acid peptide from AmpR which undergoes conformational changes resulting in the transcription of *ampC* (**Tamma et al, 2019**).

Mutations in regulatory genes can occur in response to an antibiotic therapy and cause an overexpression of AmpC production (*ampD* mutants, the more frequent) or a derepression (*ampR* mutants, less frequent) of *ampC* transcription, even in absence of the β-lactam (**Schmidtke & Hanson, 2006 & Kuga et al, 2000**).

E. coli expresses constitutively cAmpCs at low level. It does not possess regulatory elements allowing an inducible expression of AmpC. The strain ensures a higher level of cAmpCs production by a gene duplication and/or mutations in the *ampC* promotor (**Peter-Getzlaff et al, 2011**).

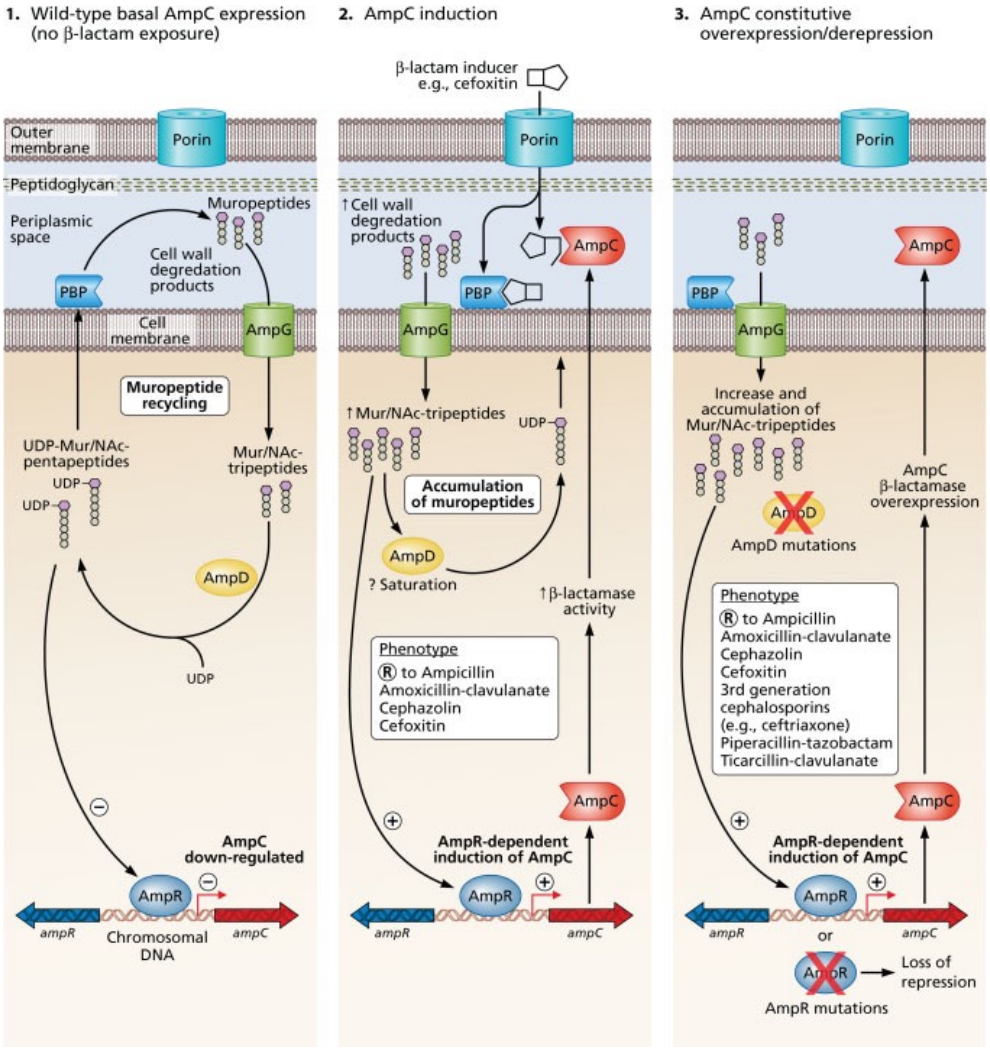

Fig 1.20. *cAmpC expression regulation without exposure to a β-lactam (1), under an induced β-lactam (2) and under the apparition of mutations in regulatory elements (AmpD and AmpR) (3) (**Harris, 2015**).*

Aminopenicillins, amoxicillin, the first generation cephalosporins and the cephamycins highly induce the expression of the cAmpCs which effectively hydrolyze those antibiotics. Carbapenems are also considered as potent inducers of the enzyme overexpression, but it remains stable resulting in a general non-susceptibility of strains, excepted in presence of porins mutations or efflux pumps overexpression. Piperacillin, the third generation cephalosporins and aztreonam are weak inducers rendering susceptible the strains in a basal level expression. However, strains with a constitutive expression of the cAmpC display a resistant profile due to the good kinetic features for those substrates. Finally, cefpirome and cefepime are both weak inducers and stable acyl-enzyme compounds conferring a resistance in nearly all cases (**Meini et al, 2019**).

1.5.4.4) Plasmid-mediated AmpCs (pAmpCs)

The first discovered plasmid-encoded AmpC corresponded to MIR-1. It was isolated from *Klebsiella pneumoniae* Isolates in the United States by *Papanicolaou* (**Papanicolaou et al, 1990**). This enzyme hydrolyzed the oxymino-β-lactams and has a 90 % sequence identity with the chromosomal *ampC* of *E. cloacae*.

The majority of pAmpCs are originated from chromosomal AmpCs expressed by Gram-negative bacteria and are mainly spread in five phylogenetic groups: The *Enterobacter* group (MIR, ACT), the *Citrobacter freundii* group (CMY-2-like, LAT), the *Morganella morganii* group (DHA), the *Hafnia alvei* group (ACC) and the *Aeromonas* group (CMY-1-like, FOX). The sequence identity between the species-specific chromosomal AmpC and the related plasmid-encoded AmpC is very close (**Philippon et al, 2002**).

The pAmpCs are mainly expressed constitutively but some are inducible such as DHA-1 (**Luan et al, 2014**) and ACT-1 (**Reisbig & Hanson, 2002**). The kinetic properties of the plasmid-encoded AmpCs are very similar to cAmpCs with low K_m values for the majority of substrates and a higher activity against the penicillins, the first and the second generation of cephalosporins than the oxymino-cephalosporins. The profile of inhibition is also very similar (**Philippon et al, 2002**).

CMY-2 is the most prevalent pAmpC and is now geographically distributed worldwide (**Bauernfeind & Yunsop, 1998**). It has been intensively studied since the first publication in 1996 (**Bauernfeind et al, 1996**) and is often co-expressed with ESBLs (e.g. SHV, CTX-M) or oxacillinases (e.g. OXA-1-like) (**Pietsch et al, 2018**). Even though this category of β-lactamases is not a high risk in human medicine, the dissemination of pAmpCs in the environment is frightening and their surveillance is crucial for the management and prevention. We notably found a high prevalence of pAmpCs in the aquatic environment (**Coertze & Bezuidenhout, 2020**), in healthy food animals (**Ewers et al, 2021**), in wildlife (**Palmeira et al, 2021**) and in livestock (**Ewers et al, 2012**).

1.5.4.5) Catalytic mechanism of the AmpC

Initial studies suggested that the Y150 acts as general base for the acylation and deacylation steps, resulting in a deprotonated form of the tyrosine along all the catalytic mechanism (**Oefner et al, 1990**). It was discredited by other crystallographic models (**Chen et al, 2006**) and NMR experiments (**Kato-Toma et al, 2003**) that highlighted the neutral form of the tyrosine in all phases.

Then, QM/MM studies on a complex AmpC/aztreonam highlighted that the K67 (conserved motif $S_{64}XXK_{67}$) was involved in the acylation of the substrate, while the Y150 was mainly implicated in the protonation of the β-lactam ring N-atom (**Fig 1.21**). Similar observations were observed for the complex AmpC/cephalotin (**Tripathi & Nair, 2013**).

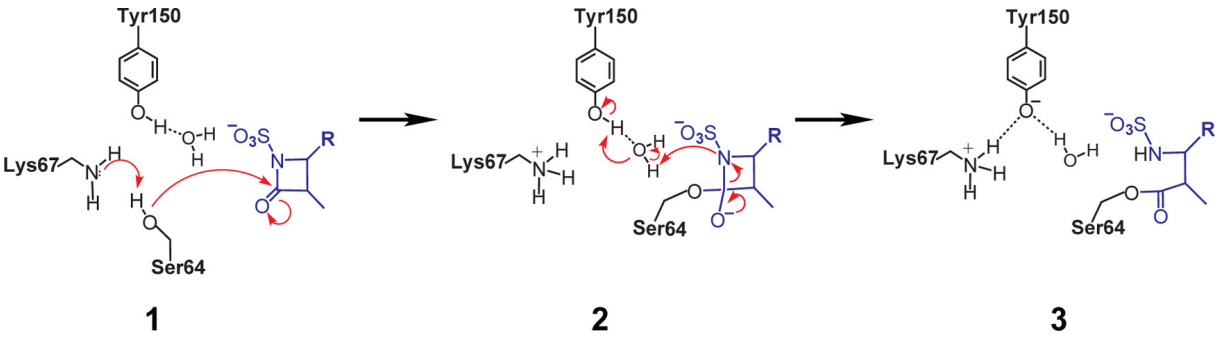

Fig 1.21. *Schematic representation of the acylation mechanism based on QM/MM studies on the complex AmpC/aztreonam. Y67 acts as an acceptor of proton allowing the nucleophilic attack of the β-lactam ring by the S64 (1). Y150 acts as a donor of proton, permitting the protonation of the β-lactam ring N-atom via a water molecule (2) and leading to a stable acyl-enzyme (3) (**Tripathi & Nair, 2013**).*

Authors also hypothesized two different ways to explain the deacylation phase. At first, a proton is transferred between the K67, Y150 and a catalytic water molecule resulting in the hydrolysis of the acyl-enzyme and the release of the cleaved antibiotic (**Fig 1.22A**) (**Tripathi & Nair, 2016**). The second option consists in the deprotonation of the catalytic water molecule via the β-lactam ring nitrogen (**Fig 1.22B**) (**Patera et al, 2000**).

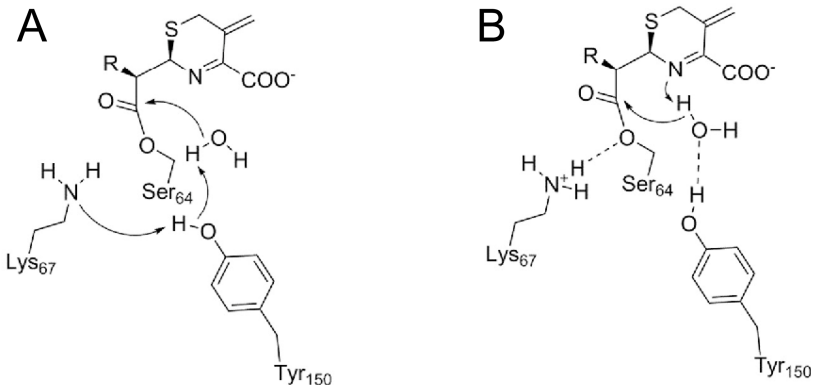

Fig 1.22. *Class C β-lactamases deacylation mechanisms involving a proton transfer between the K67 and Y150 to activate the catalytic water molecule (A), or via the β-lactam ring nitrogen (**Tooke et al, 2019a**).*

1.5.5) Class D β-lactamases

The class D β-lactamases are called OXA due to their capability to hydrolyze oxacillin, a semisynthetic penicillin. They are mainly expressed by *Acinetobacter baumannii*, *Pseudomonas aeruginosa*, *Escherichia coli* and *Proteus mirabilis*. We currently count more than 250 different OXA enzymes belonging to three major groups: the narrow-spectrum OXAs (e.g. OXA-1 and OXA-20) (**Naas et al, 1998**), the ESBL OXAs (e.g. OXA-14) (**Danel et al, 1995**) and the carbapenemases OXAs (e.g. OXA-24/40 and OXA-48) (**Bou et al, 2000**).

The topology of the class D β-lactamases is similar to other active-site serine β-lactamases despite a very low sequence identity (e.g. 8 % between OXA-10 and TEM-1). The α/β domain includes a seven-stranded antiparallel β sheet, while 6 α-helices compose the α domain (**Fig 1.23A**). The active site is located between both domains and is mainly structured by the α3-helix, one short loop between the α4 and α5-helices, and the β5-strand. Their ω loop (residues 145-161) is shorter than in class A and C β-lactamases and carries mainly hydrophobic residues oriented toward the active site. Those structural elements carry the three conserved motifs (**S**67XX**K**70, **K**205**T**/**S**206**G**207 and **S**115X**V**117) involved in the binding of the substrate and crucial for the catalytic activity of the enzyme (**Fig 1.23B**) (**Maveyraud et al., 2000**).

The class D β-lactamases possess a more hydrophobic active site than other β-lactamase classes. On one hand, this correlates with the oxacillinase activity of OXA enzymes since a hydrophobic patch complements the hydrophobic R1 side chain of the oxacillin explaining a very efficient activity of OXA-1 for this substrate (**Fig 1.23C**) (**June et al, 2014**). In the other hand, the hydrophobic nature of the class D BLAs active site also promotes the carboxylation of the general base K70 resulting in a carbamate functional group. Indeed, it was suggested that non-polar residues (e.g. V117) decrease the pK_a of the catalytic lysine favoring the deprotonation at neutral pH required for the attack on the CO_2 (**Golemi et al, 2001**). The carbamate moiety is stabilized by a number of hydrogen bonds, notably to the S67, the S115 and the conserved residue W154 ensuring the correct positioning of the functional group crucial for both acylation and deacylation steps (**Fig 1.23B&D**) (**Leonard et al, 2013**).

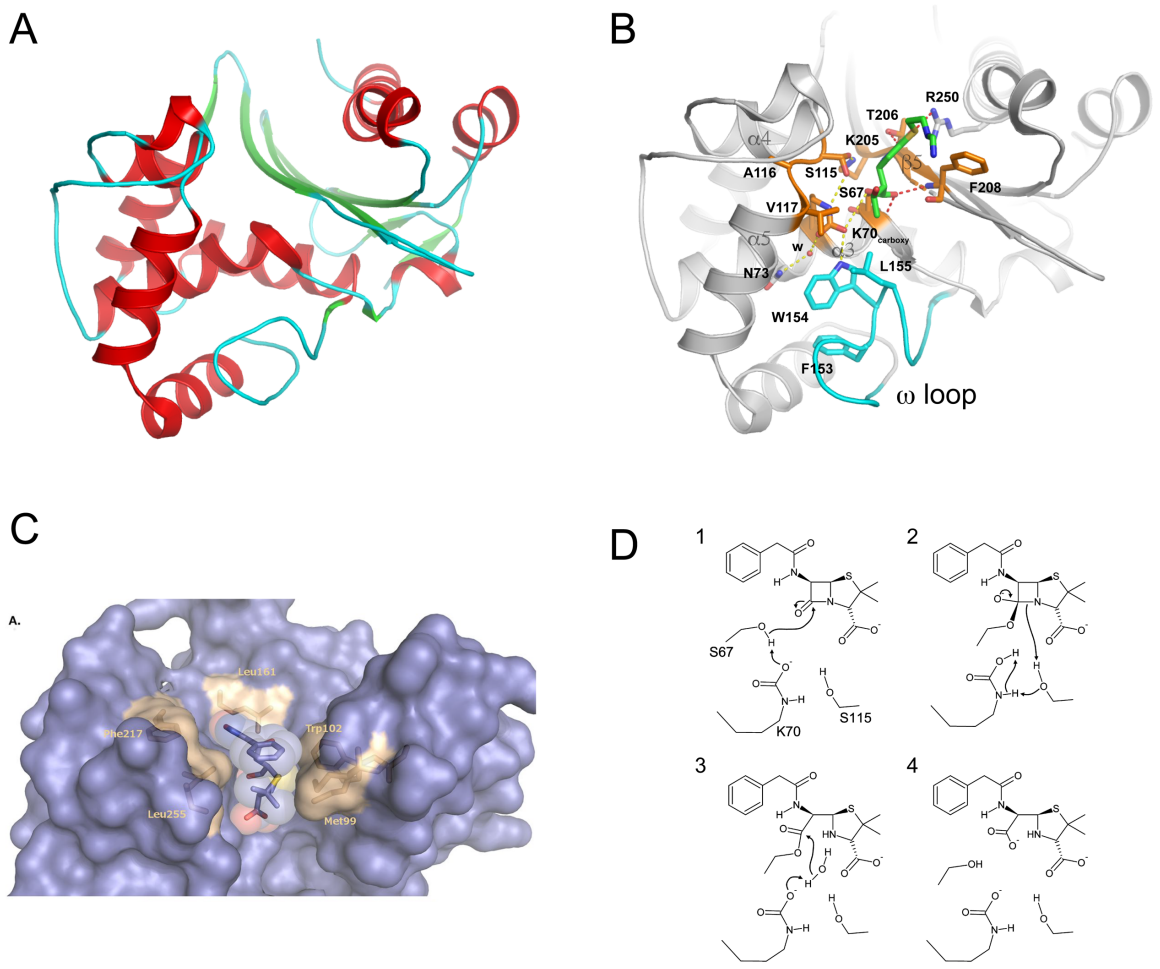

Fig 1.23. *Active site description of class D β-lactamases. (A) General overview of class D β-lactamases. (B) Zoom on the OXA-10 active site in complex with the imipenem (PDB code 6SKP). The H-bond networks stabilizing the carbamate moiety (S67-S115-W154) and ensuring the deprotonation of the K70 (K205-S115-K70) are illustrated by yellow dotted lines, while the oxyanion hole and the "carboxylic pocket" by red dotted lines. (C) Hydrophobic patch representation of OXA-1 in complement with the R1 side chain of the oxacillin (**June et al, 2014**) (D) Catalytic mechanism of class D β-lactamases where the carboxylate K70 activates the S67 which makes a nucleophile attack on the lactam carbonyl (1) to form a tetrahedral intermediate (2). Then, the ester linkage is cleaved by an activated water molecule (3) with the release of the inactivated product (4) (**Leonard et al, 2013**).*

The first OXA β-lactamases (e.g. OXA-1, OXA-10) cannot hydrolyze carbapenems. As described for class A and C β-lactamases, the reorientation of the 6α-hydroxyethyl function of the antibiotic which binds the carbamate moiety of the K70 and the absence of the deacylation water molecule prevent the hydrolysis of the acyl-enzyme, resulting in a very low deacylation rate (**Fig 1.24A**) (**Schneider et al, 2009**).

The emergence of OXA carbapenemases started in 1995 with the first identified enzyme OXA-23 (**Scaife et al, 1995**). Nowadays, dozens of new OXA carbapenemase have been identified and were classified in five sub-groups: OXA-23, OXA24/40, OXA-48, OXA-51 and OXA-58 presenting different subtitle mechanisms. For example, the complex doripenem/OXA-24 revealed a hydrophobic bridge between the residues Y112 and M223 establishing nonpolar interactions with the pyrrolidine ring of the doripenem side chain, while the doripenem's hydroxyethyl group points away from the carbamate of the carboxy-K70 (**Fig 1.24B**) (**Schneider et al, 2011**). By contrast, OXA-48 does not present this hydrophobic bridge. However, a more open configuration of its active site and the positioning of the β5-β6 loop (T213) disrupts the interaction of the hydroxyl group of the meropenem and the carbamate group of the carboxy-K70 creating space for the deacylating water molecule (**Fig 1.24C**) (**Stojanoski et al, 2021**).

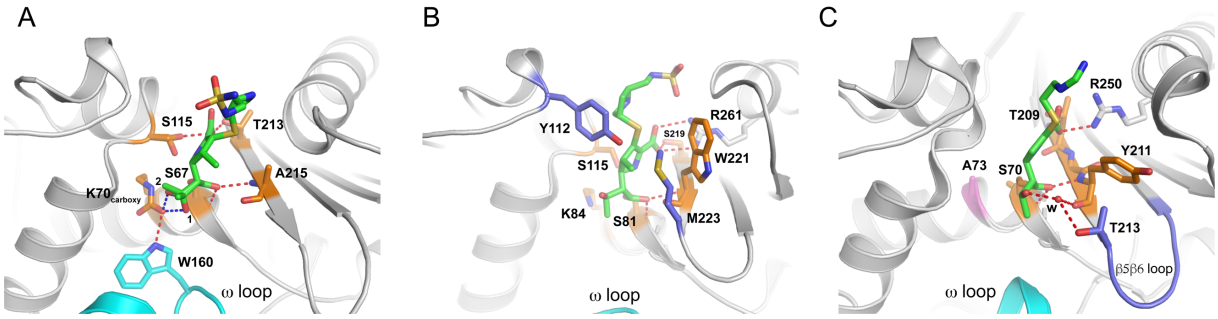

Fig 1.24. *Active site of OXA carbapenemases. (A) OXA-1 in complex with the doripenem (PDB code 3ISG) where the interaction of the two configurations of antibiotic 6α-hydroxyethyl group with the carbamate moiety of the K70 is illustrated by a blue dotted line. (B) Representation of the complex doripenem/OXA-24 V130D (PDB code 3PAG) where residues Y112 and M223 forming the hydrophobic bridge are colored in purple. (C) Zoom on the OXA-48 K73A mutant active site in complex with the imipenem (PDB code 7KH9). The A73 is highlighted in rose, while the β5β6 loop is illustrated in purple.*

Since it first identification from *Klebsiella pneumoniae* in Istanbul in 2001 (**Poirel et al, 2004**), OXA-48-like β-lactamases largely disseminated worldwide and currently cause a real health concern. Frighteningly, OXA-48 enzymes are detected in human bacterial Isolates, but also in the environment as in rivers or livestock. They disseminate rapidly since the *bla* gene is commonly harbored by the plasmid IncL which acquired an upstream transposon Tn1999 and the downstream insertion sequence IS1999. It is often not detected correctly resulting in

a wrong diagnosis and making the treatment complicated (**Boyd et al, 2022**). More and more studies describe an increasing number of OXA-48-like/NDM co-producers providing a high level of resistance to carbapenems and current inhibitor therapies (**Bush & Bradford, 2020**).

1.5.6) Class B β-lactamases, the metallo-β-lactamases (MBLs)

1.5.6.1) Classification of MBLs

The metallo-β-lactamases can be divided in three sub-groups following their amino acids sequence (**Galleni et al, 2001**). All sub-groups present different substrate profiles and loop configurations intervening in the enzyme activity.

Historically, the first described metallo-β-lactamases belonged to the subclass B1 which hydrolyze all β-lactams excepted the monobactams (**Marcoccia et al, 2016**). However, this isolated susceptibility can be hindered by the co-expression with β-lactamases belonging to other classes (**Gao et al., 2020**). They are mono-zinc or bi-zinc and studies on BCII demonstrated that the binding of a second zinc ion improves its activity (**Davies & Abraham, 1974**). But a more recent study showed that the bi-zinc form is essential for the activity of BCII (**Jacquin et al, 2009**). BCII was discovered in 1966 in *Bacillus subtilis* and is chromosomally encoded (**Sabath et Abraham, 1966**). However, the majority of the sub-class B1 genes are carried by plasmids such as IMP-1 (Imipenemase) firstly isolated from *Pseudomonas aeruginosa* and *Serratia marcescens* in Japan in 1990 and actually counting for 85 variant sequences (**Watanabe et al, 1991**); the most relevant Verona-Integron-encode metallo-β-lactamase (VIM) found in *Pseudomonas aeruginosa* in 1997 and represented by 69 variants (**Lauretti et al, 1999**); NDM-1 (New-Delhi metallo-β-lactamase) corresponding to the most prevalent MBL in *Enterobacterales* (55 variants) and identified for the first time in *Klebsiella pneumoniae* and *E. coli* in 2008 (**Yong et al, 2009**).

The subclass B2 MBLs are exclusively mono-zinc and are inhibited by the association with a second zinc ion (**Hernandez Valladares et al, 1997**). They are strictly carbapenemase and are inefficient against other penam families (**Bebrone et al, 2008**). CphA is the most known subclass B2 MBL and was discovered in 1991 in *Aeromonas hydrophila* (**Massidda et al, 1991**). Up to date, 17 variants of CphA are found in *Aeromonas*.

The subclass B3 MBLs have a broad spectrum activity against all penams and coordinate two zinc ions (**Horsfall et al, 2011**). Their genes are generally encoded by the chromosome and are species-specific such as the MBL L1 isolated from *Stenotrophomonas maltophilia*, previously called *Pseudomonas maltophilia*, in 1982 (**Saino et al, 1982**) and GOB enzymes expressed by the species *Chryseobacterium meningoseptica* (**Bellais et al, 2000**). Furthermore, some horizontally transferable *bla* genes are also present in this subgroup as AIM-1 firstly identified in the chromosome of *Klebsiella pneumoniae* in 2019 (**Zhou et al, 2019**) or LMB-1 found on a plasmid in *Rheinheimera pacifica* and flanked by immobilization sequences (**Lange et al, 2018**).

1.5.6.2) Structure and active site

The three subclasses present an $\alpha\beta\beta\alpha$ fold with two central β-sheets and α helixes on each side (**Fig 1.25A-C**). The active site is located between both domains and contains the Zn^{2+} ions coordinated by conserved motifs and crucial for the activity of the enzyme (**Table 1.2**) (**Boyd et al, 2020**).

MBLs	Histidine site	Cysteine site
B1	Zn_1 **H**116-**H**118-**H**196	Zn2 **D**120-**C**221-**H**263
B2	Zn_2 **H**118-**H**263	Zn1 **D**120-**C**221-**H**263
B3	Zn_1 **H**116-**H**118-**H**196	Zn2 **D**120-**C**221-**H**263

Table 1.2. *Zinc ions coordination by motifs conserved in the three MBL subclasses. The Zn_2 ion coordinated by the histidine site in the subclass B2 is unfavorable (indicated in red).*

The subclass B1 MBLs carry a flexible loop (flapping loop) between the β2 and β3-strands (residues 65-73) where some hydrophobic residues (L65, M67, F70 and V73) tightly bind the lateral chain of the antibiotic as illustrated by the complexes NDM-1/ampicillin (**Fig. 1.25D**) and NDM-1/imipenem (**Fig. 1.25G**). Those hydrophobic residues combined with an important flexibility of the flapping loop accommodate a large panel of substrates (**King & Strynadka, 2011**). W94 on the L5 loop closes the active site what is essential for the activity of the enzyme (**Huntley et al, 2003**). Moreover, the L10 loop contributes to the substrate binding via their residues K211 and N220 interacting with the carboxylate group of the antibiotic. It also carries the residue C221 crucial for the coordination of the zinc ion (**King &**

Strynadka, 2011). Mutations on the L10 loop totally disrupt its dynamic and reduce the activity of NDM-1 (**Piccirilli et al, 2021**).

On the contrary, the subclass B2 MBLs do not possess a long flexible loop between the β2 and β3-strands (**Fig 1.25F**). However, the model CphA/biapenem highlighted an elongated α3-helix (residues 140-161) which carries steric and hydrophobic residues (e.g. I153 and F156). They reduce the size of the active site and restrain the CphA activity to carbapenems. On the other hand, the involvement of residues T119 and T157, able to establish H-bonds with the C7 carbonyl group of the biapenem, combined to the L10 loop, contributes to the optimal activity of the enzyme (**Garau et al, 2005**). Finally, mutagenesis experiments demonstrated the essential role of different prolines brought by the highly conserved L8 loop (**Bottoni et al, 2016**).

The structure of the subclass B3 MBL L1 in complex with moxalactam also revealed hydrophobic interactions via the L9 loop (mobile loop) located between the α3-helix and the β7-strand with the lateral chain of the substrate (**Fig 1.25E**). Some additional H-bonds between the residues S221 and S223 on the L13 loop and the carboxylate group brought by the carbon C4 of the moxalactam complete the stabilization of the acyl-enzyme (**Ullah et al, 1998**). The β-lactamase L1 has the particularity to form a tetramer via its 20-AA N-terminal extension ensuring the interaction between subunits A-B and C-D (**Fig 1.25H**). Moreover, the residue M175 from the subunit A penetrates in a hydrophobic pocket on the subunit B (the same between subunits C and D) (**Simm et al, 2002**). Finally, both L40 and L43 take place in an apolar cavity of the opposite subunit and constitute the main contacts between the subunit A and C with B and D, respectively (**Ullah et al, 1998**). The majority of class B3 MBLs are monomeric such as FEZ-1 which lacks the N-terminus region making electrostatic and hydrophobic interactions essential for the tetramerization. Moreover, the residue M175 is mutated in a positively charged residue H175 unfavorable for its insertion in the hydrophobic pocket (**Garcia-Sáez et al, 2003**).

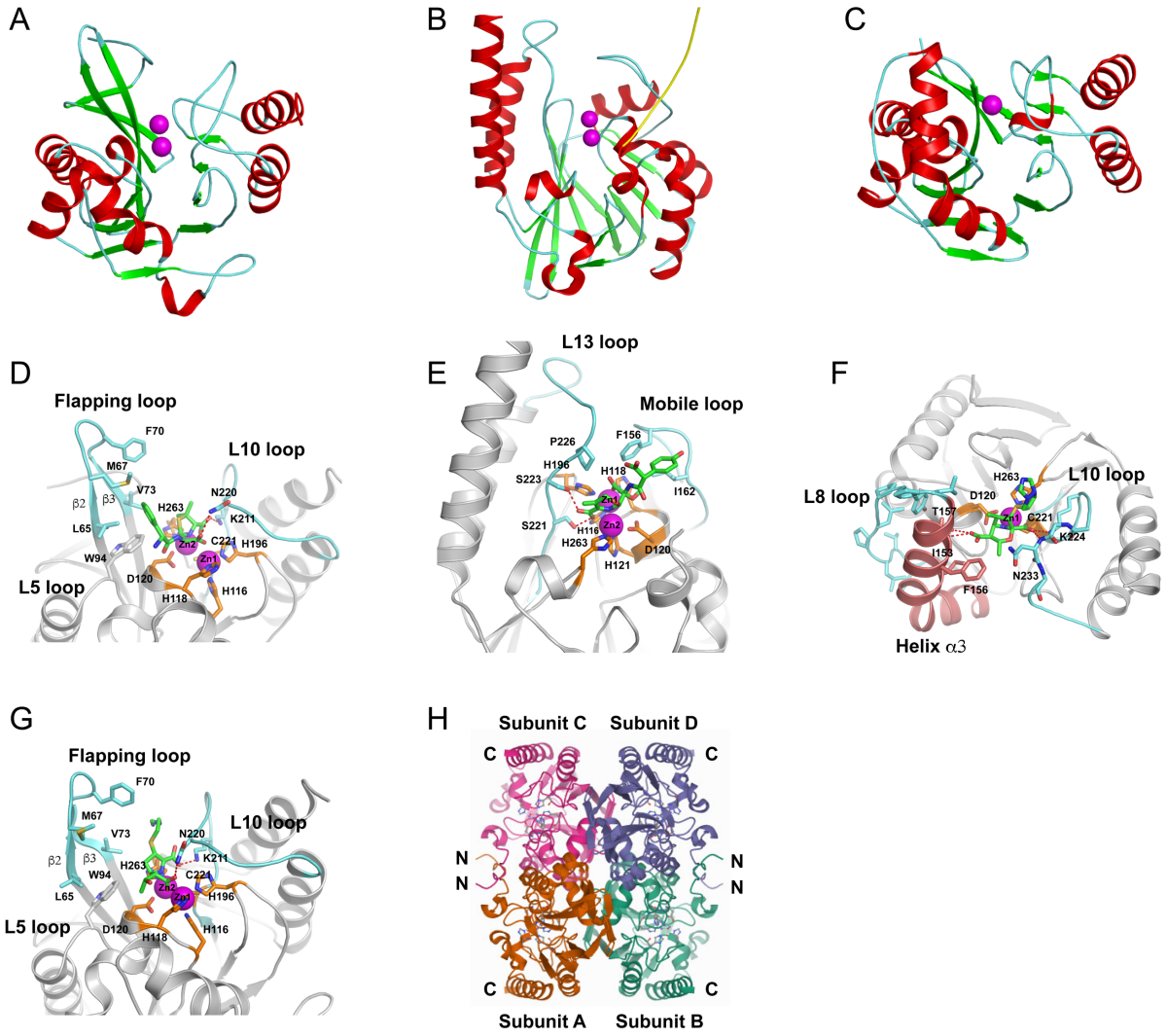

Fig 1.25. *Global representation of the subclass B1 MBL NDM-1 (PDB code 4H0D) (A), the subclass B3 MBL L1 (PDB code 2AIO) (B) and the subclass B2 MBL CphA (PDB code 1X8I) (C). The helixes, the β-strands and the loops are colored in red, green and blue, respectively. Active site of NDM-1 in complex with the ampicillin (D) and the imipenem (PDB code 5YPL) (G), of L1 with the moxalactam (E) and CphA with the biapenem (F). Tetrameric complex of the MBL L1 (**Ullah et al, 1998**) (H). Zinc ions (purple) are coordinated by residues represented in orange. The N-terminal extremity of the MBL L1 is illustrated in yellow.*

1.5.6.3) NDM-1, the most spread and critical subclass B1 MBL

NDM-1 catalyzes the hydrolysis of all β-lactam antibiotics with the exception of monobactams and resist to all available inhibitors. It was first identified in a Swedish patient presenting a urinary tract infection in 2009 due to a *Klebsiella pneumoniae* and hospitalized

in New-Delhi (**Yong et al, 2009**). NDM-1 presents a low sequence identity with other B1 MBLs (e.g. 34 % for IMP-1 and 35 % for VIM-2) (**Bush, 2013**).

1.5.6.3.1) NDM-1 as a lipoprotein

NDM-1 is anchored to the outer membrane of the Gram-negative bacteria via a lipidation amino acids sequence LSGC called “lipobox” at the end of the signal peptide. It stabilizes the apo-enzyme when the concentration of zinc ions decreases in an infection site where the metal-chelating protease calprotectin is released. The NDM-1 C26A mutant presents an important instability and a high rate of degradation. Moreover, the secretion of NDM-1 in outer-membranes vesicles (OMV) also provides bacterial resistance to external β-lactams secreted by neighboring producers (**Fig 1.26**) (**Gonzalez et al, 2016**).

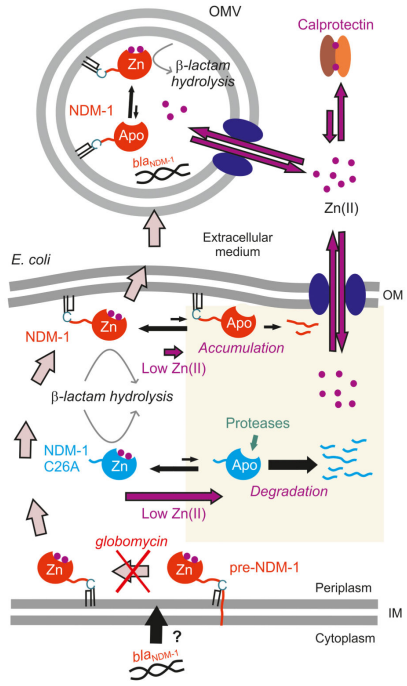

Fig 1.26. *Membrane-anchoring NDM-1 mechanism for the enzyme stabilization in a low zinc ions concentration environment and the outer-membrane vesicles (OMV) formation for resistance to the external presence of antibiotics (**Gonzalez et al, 2016**).*

1.5.6.3.2) NDM variants

The NDM family contains a lot of variants with mutations spread on 17 AA (**Fig 1.27**). The mutations are generally located far from the active site (**Wu et al, 2019**). M154L is the more largely identified mutation and increases the activity against penicillins, also at lower zinc ions concentration (**Stewart et al, 2017**). It reflects the ability of NDM-1 to evolve in

function of the scarcity of zinc ions in the environment. The substitution V88L is also largely represented and is generally co-expressed with the mutation M154L (e.g. NDM-5) (**Zou et al, 2020**). The association of the two mutations contributes to increase the carbapenemase activity notably due to a higher stability of NDM-5 with carbapenems (**Ali et al, 2018**).

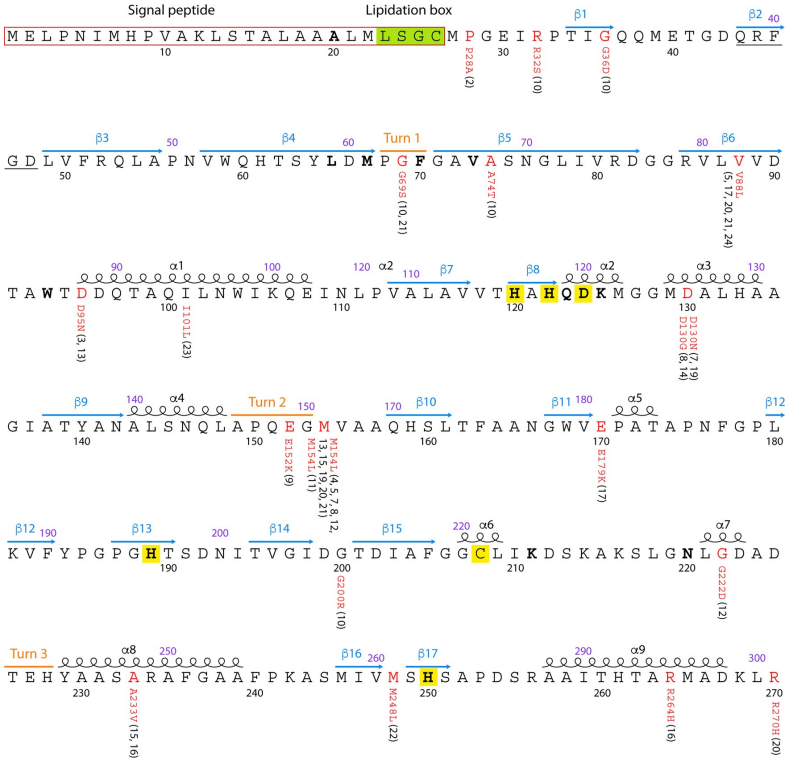

Fig 1.27. *NDM-1 sequence and mutants. All mutations are illustrated in red, while the related NDM variants are indicated in parentheses (**Wu et al, 2019**).*

1.5.6.3.3) Worldwide expansion of the NDM family

Since its first apparition in 2008, some studies reported a high distribution and the prevalence of NDM MBLs worldwide. The Study for Monitoring Antimicrobial Resistance Trends (SMART) provided a global surveillance on 103960 Isolates of *Enterobacterales* from 55 countries isolated between 2008 and 2014 (**Karlowsky et al, 2017**). It revealed a significant proportion of NDM variants everywhere in the world, especially in the Middle East (UAE), in Asia (Pakistan, India), in North Africa (Egypt) and in South Pacific (Philippines). They are mainly expressed in *Klebsiella pneumoniae*, *Escherichia coli* and *Enterobacter cloacae*. NDM variants represent the third most widespread carbapenemases (19 %), just after the OXA (20 %) and

KPC (50 %) β-lactamases (**Fig 1.28**). The SMART study did not take into account China where recent studies demonstrated that NDM MBLs could reach 30 % of total carbapenemases (**Dong et al, 2022**).

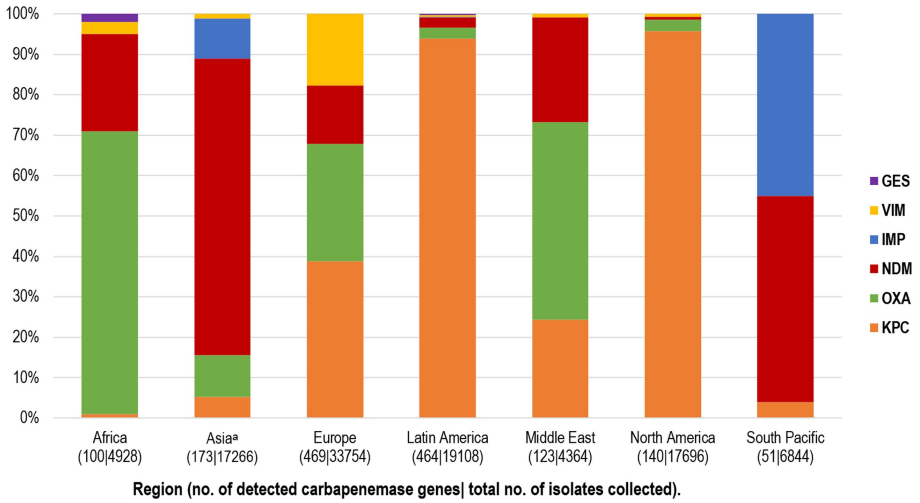

Fig 1.28. *Geographical distribution of carbapenemases based on the Study for Monitoring Antimicrobial Resistance Trend (SMART) (**Karlowsky et al, 2017**). The positive strains/tested strains ratio is indicated in parentheses.*

Traveling remains the main factor explaining the large spread of β-lactamases. The appearance of NDM MBLs in Europe like in Italy (**Gaibani et al, 2011**) or in Greece (**Voulgari et al, 2014**), in 2011. This is a consequence of patients traveling in India and being hospitalized in their respective country after their return.

NDM-1 is carried by more than 11 bacterial families and particularly by *Enterobacterales*. It is also expressed by *Klebsiella pneumoniae* species associated with multiple pathologies such as bloodstream infections, intra-abdominal infections, meningitis, or urinary tract infections. Genes coding for NDM variants are essentially found on plasmids rendering possible their rapid dissemination by a horizontal gene transfer. Nowadays, around 20 replicon types of *blaNDM* carrying plasmids were identified with the more represented IncX3 (**Wu et al, 2019**). NDM-encoding genes are usually located in tandem with mobile genetic elements as insertion sequences, transposons… allowing their mobilization between different plasmids or between a plasmid and a chromosome (**Poirel et al, 2011**).

1.5.6.3.4) Mechanism for β-lactam hydrolysis by MBLs

Despite the catalytic activity of bi-zinc MBLs slightly vary depending on the active site and substrate, MBLs share a general mechanism for β-lactam antibiotics hydrolysis. *Feng et al* performed NMR and structural studies on carbapenem/NDM-1 complexes. They demonstrated identical features during the hydrolysis of penicillins and cephalosporins but also some peculiar aspects (**Fig 1.29**). Similarly, the delocalization of the negative charge from positions N4 to C2 by tautomerization also follows the nucleophilic attack by the hydroxide group. An equilibrium is established between the two species EI_1 and EI_2 shifted toward the second intermediate. Then, the protonation of the intermediate EI_2 takes two different pathways: (I) it is directly undertaken on the C2 carbon leading to the intermediate EI_3 that evolves to EP and the release of the final product; (II) EI_2 undergoes some structural modifications (EP') facilitating its protonation and resulting in the complex EP. On contrary with the cephalosporin hydrolysis (**Feng et al, 2014**), the proton uptake corresponds to the rate-limiting step for the protonation of the intermediate EI_2 and they demonstrated that the protonation was only possible by a bulky solvent molecule entering in the pocket from the exterior space. By consequence, it exclusively attacks the β-lactam ring configuration with the negative charge delocalized on the C2 carbon (**Feng et al, 2017**).

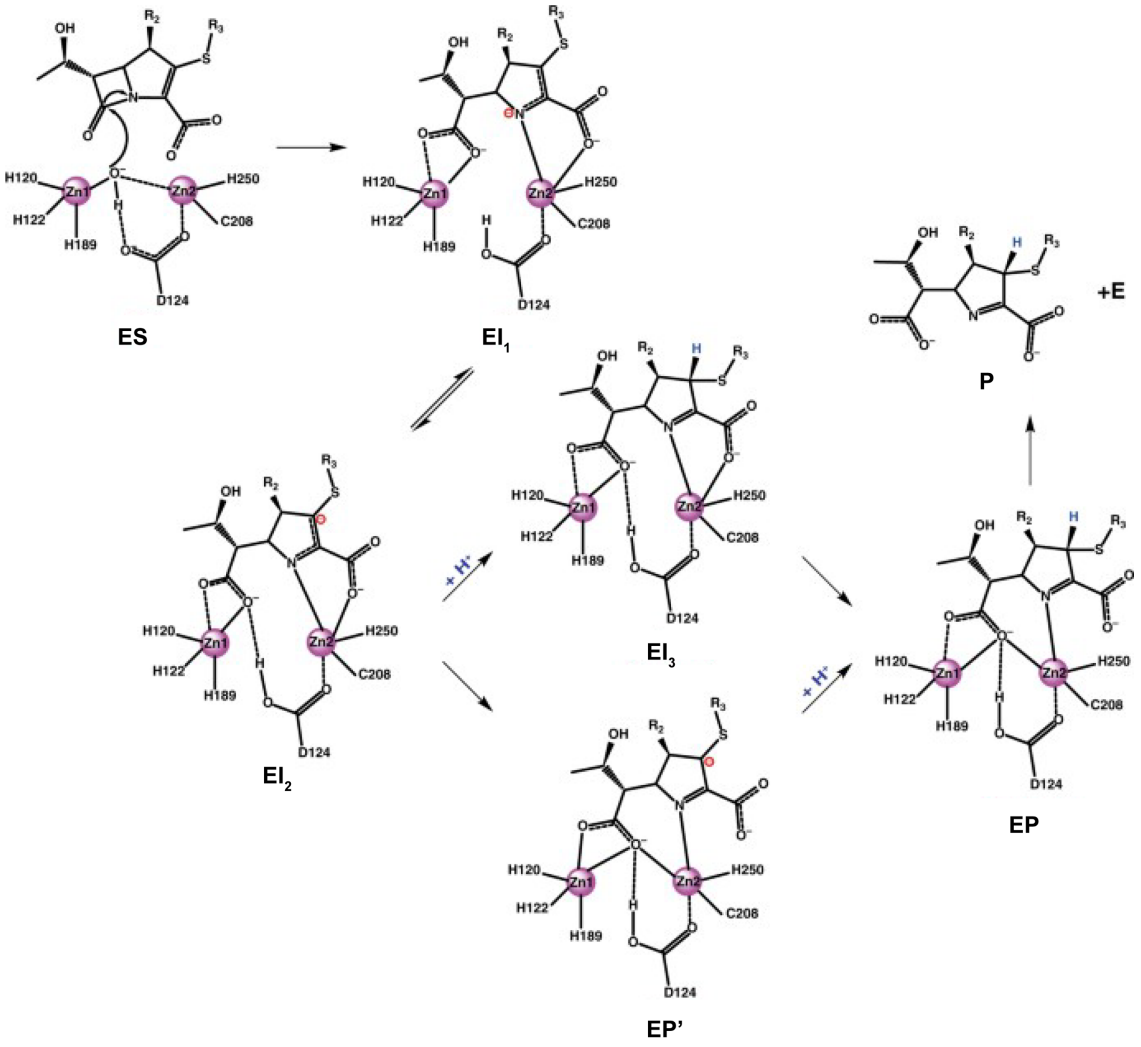

Fig 1.29. *Carbapenems hydrolysis catalyzed by NDM-1. The Michaelis Menten complex (ES) undergoes a nucleophile attack by the hydroxide group leading to the intermediate EI_1 in equilibrium with EI_2 by tautomerization. Then, the protonation immediately occurs (EI_3) or after some changes of the complex EI_2 (EP') finally leading to the release of the product and the regeneration of NDM-1 (**Feng et al, 2017**).*

1.5.7) β-lactamase inhibitors (BLI)

1.5.7.1) The old-age β-lactamase inhibitors

The old-age β-lactamase inhibitors act as irreversible "suicide" substrates and inactivate the β-lactamase by forming a stable BLI/Enzyme complex. The common clinically used inactivators are clavulanic acid, a natural inhibitor first isolated from *Streptomyces clavuligerus* in 1970s (**Reading & Cole, 1977**), and sulbactam and tazobactam (**Fig 1.30**), two synthetic penicillinate sulfones developed by pharmaceutical companies in 1978 and 1980, respectively (**Fisher et al, 1980**). Those inhibitors disrupt the activity of class A β-lactamases with high association and low dissociation rates. They however present a lower efficiency against class B, C and D β-lactamases (**Drawz & Bonomo, 2010**).

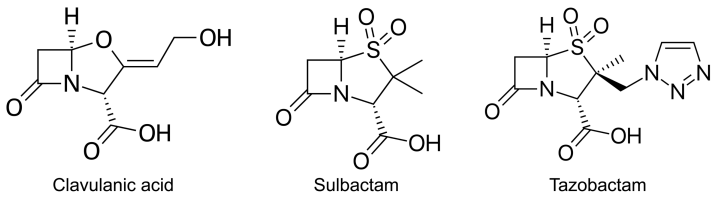

Fig 1.30. *Chemical structure of irreversible mimicking β-lactam inhibitors*

Those inhibitors follow a similar pathway beginning with the formation of an acyl-enzyme species (**Fig 1.31**). The five-membered ring of the inhibitor is opened and leads to a transient imine intermediate. The imine species follows different pathways and results in alternate products varying in function of the enzyme and the BLI. The imine species can be rearranged in a *cis* or a *trans* enamine configuration (e.g. clavulanate/SHV). The stabilization of those transient intermediates is crucial for the prolonged enzyme inhibition. Moreover, the ratio between the different species depends on the inhibitor considered: the acyl-enzyme tazobactam/SHV undergoes mainly to a trans-enamine population, whereas the clavulanate and the sulbactam form a mixture of intermediates (**Meroueh et al, 2002**). Mass spectroscopy experiments also revealed a series of irreversible inactivation products as the cross-linking between the residues S70 and S130 rendering possible via the water molecule stabilized by the residue R244 and the carbonyl function of the V216 (**Sulton et al, 2005**).

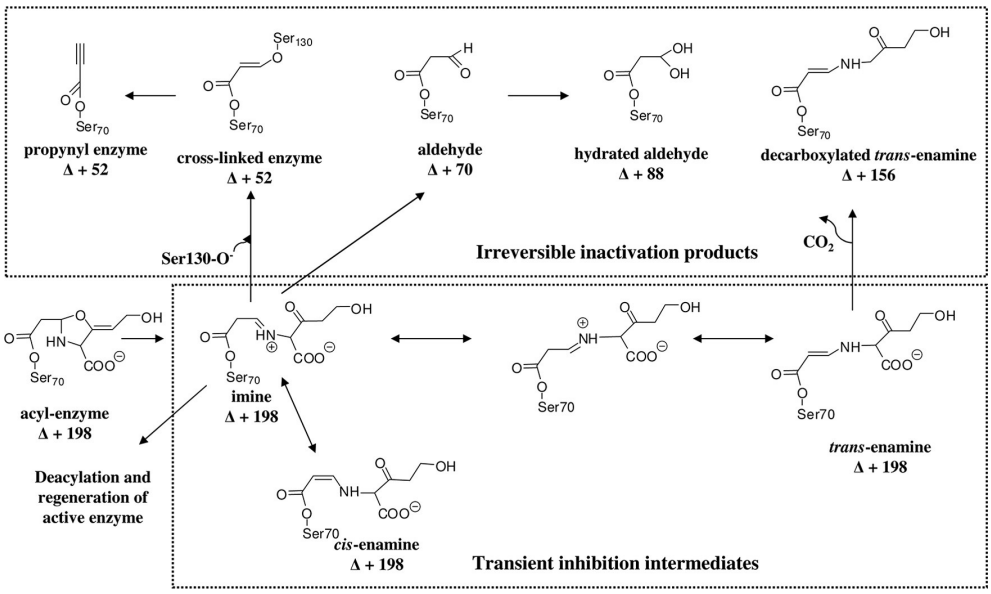

Fig 1.31. *Mechanism of class A β-lactamases inhibition by clavulanate, sulbactam and tazobactam (**Drawz & Bonomo, 2010**).*

The BLI are generally combined with different β-lactams. Clavulanate is associated to amoxicillin (Augmentin, GlaxoSmithKline) to expand its activity against a large variety of bacteria such as *Staphylococcus aureus*, *E. coli* and *Klebsiella spp*. It corresponds to the only combination for the oral use and is commonly employed in the therapy of primary care settings and community-acquired respiratory infections. The sulbactam also restores the activity of the ampicillin against a wide range of bacteria as *S. aureus*, *E. coli* and *Klebsiella spp*. It was marketed in 1987 and is indicated for ventilation-associated pneumonia, for polymicrobial infections (e.g. abdominal and gynecological surgical infections) and diabetic foot infections. It is not well suited for an oral use and is administrated parenterally. Sulbactam can also be associated to cefoperazone, a third-generation cephalosporin, which exhibits a better antimicrobial activity against ESBL and AmpC-producing *Enterobacterales*. Finally, the combination tazobactam/piperacillin (Tazocin) has an activity against Gram-positive and Gram-negative bacteria. This association is notably utilized in the treatment of complicated intra-abdominal infections, pneumonia and sepsis (**Schonning & Tvede, 2002**).

1.5.7.2) Diazabicyclo[3.2.1]octanone (DBO) family

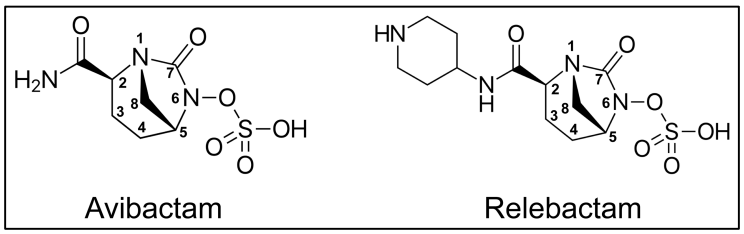

Fig 1.32. *Avibactam and relebactam, two major DBO family members.*

1.5.7.2.1) Avibactam (NXL-104)

Avibactam (NXL-104) (**Fig 1.32**) belongs to the bridged diazabicyclo[3.2.1]octanone (DBO) non β-lactam family and inhibits the activity of class A ESBL and CPE (e.g. CTX-M-15 and KPC), but also class C and class D β-lactamases (e.g. OXA-48) (**Krishnan et al, 2015**).

Avibactam acts as a reversible inhibitor since it recovers a closed-ring conformation during the deacylation step (**Fig 1.33A**). This recyclization results from the proximity of the sulfactam nitrogen N6 able to make a nucleophilic attack to the carbamoyl carbonyl C7 leading to the release of the avibactam in its original configuration.

In class A β-lactamases (e.g. CTX-M-15), the general base E166 is protonated during the deacylation phase rendering the hydrolytic water molecule ineffective and enables to hydrolyze the avibactam (**Fig 1.33B**). In class C, the sulfamate group of the avibactam provokes the displacement of the water molecule involved in the hydrolysis of the substrate (**Fig 1.33C**) (**Lahiri et al, 2013**). Finally, the change in charge distribution upon avibactam binding in the proximity of the carboxy-K84 of OXA-48 induces the decarboxylation of K84 and its inability to activate the hydrolytic water molecule (**Lahiri et al, 2014**).

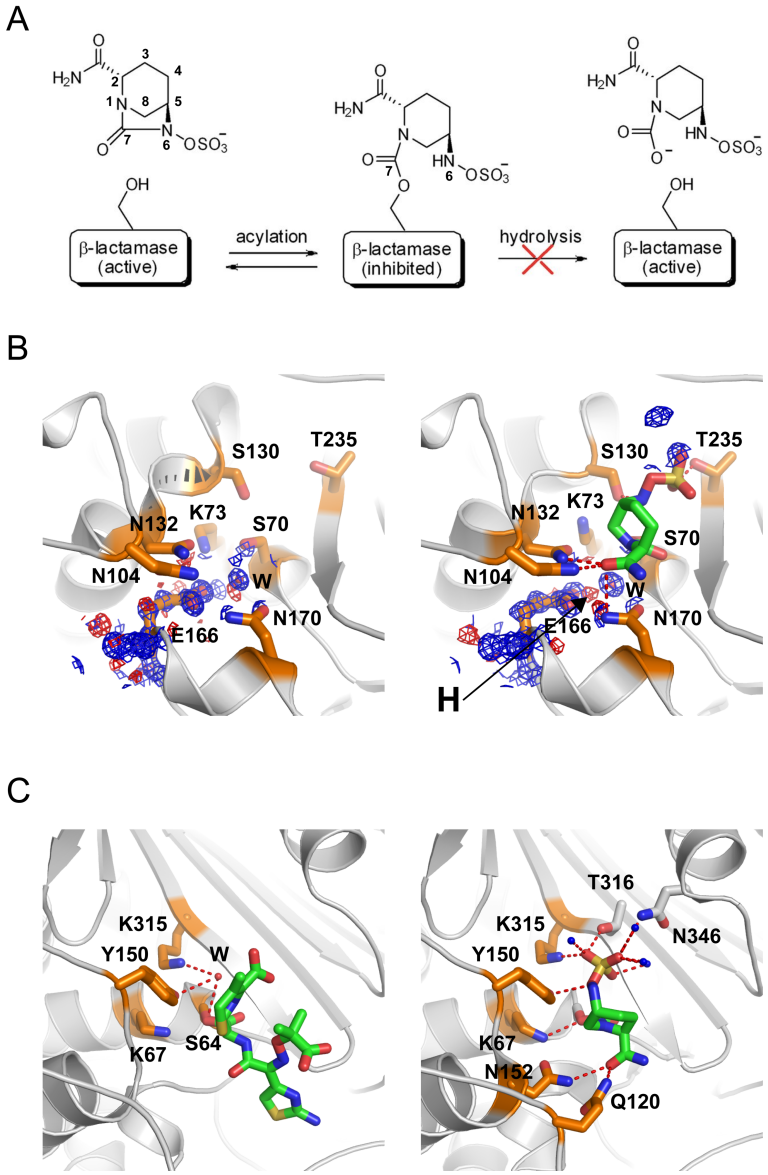

Fig 1.33. *Inhibitory mechanism of the avibactam. (A) Illustration of the general pathway for the avibactam inhibition. (B) Active site representation of the native CTXM-15 (PDB code 4HBT, on left) and the acyl-enzyme CTXM-15/avibactam (PDB code 4HBU, on right). The 2Fo-Fc and Fo-Fc were represented in blue and red, respectively, on the residue E166 and the catalytic water molecule (red circle, w). The protonated state of the residue E166 in the complex CTXM-15/avibactam is highlighted by the symbol H. (C) Active site of complexes AmpC/ceftazidime (PDB code 1IEL, on left) and AmpC/avibactam (PDB code 4HEF, on right). The hydrolytic water is present in the complex AmpC/ceftazidime (red circle, w) and absent in the complex AmpC/avibactam. Water molecules stabilizing the sulfonate function of the avibactam are represented by blue circles, whereas H-bonds stabilizing the acyl-enzyme are illustrated by red dotted lines. Pictures are adapted from Lahiri et al, 2013.*

Avibactam combined with the ceftazidime displays the highest efficiency against the ESBL and CPE class A β-lactamases, the AmpC and the OXAs found in some *Enterobacterales* and *Pseudomonas aeruginosa* Isolates (**Aktas et al, 2012**). This association (Avycaz, Zavicefta) was officially approved by FDA and commercialized in 2015 to treat complicated urinary tract infections (cUTI) and complicated intra-abdominal infections (cIAI) (**Mosley et al, 2016**). More recently, ceftazidime/avibactam was used in combination with aztreonam to treat infections due to isolates of *Enterobacterales*, *Pseudomonas aeruginosa* and *Acinetobacter baumannii* co-expressing serine and metallo-β-lactamases. Indeed, avibactam efficiently inhibits serine β-lactamases which could hydrolyze aztreonam, allowing restoration of susceptibility to aztreonam spread by metallo-β-lactamases (**Mauri et al, 2021**).

Resistant β-lactamases such as CMY-172 and KPC-41 emerged directly after the use of avibactam/ceftazidime. CMY-172 carries a deletion in its R2 loop (K290-V291-A292) creating more space in the active site of the enzyme which is more active against ceftazidime. Moreover, the N346I substitution disrupts the binding of the enzyme with the sulfate group of the avibactam due to a steric clash with the isoleucine (**Xu et al, 2021**). On the other hand, KPC-41, first identified in a clinical *Klebsiella pneumoniae* isolate in Switzerland, presents a three AA insertion (Pro-Asn-Lys) between residues 269 and 270 leading to an increased affinity for ceftazidime and a decreased sensitivity to avibactam. (**Hobson et al, 2022**).

1.5.7.2.2) Relebactam (MK-7655)

Relebactam differs from avibactam by the presence of a piperidine ring at position C2 (**Fig 1.32**). It is marketed in combination with imipenem and the renal dehydropeptidase inhibitor cilastatin for the treatment of hospital-acquired pneumonia and ventilator-associated bacterial pneumonia (**Theuretzbacher et al, 2020**). Relebactam inhibits clinically-relevant ESBL and CPE class A β-lactamases such as CTX-M-15 or KPC-2 (**Tooke et al, 2019b**), the AmpC PDC-3 (**Barnes et al, 2018**), but not OXA-48 (**Canver et al, 2019**).

It acts as a reversible inhibitor with a binding affinity generally 10 to 100-fold lower than the avibactam (e.g. IC_{50} AVI/CTX-M-15 = 3.4 nM versus IC_{50} REL/CTX-M-15 = 400 nM). Its

piperidine ring presents unfavorable clashes with some residues of class A β-lactamases (e.g. N104 of CTXM-15) (**Fig 1.34**) (**Tooke et al, 2019b**).

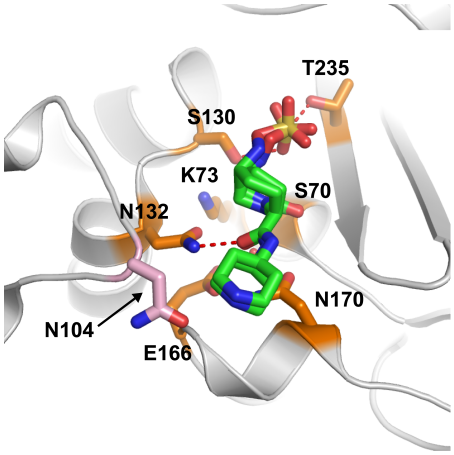

Fig 1.34. *Schematic representation of the acyl-enzyme CTXM-15/relebactam (PDB code 6qw8). The BLI (in green) has a dual configuration. The residue N104 colored in pink makes unfavorable clashes with the relebactam piperidine ring.*

1.5.7.3) Bicyclic boronate family

The cyclic boronic acids pharmacophore is another important family of inhibitors able to mimic the tetrahedral intermediate formed by the serine or the MBL β-lactamases with the antibiotic (**Fig 1.35**), (**Langley et al, 2019**). The bicyclic boronate family presents a better activity against the serine β-lactamases than the MBL β-lactamases.

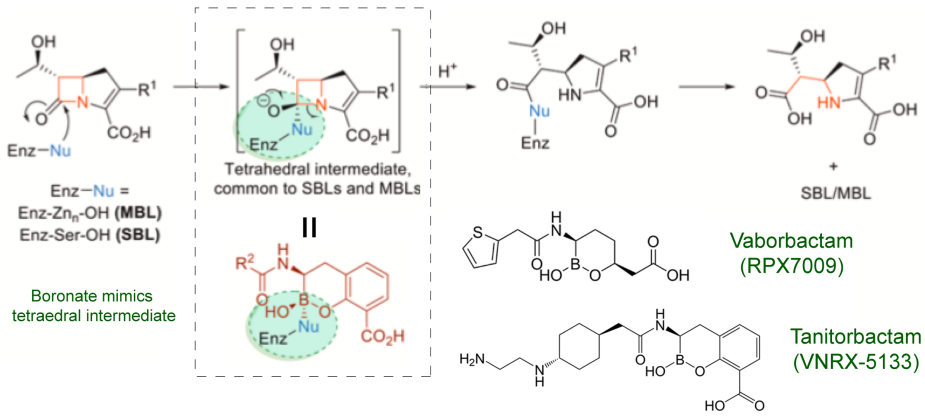

Fig 1.35. *Schematic representation of the β-lactam catalysis by the SBL and MBL with the formation of a tetrahedral intermediate mimicked by the cyclic boronate (**Langley et al, 2019**).*

1.5.7.3.1) Vaborbactam (RPX7009)

The vaborbactam was the first cyclic boronic compound initially developed against class A carbapenemases (KPC) in 2015 (**Fig 1.35**). It inhibits all class A and class C β-lactamases, while MBLs and class D carbapenemases are not impacted (**Tsivkovski & Lomovskaya, 2020**).

The vaborbactam behaves as a two-step tight-binding inhibitor. Firstly, the formation of a non-covalent complex with the enzyme via a sub-micromolar binding affinity results from favorable interactions between the lateral groups of the vaborbactam and the enzyme (**Fig 1.36A**) (**Pemberton et al, 2020**). This is followed by the enzyme inactivation during the formation of the covalent bond between the boron residue and the active-site serine (**Fig 1.36B**). Interestingly, the rate of dissociation is low, rendering the complex Vaborbactam/enzyme very stable (e.g. k_{off} VAB/KPC-2 = 4.3 X 10^{-5} s^{-1}). It illustrates the high potency of this compound to restore the activity of the antibiotics against ESBLs and class A carbapenemases producing strains (**Langley et al, 2019**).

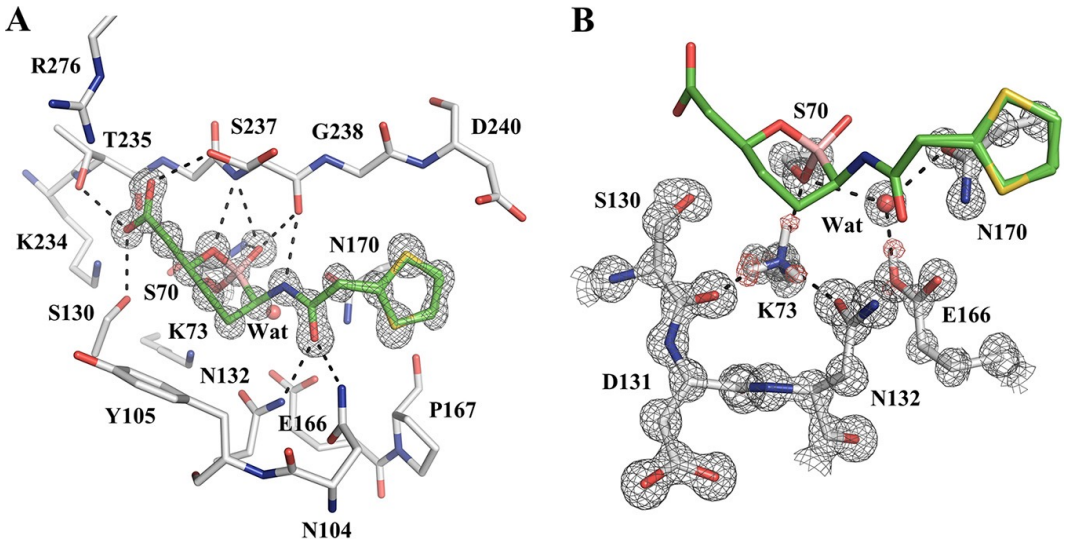

Fig 1.36. *Crystal structures of CTX-M-14 in complex with vaborbactam. (A) Interactions (black dotted line) between CTX-M-14 and the BLI explaining the high affinity of the enzyme for the inhibitor. (B) Protonation state (red mesh) of the residues K73 and E166 and the distance between residues S130 and K73 preventing the deacylation (**Pemberton et al, 2020**).*

The microbiological studies demonstrated the vaborbactam restores the activity of the ceftazidime (**Castanheira et al, 2016a**) and carbapenems (**Castanheira et al, 2016b**) against KPC and other class A and class C β-lactamases producing *Enterobacterales* Isolates. Its association with the meropenem (Vabomere) represents the highest efficient combination against KPC-producing *Enterobacterales*. It was approved by the FDA in 2017 to treat complicated urinary tract infections (cUTI), the acute pyelonephritis and the hospital-acquired or the ventilator-associated bacterial pneumonia (**Lee et al, 2019**).

Interestingly, the vaborbactam can cross the outer membrane of some KPC-producing *Klebsiella pneumoniae* using the OmpK35 and OmpK36 porins. Nevertheless, their down-expression or mutated porins lead to a lower activity of the vaborbactam. On the other hand, the vaborbactam is not a suitable substrate of the AcrAB-TolC efflux pump and the overexpression of the pump impacts less the activity of the vaborbactam (**Lomovskaya et al, 2017**).

1.5.7.3.2) Tanitorbactam (VNRX-5133)

Tanitorbactam was designed from classical boronic compounds where a hydrophobic linker establishes more interactions with the hydrophobic environment of the enzyme active site, while a polar group favors the penetration of the BLI through the outer membrane of Gram-negative bacteria (**Fig 1.35)**. The tanitorbactam inhibits class A and C β-lactamases. Interestingly, it is also active against the carbapenemase OXA-48 and the sub-group B1 MBLs (**Liu et al, 2019**).

As for the vaborbactam, it acts via a two-step model with the formation of a non-covalent complex followed by a tetrahedral intermediate where a covalent bound is established between the boron ion and the active-site serine of class A, C and D β-lactamases (**Fig. 1.37A**). This intermediate is observable in the complex tanitorbactam/VIM-2 where the boron atom interacts with the Zn_1 ion and the conserved residues N233 and D120, while the carboxylate and the oxygen atom of the cyclic oxaborinane binds to the Zn_2 ion mimicking the tetrahedral intermediate in sub-class B1 MBL (**Fig. 1.37B**) (**Hamrick et al, 2020**).

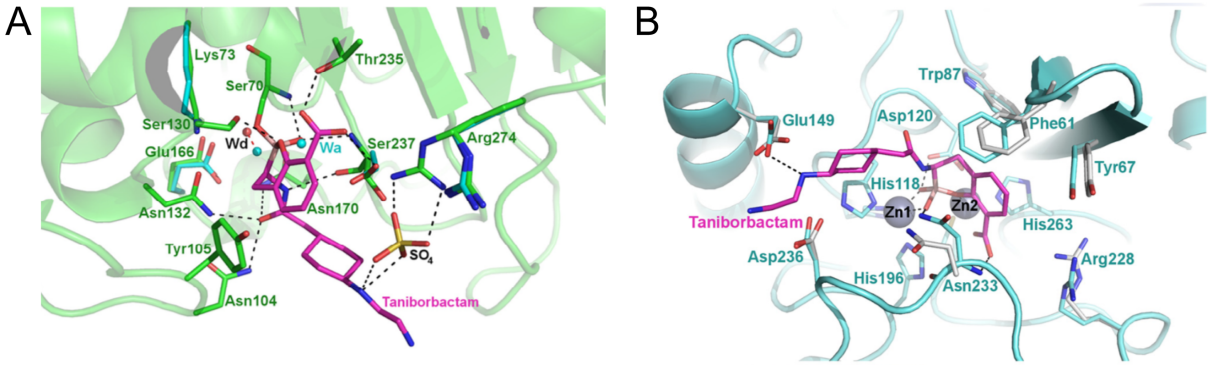

Fig 1.37. *(A) Overall representation of the complex CTX-M-15/tanitorbactam (green) superimposed to the apo-enzyme CTX-M-15 (cyan). The binding with the inhibitor displaces the deacylation water molecule (wd, red circle for the complex) decreasing the deacylation efficiency. (B) In comparison with the native VIM-2 (grey), the interaction of VIM-2 with the tanitorbactam (cyan) induces motion of the conserved residue N233 creating a H-bond with the boronate (**Hamrick et al, 2020**).*

This BLI restitutes the susceptibility to the cefepime against most of the *Enterobacterales* and *Pseudomonas aeruginosa* Isolates (**Kloezen et al, 2021**). This combination is currently in phase III clinical trials for the treatment of complicated urinary tract infections (cUTIs) and hospital-acquired bacterial pneumonia or ventilator-associated bacterial pneumonia (Venatorx Pharmaceuticals).

1.5.7.4) Thiol derivatives

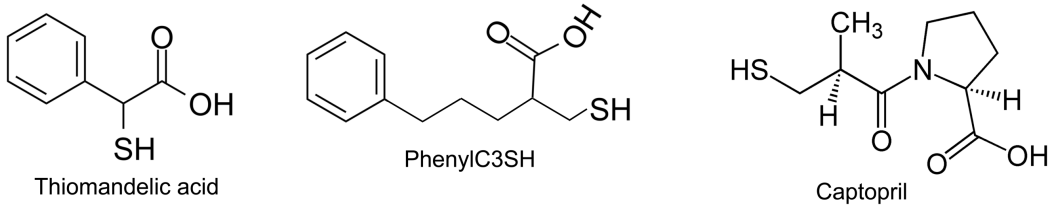

Fig 1.38. *Structures of thiol derivatives*

So far, the discovery of inhibitors against the metallo-β-lactamases remains the most crucial challenge to fight bacterial resistance, mainly due to the absence of a covalent intermediate during the catalytic mechanism and the diversity of structures. Therefore, the MBLs are not sensitive to old age inhibitors (e.g. clavulanic acid, sulbactam and tazobactam) and present a low sensitivity to new generation of inhibitors.

However, the thiol derivatives as the mercaptocarboxylate and the thiomandelic acid represent a real potential for the neutralization of the metallo-β-lactamases (**Fig 1.38**). They interact with the sub-classes B1 and B3 MBLs with affinities inferior to the micromolar, whereas K_i values are at least 200 times higher for the sub-class B2 MBLs such as CphA (**Mollard et al, 2001**). Those substrates present a binding mode mimicking the classical β-lactam antibiotics (**Concha et al, 2000**). Indeed, the thiol group chelates the Zn^{2+} ions and interferes with the binding network established between the hydrolytic water molecule and the zinc ions. Moreover, it presents a hydrophobic lateral group entering in a hydrophobic pocket formed by the flapping loop and the L5 loop. Finally, the function COOH associated to the thiol group of the BLI makes H-bonds with the mobile L10 loop increasing their affinity for the enzyme (**Fig 1.39A&B**) (**Yamaguchi et al, 2007 & Karsisiotis et al, 2013**).

The captopril is another thiol derivative inhibiting the three MBLs sub-classes β-lactamases (**Fig 1.38**). It was developed in the 1970s and targets the zinc ion-utilizing human angiotensin-converting enzyme (ACE) regulating the arterial pressure. Actually, it is employed as treatment for the arterial hypertension. The captopril binds the subclass B1 MBLs following the same binding mode than other thiol derivatives (**Fig 1.39C**) (**King et al, 2012**). However, the binding mode for the subclass B2 CphA from *A. hydrophila* is deeply different since the captopril interacts mainly with the single zinc ion via its carboxylate group (**Fig 1.39D**) (**Brem et al, 2016**). Interestingly, it also inhibits MBLs from the subclass B3 as illustrated by the complex D-captopril/FEZ-1 but without chelating the zinc ions leading lower affinities (**Fig 1.39E**) (**Garcia-Sáez et al, 2003**). The captopril is among the more potent thiol-derivative molecule for MBLs inhibitors and is actually utilized as a scaffold in the development of the new generation of inhibitors (**Ma et al, 2021**).

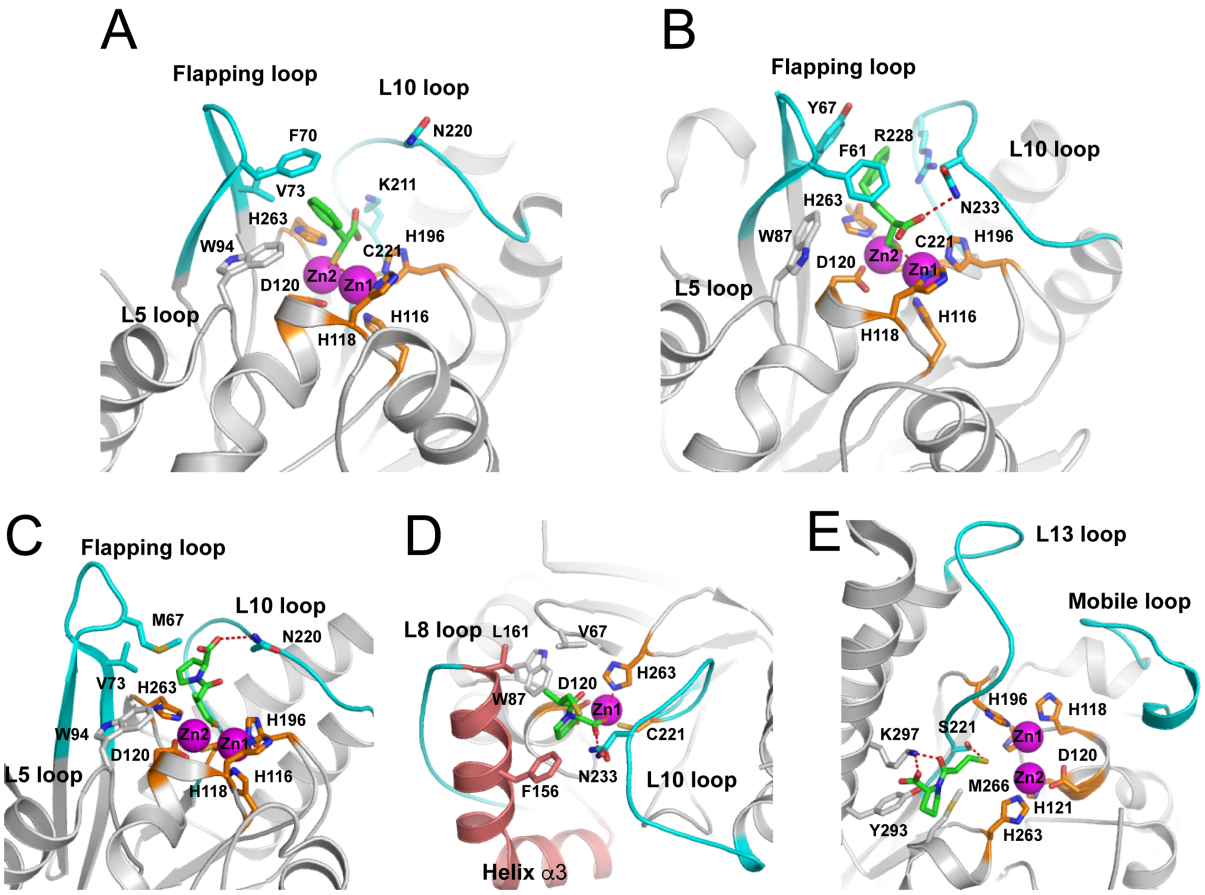

Fig 1.39. *Schematic representation of BCII in complex with the thiomandelic acid (PDB code 2M5D) (A), VIM-2 in complex with the PhenylC3SH (B) (PDB code 2YZ3), NDM-1 in complex with the L-captopril (PDB code 4EXS) (C), CphA in complex with the D-captopril (PDB code 2QDS) (D) and FEZ-1 in complex with the D-captopril (PDB code 1JT1) (E).*

1.6) The nanobody, an antibody fragment from camelids

1.6.1) Canonical antibodies versus Heavy-Chain Only Antibodies (HCAbs)

Antibodies constitute the central point of the adaptive immunity and are produced by lymphocytes B. They ensure functions to efficiently detect and neutralize foreign bodies by preventing the entry of the microbe into the cells, by activation of the complement system and finally, by ensuring the opsonization activity via macrophages.

A classical immunoglobulin is composed by two heavy chains (50 kDa) and two light chains (25 kDa). Each heavy chain contains three constant domains (C_H1, C_H2, C_H3) and one variable domain (V_H), while each light chain comprises one constant domain (C_L) and one variable domain (V_L) (**Fig 1.40**). Both variable domains V_H and V_L constitute the antibody paratope which binds to its specific antigen while the C_H2 and C_H3 domains form the crystallisable fraction (F_C). It corresponds to the effector domain of the antibody recognized by FC receptors on cellular membranes triggering the phagocytose, the release of cytokines or the complement activation.

In bioengineering, the use of the entire immunoglobulin is often difficult because of its voluminous size, its high immunogenicity and its very long half-life time in the serum. Moreover, the recognition of the effector domain by cellular receptors could impede some *in-vivo* experiments due to an important background. The use of antibodies fragments as F_{ab} (57 kDa) or $F_{ab}2$ (110 kDa) obtained by enzymatic digestion are more favorable, notably by removing the effector domain (F_C). The ScFv domain (28 kDa) is also largely utilized and consists in the assembly of both variable domains via a linker. However, despite all these interesting features, their use remains challenging because of their tendency to oligomerize, their poor solubility, stability and their challenging production.

The *Camelidae* family (llamas, camels, dromedaries and alpacas) also owns another type of antibodies named HCAb (Heavy-Chain Only Antibody) (90 kDa) smaller than classical antibodies (150 kDa). HCAbs comprise two heavy chains lacking the C_H1 domain and the light chains. This kind of antibodies probably appeared 25 million years ago and surprisingly, they

are not present in very close families as for the ruminant (bovine) and the suiformes (pig) (**Flajnik et al, 2011**). Cartilaginous fishes possess also heavy-chain antibodies called IgNARs carrying five constant domains (**Feige et al, 2014**). Both HCAbs and IgNARs possess a unique variable domain, VHH and VNAR, respectively, corresponding to the smallest antibody fragment (15 kDa) able to bind the antigen with a comparable specificity and affinity than classical immunoglobulins (**Fig 1.40**).

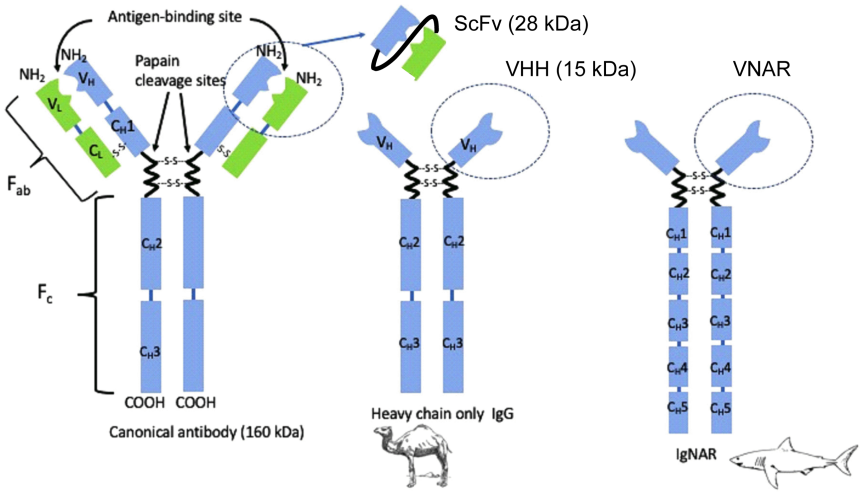

Fig 1.40. *Schematic illustrations of a canonical antibody (IgG) and Heavy-Chain Only Antibodies produced by camelids (HCAb) and cartilaginous fishes (IgNAR) (**https://synapse.koreamed.org/**).*

1.6.2) Physical and chemical features of variable domains

The VHH is organized in two β-sheet domains formed by 4 and 5 β-strands (**Fig 1.41**). It is organized in four highly conserved regions called framework (FR) separated by three complementary determining regions (CDR1, CDR2 and CDR3) presenting a high sequence variability. CDRs are located in the N-terminal part of the VHH and are involved in the binding to the antigen. On contrary with VH, the VHH possesses a conserved intramolecular disulfide bound between cysteines at positions 23 and 94 in the FR1 and FR3, respectively.

The high sequence identity between the V_H and the VHH domains results in a low immunogenicity of the VHH for *in-vivo* applications. However, few differences are noticeable between both variable domains. Within the FR2, some conserved hydrophobic residues (V47,

G49, L50 and W52), involved in the classical immunoglobulin V_H-V_L pairing, are replaced by hydrophilic amino acids (F42, E49, R50, G52) rendering the VHH more soluble and decreasing the risk of aggregation.

Another important difference between the V_H and the VHH concerns the length of the CDR loops. Indeed, the VHH carries CDR1 and CDR3 generally longer than the V_H compensating the lack of V_L domain in HCAbs. Usually, a VHH interacts with its antigen via a rapid association rate (10^4-10^5 M^{-1} s^{-1}) and a low dissociation trend (10^{-2} and 10^{-4} s^{-1}) leading to a nanomolar affinity comparable to classical antibodies (V_H-V_L).

As opposed to V_H-V_L pair which generally presents a groove or a flat paratope, the CDR3 presents in the VHH can form a convex paratope able to enter easily in hidden cavities or enzyme active sites. For example, the cAb-Lys3 developed against the lysozyme is able to form a protruding loop via its CDR3 entering in the enzyme active site and inhibiting the enzyme activity (**Desmyter et al, 1996**).

The nanobodies present a high robustness to extreme conditions. It resists to high temperatures (60-80°C) and acidic pH allowing oral administration of VHHs as therapeutic agents or in organic solvents generally utilized to solubilize pesticides in diagnostic assays (**Amcheslavsky et al, 2021**).

Finally, the small size (2.5 nm diameter) and the globular aspect of the VHH is exploited to easily penetrate tissues such as tumors. This allows a better visualization of cancer markers. Its small size also ensures a rapid clearance from blood by kidneys decreasing the risk of toxicity (**Wang et al, 2016**).

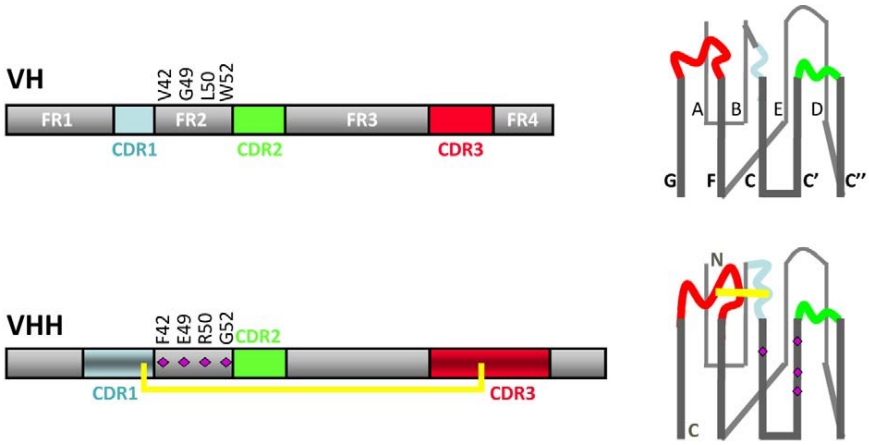

Fig 1.41. *Illustration of the VH domain (classical immunoglobulin) and the VHH (HCAb). Hydrophobic residues (V42, G49, L50 and W52) implied in the VH-VL pairing are mutated in hydrophilic residues in the VHH. A disulfide bond (yellow) between the CDR1 and CDR3 can take place in case of a remarkably long CDR3 (**Flajnik et al, 2011**).*

1.6.3) Genome H-locus organization in camelids.

Genes coding for the heavy chain of classical immunoglobulins and the HCAbs are located on the H-locus carried by the chromosome 6. The first part consists in a multitude of V, D and J elements forming the variable domain of the heavy chain, whereas downstream *IGH* genes code for the constant domains (**Fig 1.42**).

Interestingly, the *IGHG2* gene codes for the constant domains C_H1, C_H2 and C_H3 of the HCAbs (**Fig 1.42**). However, the C_H1 exon is removed during the mRNA splicing. This difference impacts directly the ontogeny of antibodies. Indeed, the translated heavy polypeptide chain is retained in the reticulum endoplasmic via the chaperone protein BiP which recognizes the unfolded C_H1 domain (**Feige et al, 2010**). The BiP protein contributes to the complete folding of the heavy chain and can be substituted by the light chain forming the heterodimer H_2L_2. HCAbs do not express the C_H1 domain resulting in the inability of the BiP protein to anchor the heavy chain in the reticulum and results in the secretion of a homodimer H_2 antibody (**Muyldermans, 2020**).

The camelid genome harbors, on the same H-locus, a lot of VHH (IGHVH3) and V_H germlines (IGHV3) (e.g. 50 IGHV and 40 IGHVH genes for the dromedary). These genes are

very distinguishable, notably by the expression of hydrophobic or hydrophilic residues in the FR2 for the V_H and the VHH, respectively. These residues are essential for the good V_H-V_L pairing and for the VHH solubility. *IGHVH* genes present a larger panel of particular sequences, as palindromic sequences, leading to more often DNA recombinations, mutations and gene conversions. This results in a faster gene evolution increasing the VHHs repertoire.

Interestingly, D and J elements, coding for the CDR3 and the FR4, are common for the V_H and the VHH. But the differences observed in the CDR3 are still controversial. The VHHs with a shorter CDR3 would be eliminated during the B-cells maturation since they are enabled to compensate the absence of the VL domain rendering them less functional. Furthermore, a longer CDR3 in the VHH generally requires a second disulfide bond with the CDR1 or the FR2 due to somatic hypermutations of IGHVH and D elements and the acquisition of 2 cysteines. The absence of one cysteine disrupts the disulfide bond rendering inefficient the VHH (**Muyldermans, 2013**).

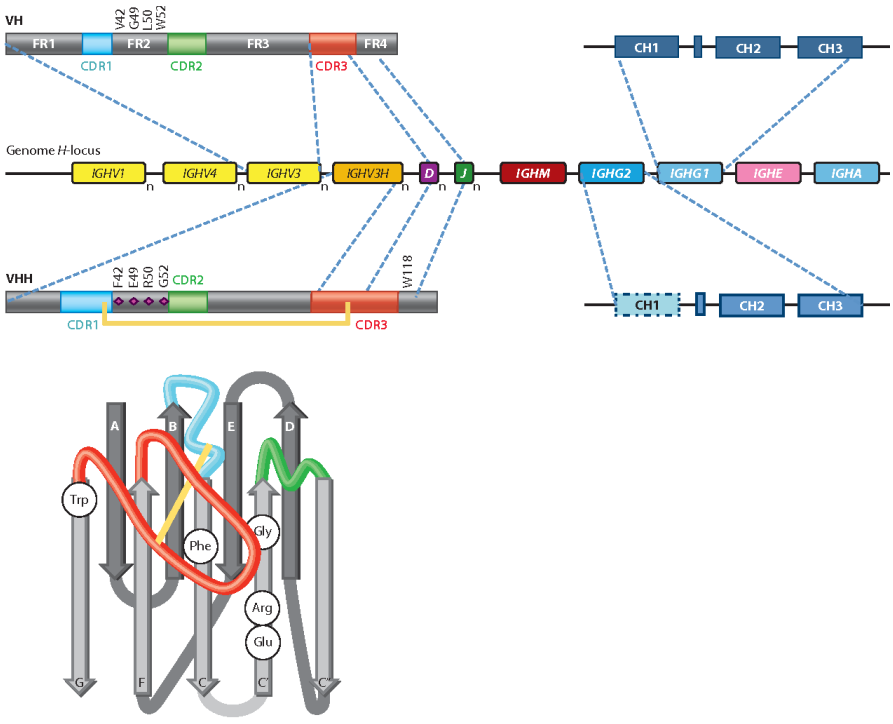

Fig 1.42. *Genome H-locus on the camelid chromosome 6. The IGHV and IGHVH genes code for the FR1-FR3 regions of the VH and the VHH, respectively. The D and J elements commonly express the CDR3 and the FR4 for both domains. They are followed by regions coding for the constant domains of the conventional immunoglobulins (IGHM, IGHG1, IGHE and IGHA) and the HCAb (IGHG2) (**Muyldermans, 2013**).*

1.6.4) Engineering and selection of VHHs

The use of VHHs in biotechnological applications exploded since the HCAb discovery in 1989 at the Vrije Universiteit Brussel (VUB, Brussels, Belgium). This was facilitated by the development of a method allowing the selection of VHH against an antigen (**Fig 1.43**).

The process starts with the camelid immunization with repetitive injections of the immunogen. Then, blood is recovered from the animal, peripheral blood mononuclear cells (PBMCs) are isolated and the total mRNA is extracted from PBMCs. A reverse transcription and a nested PCR are carried out to amplify genes coding for the VHHs in tandem with a restriction enzyme sequence on each side. The VHH genes are subcloned into a phagemid vector forming the final immune library and permitting the replication of phages. They co-express the VHH to the phage capsid protein GIII for the selection of binders by phage display. Successive rounds of bio-panning enrich the VHH library meaning the number of binders is amplified, but the diversity of the VHH repertoire decreases. Then, the selected clones are sequenced and the VHHs are produced to verify their capacity to bind the antigen. Finally, the positive clones are generally sub-cloned in another vector for a large-scale production and their use as diagnostic or therapeutic agents (**Dmitriev et al, 2016**).

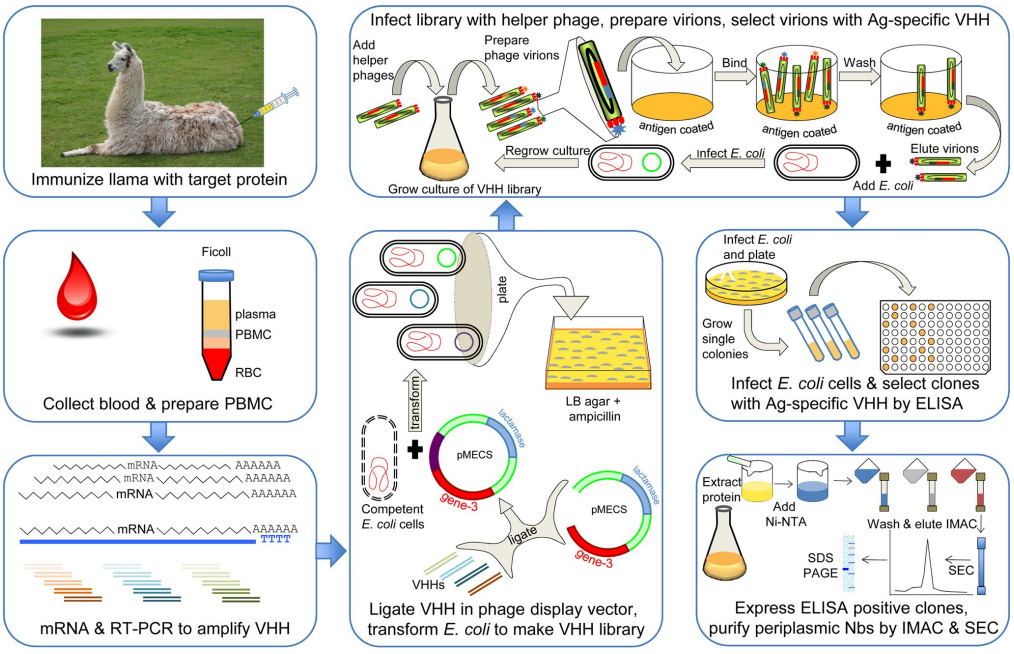

Fig 1.43. *Illustration of the VHHs selection process (**Dmitriev et al, 2016**).*

Camelid immunization is sometimes more complicated due to the non-immunogenic feature of the antigen, its instability or its toxicity. We can consider the construction of a VHH naïve library generated from a large volume of non-immunized animal blood (**Sabir et al, 2014**). Another alternative is the development of a synthetic library with an *in vitro* optimized gene synthesis (**Moutel et al, 2016 & Cawez et al, 2018**). Due to the lack of lymphocytes maturation, those libraries require a significant larger amount of transformants: 10^{10} against 10^{7} transformants for an immune library.

Nowadays**,** the phage display remains the "best-seller" technique to develop nanobodies. However, other methods are more and more used to substitute this technique as the cell surface display consisting in the expression of the antibody in tandem with a cell surface protein. For example, the yeast display, first published by the laboratory of professor *K. Dane Wittrup* (**Boder & Wittrup, 1997**), corresponds to the expression of the nanobody with the Aga2p subunit on the surface of the yeast (**Fig 1.44A**). One tag brought by the VHH is recognized by a fluorescence dye coupled antibody allowing the revelation of the system (**Uchański et al, 2019**). The ribosome display is another largely spread method with the advantage to be performed *in vitro* (**Fig 1.44B**). A library of DNA coding for nanobodies is transcripted. The mRNA is translated *in vitro* and forms a tertiary complex (ribosome-mRNA-native protein). Successive rounds of panning allow the selection of complexes binding to the antigen. Once the elution completed, a lysis buffer dissociates the selected complexes and the genetic information will be recovered from the mRNA by a RT-PCR (**Amstutz et al, 2006**).

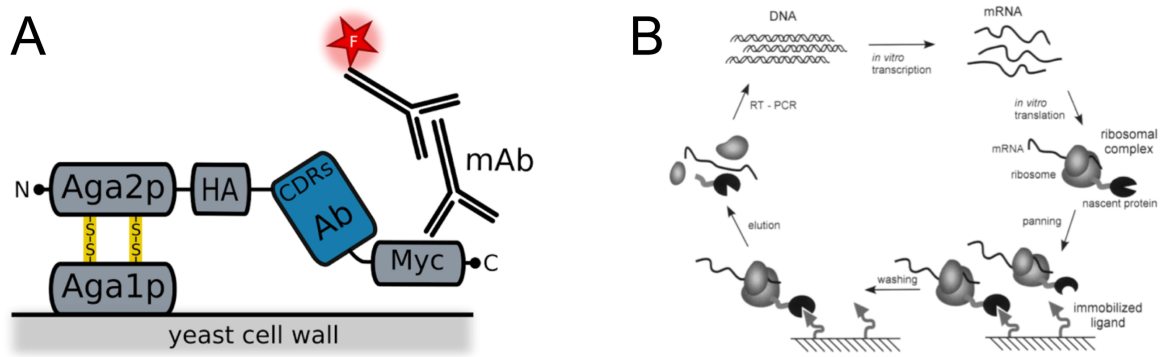

Fig 1.44. *Alternative VHH selection methods: Yeast display (A) (**Uchański et al, 2019**); Ribosome display (B) (**Amstutz et al, 2006**).*

1.6.5) The nanobody, a multi-functional antibody fragment

Initially, nanobodies were largely utilized for biotechnological applications such as a chaperone protein for co-crystallization. It facilitates the packing of the crystal by increasing crystal contacts and can be utilized for the phasing of the crystal via the molecular replacement technic. Moreover, it could rigidify flexible structures, which are not compatible with crystal (**Koide, 2009**).

The bivalent VHH, corresponding to two identical VHHs separated by a linker, presents an important advantage for *in vitro* diagnostic. This construction increases the avidity of the system improving the sensibility of detection assays as by ELISA (**Morales-Yanez et al, 2019**). VHHs are robust to extreme conditions (e.g. pH, organic solvents, desiccation…) rendering them exploitable to detect pesticides (**Li et al, 2021**), or to be utilized for more actual detection methods as the Lateral Flow Assay (LFA) useful for a rapid detection in field tests (**Doerfilinger et al, 2016**). The nanobody can be associated with a fluorescent dye to ensure a simple therapeutic drug monitoring as the Quenchbody (Q-body) (**Inoue et al, 2020**).

The linkage of the VHH with a radioisotope represents a useful tool for the non-invasive *in vivo* diagnostic (**Liu et al, 2021**). Indeed, their small size ensures an efficient tissue penetration and a rapid clearance by kidneys avoiding a too long exposure to the isotope. Moreover, the lack of crystallisable fraction decreases background in non-targeted organs. It is mainly employed for the visualization of cancer markers such as the detection of HER2 overexpressed breast cancer carcinoma via an anti-HER2 nanobody conjugated ^{68}Ga currently in a phase II study (**Keyaerts et al, 2016**).

Its small size, its stability and its easy manufacturing are interesting for the selection of VHHs as therapeutic agents. Caplacizumab (Cablivi) was the first VHH approved by the FDA in 2019. This humanized bivalent VHH was developed by Ablynx-Sanofi and prevents the interaction between the von Willebrand A1 domain factor (vWF) and platelets causing the acquired thrombotic thrombocytopenic purpura, a rare blood disorder leading to blood clots limiting or blocking the flow of blood to organs such as kidneys and heart (**Blair & Williamson, 2019**). Since the Caplacizumab, several companies initiated VHHs constructions (e.g.

multivalent, multispecific, with an effector domain) as therapeutic agents against cancer markers, neurological diseases… (**Muyldermans, 2020**). Developers are unanimous that the use of radionuclide VHHs for therapy, such as the ^{131}I-labeled VHH_1028, presents a real potential as radiopharmaceutical agent (**Feng et al, 2022**).

2. Objectives

This thesis was part of a project funded by the SPF (Service Public Fédéral) Santé Publique (RU-BLA-ESBL-CPE RF 17/6317) and was collaboration a collaboration between the Center for Protein Engineering (CIP, ULiege), the Department of Infectious Disease (DMI) from the Faculty of Veterinary Medicine (ULiege) and the ARSIA (Association Regional de Santé et d'Identification Animale). This project has two major aims: (I) the determination of the repertoire of *bla* genes found in bovine enterobacteria in Wallonia following the new regulation for the use of antibiotics in the veterinary medicine (2016), (II) the targeting of the main β-lactamases identified with VHHs, specific camelid antibody fragments, in order to develop a system of detection and inhibitors.

Based on results obtained by Dr. Virginie Guérin (Department of Infectious Disease, Uliege) and published in Microb Drug Resist in 2021 (**Annexe 1**), I focused my work mainly on the class A β-lactamase TEM-1 (**section 4**) and the class C β-lactamase CMY-2 (**section 5**) with a publication as first author accepted in AAC in 2023 (**Annexe 2**). Despite no carbapenemase was detected in bovine isolates, we also developed nanobodies against the metallo-β-lactamase NDM-1 (**section 6**) which remains a huge concern in human health.

For TEM-1, we chose to work with a VHH published by *Conrath* in 2001 (cAb_{TEM-1} (13)) acting like a tight inhibitor for the activity of TEM-1 (**Conrath et al, 2001**). For CMY-2 and NDM-1, the strategy was to immunize alpacas and select VHHs by phage display with Dr. Rita Maalouf (ALPANANO, CIP, ULiege) and Dr. Francisco Morales (NEPTUNS, CIP, ULiege) under the supervision of the Dr. Mireille Dumoulin (NEPTUNS, CIP, ULiege).

The second phase was the characterization of the affinity and the specificity of all the VHHs for their target by bio-layer interferometry and the selection of the one able to inhibit the activity of the β-lactamases. This included the implementation of different steady-state kinetic experiments to check the ability of VHHs to inhibit the activity of the β-lactamases for a multitude of substrates.

In addition, we also intended to demystify the molecular mechanism by which the different VHHs were able to inhibit the activity of the β-lactamases by determining the structures of the VHH/β-lactamase complex by x-ray crystallography. This part was realized under the supervision of Frédéric Kerff (CIP, ULiege). Because in the case of the cAb_{TEM-1} (13)/TEM-1 complexe, molecular dynamic was involved, three different techniques were considered to further our understanding of the phenomenon: (I) circular dichroism with the help of Mireille Dumoulin (NEPTUNS, CIP, ULiege), (II) molecular dynamic simulations with the help of the Pr. Maximiliano Figueroa (university of Conception, Chile) and NMR relaxation experiments realized by Marius Wanko (Department of Chemistry, ULiege) under the supervision of Pr. Christian Damblon (Department of Chemistry, ULiege). For the latter technique, I mainly provided the labelled-proteins and interpreted the biological significance of the results.

In parallel with these characterizations, we developed efficient sandwich ELISAs for the detection of TEM-1 and CMY-2. Because these assays require the use of two different VHHs with non-overlapping epitopes that were not available, we considered the development of rabbit polyclonal antibodies. In the optimization phase, we verify if the bivalent VHHs, known to improve the stability of the antibody/antigen complex, were able to improve the sensitivity of the ELISA, without impeding the specificity of the assay.

3. Material and method

3.1) Production and purification of TEM β-lactamases

3.1.1) Production of TEM β-lactamases

Two plasmids (ptac11 (**Fig 3.1A**) and pET26b (**Fig 3.1B**)) were used for the recombinant production of TEM_{WT} and TEM variants. The strain *E. coli* JM-109 hosted the ptac11 for the production of wild type TEM-1. The genes coding for all TEM mutants (TEM-121, TEM-1 D214A, TEM-1 R244S and TEM-121 S244R) were inserted between the NdeI-BamHI restriction sites of the pET26b to yield the pET26b-*tem* plasmids. The plasmids were incubated in presence of competent *E. coli* BL21(DE3) to generate the recombinant strains to produce the mutants. The recombinant strains were plated on LB agar supplemented by 100 μg/mL ampicillin for the ptac11 and 70 μg/mL kanamycin for the pET26b. They were incubated overnight (ON) at 37°C. One picked colony was added to 100 mL of M9 minimal medium (3 g/L KH_2PO_4, 7 g/L K_2HPO_4, 0.5 g/L sodium citrate, 0.1 g/L $MgSO_4.7H_2O$, 1 g/L NH_4Cl and 4 g/L of D-glucose). The preculture was grown at 37°C ON in presence of the requisite antibiotic. The cultures (flasks) were started by adding the preculture into fresh M9 medium to a final $OD^{600} \approx 0.2$. They were incubated at 37°C until the $OD^{600} \approx 0.6$. The production of the β-lactamase was induced by adding ITPG (400 μM final concentration). After 6 hours of growth at 37°C, the cultures were centrifuged for 30 minutes at 10000 g, and the supernatant was recovered. Interestingly, most of the β-lactamases were secreted into the culture medium and not in the periplasmic space as expected. This constituted an advantage since the crude extract contains less contaminants. The solution was concentrated by ultrafiltration using a semi-permeable membrane with a cutoff = 10 kDa. Finally, the samples were dialyzed overnight at 4°C against 20 mM TRIS-HCl pH 7.8 buffer using a dialysis membrane (cutoff = 10 kDa).

For the NMR experiments, ^{15}N TEM-1, ^{15}N ^{13}C TEM-1 (deuterated ^{2}D or not) were produced in M9 media as described above. However, we used $^{15}NH_4Cl$ and/or ^{13}C glucose to favor the labelling of the enzyme. The ^{2}D TEM-1 was obtained by growing the bacteria in the

minimal media made with D_2O. The production was done overnight at 25°C in presence of 400 µM IPTG. The cells were centrifuged at 6000 g, and the culture media was discarded. The pellets were suspended in 20 mM TRIS-HCl pH 7.8. The bacterial suspension was lysed with a French Press system. The cell extracts were centrifuged at 20000 g for 30 minutes. The supernatants were dialyzed against 20 mM TRIS-HCl pH 7.8.

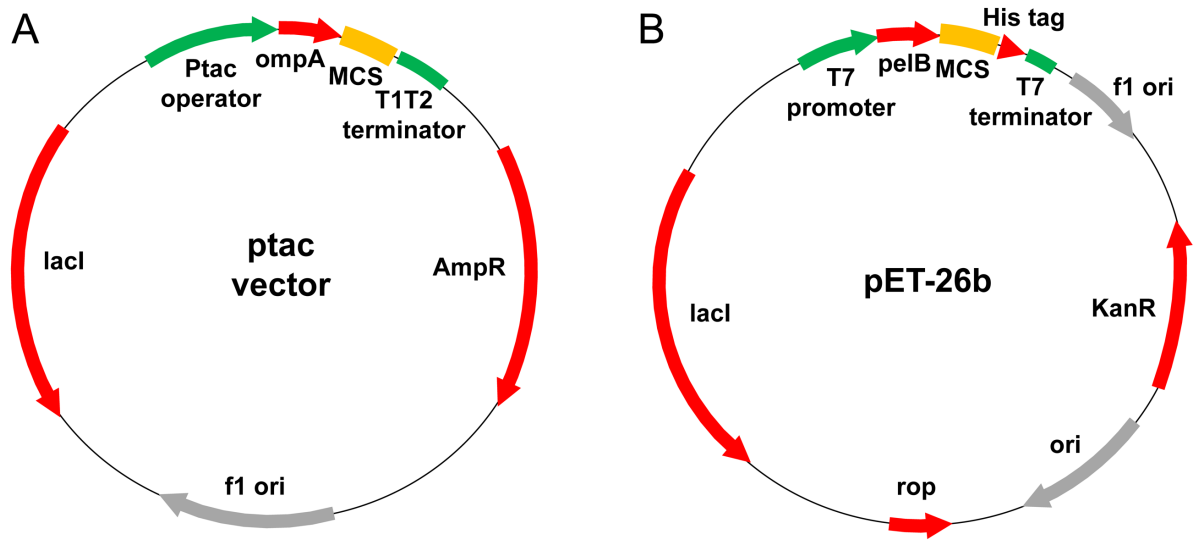

Fig 3.1. *Map of the Ptac vector (A) and the pET26b vector (B). The Ptac vector carries a resistance to ampicillin (amp^r), a MCS (multiple cloning site) preceded by an inducible Ptac promotor and the ompA allowing the protein expression in the periplasm and the upstream T1T2 terminator. The pET26b carries the gene coding for the resistance to kanamycin (Kan^R) and a MCS with an inducible T7 promotor a signal peptide pelB and a T7 terminator.*

3.1.2) Purifications of TEM-1

TEM-1, labelled-TEM-1, and the D214A and R244S mutants were purified by an anion-exchange chromatography using a Q Sepharose HP 24 mL column (Cytiva, United-States). The column was first equilibrated with 5 column volumes (CV) of 20 mM TRIS-HCl pH 7.8 buffer. The samples were loaded on the column. A washing step was realized in 5 CV of equilibration buffer until the A^{280} was lower than 0.05. Then, TEM enzymes were eluted using a linear salt gradient (0-100 %) in 10 CV using 20 mM TRIS-HCl pH 7.8 with 500 mM NaCl. Fractions (4 mL) were collected and the presence of the β-lactamase was checked by electrophoresis on a precast polyacrylamide gel (Bio-Rad, United-States) in denaturing conditions (SDS-PAGE).

Fractions containing the β-lactamase were pooled and dialyzed against 10 mM cacodylate pH 6.0 buffer ON at 4°C.

The second purification was carried out using the same column but equilibrated in 10 mM cacodylate pH 6.0 buffer. The samples were loaded, and the column was washed with the equilibration buffer. The proteins were eluted in a multistep gradient (0-20 % in 4 CV, 20-50 % in 5 CV and 50-100 % in 1 CV of 10 mM cacodylate pH 6.0, 500 mM NaCl). All fractions containing the β-lactamase were dialyzed twice against 20 mM HEPES pH 7.8. The labelled-TEM-1 enzymes were dialyzed against a 50 mM NaH_2PO_4/Na_2HPO_4 pH 6.6 buffer. The purity and the activity of the samples were controlled by: (I) UV spectrum between 240 nm and 340 nm to assess a possible nucleic acid contamination (A^{260}>>A^{280}) and the presence of aggregates (A^{320}), (II) the electrophoresis pattern of increasing quantities of protein on a polyacrylamide gel in denaturing conditions (SDS-PAGE), (III) the determination of the exact mass of the protein by ESI-Q-TOF mass-spectroscopy and (IV) by measuring the specific activity of the different samples.

3.1.3) Purifications of TEM-121

The flow chart for the purification of TEM-121 and TEM-121 S244R was similar of the TEM-1 purification. In this case, the anion-exchange chromatography step was realized by using a capto-Q HP 10 mL column (Cytiva, United-States) equilibrated with 10 CV of 20 mM TRIS-HCl pH 7.8. Even though TEM-121 has an isoelectric point largely inferior to the pH of the buffer, we observed that the β-lactamase passed through the column during the sample loading. The flow-through was concentrated until 500 µL with an Amicon 10 kDa (Merck, Germany) and loaded on a Superdex 75 10/300 GL 20 mL column equilibrated in 20 mM HEPES pH 7.8 buffer. The fractions containing the protein were collected and the presence of the β-lactamase was detected by SDS-PAGE. All fractions with the β-lactamase were pooled together. The purity and the activity of the enzyme were determined as described in **section 3.1.2**.

3.2) CMY-2 and NDM-1 β-lactamases

CMY-2 was produced as previously described by *Cédric Bauvois* (**Bauvois et al, 2005**). The CMY-2 protein was stored at -20°C in 50 mM MOPS buffer at pH 7.0 containing 10 % glycerol (w/v). Its integrity was verified on a polyacrylamide gel by Coomassie-stained SDS-PAGE and mass-spectroscopy (ESI-Q-TOF). The concentration of the enzyme was determined by its absorbance at 280 nm (ε^{280} = 93850 M^{-1} cm^{-1}).

NDM-1 was produced by the Purification Platform (Protein Factory) of the Center for Protein Engineering (CIP) at the University of Liège (**Marcoccia et al, 2016**). The protein was stored at -20°C in a 50 mM TRIS pH 8.0 buffer supplemented by 50 μM $ZnCl_2$. The sample was analyzed by Coomassie-stained SDS-PAGE and the concentration was measured via its absorbance at 280 nm (ε^{280} = 27960 M^{-1} cm^{-1}).

3.3) Development of VHHs against the β-lactamases NDM-1 and CMY-2

3.3.1) Immunization of alpacas and immune library development

One alpaca (*V. pacos*) was weekly immunized by a sub-cutaneous injection of 100 μg of LPS-free antigen mixed with a Gerbu adjuvant. Five days after the last injection, 80 mL of peripheral blood was recovered, and lymphocytes were extracted by a density gradient centrifugation using Lymphoprep™ tubes (Nycomed, Switzerland). Total mRNA was extracted with RNeasy Mini Kit (Qiagen, United States). The immune library was constructed following a protocol developed by *Conrath* (**Conrath et al, 2001**). The amplified genes coding for the VHHs against CMY-2 were ligated into a phagemid vector derived from the pHEN4 plasmid in frame with a myc tag (c-myc derived gene) and a His_6 tag (**Fig 3.2A**). The anti-NDM-1 VHHs were sub-cloned into the phagemid pMECS (**Vincke et al, 2012**) in frame with a HA tag (Hemagglutinin gene derived) and a His_6 tag (**Fig 3.2B**). The VHH repertoire was transformed in *E. coli* electrocompetent TG1 cells (Lucigen, United States). The recombinant strains were collected in LB medium supplemented with 10 % glycerol (w/v) and stored at -80°C.

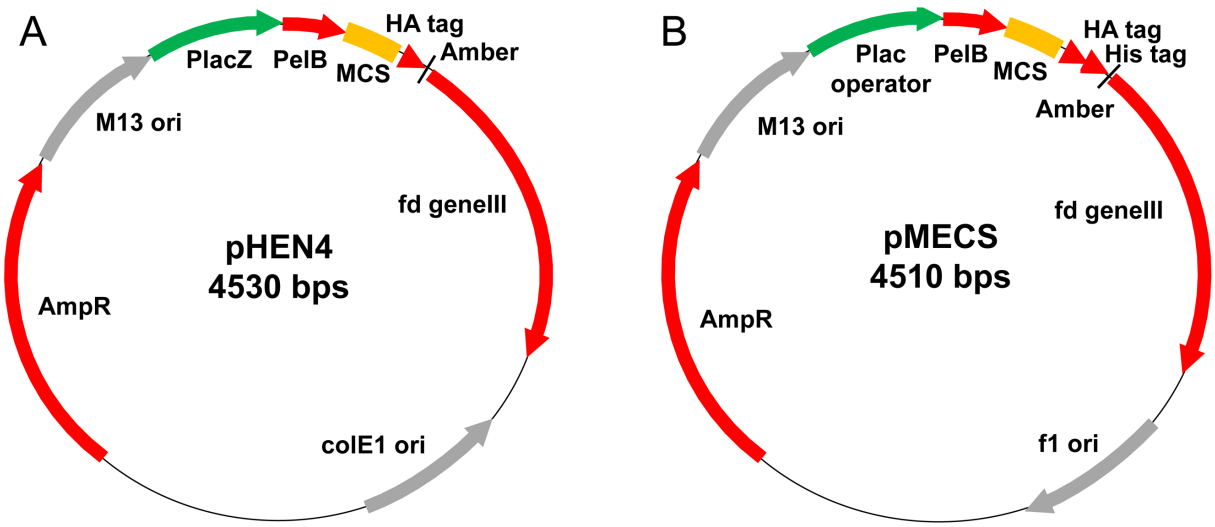

Fig 3.2. *Maps of the pHEN4 vector (A) and the pMECS vector (B). Both vectors possess a replication origin of M13 phages (M13 ori), a resistance gene to ampicillin (ampR), a promotor/operator Plac and a sequence signal (pelB) upstream the VHH gene insertion site (MCS). The VHH is in-tandem with different tags (HA tag for both vectors and a His_6 tag only for the pMECS) and the protein GIII (from the capsid of the phage M13). An amber stop codon is found downstream tags and upstream the gene coding for the protein GIII. The E. coli TG1 strain is a suppressor strain, not able to recognize the amber codon (UAG) allowing the full-length protein translation.*

3.3.2) Selection of VHHs by phage display

Three rounds of panning from the immune library were performed by phage display to enrich the library of anti-CMY-2 and anti-NDM 1 VHHs binders as described by *Pardon* (**Pardon et al, 2014**). One mL of the VHH library was cultured at 37°C in a 2XTY medium supplemented with 1 % glucose (v/v) and 100 µg/mL ampicillin. When the OD^{600} of the culture reached 0.6-0.8, the cells were incubated in presence of 10^{12} particles of the phage helper M13K07 (ThermoFisher Scientific, United States) for 30 minutes at room temperature (RT) and without agitation. Then, the infected cells were centrifuged and resuspended in a 2XTY medium, 100 µg/mL ampicillin (resistance brought by the phagemid) and 70 µg/mL of kanamycin (resistance brought by the phage helper). The cells were incubated ON at 37°C under agitation. The next day, they were centrifuged for 30 minutes at 12000g at 4°C. The supernatant was recovered, and the phages were precipitated by the addition of 30 mM polyethylene glycol-6000/2.5M NaCl solution (20 % w/v). The solution was incubated for 30 minutes on ice and centrifuged at

4000 g at 4°C. The pellets corresponding to the phages were resuspended in 1 mL of 50 mM PBS pH 7.5 buffer. The concentration of phages was determined by measuring the absorbance of the suspension at 260 nm (OD^{260} = 1 equals 3 x 10^{10} phage particles/mL). Two strategies of panning were undertaken to select the VHHs: (I) by antigen adsorption on a 96-well plate (CMY-2 and NDM-1) and (II) in solution (NDM-1, confidential, not detailed in this work).

For the panning by adsorption, 1 μg/well of antigen (CMY-2 and NDM-1 β-lactamases) diluted in 50 mM MES pH 5.5 buffer was coated by adsorption on a 96-well multisorp NUNC ELISA plate (ThermoFisher Scientific, United States) ON at 4°C. The negative control corresponded to a well filled with the coating buffer only. The next day, the wells were washed five times with a 50 mM PBS with 0.05 % tween-20 (PBST). They were blocked by addition of 0.1 % casein (w/v), 0.1 % BSA (w/v) and protein free buffer (ThermoFisher Scientific, United States) in rounds 1, 2 and 3 of panning, respectively. The panning was realized by adding 10^{11} phages particles per well. The plates were incubated for an hour at RT. Then, 20 washes with PBST were carried out to eliminate the unspecific binders. The elution of the specific VHHs was performed by a pH shock with the addition of 100 μL of 100 mM TEA (Triethanolamine) pH 11.5 in each well. After an incubation of 10 minutes at RT, the supernatant was recovered and neutralized with 100 μL of 1 M TRIS-HCl pH 8.0.

10 μL of the eluted phages were diluted 10^7-fold and incubated in presence of 90 μL of competent TG1 *E. coli* for 30 minutes at RT. 50 μL of the suspension was plated on a LB agar plate with 100 μg/mL of ampicillin, 2 % glucose (w/v) and incubated ON at 37°C to obtain individual colonies. Moreover, 10 μL of each dilution (10^1 -10^7) were also deposited on square LB agar plate supplemented with 100 μL of ampicillin to check the enrichment of the positive assay compared to the negative control where no antigen was present. Finally, the remaining fraction of the eluted phages was used to infect TG1 cells for the subsequent round of panning.

3.3.3) Screening of binders by indirect ELISA

90 colonies from each round of selection were picked with the MicroLab Star robot (HAMILTON, United States) from ROBOTEIN^{TM} platform. The colonies were grown in 100 μL of 2XTY medium supplemented with ampicillin (100 μg/mL), 0.1 % glucose (w/v) and 10 % glycerol (w/v) in a 96-well flat-bottom plate (Greiner-BioOne, Belgium) ON at 37 °C. 10 μL of each glycerol stock were added to 1 mL of 2XTY medium supplemented with ampicillin and glucose in 96-deep well plates. After an incubation of 4 hours under constant agitation at 37°C, the production of the VHHs was induced by the addition of 1 mM IPTG. Then, the cultures were incubated for 5 hours at 37°C or ON at 28°C. The cells were recovered by centrifugation and an extraction of the VHHs was performed by one cycle freeze-thaw at minus 80°C. The selection of VHHs was performed by an indirect ELISA. 96-well NUNC multisorp plates (ThermoFisher Scientific, United States) were coated with 1 μg of antigen diluted in a 50 mM MES pH 5.5 buffer. After an incubation ON at 4°C, the plate was blocked by addition of 1 % (w/v) non-fat dried milk solution for 2 hours at RT. We used a different blocking agent in order to avoid selection of VHHs directed against the blocking agents used for the panning's steps. Once the blocking step ended, the plates were incubated with the *E. coli* crude extract containing the VHHs for one hour at RT. We considered one negative control (one well without coated antigen for each VHH). Finally, the revelation was carried out using a primary antibody corresponding to a 1/2000 diluted mouse anti-His antibody (Biolegend, United States) and a 1/2000 diluted mouse anti-HA antibody (Biolegend, United States) for CMY-2 and NDM-1, respectively. In both cases, this primary antibody was recognized by a 1/2000 diluted goat anti-mouse antibody coupled to a phosphatase alkaline (PA) (Bethyl Laboratories, United States). We used the 4-phenyl phosphate disodium (Sigma-Aldrich) (2 mg mL^{-1}) as PA substrate and the plates were read at 405 nm with a SpectraMx M2 microplate reader (Molecular Devices, United States). All steps were followed by 10 washes with a 50 mM PBS buffer supplemented by 0.05 % Tween-20 (PBST). Primary and secondary antibodies were also diluted in PBST. A clone was considered positive if the signal ratio positive/negative was larger than 1.5. All positive VHHs were sequenced and grouped in families in function of the CDRs sequences.

3.4) VHHs sub-cloning, production and purification

3.4.1) Sub-cloning of the VHHs into the vector pHEN14

All the candidates were subcloned into the phagemid pHEN14. This plasmid derived from the pHEN6 vector where the cassette coding for the resistance to ampicillin was substituted by a gene coding for the resistance to chloramphenicol (**Fig 3.3**).

Firstly, 20 μg of pHEN4-derived-VHH or pMECS-VHH plasmids were digested ON at 37°C, by 40 units of *Hin*dIII HF and *Bst*EII HF (New-England BioLabs, United-States) restriction enzymes at extremity 5' and 3', respectively. The digestion allowed the recovery of the DNA fragment containing the PelB signal peptide in frame with the sequence of the VHH. All digested fragments were deposited on a 1 % Agar gel and the desired DNA bands (around 400 BP) were purified with a NucleoSpin® Plasmid EasyPure (Macherey-Nagel). 150 ng of digested fragments coding for the VHHs were ligated in 50 ng of pHEN14 digested by the same restriction enzymes (ratio 3:1) using 10 U of the T4 ligase (ThermoFisher Scientific, United-States) ON at 16°C. Competent *E. coli* DH5α cells were transformed with the ligation product by a thermic shock and deposited on LB agar plate supplemented by 25 μg/mL of chloramphenicol. Some individual colonies were picked and transferred in LB medium in order to extract the plasmid and to verify their nucleotide sequences by sequencing.

Genes coding for the bivalent VHHs, corresponding to two identical VHHs in tandem repeats and joined by a peptide linker $(GGGS)_3$, were ordered into the pHEN14 from Genecust (Boynes, France) and were integrated with the same restriction enzymes (**Morales-Yanes et al, 2019**).

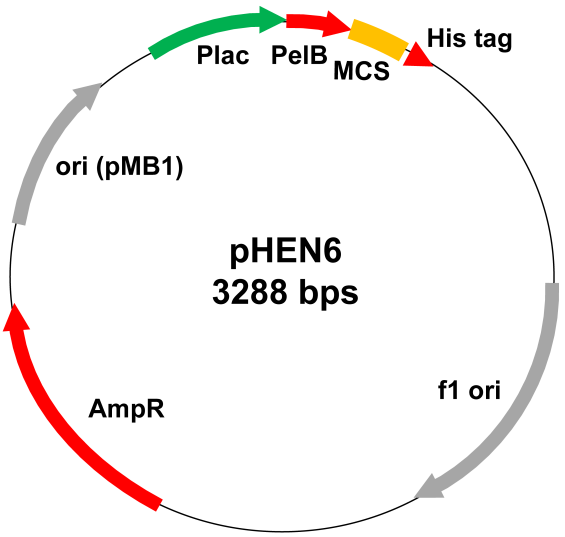

Fig 3.3. *Vector map of the phagemid pHEN6. It is derived from the pHEN4 phagemid where the HA tag is replaced by a His_6 Tag and the gene coding for the protein GIII is deleted.*

3.4.2) Scale-up Production

The production of the monovalent and bivalent VHHs started with the transformation by thermic shock of competent *E. coli* cell WK6 by the plasmid pHEN14-VHH. The cells were plated on LB agar supplemented by chloramphenicol 25 µg/mL. The next day, one colony was cultured ON at 37°C in a LB medium added with the same antibiotic. VHHs were produced in flasks in a Terrific Broth medium (24 g/L yeast extract, 12 g/L tryptone, 17 mM KH_2PO_4, 72 mM K_2HPO_4, glucose 0.1 % (w/v)) containing chloramphenicol (25 µg/mL) and few milliliters of the preculture to reach an initial $OD^{600} \approx 0.2$. The growth was realized at 37°C until the beginning of the exponential phase ($OD^{600} \approx 0.8$). Then, 1 mM of IPTG was added to induce the production of the VHH ON at 25 °C.

3.4.3) Periplasmic extraction by osmotic shock

Since the VHHs were expressed in the periplasm via their signal peptide (PelB), a periplasmic extraction was realized by osmotic shock. First, the cells were centrifuged for 30 min at 10000 g and the supernatant was discarded. The cells were resuspended in a solution of TES (30 mL/liter culture) and incubated for 45 minutes at 4°C using a rotation shaker. The TES solution contained 20 mM TRIS-HCl pH 8.0 corresponding which is not well tolerated by

cells, 500 μM of EDTA able to chelate metal ions and 500 mM sucrose allowing the destabilization of the outer membrane of cells by an osmotic shock. 50 U/liter culture of benzonase (Merck, Germany) was added in presence of 1 mM $MgCl_2$ to avoid contamination by nucleic acids. Mg ions are essential for the benzonase activity. Then, a second incubation with the solution TES diluted four times was performed for 90 min at 4°C using the rotation shaker. The suspension was centrifuged at 45000 g for 20 minutes. The supernatant, corresponding to the periplasmic extract, was recovered and filtered on 0.22 μm filter.

3.4.4) Purification by affinity chromatography

The VHHs containing a His_6 tag at their c-terminal end allowed their purification by Immobilized metal affinity chromatography *(*IMAC). We used a HisTrap™ HP 5 mL column (Cytiva, United-States). The presence of nitrilotriacetic acid (NTA) chelates Ni ions that will interact with the poly-His sequence of the protein. The column was first equilibrated by 10 CV in 20 mM HEPES pH 8.0 buffer, 100 mM NaCl, 10 mM imidazole. The periplasmic extract was loaded on the column. The washing step was realized with 5 CV of the equilibration buffer to eliminate contaminants. Finally, the VHHs were eluted with a linear gradient of imidazole (0-100 %) on 20 CV using 20 mM HEPES 20 mM pH 8.0 buffer, NaCl 100 mM and 500 mM imidazole. Fractions of 2 mL were collected and the presence of the VHH was checked by SDS-PAGE. All fractions containing the VHH were pooled and purified by size exclusion chromatography.

3.4.5) Purification by size exclusion chromatography

Pooled fractions were firstly concentrated until 500 μL with an Amicon 3 kDa (Merck, Germany). The sample was loaded on a Superdex 75 10/300 GL equilibrated in 50 mM HEPES pH 7.2 buffer, 100 mM NaCl for the anti-TEM-1 VHH, 50 mM PBS pH 6.1 buffer for VHHs against CMY-2 and 50 mM PBS pH 7.5 buffer for anti-NDM-1 VHHs. Fractions containing the VHH were pooled together and some controls were carried out with: (I) a UV-spectrum between 240 and 340 nm, (II) growing quantities of VHH on a polyacrylamide gel (SDS-PAGE), (III) mass-spectroscopy (ESI-Q-TOF) and (IV) an activity assay by bio-layer interferometry.

3.5) Production and purification of polyclonal antibodies (pAbs)

Rabbit immunizations were carried out by the CER group (Marloie, Belgium) to obtain polyclonal antibodies (pAbs). 4 subcutaneous injections of 500 μg of antigen were done every two weeks. The sera were recovered from blood and were conditioned in a 50 mM PBS pH 7.5 buffer. The pAbs were purified with a HiTrap Protein A HP 1 mL column (Cytiva, United-States). After an equilibration with 10 CV and the load of the sample, the pAbs were eluted with a 20 mM glycine pH 2.0 buffer and directly neutralized via a 100 mM TRIS-HCl pH 8.5 buffer. Fractions containing the pAbs were pooled and dialyzed against a 50 mM PBS pH 7.5 buffer ON at 4°C. The integrity and the purity of the pAbs were assessed by a coomassie-stained SDS-PAGE, whereas the concentration of the pAbs was measured by BCA (Bicinchoninic Acid Assay).

3.6) *In-vitro* biotinylation

Some bio-layer interferometry experiments and ELISAs required biotinylated proteins. To this aim, we used the EZ-link$^{@}$NHS-PEG_4 biotin kit (ThermoScientific, United States) to covalently bind a NHS-PEG_4-Biotin to primary amines such as on the side-chains of lysines. This reaction was performed at RT, for 30 minutes in presence of a [Biotin]:[protein] ratio of 3:1. The excess of free biotin was removed using a Sephadex G25 1 mL desalting column (Cytiva, United-States) and the biotinylated proteins were conserved in a 50 mM PBS pH 7.5 buffer. The protein concentration was determined by BCA.

3.7) Binding study by bio-layer interferometry

3.7.1) Principle

Bio-layer interferometry is a label-free method consisting in the measure of an interference pattern for the wavelengths of light in function of time (**Fig 3.4**). Briefly, the light is directed down a fiber-optic biosensor and is reflected from an internal reference layer and the biocompatible layer. It creates an interference pattern for all wavelengths of light. When molecules bind at the biocompatible layer, the distance between the reflected light from the

internal reference and the biocompatible surface increases creating a shift in the interference pattern of light ($\Delta\lambda$) which can be monitored in real time providing kinetic data on molecular interactions (**Fig 3.5D**).

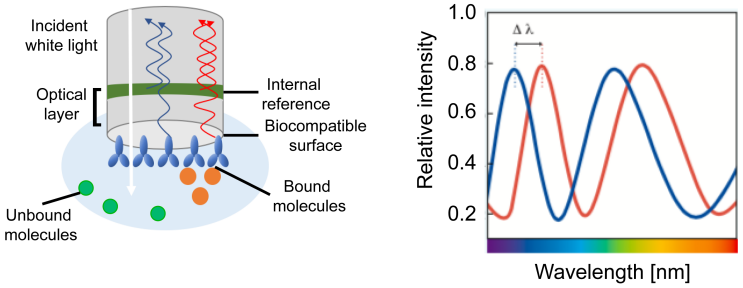

Fig 3.4. *Schematization of the bio-layer interferometry principle used by the OCTET HTX (ForteBio, Sartorius). Illustrations were adapted from Renee Tobias, Application note 14, ForteBio.*

3.7.2) Experimental setup

All bio-layer interferometry experiments were performed on the OCTET HTX instrument (ForteBio, Sartorius) at 30°C using 96-well polypropylene microplates (Greiner BioOne, Belgium). All proteins were diluted in a kinetic buffer (KB) corresponding to 50 mM PBS pH 7.4 with 0.1 % BSA (w/v) and 0.05 % tween-20 (v/v). All data were analyzed with the OCTET software version 12.0 (Sartorius, France). All negative controls corresponded to the load of the analyte directly on the biosensor.

Qualitative and quantitative measurements were carried out using His1K biosensors (Sartorius, France) to determine the specificity and the affinity of the VHHs, respectively (**Fig 3.5A**). These biosensors are coated by anti-His antibodies able to recognize the His_6 tag of VHHs that were loaded in a range of concentrations between 0.5 and 5 $\mu g\ mL^{-1}$. Then, a baseline was realized using the KB for 60 s. The binding of the β-lactamase to the VHH was monitored by immersing the bio-activated sensor into a solution of 500 nM of different representative of β-lactamases for the specificity assays and into solutions of at least 4 different concentrations of their specific antigen for quantitative measurements (indicated on

each sensorgram). The dissociation rate was measured by dipping the biosensor into wells containing the KB.

Avidity studies were performed using streptavidin biosensors (SA sensor, Sartorius) on which biotin-TEM-1 and biotin-CMY-2 were immobilized at 2 μg mL^{-1} and between 10 and 50 μg mL^{-1}, respectively (**Fig 3.5B**). A quench reaction was carried out by immersing the sensors into 10 μM biocytine for 300 s followed by a baseline for 60 s in the KB. Then, the binding of rabbit pAbs or the bivalent VHH were monitored with at least 5 different concentrations (indicated on each sensorgram). The dissociation of the complexes was measured for 600 s in the KB.

The specificity of the pAbs was also monitored on streptavidin bio-sensors using only a concentration of 500 μM of pAbs to determine the binding to representative biotinylated β-lactamases (**Fig 3.5B**).

Finally, competition binding assays were performed by a premix method with SA biosensors (**Takkar et al, application note 16**) (**Fig 3.5C**). Firstly, a biotinylated anti-CMY-2 VHH at 2 μg mL^{-1} was immobilized on the biosensor to reach a variation of signal ($\Delta\lambda$) around 1 nm. Complexes VHH/CMY-2 were obtained by incubating CMY-2 (200 nM) and the VHH (100 nM – 4 μM) for 15 min at 30°C. Then, the biosensors were immersed into the solutions containing the preformed complexes in order to assess the association between the immobilized VHH and the complexes VHH/CMY-2. Binding rates were measured for the first 120 s of the association phase with an exponential model (not described by the manufacturer). The same experimental setup was used to check the presence of an overlapping epitope of the anti-NDM-1 VHHs on NDM-1. However, in this case, we only performed a qualitative binding measurement with the complex formed by NDM-1 at 200 nM and 1 μM of VHH.

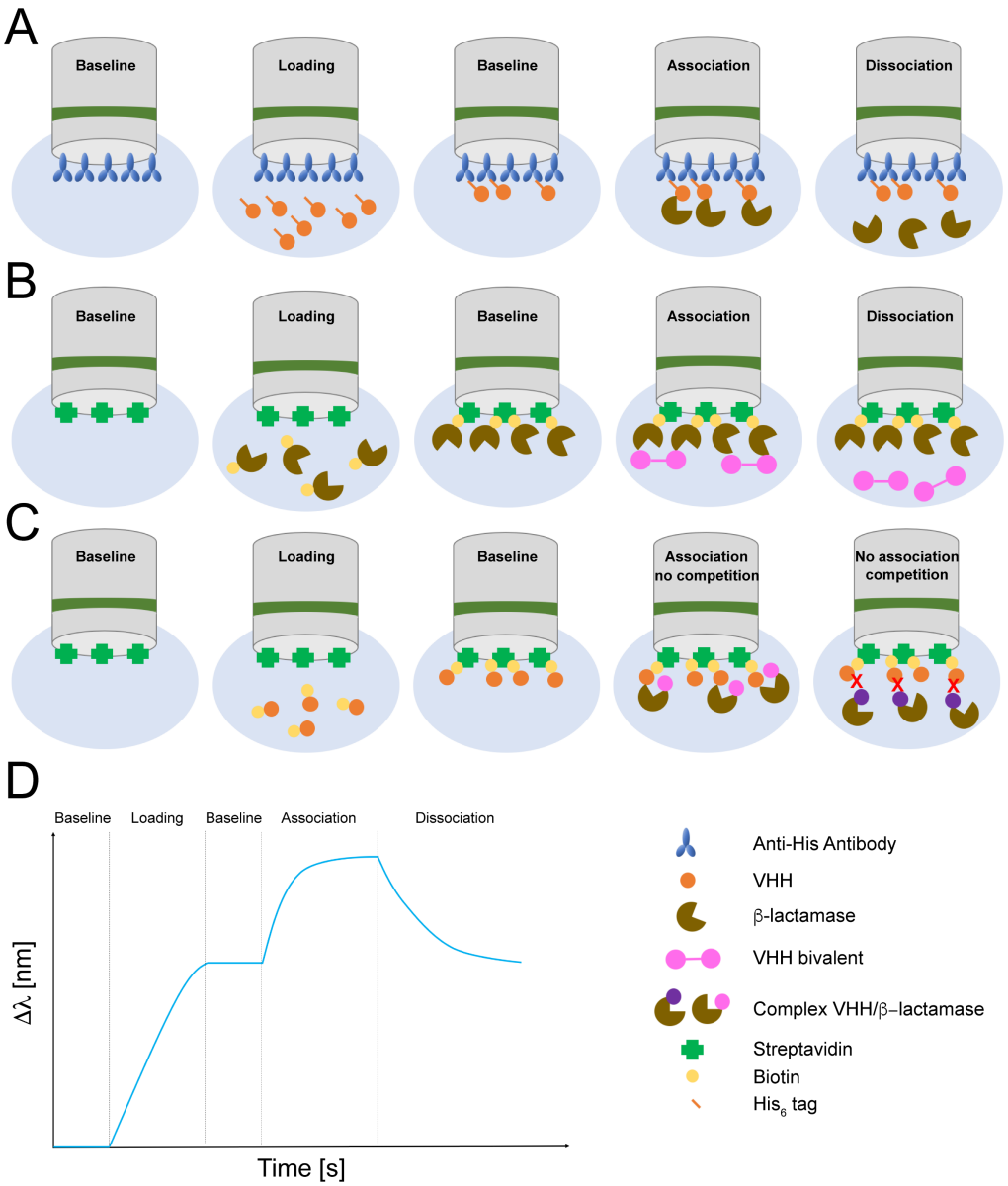

Fig 3.5. *Experimental setups using Anti-His biosensors (His1K sensor) (A) and streptavidin biosensors (SA sensor) (B) for qualitative and quantitative binding measurements. The only difference consists in a quench reaction to block all free sites on streptavidin for SA biosensors (not indicated on the illustration). (C) Competition binding assays using SA biosensors and where only associations were monitored. The epitope overlapping results in no association (red crosses on the picture). (D) Typical sensorgram obtained by a bio-layer interferometry experiment (quench reaction for the SA biosensors not indicated).*

3.7.3) Binding kinetics model

The kinetics constants (k_{on}: kinetic constant for the association of the antigen/VHH complex and $k_{off:}$ kinetic constant for the dissociation of the complex) and the thermodynamic equilibrium constant (K_D) were calculated using a 1:1 interaction model (scheme 1) where A corresponds to the ligand immobilized on the biosensor and B the analyte in solution (**Tobias, Application note 14**).

$$A + B \underset{k_{on}}{\overset{k_{off}}{\leftrightharpoons}} AB$$

Scheme 1. *1:1 binding model reflecting the interaction of one molecule of ligand (A) with one molecule of analyte (B) to form a complex AB.*

The equation I describes the association of two Interactants:

$$Y = Y_0 + A\,(1 - e^{-k_{obs} * t}) \quad (I)$$

Where Y reflects the association between A and B in function of time t, Y_0 corresponds to the binding at start of association, A the constant reflecting the nature of the reactants and k_{obs} the observed kinetic rate constant.

Once the biosensors are dipped into wells containing only the KB, complexes AB start to dissociate in function of the dissociation rate and the concentration of complex at the beginning. This is described by the equation II:

$$Y = Y_0 + A\, e^{-k_{off} * t} \quad (II)$$

Where Y_0 is the level of binding at start of dissociation and the k_{off} is the first order rate constant (s^{-1}) that corresponds to the dissociation of the complex.

The association rate constant k_{on} can be calculated based on both k_{obs} and k_{off} constants following the equation III:

$$k_{on} = \frac{k_{obs} - k_{off}}{[Analyte]} \quad (III)$$

where k_{on} (M^{-1} s^{-1}) illustrates the second order kinetic constant for the formation of the complex AB.

The equilibrium constant (K_D) assesses the stability of the AB complex. It corresponds to the ratio k_{off} /k_{on} ratio described in equation IV:

$$K_D = \frac{[A]*[B]}{[AB]} = \frac{k_{off}}{k_{on}} \quad (IV)$$

Where K_D is expressed in molar (M) and is generally considered as the concentration of analyte at 50 % of complexes. Obviously, higher is the K_D value, lower is the affinity and inversely.

3.8) pAbs specificity by indirect ELISA

The specificity of pAbs was determined by indirect ELISA. First, 500 ng of all classes representing β-lactamases diluted in 50 mM MES pH 5.5 buffer were coated by adsorption on a 96-well NUNC maxisorp plate (ThermoScientific, United States) ON at 4°C. The next day, the plate was blocked using a 1 % BSA (w/v) solution for two hours. Then, 500 ng of pAbs were added in each well. Finally, the presence of complex β-lactamase/pAbs was revealed by addition of a 1/2000 diluted goat anti-rabbit antibody conjugated to horseradish peroxidase (HRP) (Abcam, UK). All steps were followed by 5 washes with PBST. All proteins were diluted in the wash buffer and the incubation was performed for 1 hour at 28°C. TMB (*3,3',5,5'-Tetramethylbenzidine*, Merck, Germany) was used as substrate for the system revelation. The reaction was quenched with 1M H_3PO_4 and the absorbance of the wells was measured at 450 nm with the help of an Infinite M200 Pro microplate reader (Tecan, Switzerland).

3.9) Development of a sandwich ELISA for the detection of TEM-1 and CMY-2

A sandwich ELISA was carried out to assess the limit of detection (LOD) and the specificity of the different assays for the detection of TEM-1 and CMY-2. In this aim, several combinations of capture and detection antibodies were tested (**Fig 3.6**).

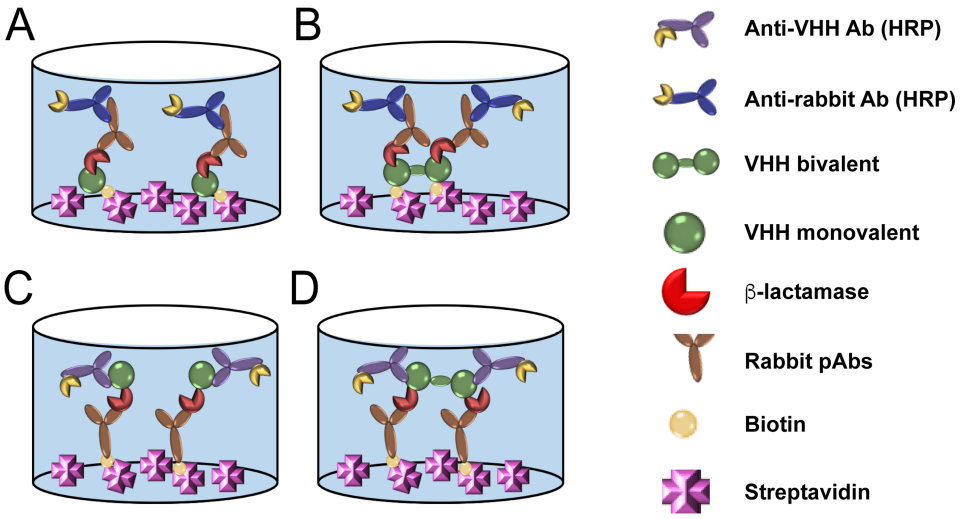

Fig 3.6. *Sandwich ELISA format for TEM-1 and CMY-2 detection. The first assays consisted in immobilizing the biotinylated monovalent (A) and the bivalent VHH (B) on a streptavidin coated plate, while the detection was ensured by rabbit polyclonal antibodies recognized by a secondary antibody conjugated to HRP. Inversely, two other assays were carried out with the biotinylated polyclonal antibodies as capture antibody, while the monovalent (C) and the bivalent VHH (D) recognized by the anti-VHH antibodies coupled to HRP allowed the revelation of the system.*

Briefly, 500 ng of biotinylated cAb_{CMY-2} (254) VHH (monovalent or bivalent) or 2 µg of biotinylated anti-CMY-2 pAbs were used as capture agent on a 96-well NUNC streptavidin polysorp plate incubated ON at 4°C. Only 200 ng of biotinylated monovalent cAb_{TEM-1} (13) VHH was utilized to detect TEM-1. The plate was blocked with a 1 % BSA (w/v) solution.

Then, the purified TEM-1 and CMY-2 were added in serial dilutions from 10^{-4} to 1 µg mL^{-1} and 10^{-4} to 2 µg mL^{-1}, respectively, to determine the limit of detection (LOD) of all assays.

The LOD value was calculated with a sigmoidal model illustrated by the equation V:

$$\mathrm{LOD} = \frac{\mathrm{B}+(\mathrm{T}-\mathrm{B})}{1+\ 10^{(\mathrm{LogIC50}-\mathrm{X})*\mathrm{cut-off}}} \quad \text{(V)}$$

Where T corresponds to the top of the curve and B to the pre-transition state, the IC50 is the concentration of antigen at 50 % of the top Y value and the cut-off represents the average absorbance at 450 nm of the negative control plus three times the standard deviation.

The *in vitro* specificity assays were evaluated with 200 ng of purified β-lactamases belonging to the four classes of β-lactamases. We used at least three wells where antigen was omitted as blank for all assays.

Moreover, we also decided to verify the *in vivo* specificity of our assays by the detection of TEM-1 and CMY-2 in human and bovine bacterial Isolates. The bacteria were grown in TB medium supplemented by 100 μg mL^{-1} ampicillin for 4 hours at 37°C. We discarded the medium by centrifugation at 4800 g. Then, the cells were lysed by sonication with a Bioruptor Plus (Diagenode, Belgium) and centrifuged at 18000 g to recover the soluble fraction of the bacteria. All assays on bacterial isolates were realized using 5 μg of the bacterial crude extract. *E. coli* DH5α strain was employed as negative control.

The detection of CMY-2 was performed as follows. 500 ng of anti-CMY-2 pAbs was added to the different wells and the immobilized antibodies were recognized by a 1/2000 diluted goat anti-rabbit antibody conjugated to HRP (Abcam, UK). In the other way, we added 200 ng/well of cAb_{CMY-2} (254) VHH (monovalent, bivalent) followed by a 1/2000 diluted rabbit anti-VHH antibody conjugated to HRP (Genscript, United-States). The detection of TEM-1 was ensured with 500 ng/well of anti-TEM-1 pAbs recognized by 1/2000 diluted goat anti-rabbit antibody conjugated to HRP (Abcam, UK). TMB was used as substrate and the reaction was stopped by addition of 1 M H_3PO_4. Absorbance at 450 nm was recorded using an Infinite M200 Pro microplate reader (Tecan, Switzerland). All steps described above were performed for one hour at 28°C and were followed by 5 washes of PBST. All samples were diluted in the same buffer.

3.10) Steady-state kinetic studies

3.10.1) Binding kinetics model

Steady-state kinetics were performed at 30°C using a 50 mM PBS pH 7.5 buffer supplemented by 50 μg/mL BSA. Experiments with NDM-1 required also the addition of 50 μM $ZnCl_2$. Absorbances were measured with a Specord 75 spectrophotometer (AnalytikJena, Germany) and a SpectraMx M2 microplate reader (Molecular Devices, United States).

Initial rates and a complete hydrolysis of substrate by CMY-2 were measured for the hydrolysis of: 50 μM ampicillin ($\Delta\varepsilon^{235}$ = -820 $M^{-1} \cdot cm^{-1}$), 100 μM cefalotin ($\Delta\varepsilon^{273}$ = -6300 $M^{-1} \cdot cm^{-1}$), 100 μM cephaloridin ($\Delta\varepsilon^{260}$ = -10000 $M^{-1} \cdot cm^{-1}$) and 40 μM nitrocefin ($\Delta\varepsilon^{482}$ = + 15000 $M^{-1} \cdot cm^{-1}$). The CMY-2 concentration for the hydrolysis of the substrates was comprised between 0.2 nM to 5 nM and was mixed with increasing amounts of the cAb_{CMY-2} (254) VHH (0-1500 nM).

For TEM experiments, we firstly measured initial rates for a fixed substrate concentration: 300 μM benzylpenicillin ($\Delta\varepsilon^{235}$ = -775 M^{-1} cm^{-1}), 200 μM cefalotin and cephaloridin, 100 μM nitrocefin. The TEM-1 and TEM-121 concentrations used for the hydrolysis of the different substrates were in a range of 0.07– 20 nM and were mixed with increasing amounts of the cAb_{TEM-1} (13) VHH (0-1000 nM). Moreover, initial rates were measured for cefalotin (250-1000 μM) in presence of TEM-1 (10 nM) pre-incubated with at least three concentrations of VHH (5-100 nM). The same experiments were realized for the hydrolysis of nitrocefin (25-300 μM) by TEM-1 (0.5 nM) or 3.7 nM TEM-121 (3.7 nM), respectively, in complex with the inhibitor cAb_{TEM-1} (13) (0.25-0.75 nM for TEM-1 and 5-25 nM for TEM-121). Those experiments allowed the determination of the inhibition mechanism by Hanes linearization of the Michaelis-Menten equation. Finally, the initial rates of hydrolysis of the four substrates described above by the TEM-1 R244S and TEM-121 S244R mutants in complex with 1 μM of cAb_{TEM-1} (13) VHH were calculated to determine the role of the arginine at position 244 in the inhibition mechanism.

Similar experiments were carried out for the hydrolysis of 100 μM of imipenem ($\Delta\varepsilon^{300}$ = -9000 M^{-1} cm^{-1}) and meropenem ($\Delta\varepsilon^{297}$ = -6500 M^{-1} cm^{-1}) by 1 nM of NDM-1 or variants in complex with the VHH (between 0 and 600 nM).

3.10.2) Steady-state kinetic constants

All graphs and equations are adapted from **Cornish-Bowden et al, 2005**.

The steady-state kinetic constants were calculated from the Henri-Michaelis-Menten equation VI:

$$v = \frac{V_m\,[S]}{K_m + [S]} \quad \text{(VI)}$$

Where v (expressed in M/s) is the initial velocity of hydrolysis of the substrate by the enzyme, K_m (the Henry-Michaelis-Menten constant expressed in M) corresponds to the concentration of substrate for what $v = V_m/2$, V_m (M/s) is the maximum rate reached by the system and [S], the concentration of substrate (M).

The turnover number k_{cat} (in s^{-1}) was calculated from the equation VII. It reflects the number of substrate molecules transformed by molecule of enzyme and per second. E_0 corresponds to the total enzyme concentration.

$$V_m = k_{cat}\,E_0 \quad \text{(VII)}$$

Then, the adjustment of the Henry-Michaelis-Menten equation on the experimental data was achieved by a linear regression following the Hanes-Woolf equation VIII:

$$\frac{[S]}{v} = \frac{1}{V_m}[S] + \frac{K_m}{V_m} \quad \text{(VIII)}$$

Plotting [S]/v versus [S] (**Fig 3.7**) gives an intercept of K_m/V_m on the y axis and an intercept of $-K_m$ on the x axis. The slope of the line is $1/V_m$. Knowing the V_m value and the initial concentration of enzyme, the k_{cat} value can be calculated via the equation VII.

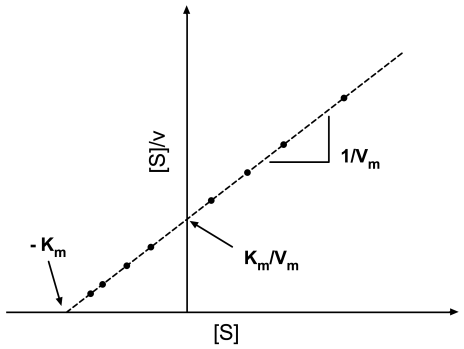

Fig 3.7. *Hanes-Woolf graph*

A second methodology to assess the steady-state kinetic constant K_m and k_{cat} consisted in linearizing curves resulted from the complete hydrolysis of the substrate using the equation IX:

$$\frac{1}{t}\ln\left(\frac{S_0}{S_0 - P}\right) = \frac{1}{K_m}\left(V_m - \frac{P}{t}\right) \quad \text{(IX)}$$

Where t corresponds to the time of reaction, S_0 the initial concentration of substrate and P the final concentration of product. Plotting $\frac{1}{t}\ln\left(\frac{S_0}{S_0 - P}\right)$ versus $\frac{P}{t}$ (**Fig 3.8**) gives an intercept of V_m/K_m on the y axis and an intercept of V_m on the x axis. The slope of the line is $-1/K_m$. Knowing the V_m value and the initial concentration of enzyme, the k_{cat} value can be calculated via the equation VII.

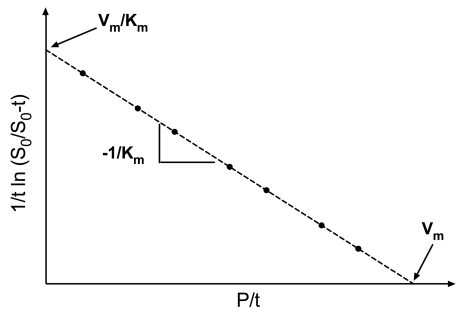

Fig 3.8. *Linearization of the complete hydrolysis of the substrate*

3.10.3) Inhibition models

3.10.3.1) Competitive inhibition

In a competitive inhibition, the substrate and the inhibitor present the same site of fixation on the enzyme, generally in the active site (**scheme 2**).

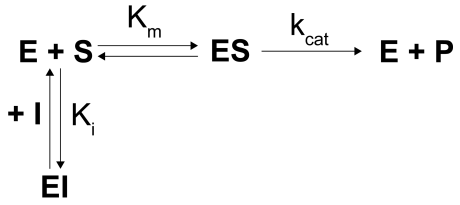

Scheme 2: *Competitive inhibition model*

The equation defining a competitive inhibition mechanism corresponds to equation X:

$$v_i = \frac{V_m\,[S]}{K_m\left(1+\frac{[I]}{K_i}\right)+[S]} \quad (X)$$

with $V_m^{app} = V_m$ and $K_m^{app} = \left(1+\frac{[I]}{K_i}\right) K_m$. Then, the presence of a competitive inhibitor does not influence V_m but K_m^{app} will be higher than K_m. Hanes plot in presence of different concentrations in inhibitor give parallel straight lines with an identical slope, but with an intercept on the abscissa decreasing when the inhibitor concentration increases (**Fig 3.9**).

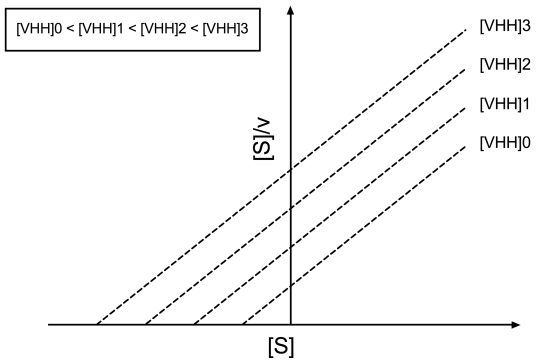

Fig 3.9. *Hanes-wolf profile for a competitive inhibitor*

In presence of a competitive inhibitor, the inhibition constant (K_i) can be determined via the equation XI:

$$\frac{v_0}{v_i} = 1 + \frac{K_m}{(K_m+[S])} \frac{[I]}{K_i} \quad \text{(XI)}$$

Plotting v_0/v_i versus [I] gives an intercept of 1 on the y axis and an intercept corresponding to $-K_i$ on the x axis (**Fig 3.10**). The slope of the straight line corresponds to $\frac{K_m}{(K_m+[S])} \frac{1}{K_i}$.

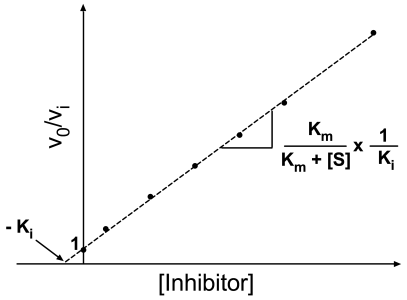

Fig 3.10*. Linearization of the initial rate hydrolysis of an enzyme in complex with a competitive inhibitor.*

3.10.3.2) Uncompetitive inhibition

An uncompetitive inhibitor is not able to bind to the free enzyme but only to the enzyme complexed with the substrate (**scheme 3**). It is generally accepted that the interaction with the substrate leads to conformational modifications on the enzyme whose aids the interaction with the inhibitor resulting in an inactive or poorly active ternary complex. Then, this mechanism does not require the same site of fixation for the substrate and the inhibitor and is uncommon.

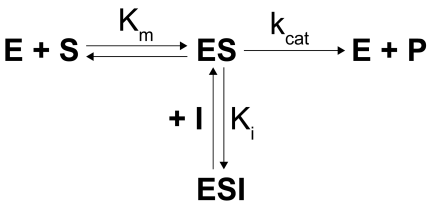

Scheme 3: *Uncompetitive inhibition model*

This results in both K_m^{app} and V_m^{app} reduced by $\left(1+\frac{[I]}{K_i'}\right)$ compared to K_m and V_m as illustrated by the equation XII. Hanes linearization gives the convergence of straight lines on the y axis (**Fig 3.11**).

$$v = \frac{V_m\,[S] \;/\left(1+\frac{[I]}{K_i'}\right)}{[S]+K_m \;/\left(1+\frac{[I]}{K_i'}\right)} \quad \text{(XII)}$$

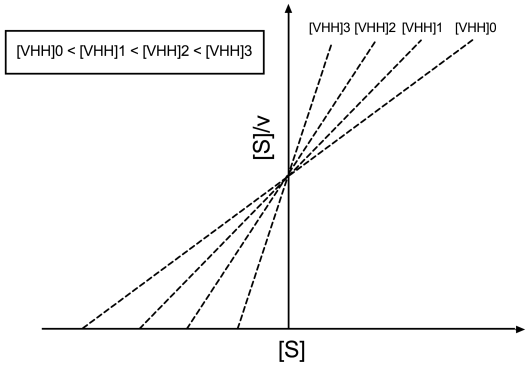

Fig 3.11. *Hanes-wolf profile for an uncompetitive inhibitor*

3.10.3.3) Non-competitive inhibition

The non-competitive model is the more complete kinetic model, where the inhibitor binds to the free enzyme and the ES population to form the complexes EI and ESI, respectively (**scheme 4**).

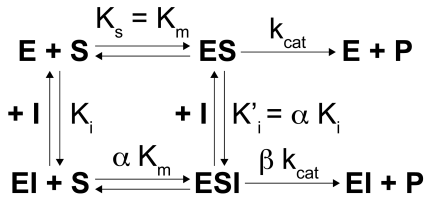

Scheme 4: *Non-competitive model*

V_m^{app} decreases in all configurations defining the parameter $\beta < 1$ and a decreased deacylation rate of the complex ESI. On the other hand, K_m^{app} could be superior, equal or inferior to K_m following a K_i inferior ($\alpha > 1$), equal ($\alpha = 1$) or superior ($\alpha < 1$) to K_i' (equation

XIII). Hanes linearization will describe straight lines which converge above, on, or below the x axis in the first, second and third case, respectively (**Fig 3.12**).

$$v = \frac{V_m\,[S]\ /\left(1+\frac{[I]}{K_i'}\right)}{[S]+K_m\left(\frac{1+\frac{[I]}{K_i}}{1+\frac{[I]}{K_i'}}\right)} \quad \text{(XIII)}$$

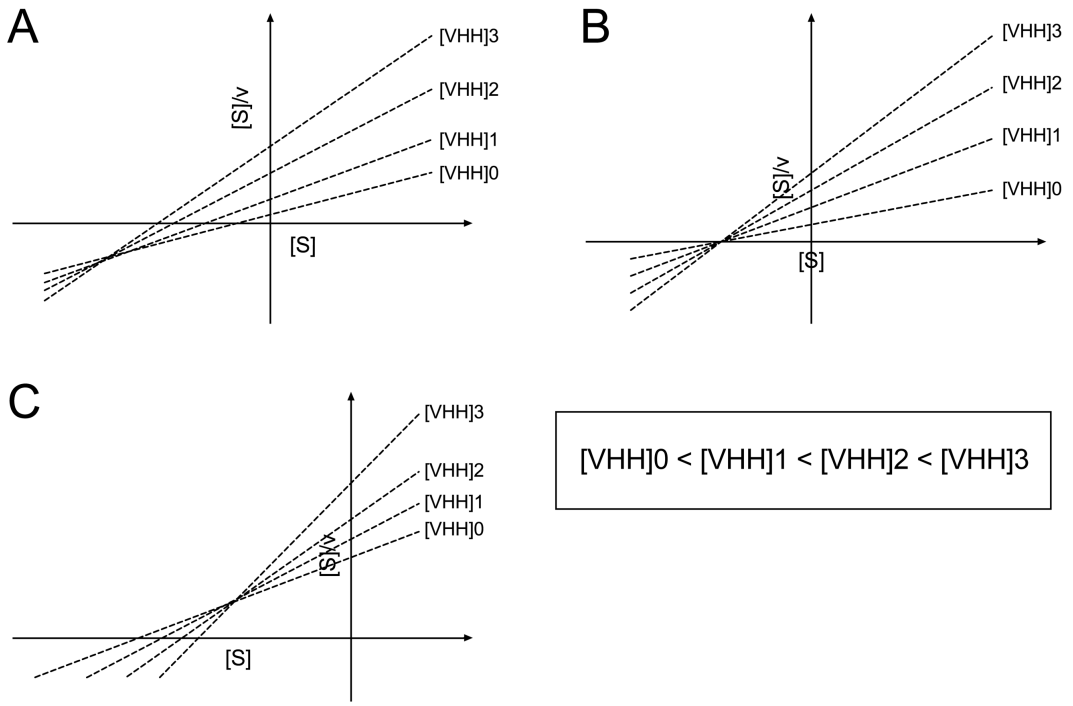

Fig 3.12. *Hanes-Wolf profile for a non-competitive inhibitor considering the parameter α inferior (A), equal (B) or superior (C) to 1.*

The plot of $1/k_{cat}^{app}$ in function of the concentration in inhibitor allowed to determine the impact of the inhibitor on the deacylation constant:

- A straight line fitted with equation XIV indicates the ability of the inhibitor to suppress completely the deacylation of the acyl-enzyme ($\beta = 0$) (**Fig 3.13**). Combined with a K_m^{app} equals K_m, this described a pure non-competitive inhibition.

$$\frac{1}{k_{cat}^{app}} = \frac{1}{\alpha K_i k_{cat}} I + \frac{1}{k_{cat}} \quad \text{(XIV)}$$

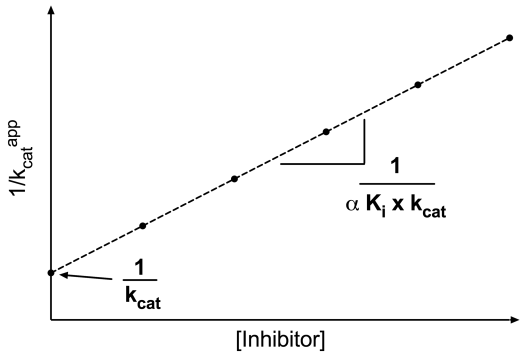

Fig 3.13. *Pure tendency of a non-competitive inhibitor.*

- A hyperbole fitted with the equation XV can be interpreted as the ability of the inhibitor to partially reduce the deacylation rate ($0 < \beta > 1$) resulting in a mixed non-competitive inhibition where both complexes ES and ESI are functional (**Fig 3.14**).

$$\frac{1}{k_{cat}^{app}} = \frac{1}{k_{cat}} \frac{(1+\frac{I}{\alpha K_i})}{(1+\frac{\beta I}{\alpha K_i})} \quad \text{(XV)}$$

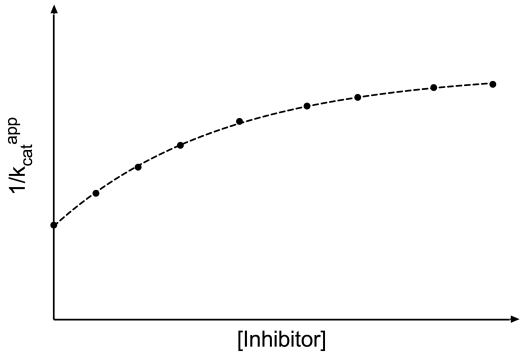

Fig 3.14. *Mixed tendency of a non-competitive inhibitor.*

3.11) X-ray crystallography

3.11.1) Crystallization conditions

All complexes were previously purified by a size-exclusion chromatography using a Superdex 75 10/300GL (Cytiva, United-States) to ensure the homogeneity of the sample. Crystals were grown at 20°C using the sitting drop vapor diffusion method. It consists in a drop containing a mixture of the protein sample and reagents (buffer, adduct, salts) which is in vapor equilibration with a reservoir containing also reagent but more concentrated than the drop. Then, water vapor leaves the drop and has for consequence to concentrate the sample and the reagent in the drop to reach the supersaturation state and to obtain crystals of our sample (**Chayen, 2004**). Four 96 conditions screening were setup for each protein sample, Crystalscreen HT (Hampton Research), Wizard screen (Molecular Dimension), Index screen (Hampton Research) and a homemade salt screening.

The crystal of CMY-2 in complex with the cAb_{CMY-2} (254) VHH were obtained by mixing a 0.2 µL drop of the protein sample at a 14 mg/mL concentration and 0.2 µL of 0.1 M TRIS-HCl pH 8.5, 1.4 M $(NH_4)_2$ tartarate. For the cAb_{TEM-1} (13)/TEM-1 and cAb_{TEM-1} (13)/TEM-121 complexes, the protein concentrations were 14 and 14.5 mg/ mL, respectively. The crystallization solutions were 0.1 M Bis-Tris propane pH 7.0, 1 M tri-ammonium citrate for the first complex and a 0.1 M Tacsimate pH 5.0 containing a mixture of organic acids (HAMPTON Research) for the second one. Crystals were transferred in a cryo-protectant solution containing 1.8 M ammonium sulfate and 45 % (v/v) glycerol for the cAb_{TEM-1}(13)/TEM-1 complex, 4.5 M Na formate and 50 % (v/v) glycerol for the cAb_{TEM-1}(13)/TEM-121 complex, and finally 50 % (v/v) polyethylene glycol 400 and 50 % (v/v) glycerol for the cAb_{CMY-2} (254)/CMY-2 complex. All were frozen in liquid nitrogen.

3.11.2) Data collection, phasing, model building and refinement

Data were collected at the Proxima 1 beam line of the Soleil synchrotron (Saint Aubin, France) for cAb_{TEM-1}(13)/TEM-121 and cAb_{CMY-2} (254)/CMY-2 complexes and at the Proxima 2a beam line for the cAb_{TEM-1}(13)/TEM-1 complex. Indexing, integration and scaling of the data

were performed using XDS (**Kabsch, 2010**). For the cAb_{CMY-2} (254)/CMY-2 complex, the initial phases were obtained by molecular replacement with the CMY-2 structure (PDB code 1ZC2) and a lama antibody fragment (PDB code 6GKU) as search model using Phaser (**McCoy, 2007**). For the model of the cAb_{TEM-1} (13)/TEM-1 complex, we applied the molecular replacement with the TEM-1 structure (PDB code 1m40) and the lama antibody fragment against the β-lactamase BlaP (PDB code 4M3J), whereas the cAb_{TEM-1} (13)/TEM-121 complex was based on our previously determined model of the complex with TEM-1. Structures were built with Coot (**Emsley et al, 2010**) and refined with Phenix refine (**Liebschner et al, 2019**). All figures were prepared using PyMOL (The PyMOL Molecular Graphics System, Version 2.4.1 Enhanced for Mac OS X, Schrödinger, LLC.).

3.12) Thermal denaturation by circular dichroism and intrinsic fluorescence

3.12.1) Circular dichroism (CD)

CD spectra were recorded in the far-UV (210-260 nm) using a Jasco J-810 spectropolarimeter equipped with a thermostated cell holder. TEM alone and in complex with the VHH (molar ratio 1:1) were diluted at a final concentration of 3.4 μM in a 50 mM NaH_2PO_4/Na_2HPO_4 pH 7.0 buffer. The CD spectra were acquired in a 0.1 cm path length cell with a scan rate of 50 nm/min, a 1 nm bandwidth and an integration time of 2 seconds. All CD spectra resulted from the average of four accumulations and were subtracted by the buffer spectrum measured in identical conditions.

Denaturation curves were realized at 224 nm since the higher transition between the native and the denatured form of the enzyme TEM was observed at this wavelength. A temperature gradient from 30°C to 80°C at a rate of 0.5°C min^{-1} was used, with a 1 nm bandwidth and an integration time of 4 seconds.

3.12.2) Intrinsic fluorescence

Intrinsic fluorescence emission spectra were performed using a Carry Eclipse Fluorimeter (California, United-States) in a 50 mM NaH_2PO_4/Na_2HPO_4 pH 7.0 buffer with

proteins concentrated at 3.4 μM. The excitation and emission spectra were recorded at 280 nm and between 305 and 440 nm, respectively, with slit widths of 4 nm, a 1 cm path length cell and a scan speed of 600 nm/min.

Denaturation curves were carried out at 0.5 nm/min from 25°C to 90°C with an excitation wavelength at 280 nm and an emission signal at 333 nm corresponding to the higher transition between the native and unfolded form.

3.12.3) Thermal denaturation curve analysis

The thermal denaturation of the proteins measured by CD and fluorescence experiments were interpreted following an apparent single transition curve (N ⇆ U) according to a two-state model (**Hajjaji et al, 2009**). The experimental curves were fitted using the equation XVI:

$$y_{obs} = \frac{(y_N + pT) + (y_U + qT) x \exp\ [a]}{1 + \exp\ [a]} \quad \text{(XVI)}$$

$$a = -(\Delta H_m (1 - T/T_m))/RT$$

Where y_{obs} corresponds to the observed signal at a given wavelength and temperature, y_N and y_U to values for the native and unfolded states, respectively, p and q to the slopes of the pre- and post-transition states, R the gas constant equals to 8.314 J mol^{-1} K^{-1}, T the different temperatures expressed in Kelvin, T_m the temperature of mid-transition and ΔH_m the enthalpy at the mid-transition state. Since we only performed our experiment in denaturing conditions, we only determined the apparent T_m value (T_m^{app}).

3.13) Molecular Dynamic Simulations

3.13.1) Principle

The molecular dynamic simulation (MD) is a largely used method to study the dynamics of proteins based mainly on the atomic motion in function of time. It consists in three steps crucial to ensure the best representation of the experimental conditions of proteins in solution (**Fig 3.15**) (**Pandya et al, 2018**). Firstly, the protein is placed into a box where ions and water molecules allow the solvation of the protein. Then, an energy minimization is calculated to find the minimum energy configuration of the system. Finally, the real MD is performed using a force field and the integration of the Newton's laws of motion for each atom of the system results in the equation XVII:

$$\frac{d^2 r_i(t)}{dt^2} = \frac{F_i(t)}{m_i} \quad \text{(XVII)}$$

Where $F_i(t)$ corresponds to the force applied on atom i at time t, $r_i(t)$ is the position vector of the atom i at time t and m_i which is the mass of the atom i (**Adcock & MacCammon, 2006**).

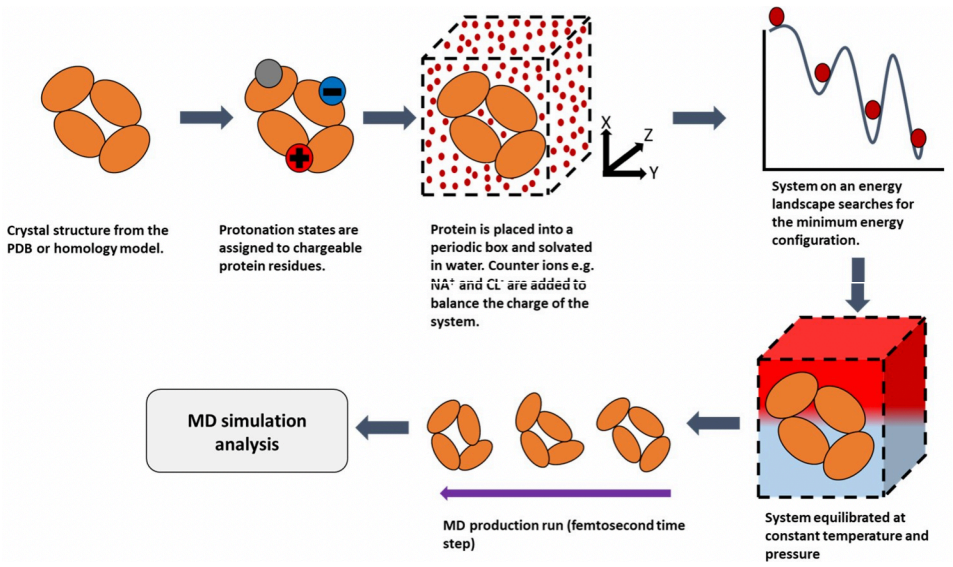

Fig 3.15. *Illustration of a classical molecular dynamic simulation divided in three steps: (I) the solvation of the protein, (II) the energy minimization and the equilibration of the system, (III) modelisation (MD) run (**Pandya et al, 2018**).*

Then, the Verlet integration (equations XVIII-XX) allows to integrate the Newton's equation for partitioned time (δt), generally in the order of the femtosecond, to assess the position and the velocity of the atom i at time t+δt with a starting time t (**Verlet, 1967**)

$$r_i\,(t+\delta t) = r_i(t) + v_i\,(t)\delta t + \frac{1}{2}\,a_i\,(t)\,\delta t \quad \text{(XVIII)}$$

$$v_i\,(t+\delta t) = v_i(t) + \frac{1}{2}\,[a_i\,(t) + a_i\,(t+\delta t)]\,\delta t \quad \text{(XIX)}$$

$$a_i\,(t) = \frac{F_i\,(t)}{m_i} = -\frac{dV\,(t)}{m_i d_{ri}(t)} \quad \text{(XX)}$$

Where $r_i(t)$, $v_i(t)$ and $a_i(t)$ correspond to position, velocity and acceleration of the atom i at time t, respectively, while $r_i(t + \delta t)$ and $v_i(t + \delta t)$ are position and velocity at time t + δt, respectively. The acceleration a_i (t) is function of the force sustained by the atom i at time t which is directly related to the potential energy V(t) issued from the force field and corresponding to the sum of potential energies due to interactions (V_{bond}), angles (V_{angle}), torsions (V_{dihed}) and non-bonded interactions (V_{nb}) summarized in equation XXI:

$$V = \sum_{i=1}^{N_{bond}} V_{bond} + \sum_{i=1}^{N_{angle}} V_{angle} + \sum_{i=1}^{N_{dihed}} V_{dihed} + \sum_{i=1}^{N_{nb}} V_{nb} \quad \text{(XXI)}$$

3.13.2) Root-mean-square deviation/fluctuation

The data generated by modelisation describes the position (r) of an atom during the time of a simulation. Therefore, it is possible to calculate two important parameters: the root-mean-square deviation (RMSD) and the root-mean-square fluctuation (RMSF). The RMSD corresponds to the distance between the structure at time t and a reference meaning we are able to follow major changes in the protein structure over time. We could compare the RMSD to the position of the Cα in a x-ray structure. Similarly, the RMSF describes the average deviation for each amino acid in function of a reference position (at time 0 s). Its value can be compared to the β-factor in crystallography (**Kuzmanic & Zagrovic, 2010**).

3.13.3) Experimental setup

Our modelisation experiments were carried out on three different models: a model of TEM-1 obtained at 0.86 Å (**TEM-1 HR**, PDB code 1m40), the cAb_{TEM-1} (13)/TEM-1 complex (**VHH/TEM-1**) and the structure of TEM-1 extracted from the X-ray structure of the complex (**TEM-1**). We removed all water molecules, buffer and other molecules to work with "naked" proteins and to let the program add water molecules to ensure more homogeneity. All simulations were performed with the GROMACS software (**Lindahl et al, 2001**) using the force field Amber03 and the model TIP3 for the water molecules.

The first step consisted in the calculation of the local energy minimum and to identify the best protein configuration. Then, the protein was placed in a box where it was able to move to remove potential steric hindrances. It was realized by the command "Steepest descent" with 10000 cycles. We also chose the option "xyz" for the periodic boundary conditions (pbc) which illustrates the periodicity of the system allowing to maintain the protein into the predetermined box.

Then, waters molecules and ions Na^+ and Cl^- (0.15 M) were added in the box and the system was equilibrated following the protocol "md" (molecular dynamics) with a δt (time between two measurements) of 2 fs with 500 000 steps (simulation of 1 ns). The option DPOSRES was applied allowing the motion of water molecules and ions but restraining the protein. This avoids mismatches between all added molecules and the protein. As previously described for the energy minimization, we chose the option "xyz" for the parameter pbc and experiments were realized at 25°C.

Finally, the dynamic molecular simulations were carried out with the system CECI (http://www.ceci-hpc.be/) using Dragon2 from UMons (University of Mons). The protocol "md" was applied but we did not consider the option DPORES meaning that the protein's motion was tolerated. We performed 5 simulations for each model to further obtain more statistically significant results. We considered a δt of 2 fs with 50 000 000 steps (simulation of 100 ns) with a periodicity xyz and at 25°C. The option gen_seed = -1 implies strength vectors in different completely random spatial orientation for each simulation.

3.14) Dynamic study by relaxation NMR experiments

This section will briefly describe the general concepts of relaxation in NMR and the relation with the dynamic of molecules for a better understanding of all biological interpretations resulting from the NMR experiments. All illustrations are derived from the M. H. Levitt book (**Levitt, 2008**) and the R.D. Majumdar's thesis (**Majumdar, 2015**).

3.14.1) Nuclear spin

The nuclear spin is a magnetic property of nucleus atoms which is characterized by two quantum numbers: I representing the total angular momentum and varying in function of protons and neutrons in the nucleus and **m** reflecting the Z-component of the angular momentum which takes values of -1/2 and 1/2 for a spin 1/2 or -1, 0 and 1 for a spin 1. The angular momentum leads to the magnetic moment $\vec{\mu}$ describes by the equation XXII:

$$\vec{\mu} = \gamma . \hbar . \vec{m} \qquad \text{(XXII)}$$

with γ reflecting the magnetogyric ratio (specific to each nucleus), $\hbar$ the reduced Planck constant and m corresponding to the z-component quantum number.

The application of an external magnetic field $\vec{B}_0$ along the Z-axis creates a population difference between the spin state leading to the sample polarization. As an example for the more studied spin equals to 1/2, two states of the magnetic moment are possible: m = 1/2 aligned in the same direction of $\vec{B}_0$ and called the α state (**Fig 3.16A**) and, m = -1/2 oriented in the opposite sense of the external magnetic field and corresponding to the β state (**Fig 3.16B**). The nuclear spin submitted to the magnetic field leads to its rotation with an angular frequency ω_0, called the Larmor frequency, which is nucleus-specific.

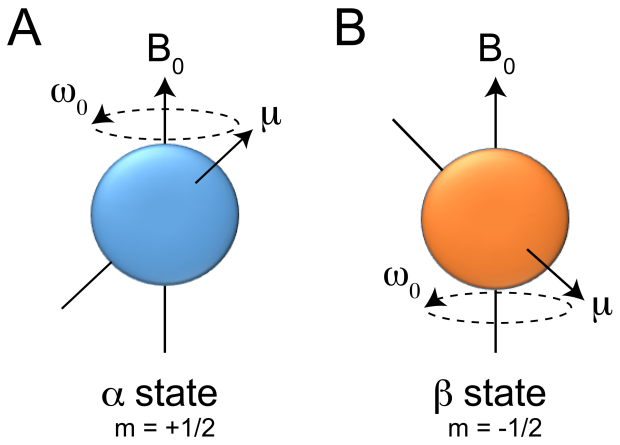

Fig 3.16. *Nuclear magnetic moment μ in an external magnetic field B_0 with a frequency ω_0. This illustrates the spin ½ at the α-state (A) and the β-state (B).*

The polarization resulting from the spins oriented in the same direction of $\vec{B}_0$ relative to those in the opposite sense (difference of populations) is represented by the Boltzmann distribution described by the equation XXIII:

$$\frac{N_\beta}{N_\alpha} = \exp\left(-\frac{\Delta E}{\kappa T}\right) \quad \text{(XXIII)}$$

with Nα and Nβ representing the number of spins at the α and β states, respectively, ΔE the difference of energy between the two states, κ the Boltzmann constant (1.38 x 10^{-23} joules/°K) and T the temperature in Kelvin. The ensemble of spins results in a net magnetization aligned and parallel to $\vec{B}_0$ (longitudinal magnetization), generally represented by the vector $\vec{M}_Z$ (**Fig 3.17**).

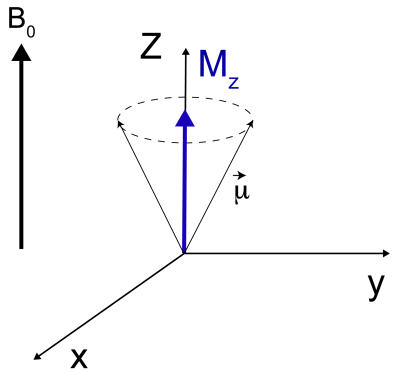

Fig 3.17. *Longitudinal magnetization $\vec{M}_Z$ aligned and parallel to $\vec{B}_0$.*

3.14.2) Excitation phenomenon in NMR

At this stage, the system is not in coherence and in order to measure an NMR signal via the relaxation, an excitation is required. It consists in the application of a secondary magnetic field B1 (B1 $\perp$ B0) that oscillates in the x,y plane at the Larmor frequency (ω_0). As a consequence, the longitudinal magnetization (M_z) is rotated to the transversal plane (x,y). The magnetization ($M_{x,y}$) of all spins becoming in phase (coherence) (**Fig 3.18**).

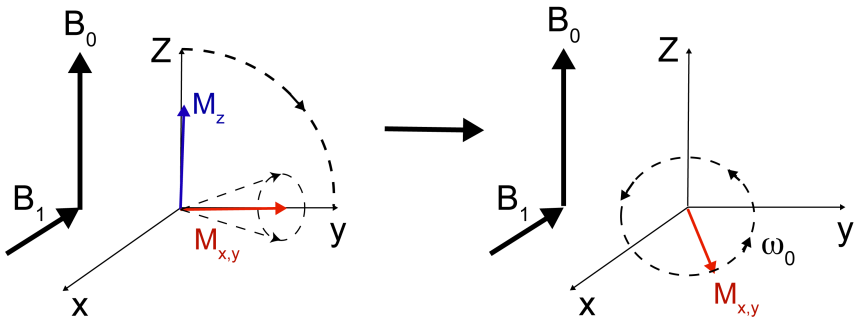

Fig 3.18. *Rotation of the longitudinal magnetization (M_z) in the transverse plan (M_{xy}) (B).*

3.14.3) Relaxation phenomenon in NMR

Once the pulse is finished, the transverse magnetization is rotating around the z-axis because of its interaction with B0. The transverse magnetization returns to equilibrium following a relaxation phenomenon divided in two components: the longitudinal relaxation (T1) and the transverse relaxation (T2). This results in a helical trajectory of the magnetization which returns along the z-axis corresponding to the external magnetic field ($\vec{B}_0$) on the z-axis (**Fig 3.19**).

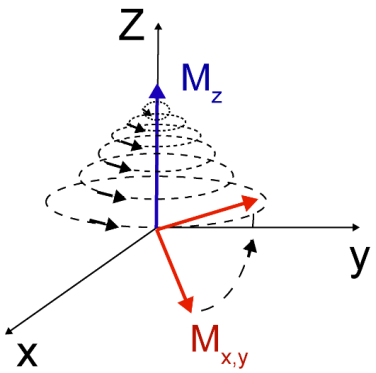

Fig 3.19. *Helical trajectory of the magnetization due to the longitudinal (T1) and the transverse (T2) relaxations.*

The longitudinal (spin-lattice) relaxation **T1** is the return to the equilibrium state due to the recovery of the z component of the nuclear spin magnetization (M_z) (**Fig 3.20A**). The transverse (spin-spin) relaxation time **T2** is the measure of time taken by the transverse magnetization ($M_{x,y}$) to lose coherence resulting from different spins precession frequencies (incoherence) (**Fig 3.20B**).

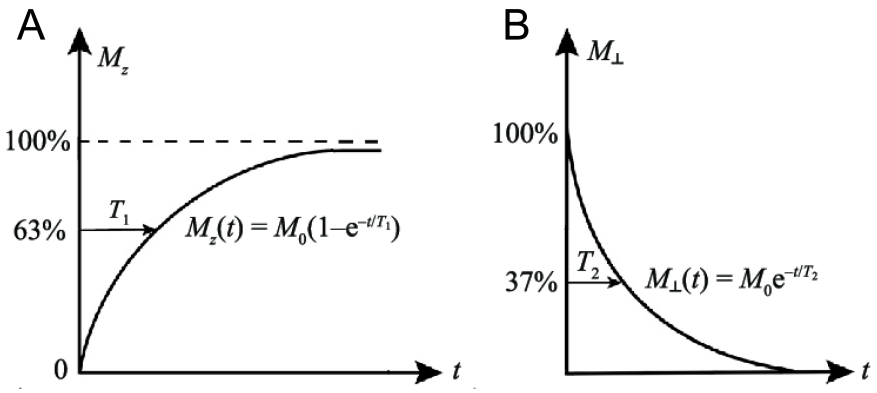

Fig 3.20*. Magnetization representations of the longitudinal relaxation time T1 (a) and the transverse relaxation time T2 (b) (**Xu et al, 2019**).*

The Nuclear Overhauser Effect (NOE) is a particular form of relaxation called the cross-relaxation and based on the dipole-dipole coupling in space. Briefly, it implies a state population change of one spin (e.g. azote) as a consequence of the saturation of a nearby spin (e.g. proton). As described by the Boltzmann equation, the vector $\vec{M}_Z$ depends on a difference of spin populations at α and β states ($\Delta N = N\alpha - N\beta$). When the proton is saturated, the system

is no longer at equilibrium $(N\alpha - N\beta)_H$ and tries to return at equilibrium via a relaxation phenomenon. This is only possible with an energy transfer to the azote (cross-relaxation).

3.14.4) The correlation time

The NMR relaxation is dependent of the rotational diffusion of the molecule corresponding on the random rotational motion of small amplitude. This is directly related to the correlation time τ_C representing the average time it takes for one molecule to rotate one radian and described by the equation XXIV:

$$\tau_C = \frac{4\pi\eta r^3}{3kT} \quad \text{(XXIV)}$$

with η corresponding to the viscosity coefficient, r the molecule radius, k the Boltzmann constant (1.38 x 10^{-23} m^2 kg s^{-2} K^{-1}) and T the temperature in kelvin. It generally occurs in the pico-nanosecond timescale and in presence of a magnetic field B2 modulated by the electronic distribution of each atom and oscillated in the Larmor frequency (ω_0). This correlation time is directly impacted by the size and the mobility of the molecule.

3.14.5) The spectral density function

The spectral density function (j(ω)) represents the molecular rotational frequency (velocity) distribution of a molecule and is illustrated by the equation XXV (**Lipari & Szabo, 1982**):

$$j(\omega) = \frac{2}{5}\left(\frac{\tau_c}{1+\omega^2\tau_C^2}\right) \quad \text{(XXV)}$$

with τ_C corresponding to the correlation time and ω the frequency.

The three NMR relaxation phenomena depend on motions at four frequencies (velocities): ω_H, ω_N, ω_{H+N}, ω_{H-N}. The NOE and T1 parameters are sensitive to high-

frequency motions (10^8-10^{12} s^{-1}) giving an information about internal motions on the fast timescale (pico-nanosecond), while T_2 values also depends on lower motions (micro-millisecond) allowing a larger point of view on the protein dynamic. R_1 and R_2 values are obtained by the inverse of their respective relaxation time (e.g. $R_1 = 1/T_1$) (**Kay et al, 1989 & Zhang et al, 2012**).

3.14.6) The Lipari-Szabo model-free analysis

Without going into details, the Lipari-Szabo model-free analysis aims the fitting of the three experimental parameters with five models derived from the spectral density function (**Mandel et al, 1995**). This allows the measurement of motions at the ps-ns timescale (Global order parameter S^2). Some of those models also integrate the R_{ex} parameter to calculate motions in the μs-ms time scale.

4. Insight on the inhibition mechanism of the cAb_{TEM-1} (13) VHH against the class A β-lactamase TEM-1

4.1) Production and purification of the cAb_{TEM-1} (13) VHH

4.1.1) Affinity chromatography by a Ni-NTA HisTrap HP column

All the nanobodies were produced in a rich medium (TB medium). They contain a N-terminal signal peptide (pelB) allowing their expression in the periplasm, and a C-terminal His_6 tag facilitating their purification by an affinity chromatography using a Ni-NTA HisTrap column. The A^{280} measured during the loading of the sample represents contaminants did not bind to the column matrix (**Fig 4.1A**). During the elution step (10 to 500 mM of imidazole), we mainly observed two peaks: one between 100 and 200 mM of imidazole and another in a range of 200 and 300 mM (**Fig 4.1B**). A polyacrylamide gel in denatured conditions confirmed that the majority of contaminants did not bind to the column (Flow-Through) or were found in the first elution fractions (**Fig 4.1C**). Some contaminants were however co-eluted with the VHH (14 kDa) requiring a second purification by size-exclusion chromatography.

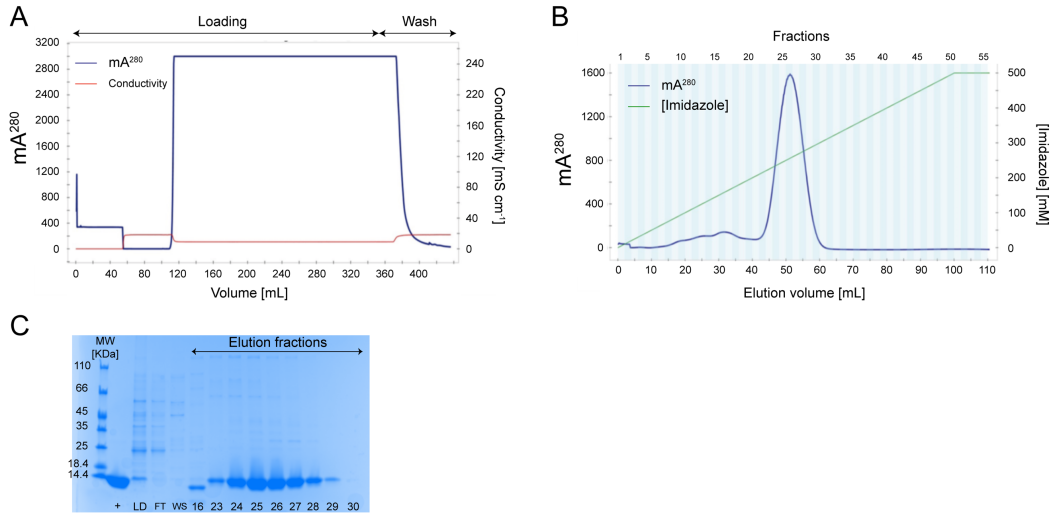

Fig 4.1. *Purification of the VHH cAb_{TEM-1} (13) by a Ni-NTA HisTrap chromatography. (A) Chromatogram illustrating the loading of the sample and the wash of the column. (B) Elution of the VHH following a 0-100 % gradient of 500 mM imidazole. (C) Coomassie-stained SDS-PAGE. The positive control (+) corresponds to purified VHH. LD: Load, FT: Flow-Through, WS: Wash*

4.1.2) Size-exclusion chromatography

The second purification by size-exclusion chromatography allowed the separation of the higher molecular weight contaminants from the VHH (**Fig 4.2**). We observed a first weak peak of absorbance in the death volume of the column (7-8 mL) corresponding to the last contaminants while the purified VHH was eluted in the second peak (fractions 12 to 16).

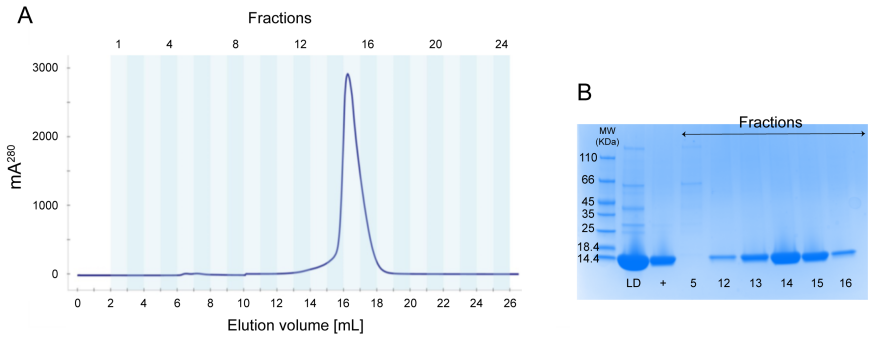

Fig 4.2. *Purification of the cAb_{TEM-1} (13) VHH by size-exclusion chromatography. (A) Chromatogram representing the elution of the sample on the column. (B) Purity assessment by Coomassie-stained SDS-PAGE.*

4.1.3) Quality controls of the purified cAb_{TEM-1} (13) VHH

Quality controls were performed to verify the purity of our VHHs. First, increasing quantities of VHHs were loaded on a polyacrylamide gel (SDS-PAGE) and a single band was observed around 14 kDa even for the large VHHs quantities (**Fig 4.3A**). Then, a UV-spectrum (240-340 nm) allowed to check the lack of nucleic acid contaminations ($A^{280}/A^{260} > 1.7$) and aggregates ($A^{320} \approx 0$) (**Fig 4.3B**). Finally, an analysis of the sample by ESI-Q-TOF mass spectroscopy confirmed the high purity of our samples with a main peak at 13860 Da corresponding to the exact mass of the VHH cAb_{TEM-1} (13) with its disulfide bonds (**Fig 4.3C**). Relative to the main peak, the one at -18 Da (13842 Da) could be due to a post translational modification (https://abrf.org/delta-mass) whether the peaks upstream the main peak (13883 and 13897 Da) are mostly due to adducts related to formulation traces (e.g. possible potassium adduct and/or two water molecules). The VHH cAb_{TEM-1} (13) was generally produced with 1-2 mg/liter yield.

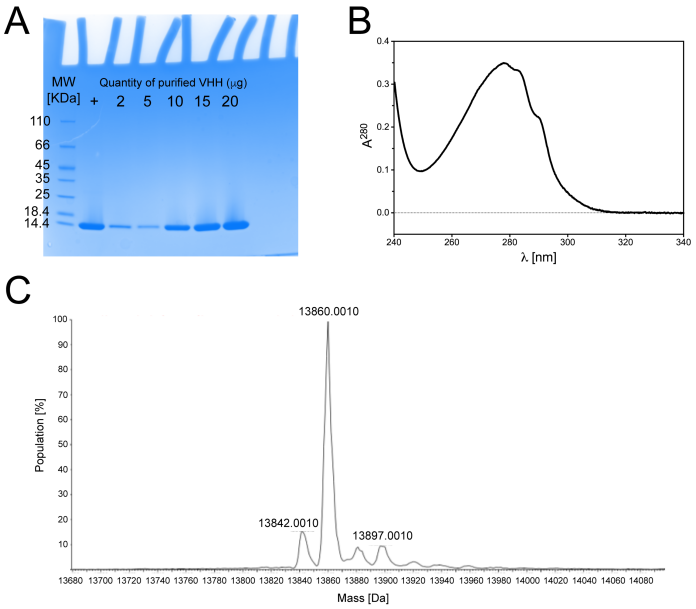

Fig 4.3. *Controls of the purity of the cAb_{TEM-1} (13) VHH. (A) Coomassie-stained SDS-PAGE with increasing quantities in VHH. (B) UV spectrum (240-340 nm). (C) Mass spectroscopy chromatogram of the VHH cAb_{TEM-1} (13).*

4.2) Production and purification of TEM β-lactamases

4.2.1) Production of TEM β-lactamases

During the productions, we noticed that the majority of the β-lactamases was found in the culture medium. It constituted an advantage since there were less contaminants than a total extraction of the cellular content. However, it required productions in a minimal medium to avoid pigments. The main explanation for the β-lactamase secretion consists probably in the production of outer-membrane vesicles (OMV) as a result of the stress undergone by the high production of the β-lactamases (**Schwechheimer & Kuehen, 2015**).

TEM-1, TEM-121 and all variants were produced in a classical M9 minimal medium for 6 hours at 37°C and were purified from the culture medium. Yields were generally comprised between 10 and 20 mg/L except for the TEM-1 D214A mutant produced at around 1 mg/L. We also produced TEM-1 labelled by ^{15}N and/or ^{13}C in deuterium for NMR experiments. The productions were performed ON at 25°C corresponding to the optimal conditions for the expression of TEM-1 in deuterated water. However, the protein stayed in the periplasm

certainly due to the reduced stresses sustained by the bacteria and deuterated TEMs were recovered by a total cellular extraction.

4.2.2) Purification of TEM-1 by an anion-exchange chromatography

Two successive purifications were performed on a Q-sepharose HP column at pH 7.8 and 6.0 where TEM-1 is able to bind to the column due to the theoretical isoelectric point (PI) of 4.95. During the first step, TEM-1 was eluted with 100-200 mM of NaCl while the majority of contaminants did not interact with the column or were eluted at higher salt concentrations (**Fig 4.4A-B&E**). The use of a pH closer to the PI value for the second step allowed the elution of the β-lactamase in lower salt concentrations (50-100 mM) separating TEM from the rest of the contaminants (**Fig 4.4C-D&F**).

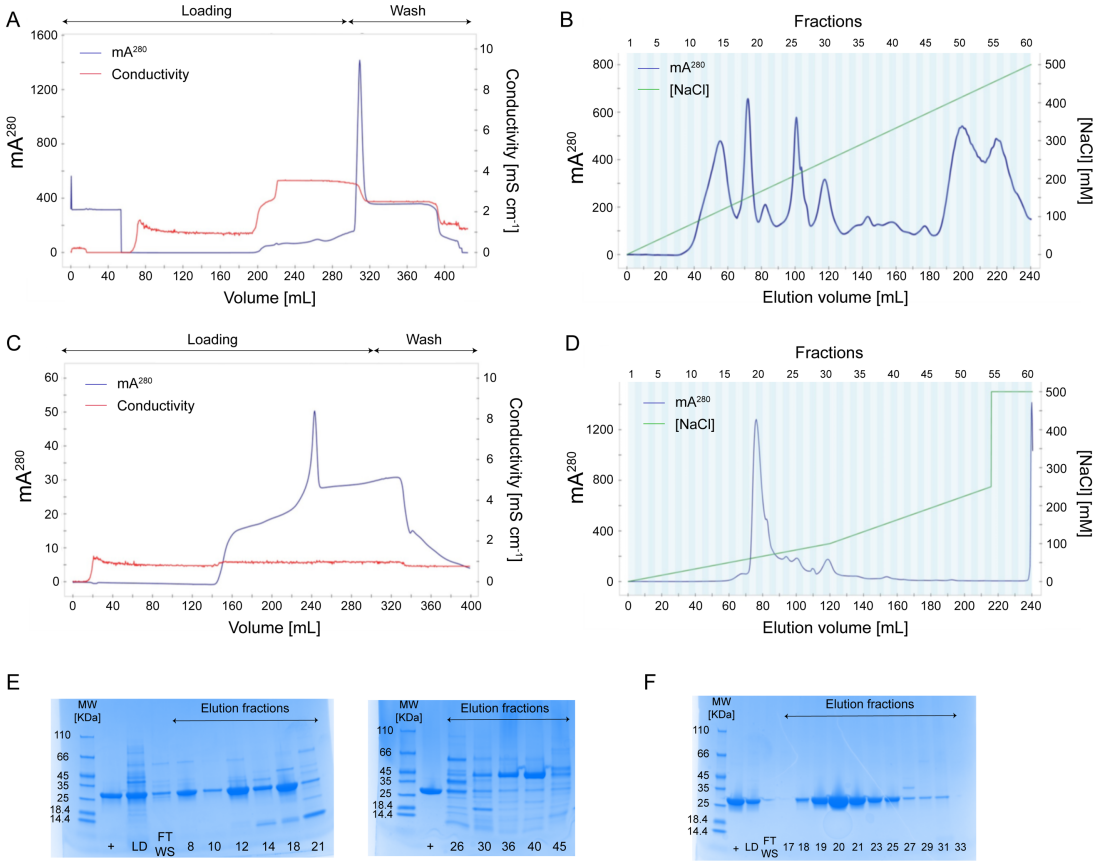

Fig 4.4. *Purification of TEM-1 by an anion-exchange chromatography using a Q-sepharose HP column. (A) Loading and (B) elution of TEM-1 in a basic buffer (pH 7.8). (C) Loading and (D) elution of TEM-1 in the second step with an acid buffer (pH 6.0). Coomassie-stained SDS-PAGE to check the purity of TEM-1 in a basic (E) and an acid buffer (F).*

4.2.3) Purification of TEM-121 by an anion-exchange and a size-exclusion chromatography

The purification of TEM-121 was more complicated. Despite a theoretical pI around 5.9, it was impossible to favor the interaction of the β-lactamase with the Q-sepharose column HP as described for TEM-1. We therefore tried an anion-exchange chromatography with a capto-Q HP column presenting a better resolution than the Q-sepharose HP. Even at a pH of 8.5, the majority of TEM-121 was found in the FT during the loading of the sample. However, a large amount of contaminants remained bound to the column allowing to discard some contaminants from TEM-121 (**Fig 4.5A-B&D**). We eliminated the last contaminants by a size-exclusion chromatography (Superdex75 column). We observed two peaks: the first corresponded to contaminants and the second to TEM-121 (**Fig 4.5C&E**).

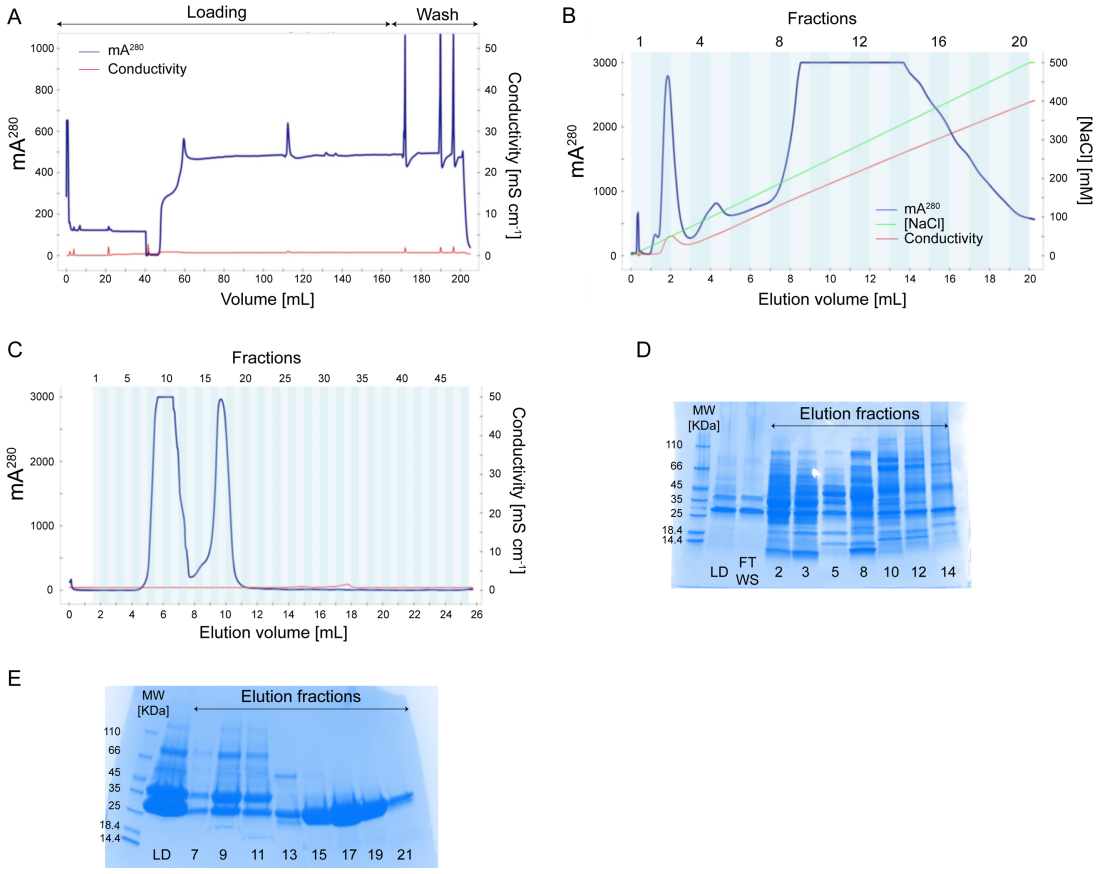

Fig 4.5. *TEM-121 purification. (A-B) Anion-exchange chromatography by a capto-Q HP column. (C) Size-exclusion chromatography with a preparative Superdex75 column. (D) Coomassie-stained SDS-PAGE of the anion-exchange chromatography. (E) Coomassie-stained SDS-PAGE of the size-exclusion chromatography.*

4.2.4) Quality Controls of the purified TEM-1

Different controls were carried out to check the purity of the produced β-lactamases TEM-1 and TEM-121. Firstly, increasing quantities of TEM-1 on a polyacrylamide gel in denatured conditions emphasized one band at 29 kDa near to the molecular mass of TEM-1 (28.9 kDa) (**Fig 4.6A**). Furthermore, we also noticed the absence of nucleic acid and aggregate contaminations (**Fig 4.6B**). Finally, an exact mass analysis by ESI-Q-TOF mass spectroscopy illustrated a main population at 28905 Da (exact mass of TEM-1 with its disulfide bond) (**Fig 4.6C**) and some intermediate peaks probably due to post-translational modifications or formulation traces. There were seemingly a few minor species, at 9635, 12386, 14452 and 16517 Da (**Fig 4.6D**) which may reflect the degradation of the main product or few contaminants. However, their proportions were clearly less predominant than the major peak corresponding to TEM-1. Similar controls were performed for TEM-121 and all the mutants.

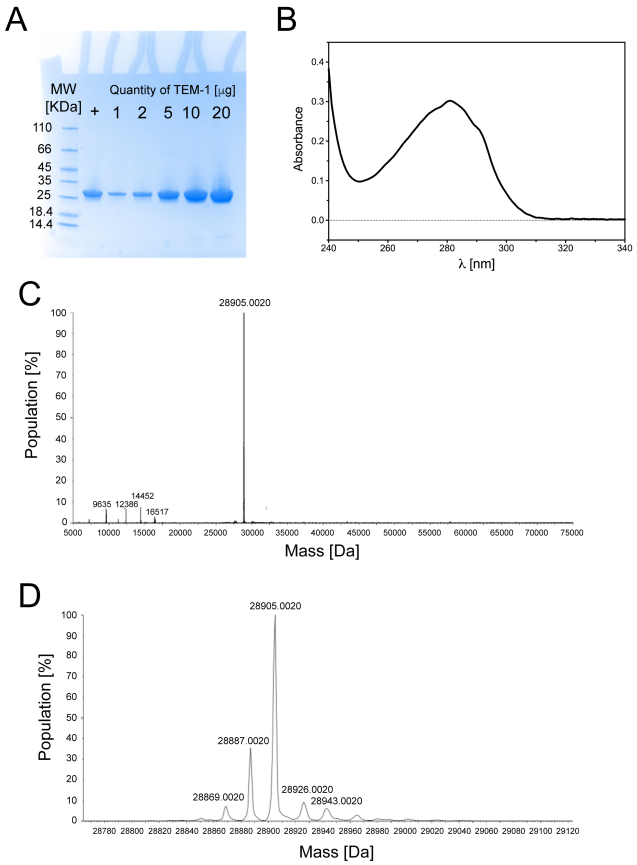

Fig 4.6. *Quality controls of TEM-1 purity. (A) SDS-PAGE of different quantities of TEM-1 (µg). (B) UV spectrum at wavelengths between 240 and 340 nm. (C-D) Mass spectroscopy chromatograms of TEM-1.*

4.3) Binding characterization of the cAb_{TEM-1} (13) VHH by bio-layer interferometry

4.3.1) Specificity of the cAb_{TEM-1} (13) VHH

Qualitative binding measurements were performed by bio-layer interferometry to determine the specificity of the cAb_{TEM-1} (13) VHH for representative β-lactamases belonging to the four molecular classes A, B, C and D. We decided to test TEM-1 and TEM-121, the second β-lactamase presenting four ESBL mutations (E104K, R164S, A237T, E240K) and one IRT mutation (R244S) located in its active site. We also checked the ability of the VHH to distinguish different class A families such as CTX-M-1 and SHV-104 (R202S mutant of SHV-1). Finally, VIM-4, a metallo-β-lactamase belonging to the class B, CMY-II, a plasmid-mediated AmpC from the class C and OXA-48, a carbapenemase belonging to the class D were used to explore all classes of β-lactamases.

The VHH was loaded on a His1K sensor by its His_6 tag, while the association and dissociation rates were measured by diving the sensor into wells containing the β-lactamases and the experimental buffer, respectively.

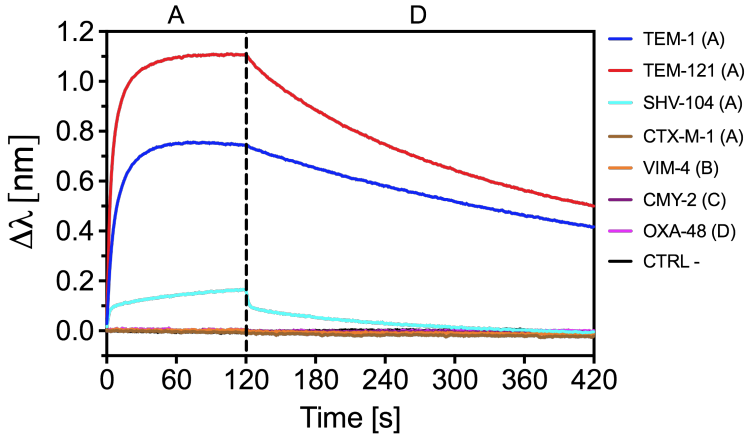

Fig 4.7. *Specificity binding between the cAb_{TEM-1} (13) VHH and different representative members of β-lactamase classes performed by BLI. Names and classes (in brackets) of the β-lactamases are indicated. The negative control (CTRL -) corresponds to the loading of TEM-1 directly on the sensor. All those experiments were performed twice independently.*
A: Association phase, D: Dissociation phase.

The interaction assay demonstrated that the cAb_{TEM-1} (13) VHH was able to specifically interact with TEM-1 and TEM-121, even though a low signal was also noticeable for SHV-104 (**Fig 4.7**). Indeed, the ability of this VHH to distinguish TEM β-lactamases from other class A β-lactamases was predictable due to the low sequence identity between the tested enzymes (98 % with TEM-121, 69 % with SHV-104 and 40 % with CTX-M-1).

4.3.2) Kinetics (k_{on}, k_{off}) and equilibrium (K_D) constants of the cAb_{TEM-1} (13) VHH

Quantitative binding measurements were performed by BLI between the cAb_{TEM-1} (13) VHH and TEM-1 (**Fig 4.8A**) and TEM-121 (**Fig 4.8B**) to determine the association (k_{on}) and dissociation (k_{off}) rates as well as the dissociation equilibrium constant (K_D) (**Table 4.1**). The association kinetic constants of the cAb_{TEM-1} (13) VHH with both β-lactamases were very similar with a value around 10^5 M^{-1} s^{-1} highlighting a rapid association of the VHH for the antigen. Moreover, with a dissociation constant near to 10^{-3} s^{-1}, all the complexes were quite stable leading to high affinities ($K_D \approx 10$ nM).

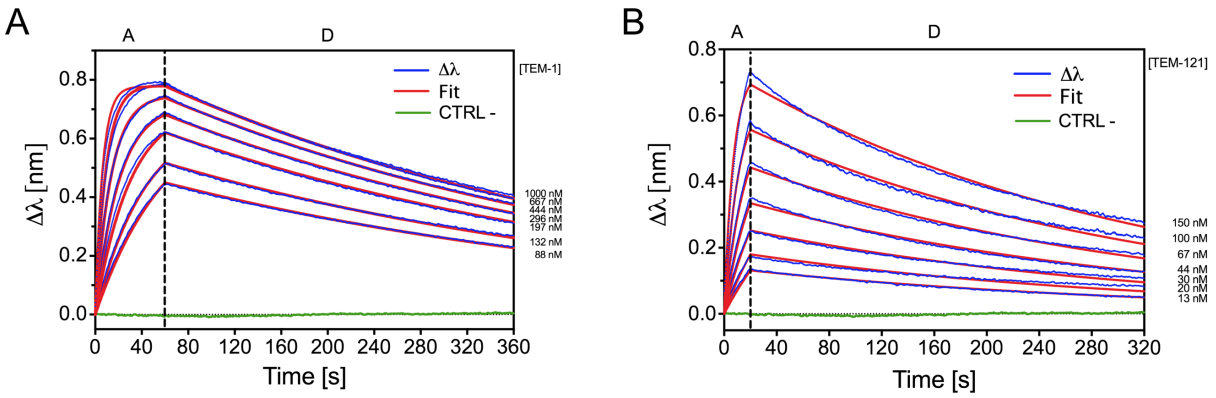

Fig 4.8. *Quantitative binding measurements of the interaction between the cAb_{TEM-1} (13) VHH and TEM-1 (A) and TEM-121 (B). Experimental data (Δλ, blue) were fitted on a global 1:1 model based on seven different analyte concentrations (red). As the previous experiment, the negative control (CTRL -) corresponds to the respective analyte directly loaded on the sensor.*

	k_{on} (10^5 M^{-1} s^{-1})	k_{off} (10^{-3} s^{-1})	K_D (nM)
TEM-1	1.7 ± 0.1	2.2 ± 0.2	13 ± 2
TEM-121	6.1 ± 2.2	3.2 ± 0.1	6 ± 1

Table 4.1. *Association (k_{on}), dissociation (k_{off}) and equilibrium (K_D) constants derived from a global fit with at least seven TEM concentrations using the equation of a 1:1 binding model. All values in the table resulted from averages and standard deviations of twice experiments realized independently.*

Identical affinity constants for VHH/TEM-1 and VHH/TEM-121 complexes seemed to indicate a similar pattern of interactions for TEM-1 and TEM-121 probably implying a conserved epitope in both antigens. Compared to VHHs directed against other β-lactamases, the cAb_{TEM-1} (13) VHH presented a high affinity for TEM-1. For example, one VHH able to partially inhibit VIM-4 displayed a K_D = 9 μM, a value 1000 times greater than the K_D of the complexes VHH/TEM (**Sohier et al, 2013**). Another example is the cAb_{BCII} (10) VHH directed against the BCII metallo-β-lactamase and presenting an IC_{50} around 200 nM (**Conrath et al, 2001**).

4.4) Binding effect of the cAb_{TEM-1} (13) VHH on TEM-1 and TEM-121 activity

The cAb_{TEM-1} (13) VHH was described to behave as a competitive inhibitor of TEM-1 in the presence of nitrocefin as reporter substrate (**Conrath et al, 2001**). In this work, we decided to compare the binding effect of the VHH on TEM-1 and TEM-121 activity. Moreover, we completed our study by testing the VHH influence on TEM activity by using four different β-lactams as reporter substrates corresponding to one penicillin (benzylpenicillin) and three cephalosporins (nitrocefin, cefalotin, cephaloridine) possessing different sizes and charges on their C3 lateral chains (C2 for the penicillin) (**Fig 1.5**).

Our results indicated an inhibitory effect of the VHH varying in function of the enzyme and the substrate. In fact, the residual activity of the VHH/TEM-1 complex for all the substrates displayed lower values than the complex VHH/TEM-121 (**Fig 4.9**). Indeed, the residual activity of the VHH/TEM-1 complex for the benzylpenicillin and the cefalotin plateaued between 25

and 30 %. On the other hand, a strong inhibition of TEM-1 was observed using cephaloridine or nitrocefin as substrate (nearly 100 %). The benzylpenicillin carries a very small C2 lateral chain with two methyl groups, while the only difference between cefalotin, cephaloridine and nitrocefin is the nature of the C3 substituent. It corresponds to an acetyloxymethyl group for cephalotin, a bulky positively charged pyridinium moiety for cephaloridine and a 2,4-dinitrophenylethenyl group for nitrocefin (**Fig 1.5**). On the contrary, the binding effect of the VHH on TEM-121 activity was identical for all the reporter substrates with an activity of the VHH/TEM-121 complex that plateaued between 50 and 60 % except for cefalotin where no inhibition was observed (**Fig 4.9B**). All results highlighted that the nature of the substrate and the mutations located in the class A active site may influence the inhibitory effect of the VHH.

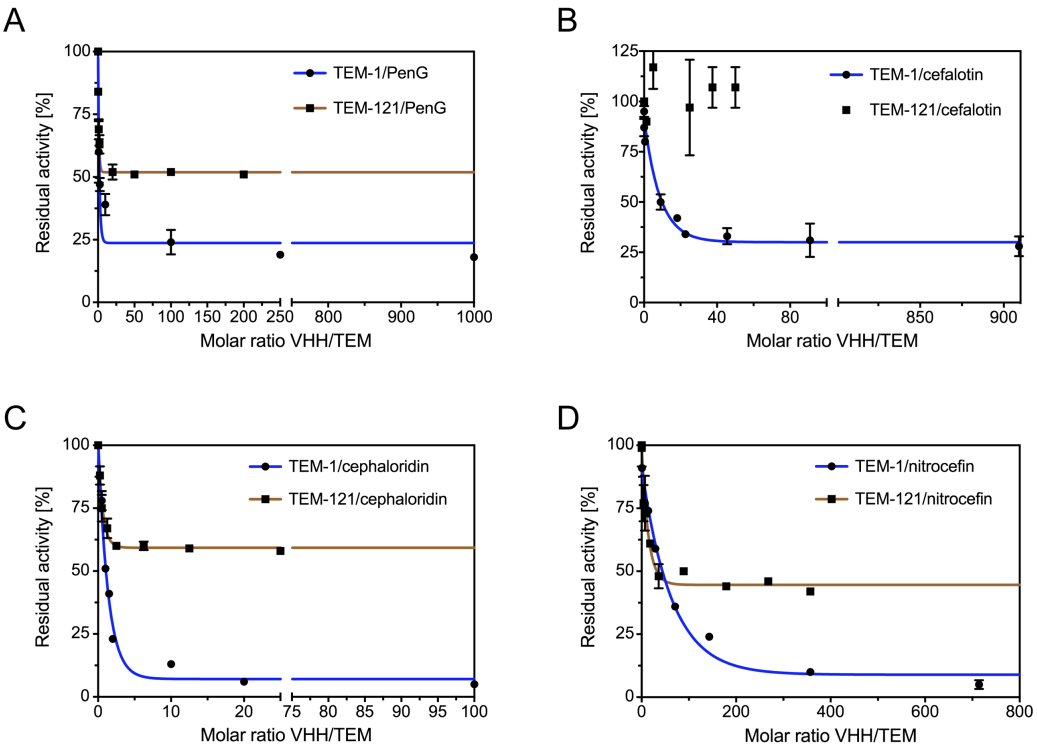

Fig 4.9. *Binding effect of the cAb$_{TEM-1}$ (13) VHH on TEM activity for 300 µM of benzylpenicillin (A), 200 µM of cefalotin (B), 200 µM of cephaloridin (C) and 100 of nitrocefin (D). Concentrations of TEM-1 and TEM-121 used for each substrate described above were 0.1 and 5 nM, 1.1 and 20 nM, 0.5 and 4 nM, 0.07 and 2.8 nM, respectively. All data were fitted on a one phase exponential decay equation. Each experiment was realized twice independently.*

4.5) Structures of the VHH/TEM complexes

4.5.1) Data collection and refinement statistics

The crystal of the cAb_{TEM-1} (13)/TEM-1 and cAb_{TEM-1} (13)/TEM-121 complexes belonged to the $P4_22_12$ and $P4_3$ space group, and diffracted at a final resolution of 1.6 Å and 2.3 Å, respectively (**Table 4.2**). The cAb_{TEM-1} (13)/TEM-1 structure includes residues H1 to W263 for TEM-1 and Q1 to H120 for the VHH. The cAb_{TEM-1} (13)/TEM-121 structure contains residues E3 to W263 for TEM-121 and Q1 to S119 for the VHH.

Table 4.2. *Data collection and refinement statistics*

Crystal	**cAb_{TEM-1}(13)/TEM-1**	**cAb_{TEM-1}(13)/TEM-121**
Data collection		
Space group	P 4_3 2_1 2	P 4_3
Cell constants		
a, b, c [Å]	94.72, 94.72, 139.68	56.97, 56.97, 139.64
α, β, γ [°]	90, 90, 90	90, 90, 90
Resolution range [Å][a]	48,4 – 1.64 (1.74-1.64)	46.55-2.2 (2.33-2.2)
Rmerge [%][a]	13.2 (330)	25.8 (218.2)
<I>/<σI>[a]	19.7 (0.96)	7.6 (0.7)
Completeness [%][a]	99.6 (97.4)	96.1 (79.8)
Redundancy[a]	26.0 (25.2)	11.7 (5.6)
CC (1/2)[a]	99.9 (51.8)	99.6 (41.1)
Refinement		
No. of unique reflections	78086	21459
R work [%]	14.7	21.63
R free [%]	18.2	24.52
No. atoms		
Protein	3030	2935
Solvent	429	98
RMS deviations from		
Bond lengths [Å]	0.015	0.005
Bond angles [°]	1.15	1.063
Mean B factor [Å^2]		
Protein	32.7	44.3
Solvent	48.1	42.4
Ramachandran plot:		
Favored region [%]	98.4	98.4
Allowed regions [%]	1.6	1.6
Outlier regions [%]	0.0	0.0

[a]*Values in parentheses are related to high resolution shell.*

4.5.2) Binding interface of the cAb_{TEM-1} (13)/TEM-1 complex

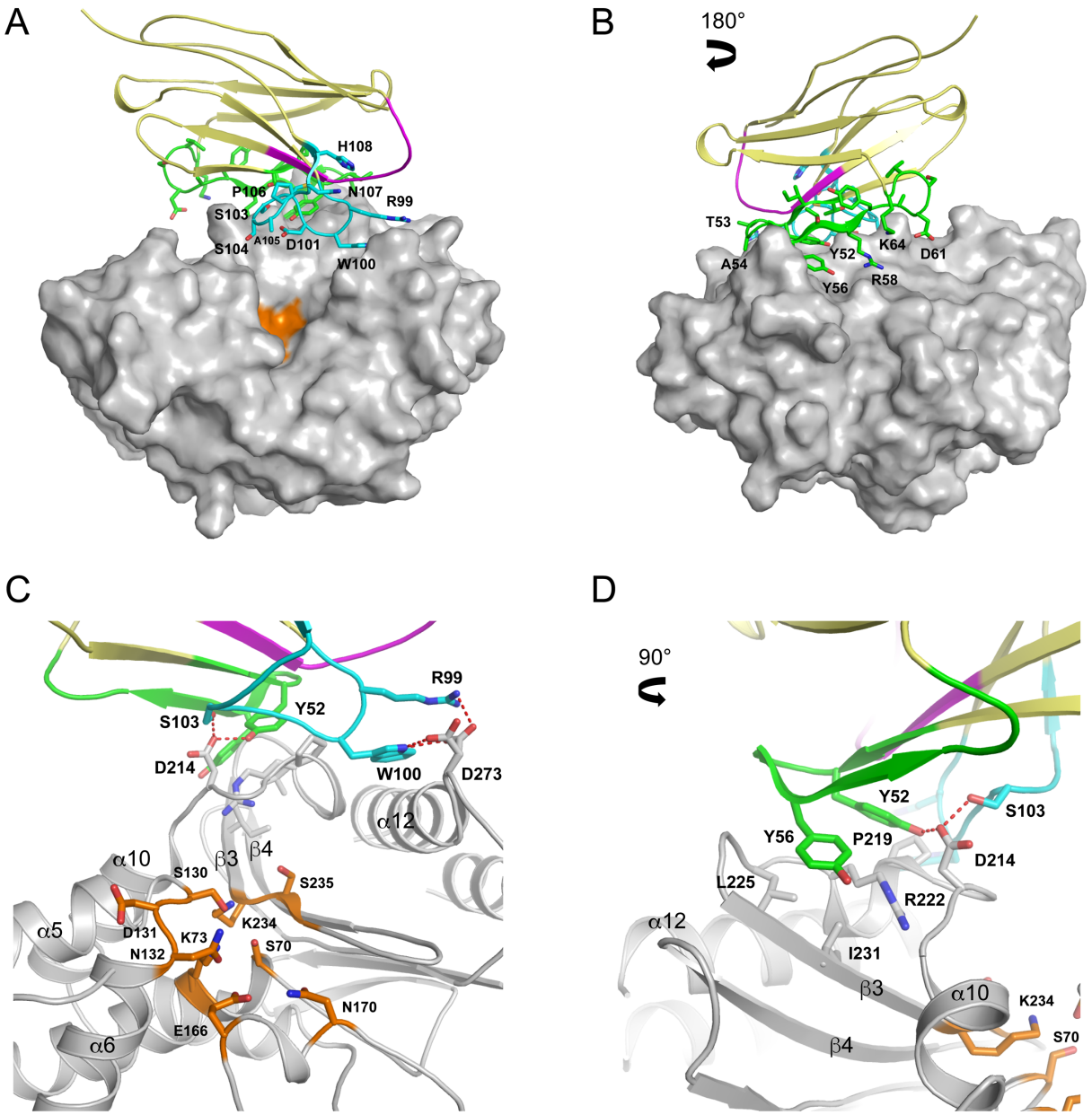

Fig 4.10. *Structure of the cAb_{TEM-1} (13)/TEM-1 complex obtained by x-ray crystallography. (A) Surface representation of TEM-1 with the VHH shown as cartoon and the relevant side chains as sticks, the CDR1 in magenta, the CDR2 in green and the CDR3 in cyan. (B) Same as A with an 180° rotation. (C) hydrogen bonds (H-bonds) representation between the cAb_{TEM-1} (13) VHH and TEM-1. TEM-1 is represented in grey and the residues forming the motif 1 (**S**70XX**K**73), the motif 2 (**S**130**D**131**N**132), the motif 3 (**K**234**S**235**G**236) and both residues E166 and N170 brought by the omega loop are colored in orange. Dotted red lines illustrate H-bonds between the VHH and TEM-1. (D) Hydrophobic interactions between the CDR2 from the VHH and residues located on TEM-1.*

The complex formed by the cAb_{TEM-1} (13) VHH and TEM-1 is characterized by a binding area of 773 $Å^2$. The VHH interacted mainly with its CDR2 (**Fig 4.10B**) and CDR3 (**Fig 4.10A**) at the junction between the α and α/β domains of TEM-1. In more detail, the residue D214 located on a loop between the α10-helix and the β3-strand on TEM-1 (hinge region) established two H-bonds with the residues Y52 and S103 on the CDR2 and the CDR3 of the VHH, respectively (**Fig 4.10C**). Furthermore, the residue D273 located on the α12-helix of TEM-1 interacts with the CDR3 of the VHH through two H-bonds with residues R99 and W100. Finally, a hydrophobic cluster was formed by both tyrosine residues (Y52 and Y56) of the CDR2 of the VHH and the side chains of residues P219, R222, L225 and I231 located on the hinge region of the β-lactamase (**Fig 4.10D**).

4.5.3) The molecular binding specificity of the cAb_{TEM-1} (13) VHH

Based on specificity binding measurements realized by bio-layer interferometry, we concluded to a high specificity of cAb_{TEM-1} (13) for TEM-1 and TEM-121. Indeed, no interaction was revealed for SHV-104 and CTX-M-1. SHV-104 presents a sequence identity of 69 % with TEM-1 and few mutations in the hinge region (**Fig 4.11**). However, the D273A mutation found in SHV-104 compared to TEM-1 disrupts the H-bonds established with residues R99 and W100 (CDR3) of the VHH. Furthermore, the hinge region of SHV-2 (no structure for SHV-104 but the epitope region is conserved) presents a different configuration than TEM-1 (**Fig 4.12A&B**). This may perturb the positioning of the VHH and decrease the strength of its interaction for SHV-104. By contrast, CTX-M-1 possesses a low sequence identity with TEM-1 (40 %) resulting in many mutations in the concerning region (**Fig 4.11**). The comparison of TEM-1 and CTX-M-15 (no structure for CTX-M-1) mainly reveals changes in the hinge region and in the α/β domain which could explain the inability of the cAb_{TEM-1} (13) VHH to bind to CTX-M-1 (**Fig 4.12C&D**).

	212	214	216	218	220	222	224	226	228	230		273	
TEM-1	E	A	D	K	V	A	G	P	L	L	R	S	A	L	P	A	G	W	F	I		D	
SHV-104	V	D	D	R	V	A	G	P	L	I	R	S	V	L	P	A	G	W	F	I		A	(69%)
CTX-M-15	K	G	N	T	T	G	A	A	S	I	Q	A	G	L	P	A	S	W	V	V		E	(40%)

Fig 4.11. *Multiple sequence alignment of the loop comprised between the α10-helix and the β3-strand (hinge region). Residues colored in red and green are involved in the H-bonds and the hydrophobic interactions, respectively, between the VHH and TEM-1. Their overall sequence identity with TEM-1 are indicated in brackets.*

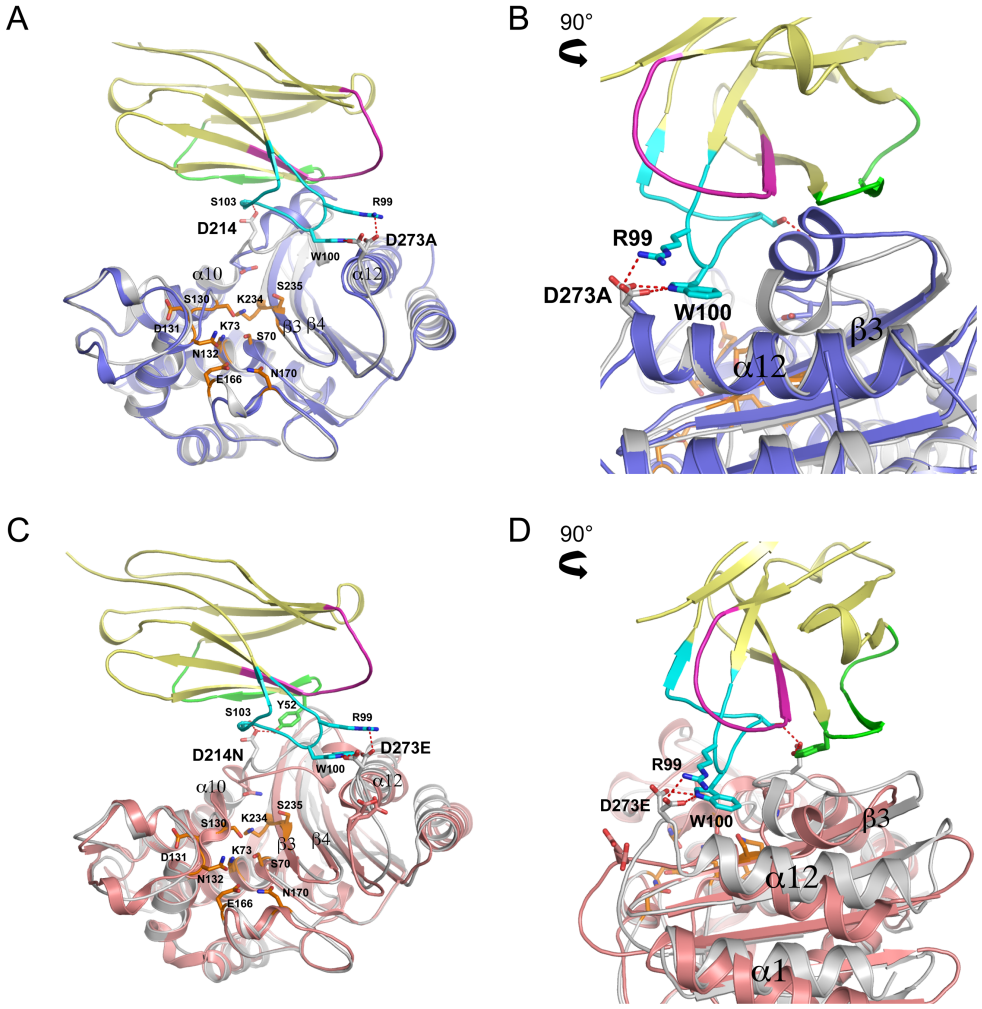

Fig 4.12. *Molecular binding specificity of the cAb_{TEM-1} (13) VHH. (A & B) Cartoons illustrating the superposition of the cAb_{TEM-1} (13)/TEM-1 complex and the β-lactamase SHV-2 (PDB code 1ONG-3) colored in purple. (C & D) Superposition of the cAb_{TEM-1} (13)/TEM-1 complex and the β-lactamase CTX-M-15 (PDB code 4HBT-2) colored in red. The residue D273 is mutated in alanine in SHV-2 and in acid glutamic in CTX-M-15. The active site residues are colored in orange while the H-bonds are represented by dotted red lines.*

4.5.4) Demystification of the cAb_{TEM-1} (13) VHH inhibition of the TEM-1 activity

The model obtained by x-ray crystallography clearly indicated that the cAb_{TEM-1} (13) VHH interacted outside of the TEM-1 active site, on the hinge region connecting the α12-helix and the β3-strand participating to the structure of the catalytic pocket. However, the comparison of the cAb_{TEM-1} (13)/TEM-1 complex and the TEM-1 apo-enzyme highlights a reduced flexibility of the hinge region in the complex. Indeed, the structure of the apo-enzyme presents multiple conformations for residues K215, V216 and A217, whereas only one conformation was visible for these residues in the complex (**Fig 4.13A**). Therefore, the cAb_{TEM-1} (13) VHH may disturb the intrinsic dynamic of TEM-1 required for its biological function (**Sohier et al, 2013**). On the other hand, the model of the cAb_{TEM-1} (13)/TEM-1 complex was obtained at a lower resolution than the apo-enzyme (1.64 Å versus 0.83 Å) which may explain the lack of visible double conformations in the hinge region of the complex. We therefore decided to more deeply investigate the influence of the VHH on the TEM-1 dynamic by (I) circular dichroism, (II) molecular dynamic simulations and (III) NMR relaxation experiments.

Our kinetic studies demonstrated a different binding impact of the cAb_{TEM-1} (13) VHH on TEM-1 and TEM-121 activity for different β-lactams. However, both complexes perfectly superimposed with the same binding area between the VHH and the hinge region (**Fig 4.13B**). We concluded that mutations on TEM-121 and more probably the R244S mutation could explain the different mechanisms of inhibition. This arginine carries a guanidium group which may lead to a steric hindrance with the reorientation of hydrophobic elements towards the active site of TEM-1 in the complex (e.g. V216, A217) (**Fig 4.13A**). This steric hindrance is less pronounced in TEM-121 since the serine brings a hydroxide group rendering less efficient the inhibition by the VHH. The variants TEM-1 R244S and TEM-121 S244R were kinetically characterized to verify this hypothesis.

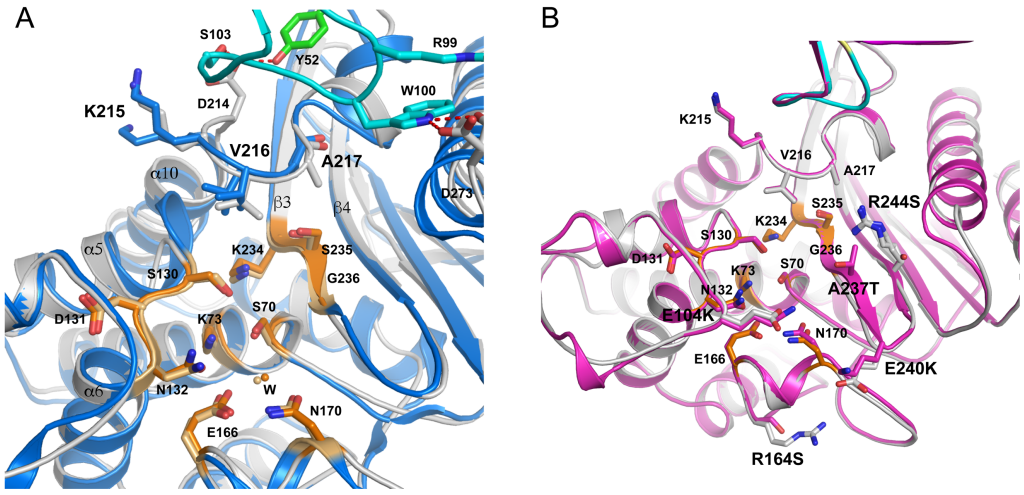

Fig 4.13. *Superposition of TEM-1 complexed to the cAb_{TEM-1} (13) VHH (grey) with the high apo-enzyme TEM-1 resolved at high resolution (PDB code 1m40, blue) (A) and with cAb_{TEM-1} (13)/TEM-121 complex (B) where TEM-121 is colored in magenta.*

Finally, the structures of the complexes highlighted a reorientation of the V216 with the switch of its carbonyl function outside the active site. As a consequence, this disrupts the H-bond network stabilizing the carboxylic function brought by the residue C3 (penicillin) or C4 (cephalosporin) of the antibiotic (**section 1.5.3.2**) (**Fig 4.14**). This may, in complement with dynamic, contributed to decrease the acylation rate and/or destabilize the acyl-enzyme.

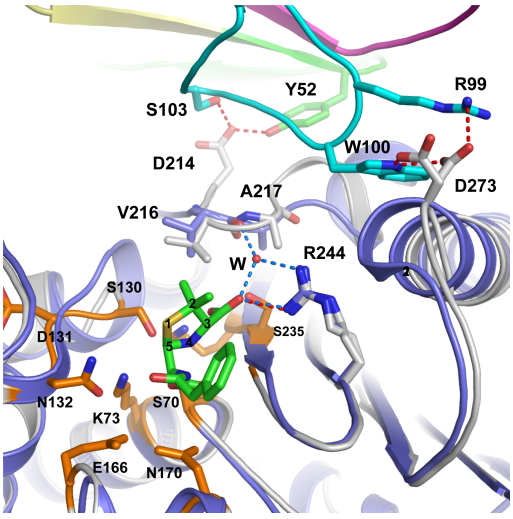

Fig 4.14. *Superposition of the VHH/TEM-1 complex and the PenG/TEM-1 acyl-enzyme (PDB code 1FQG). TEM-1 in the complex with the VHH and in the acyl-enzyme are colored in grey and purple, respectively. In the acyl-enzyme, the H-bonds forming the "carboxylic pocket" are represented by blue dotted lines. The unique hypothesized H-bond between the residue R244 and the carboxylic function of the penicillin in the complex is illustrated by a red dotted line.*

4.6) Thermal denaturation studies by far-UV Circular Dichroism (CD)

4.6.1) Far-UV CD spectra of TEM-1 and the cAb_{TEM-1} (13) VHH

To visualize the cAb_{TEM-1} (13) VHH binding impact on TEM-1 and TEM-121 dynamic, we performed thermal denaturation studies by circular dichroism (CD). We first recorded far-UV CD spectra of TEM-1 in its folded (25 °C) and unfolded (97 °C) forms to determine the wavelength where the denaturation should be followed. It appeared that the higher signal difference between both forms was measured at 224 nm (**Fig 4.15A**).

Considering our interest to check a potential change in the denaturation temperature of TEM-1 and TEM-121 by the VHH, it was essential to dissociate the thermal transition of the enzyme and the VHH in the complex. Previous studies reported a value of 51 °C for the thermal denaturation of TEM-1 (**Raquet et al, 1995**), while CD spectra of the cAb_{TEM-1} (13) VHH recorded between 25 and 97 °C highlighted a signal change at 224 nm from 65 to 70 °C (**Fig 4.15B**). We concluded the possibility to separate the thermal transitions of TEM and the VHH even in the complex.

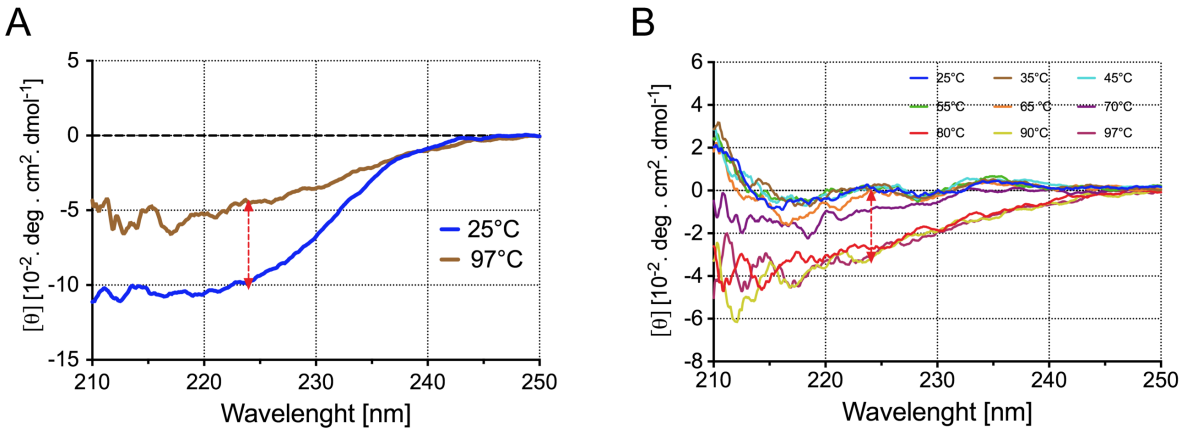

Fig 4.15. *(A) Far-UV CD spectra of TEM-1 at 25°C (blue) and 97 °C (brown). (B) Far-UV CD spectra of the cAb_{TEM-1} (13) VHH in a range of temperatures between 25 and 97 °C.*

4.6.2) CD denaturation curves of TEM enzymes and the cAb_{TEM-1} (13) VHH

The thermal denaturation experiments confirmed a two-state model (N⇔U) for the VHH with the midpoint of the transition (T_m^{app}) around 70 °C (**Table 4.3**) allowing to separate the denaturation transitions of the VHH and TEM in the complex. Thermal denaturation curves also emphasized a shift of the curves to higher temperatures for both VHH/TEM complexes (**Fig 4.16**) with increased T_m^{app} values (**Table 4.3**). However, this phenomenon is more probably due to a shift of the equilibrium to the native form of TEM by adding the VHH. A similar effect was observed for PC1 (*Staphylococcus aureus*) in the presence of various substrates (**Lejeune et al, 2001**).

	T_m^{app} [°C]
TEM-1	51.4 ± 0.1
VHH/TEM-1	61.1 ± 0.3
TEM-121	50.8 ± 0.6
VHH/TEM-121	59.0 ± 0.3
cAb_{TEM-1} (13)	69.5 ± 0.3

Table 4.3. *T_m^{app} values of TEM-1 and TEM-121 alone and in complex with the VHH. They were obtained by fitting the thermal denaturation curves using the equation XVI. Averages and standard deviations correspond to twice experiments.*

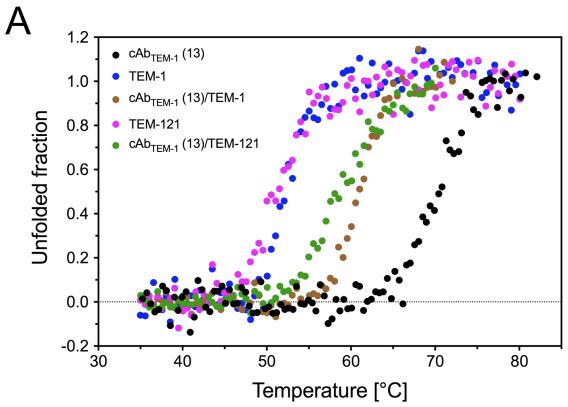

Fig 4.16. *Thermal denaturation curves of the apo-enzymes and in complex with the VHH. Experiments were performed at 224 nm using 3.4 µM of free enzymes, VHH and VHH/TEM complexes at a molar ratio 1:1.*

4.7) Dynamic simulations using the GROMACS program

The impact of the cAb_{TEM-1} (13) VHH binding on the TEM-1 dynamic was also studied molecular dynamic simulations using the program GROMACS. We carried out five simulations (100 ns) with an identical force vector, but in random three-dimensional orientations to be statistically significant (**section 3.13.3**). We decided to study three different models: the model TEM-1 at high resolution (PDB code 1m40) (**TEM-1 HR**), TEM-1 from the complex where the VHH was removed (**TEM-1**) and the complex **VHH/TEM-1**. We focused our analysis on the parameters RMSF (root-mean square fluctuation) and RMSD (root-mean square deviation) describing the flexibility of residues in the different simulations (**section 3.13.2**).

4.7.1) Root-mean square fluctuation (RMSF)

The RMSF values for the backbone and the side chains of TEM-1 HR and TEM-1 confirmed major motions of the loops compared to helices and β-strands, except for the loop connecting the β2-strand to the α2-helix carrying the active-site serine and the SDN loop (**Fig 4.17A&B**).

TEM-1 alone and in the complex present motion differences, mostly for the backbone of the protein (**Fig 4.17A**) and less for the lateral chain residues except in the hinge region (**Fig 4.17B**). The RMSF studies brought out the ability of the VHH to alter the overall flexibility of the β-lactamase with some loops and helices (α domain) presenting a higher flexibility compared to TEM-1 (**Fig 4.17C&D**). It is mainly applied to the **protruding loop** (residues 85-120) with higher RMSF values for TEM-1 complexed to the VHH (**Fig 4.18A**). The dynamic changes along TEM-1 may describe an allosteric effect of the cA_{bTEM-1} (13) VHH on the activity of TEM-1 (**Sohier et al, 2013**).

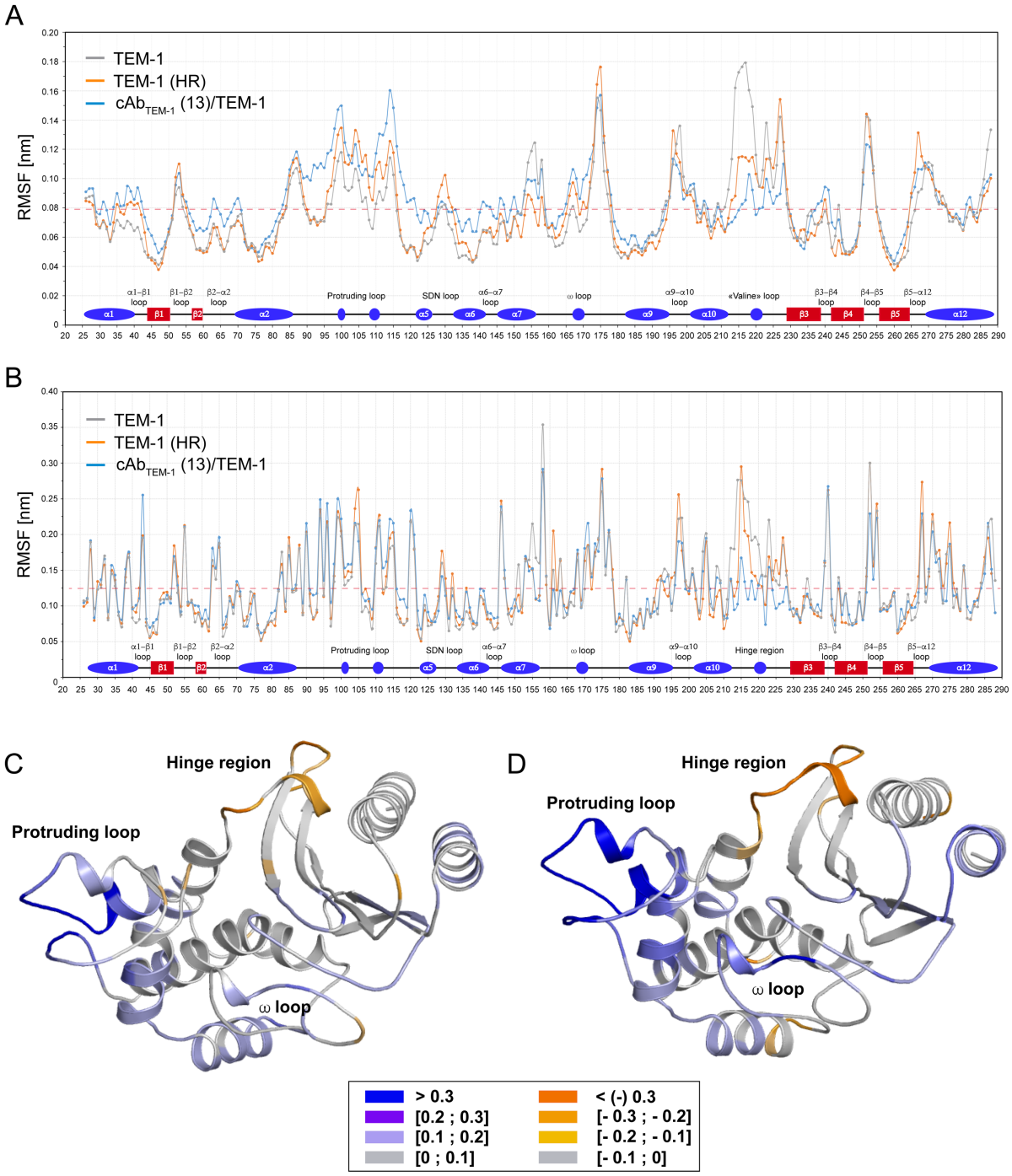

Fig 4.17. *Root-mean square fluctuation (RMSF) of the backbone (A) and the side chain (B) of all the residues from the three models TEM-1 (grey), TEM-1 HR (orange) and VHH/TEM-1 (blue). Each RMSF corresponds to the average of the five modellings. For more clarity, the standard deviations for RMSF were not indicated on these graphs. The red dotted lines correspond to the average RMSF for all the protein residues. (C-D) Representation of the flexibility (graduated blue scale) and the rigidity (graduated orange scale) brought by the VHH in TEM-1 HR (C) or in TEM-1 (D) based on the backbone RMSF.*

We also studied the dynamic of the **ω loop** (residues 164-179). It is divided in two parts: (I) the N-terminal part (164-170) carrying the general base (E166) and the N170 involved in the catalytic activity of TEM-1 and (II) the C-terminal part (171-179). It appears that the VHH does not affect the overall dynamic of the ω loop except in the region near to the residue N170 with a weak increase in flexibility for TEM-1 in complex with the VHH (**Fig 4.18B**). Interestingly, the C-terminal extremity of the ω loop was more flexible than the N-terminal part in all models. This is in agreement with other studies predicting different conformations in a μs-ms timescale (**Shcherbinin et al, 2019 & Fisette et al, 2010 & Morin & Gagné, 2009**). On one hand, the rigidity of the first part of the ω loop, carrying the general base E166, was considered as essential for the correct positioning of the catalytic residues. On the other hand, the mobility of the second part of the loop is essential for the correct substrate delivery in the active site and for the substrate gating. It is notably known that the motion of the C-terminal part of the ω loop favors the formation of a H-bond between the residues N175 and R65 ensuring the gating of the substrate and the rigidification of the N-terminal part of the loop for the correct positioning of the general base (**Roccatano et al, 2005**).

The presence of the VHH stabilized the **hinge region** as observed by x-ray crystallography (**Fig 4.18C&D**). Its stiffening mainly occurred in the region comprising the residues K215-V216-A217 located in the active site and in the C-terminal part of the loop forming the hydrophobic pocket in interaction with the CDR2 of the VHH. The decrease in the hinge region mobility was more visible for the side chain residues than for their backbone atoms. This may be related by the timescale of the simulations (100 ns) which is not sufficient to visualize the entire motion of the loop.

The RMSD (root-mean square deviation) values validated the loss in flexibility of the hinge region by the VHH binding confirming the RMSF values (**Annexe 3**). The simulation of the VHH/TEM-1 complex reached an equilibrium before 5 ns and did not present variation higher than 0.15 nm. By contrast, TEM-1 and TEM-1 HR got to the equilibrium state at 20 ns of the simulation and the RMSD fluctuated between 0.22-0.27 nm and 0.18-0.24 nm, respectively. The global RMSD for the three models reached an equilibrium state around 60 ns after the beginning of the simulation and confirmed the stability all systems (**Annexe 3**).

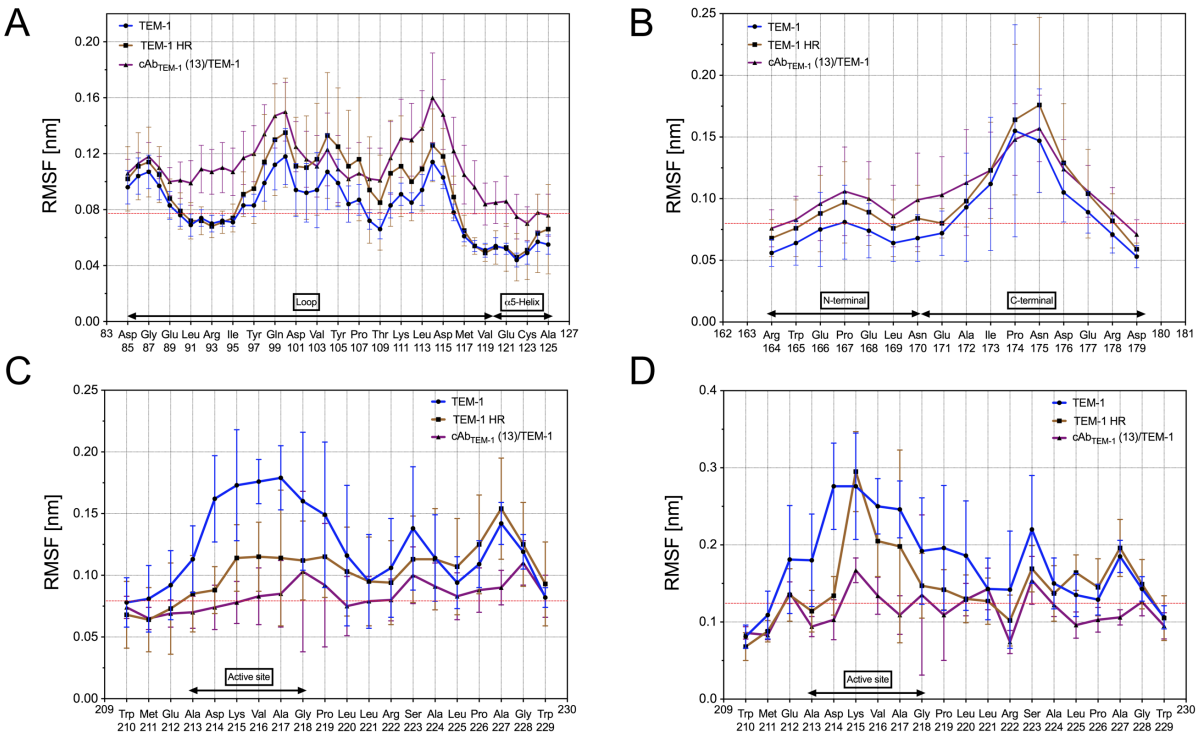

Fig 4.18. *Root-mean square fluctuation (RMSF) of the protruding loop (A), the ω loop (B) and the hinge region backbone (C) and side chain (D). Averages and standard deviations resulted from the 5 modeling experiments. The red dotted lines correspond to the RMSF average of all the protein residues.*

4.7.2) Involvement of the residue D214 in the H-bond network stabilizing the hinge region

Our dynamic simulations highlighted a higher flexibility of the hinge region for the TEM-1 model compared to TEM-1 HR (**Fig 4.18C**). Therefore, the interaction with the VHH may impact the integrity of the loop resulting in the amplified motion.

In fact, the residue D214 in TEM-1 HR established some H-bonds with the main chain of the residues K215, V216 and A217. However, the residue D214 interacted with Y52 and S103 in the VHH/TEM-1 complex, disrupting the H-bonds network in the hinge region (**Fig 4.19A**). This may explain why we observed an amplified motion of the hinge region in the dynamic simulations of the TEM-1 model. We confirmed our interpretations by the cartography of the H-bonds established by D214 with the rest of the hinge region during a 100 ns simulation (**Fig 4.19B**). We counted for an average of 3 H-bonds during the first 60 ns in

TEM-1 HR and this amount increased up to 8 H-bonds in the last ns of simulation. In contrast, the H-bond network was clearly reduced to one bond when the simulation was performed on the TEM-1 template. Therefore, we suggested that the flexibility of the hinge region in the enzyme is controlled by a H-bonds network between the residue D214 and the N-terminal part of the hinge region, probably crucial for the stability and/or the activity of the enzyme. Finally, some simulations of TEM-1 illustrated that the residue D214 was able to flip and to recover a position near to the V216 leading to new H-bonds with the hinge region and confirming the role of D214 in the integrity of the loop (**Fig 4.19C**).

The H-bond network in the hinge region is conserved among class A β-lactamases. Two configurations stand out: the first involving H-bonds between the residue D214 with the main chains of residues 215 to 217 as in TEM-1 or SHV-2; the second network where a residue N214 binds to the main chain of residues 215, 216 and the lateral chain of the T216 (e.g. KPC-1). This probably orients the carbonyl function of the V/T216 involved in the stabilization of the carboxylic function of the antibiotic (**section 1.5.3.2**).

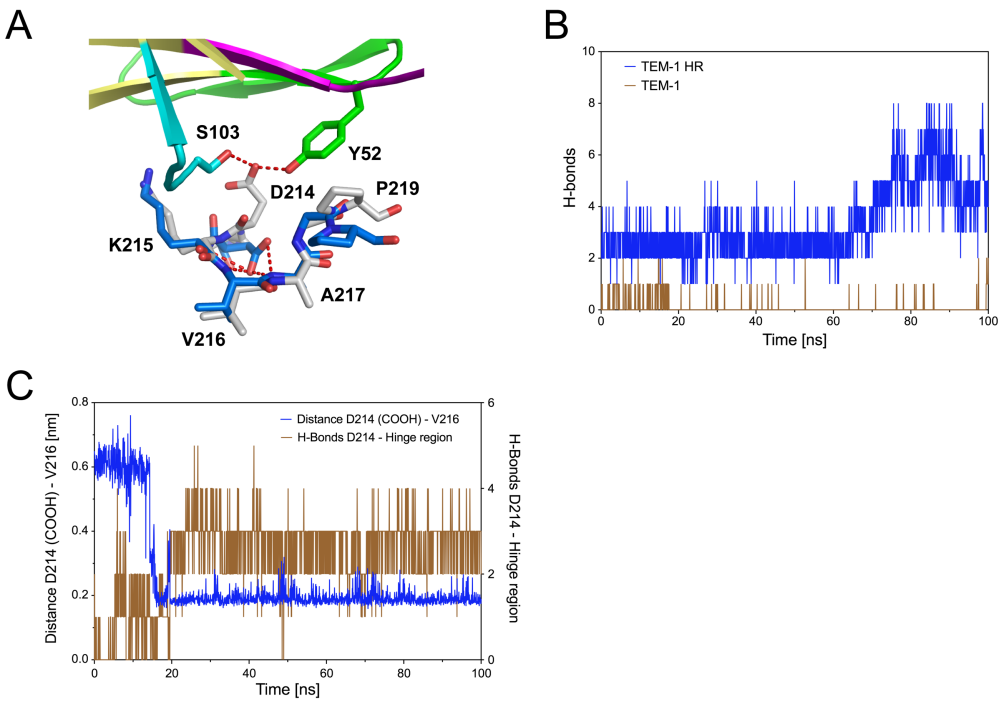

Fig 4.19. *(A) Superposition of TEM-1 (grey) in complex with the VHH and TEM-1 HR (blue, PDB code: 1m40). H-bonds are represented by red dotted lines. (B) H-bonds established between the residue D214 and the hinge region. (C) Distance and H-bonds between the residue D214 and the hinge region.*

4.8) Thermal denaturation studies of the TEM-1 D214A mutant

To verify the impact of the H-bond network established between the residue D214 and the main chains of the triad K215-V216-A217 on TEM-1 stability, we compared the thermal denaturation curves of TEM-1 WT and TEM-1 D214A by far-UV CD and fluorescence.

Thermal denaturation curves by far-UV CD and fluorescence highlighted a shift of lowest T_m^{app} for the TEM-1 D214A mutant (**Fig 4.20**). Compared to TEM-1, we obtained a lower T_m^{app} than 1.7 °C and 7 °C by CD and fluorescence experiments, respectively (**Table 4.4**). This mutation probably destabilized the enzyme by the disruption of the H-bonds between the residue 214 and the main chain triad K215-V216-A217. Furthermore, both CD and fluorescence experiments described a cooperative unfolding of TEM-1 with a single transition curve according to a two-state model. Nevertheless, the thermal denaturation of the variant did not follow a cooperative unfolding. Indeed, the T_m^{app} value was around 5 degrees lower by intrinsic fluorescence compared to the value calculated on the basis of the CD data. We concluded to the accumulation of intermediate species for the TEM-1 D214A mutant. This study proved the crucial role of the residue D214 in the stability of TEM-1 even though we did not verify the activity of the variant. This may explain why this mutation is not naturally found in actual TEM enzymes.

$\mathbf{T_m^{app}}$ [°C]	Far-UV CD	Fluorescence
TEM-1	51.4 ± 0.1	51.5 ± 0.1
TEM-1 D214A	49.7 ± 0.2	44.5 ± 1.7

Table 4.4. *T_m^{app} values of TEM-1 and TEM-1 D214A by CD and fluorescence. They were obtained by fitting the thermal denaturation curves using the equation XV. Averages and standard deviations correspond to twice experiments.*

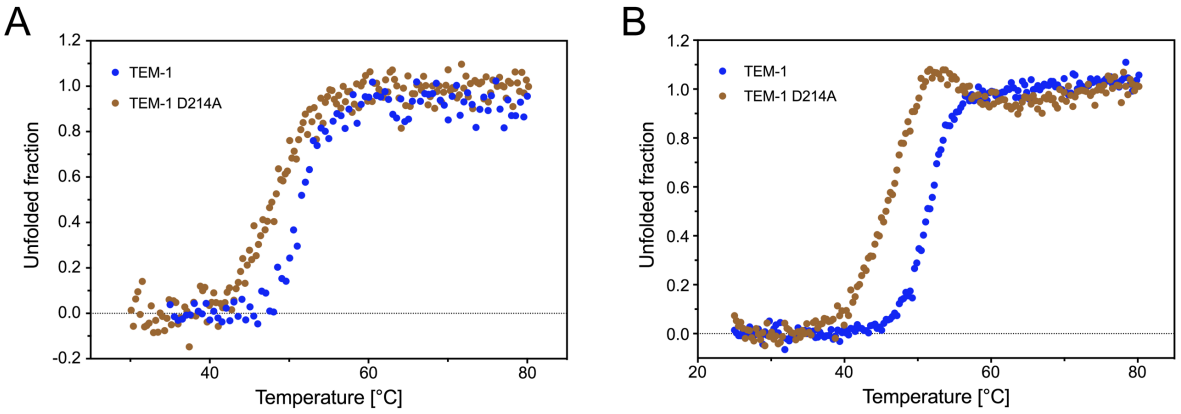

Fig 4.20. *(A) Thermal denaturation curves of TEM-1 and TEM-1 D214A mutant performed by circular dichroism recorded at 224 nm and (B) intrinsic fluorescence (λ^{exct} = 280 nm; λ^{emi} = 333 nm). The protein's concentrations were equal to 3.4 µM and the temperature's gradient was realized at 0.5 °C min^{-1}.*

4.9) Dynamic studies by NMR relaxation experiments

4.9.1) Relaxation data of TEM-1 and the VHH/TEM-1 complex

R_1 and NOE values highlighted a high rigidity of the apo-enzyme TEM-1 at timescale picosecond-to-nanosecond as already described by *Savard* (**Savard & Gagné, 2006**). Only few residues presented more flexibility, e.g. residues 43, 52, 197 and 198, all exposed to the solvent and located far from the active site. The binding with the VHH seemed did not seem to impede the global rigidity of TEM-1 in this timescale (**Fig 4.21A&B**).

R_2 pattern describes motions with a larger timescale, lower and higher values indicating motions in a range of ps-ns and µs-ms, respectively. We noticed a lower movement of the hinge region (212 and 218) for the apo-enzyme TEM-1 (**Fig 4.21C**). It was completely disrupted in the complex confirming results obtained by dynamic simulations (**Fig 4.18C**). Surprisingly, the interaction of the VHH with TEM-1 also led to rigidification in other locations of TEM-1 as for the residue T128 located at the N-terminal part of the SDN loop.

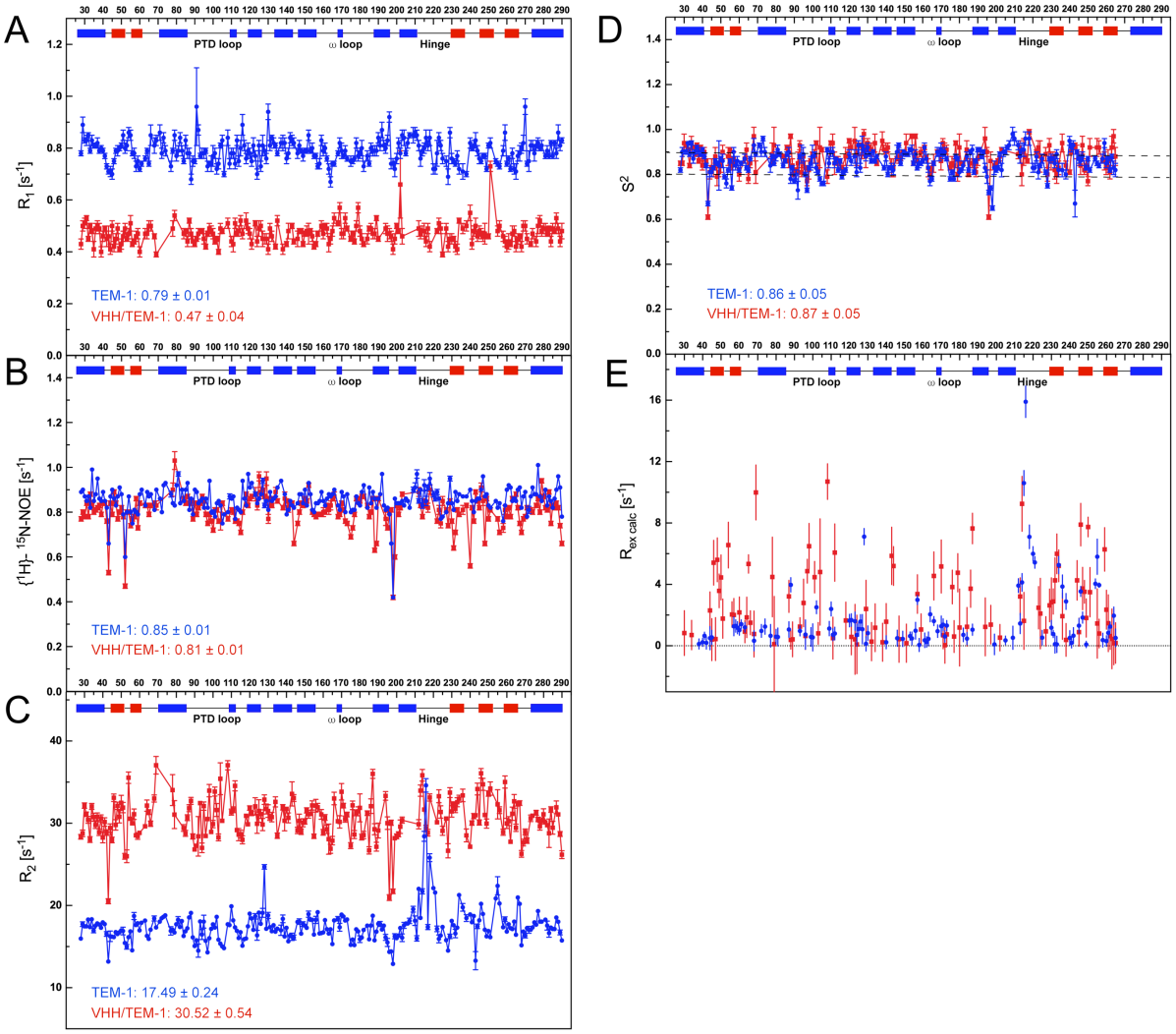

Fig 4.21. *Relaxation data for TEM-1 alone (blue) or in complex with the VHH (red). (A) ^{15}N R1, (B) $\{^{1}$H-$\}^{15}$N NOE, (C) ^{15}N R2. The different dynamic parameters derived from the model-free analysis: (D) the order parameter (S^2) and (E) the exchange parameter (R_{ex}). Black dotted lines on the S^2 graph describe the range of S^2 of residues presenting a high rigidity on the ps-ns timescale (between 0.8 and 0.9). The secondary structure of TEM-1 is represented above all graphs: helices and β-strands are illustrated by a blue and red rectangle, respectively, while loops are represented by a black line. PTD loop: protruding loop, Hinge: hinge region.*

4.9.2) The Lipari-Szabo model-free analysis

The model-free analysis aims to characterize internal motions at timescale ps-ns such as the order parameter S^2. Moreover, this also provides information on slow timescale motions from the microsecond-to-millisecond via the R_{ex} parameter (**section 3.14.6**).

We attributed a value comprised between 0 and 1 to the S^2 parameter with rigid regions comprised between 0.8 and 0.9 and inferior values for flexible regions (**Savard & Gagné, 2006**). The analysis of the global S^2 highlighted a high rigidity of the enzyme with an average value of 0.86 and 0.87 s^{-1} for TEM-1 alone and in the complex, respectively, confirming experimental R1 and NOE values (**Fig 4.21D**). Some locations had also values higher than 0.9 illustrating regions highly structured. In the two models, some punctual residues displayed more flexibility on the protruding loop. We also observed values slightly lower than 0.8 as the residue R164 able to form a salt bridge with the residue D179 forming the ω loop, or the residue N175 in the apo-enzyme establishing an H-bond with the residue R65 due to a flap-like movement of the ω loop allowing the tethering of the loop into the core of the protein and the substrate gathering (**Roccatano et al, 2005**). However, we need to stay careful since the literature generally describes a slow motion of the ω loop (**Olehnovics et al, 2021**) (**Fig 4.22**).

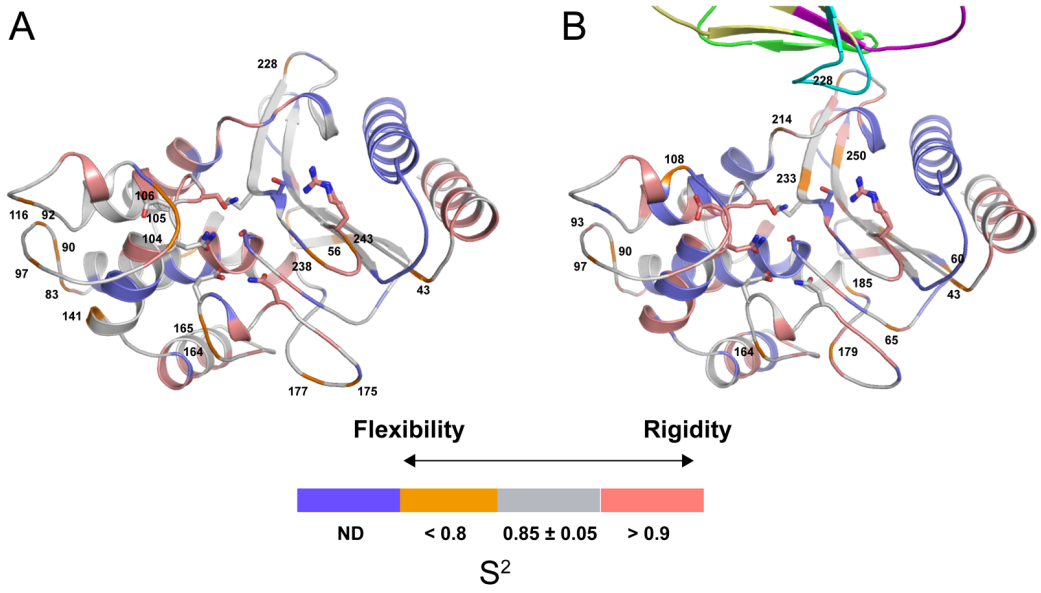

Fig 4.22. *Cartoon representations of the order parameter (S^2) for TEM-1 alone (A) and in complex with the VHH (B). Residues with values below 0.8 present a high flexibility in the ps-ns timescale while residues with S^2 above present more rigidity.*

R_{ex} confirmed results for what the binding with the VHH induced a rigidification of the hinge region, mainly residues K215-V216-A217 (**Fig 4.23C**).

The VHH induced more motions on TEM-1 (**Fig 4.23B**), specially in loops and the β3, β4 and β5-strands forming the α/β domain (**Fig 4.23C**). The VHH establishes hydrophobic interactions via the tyrosines at positions 52 (CDR2) and 56 (CDR3) with residues P219, L225 and I231 on the hinge region. These residues belong to a hydrophobic node constituted by the α11, α12-helices and the β3, β4 and β5-strands. In this hydrophobic node, the presence of a conserved class A allosteric site formed by the triad P226-W229-P252 which sets up stacking interactions modulating the flexibility of the α11-helix and their interactions with the β-sheet (**Avci et al, 2016**). The disruption of this hydrophobic node by the W229A mutant (**Meneksedag et al, 2013**) or by allosteric inhibitors (**Horn & Soichet, 2004**) led to motion changes impeding the activity of the enzyme. Moreover, recent studies describe the signal transmission of the allosteric site perturbation associated with the cooperative coupling of loops dynamic, even for loops located far from the allosteric site (**Galdadas et al, 2021**). The binding with the VHH clearly displaced P226, disrupting the stacking interactions between P226 and the W229 (**Fig 4.23D**). This may generate more flexibility in the hydrophobic node as for the β-sheet, but also for loops near or far from the VHH binding site.

Interestingly, the VHH also induces more mobility of the residue R244 (**Fig 4.23C**). This result was already observable by x-ray crystallography where one conformation was visible in the high-resolution model of TEM-1 (PDB code 1m40) and two conformations in the complex. Both residues L220 and N276 brought by the hinge region and the α12-helix, respectively, stabilize the residue R244 essential for its interaction with the carboxylic function of the antibiotic (**Fig 4.23A**) (**Olehnovics et al, 2021 & Horn & Soichet, 2004**). In the complex, residues R99 and W100 (VHH) interact with the residue D273 on the α12-helix of TEM-1, resulting in the displacement of the residue N276 abolishing its interaction with R244 (**Fig 4.23E**). Combined with the displacement of the L220, the residue R244 is less stabilized. This impedes the biological activity of TEM-1.

Our NMR data indicated that the VHH perturbs the dynamic of loops located far from the binding site by an induce-fit mechanism. It's the case of the ω loop where motions allow the correct positioning of the residue E166 for its function (**Fisette et al, 2010 & Fisette et al, 2012**). In the complex, the VHH disrupted the dynamic of the ω loop, mostly for residues E166 and N170 directly implied in the catalytic activity of the enzyme, but also for some residues involved in the configuration of the loop such as the residues R164 and D179 (**Fig 4.23C**).

The protruding loop underwent also motion perturbation as already described by molecular modelling results (**Fig 4.17C**). This loop was notably able to interact with the α4 and α5-helices required to be structured (e.g. interactions between residues V103, S106 and T133). The increased flexibility of the protruding loop may disrupt these interactions inhibiting the activity of TEM-1. Another study on the β-lactamase Inhibitor Protein (BLIP) highlighted that the interaction of the inhibitor with the protruding loop perturbed the dynamic of other loops including the hinge region demonstrating the cooperativity between loops constituting the active site of TEM-1 (**Huang et al, 2020**).

Finally, it is recognized that the binding of some substrates on TEM-1 results in fundamental dynamic changes into the enzyme leading to hydrolysis of the substrate. In its apo-form, the α and α/β domains establish rotational and translational movements each other and the enzyme "breathes". This phenomenon allows the accommodation of the substrate in the active site. During the substrate binding, the amplitude of the movements of the two domains is reduced what defines the active site. In the same vein, the ω loop makes flap-like motions, more randomly in the free enzyme and more organized during the substrate binding, allowing to anchor the loop in the protein core and stabilized by some H-bonds established between residues N175 and R43 and/or R65 (**Fisette et al, 2012**). The VHH may therefore influence the dynamic of the enzyme and may disrupt the activity of the enzyme.

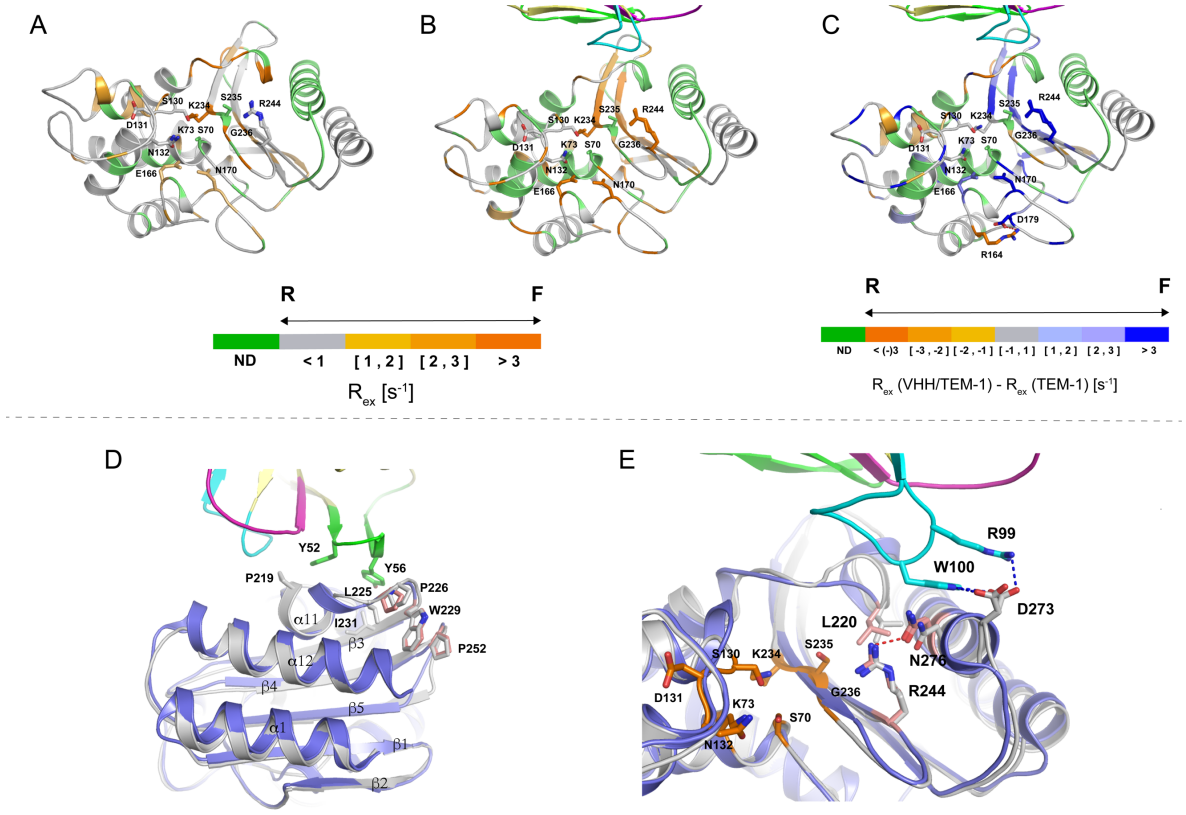

Fig 4.23. *Cartoon representation of the R_{ex} parameter for TEM-1 alone (A) and in complex with the VHH (B). (C) ΔR_{ex} corresponding to the difference between the R_{ex} of TEM-1 complexed with the VHH and the R_{ex} of the free enzyme. Higher is the value of this parameter, higher is the flexibility of the residue in the microsecond-to-millisecond timescale. (D) Illustration of the allosteric site forming by the triad P226-W229-P252. (E) Stabilization of the R244 ensured by the residues L220 and N276. For the both last pictures, TEM-1 in the free form (PDB code 1m40) and in interaction with the VHH is colored in grey and blue, respectively. Residues highlighted in red belong to the TEM-1 model.*

4.10) Steady-state Kinetic studies of TEM-1 and TEM variants

As a reminder, the cAb_{TEM-1} (13) VHH was able to interact with TEM-1 and TEM-121. Despite a shared epitope by the antibody for both antigens, we noticed that the VHH inhibited with more efficacy TEM-1 than TEM-121. The presence of an arginine at position 244 in TEM-1, mutated in serine in TEM-121, seemed to be the more plausible cause to explain the different mechanisms of inhibition. The large charged lateral chain of the arginine (guanidium group), combined with the reorientation of hydrophobic elements due to the interaction with the VHH, may lead steric hindrance and/or electrostatic repulsions preventing the entry of the substrate in the active site and/or destabilizing the acyl-enzyme. Then, the presence of a

serine in TEM-121 suppresses the positive charge and may release space in the active site decreasing the efficiency of the inhibitory activity of the VHH.

To verify this hypothesis, we carried out kinetic experiments on TEM-1 and on the TEM-121, TEM-1 R244S and TEM-121 S244R mutants. We decided to work at only one saturating concentration of the cAb_{TEM-1} (13) VHH and with four β-lactam substrates.

4.10.1) Cefalotin

Cefalotin was the most intriguing substrate. The VHH was unable to inhibit the activity of TEM-1 R244S and TEM-121, while the residual activities of TEM-1 and TEM-121 S244R plateaued at 20 and 40 %, respectively (**Table 4.5**). This highlighted the involvement of the arginine in the inhibitory activity of the VHH for the cefalotin hydrolysis by TEM-1.

Cefalotin	v_0 (μmol min^{-1} mg^{-1}) TEM	v_0 (μmol min^{-1} mg^{-1}) VHH/TEM	Residual activity [%]
TEM-1	130 ± 20	26 ± 5	20 ± 1
TEM-1 R244S	1.2 ± 0.3	1.9 ± 0.3	157 ± 13
TEM-121	3.0 ± 0.3	3.6 ± 0.3	117 ± 1
TEM-121 S244R	28 ± 13	12 ± 4	42 ± 5

Table 4.5. *Initial rates of cefalotin hydrolysis for 5 nM of TEM-1, 100 nM of TEM-1 R244S, 40 nM of TEM-121 and 10 nM of TEM-121 S244R. Measures were performed for the apo-enzymes and for complexes in one saturating VHH concentration (1μM). Rates of hydrolysis are expressed in μmol of cefalotin (200 μM) hydrolyzed per minute and per milligram of enzyme.*

In order to complete our analysis, we performed measures of TEM-1 velocity at different concentrations of cefalotin for increasing VHH concentrations. Hanes linearization revealed parallel straight lines indicating that the VHH acts as a competitive inhibitor for TEM-1 activity for the cefalotin (**Fig 4.24A**). This resulted in higher K_m^{app} values for TEM-1 in the complex. On the contrary, no effect was observable on the deacylation constant k_{cat}^{app}. The inhibition constant (K_I) of the cAb_{TEM-1} (13) VHH for TEM-1 was determined from the equation XI (**Fig 4.24B**) and is equal to 1.9 ± 0.1 nM, a slightly lower value compared to the equilibrium constant of dissociation of the complex obtained by bio-layer interferometry (**Table 4.1**). This technique enables direct measurement of biomolecular interactions, unlike the steady-state

kinetic studies where the inhibition constant is determined by an indirect method (reporter substrate). It seems that the VHH, by the intermediate of R244, directly blocks the entry of the cefalotin in the active site and/or destabilizes the correct positioning of the substrate preceding the acylation process. On the contrary, the S244R mutation in TEM-121 is sufficient to suppress the inhibitory activity of the VHH confirming the crucial function of R244 in the inhibition of TEM-1 measured in presence of cefalotin.

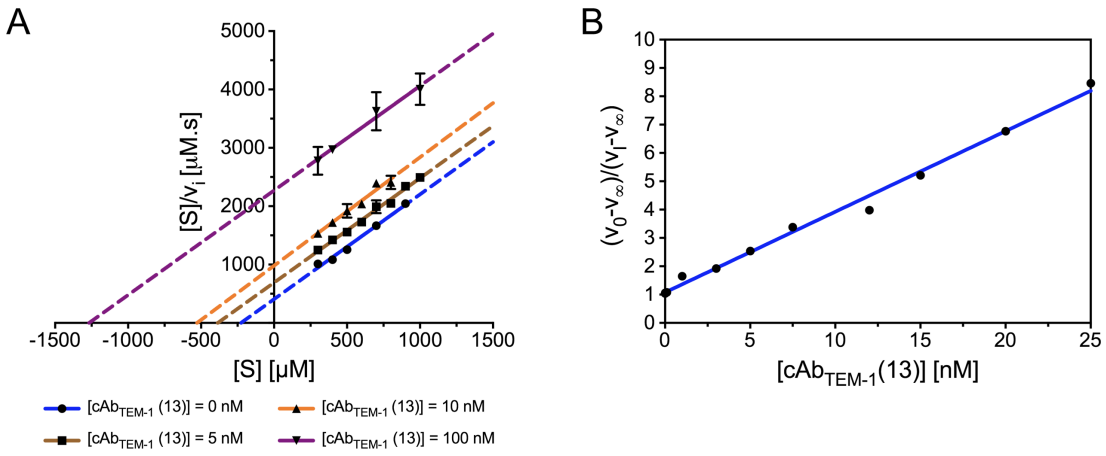

Fig 4.24. *Steady-state kinetic studies of TEM-1 inhibition by the cAb$_{TEM-1}$(13) VHH. (A) Hanes-Woolf linearization of TEM-1 activity (10 nM) for the cefalotin at concentrations of VHH indicated on the graph. (B) Linearization of the initial rates of cefalotin hydrolysis in function of the inhibitor concentration to determine the inhibition constant (K_i) from the equation XI.*

[cAb$_{TEM-1}$(13)] [nM]	K_m^{app} [µM]	k_{cat}^{app} [s^{-1}]
0	224 ± 4	139 ± 4
5	393 ± 9	138 ± 4
10	652 ± 175	138 ± 4
100	1555 ± 407	145 ± 5

Table 4.6. *Steady-state kinetic parameters of TEM-1 in complex with the VHH determined from the Hanes-Woolf linearization. The K_m^{app} corresponds to the intercept with the x-axis while the K_{cat}^{app} was calculated from the slope as described by the equation X. Averages and standard deviations result from two independent experiments.*

4.10.2) Benzylpenicillin and nitrocefin

Interestingly, the activity of the TEM-1 and TEM-121 enzymes against benzylpenicillin was not affected by the mutation at position 244 (**Table 4.7**). The presence of the β-lactam in the active site did not generate any steric hindrance and electrostatic repulsions with the R244 lateral chain and can probably diffuse more easily. The different impacts of the VHH on TEM-1 and TEM-121 may be explained by another mutation and/or by different intrinsic dynamic. We noticed similar results using the nitrocefin as reporter substrate.

PenG	v_0 (μmol min^{-1} mg^{-1}) TEM	v_0 (μmol min^{-1} mg^{-1}) VHH/TEM	Residual activity [%]
TEM-1	3473 ± 520	1016 ± 438	29 ± 8
TEM-1 R244S	1485 ± 162	551 ± 102	37 ± 11
TEM-121	36 ± 7	22 ± 4	60 ± 0.3
TEM-121 S244R	25 ± 6	15 ± 1	60 ± 11
Nitrocefin	v_0 (μmol min^{-1} mg^{-1}) TEM	v_0 (μmol min^{-1} mg^{-1}) VHH/TEM	Residual activity [%]
TEM-1	1262 ± 557	7 ± 1	1 ± 0.1
TEM-1 R244S	150 ± 17	17 ± 3	11 ± 0.5
TEM-121	133 ± 11	48 ± 7	36 ± 2
TEM-121 S244R	51 ± 1	11 ± 1	22 ± 2

Table 4.7. *Initial rates of benzylpenicillin hydrolysis for 0.5 nM of TEM-1, 1 nM of TEM-1 R244S, 10 nM of TEM-121 and 10 nM of TEM-121 S244R (table part above). Initial rates of nitrocefin hydrolysis for 0.5 nM of TEM-1, 1 nM of TEM-1 R244S, 1 nM of TEM-121 and 2 nM of TEM-121 S244R (table part above).*

Because the K_m values for benzylpenicillin are small, it is difficult to use it as a reporter substrate to determine the type of inhibition. We performed these experiments for TEM-1 and TEM-121 using nitrocefin as reporter substrate. Our data showed that the VHH behaved as a non-competitive inhibitor (**Fig 4.25A&B**). The VHH is not able to directly block the entry of the nitrocefin in the active site but acts more probably on the acyl-enzyme stability and/or on the deacylation efficacy. This was reflected by constant K_m^{app} values for any inhibitor concentrations while the deacylation constant (k_{cat}^{app}) decreased for increasing concentrations in VHH (**Table 4.8**). Moreover, the plots illustrating $1/k_{cat}^{app}$ as function of the inhibitor concentration displayed a linear and a hyperbole trend for TEM-1 and TEM-121, respectively, suggesting a pure and a mixed non-competitive inhibition (**Fig 4.25C&D**). This emphasized that the VHH was able to inhibit completely the activity of TEM-1 for the nitrocefin when the

concentration of inhibitor is significantly higher than the inhibition constant value (K_i), whereas the activity of TEM-121 was simply reduced. Based on the general kinetic scheme (**scheme 4**), the theoretical parameter α was equal to 1 in both cases while the parameter β was estimated to 0 and 0.43 $\pm$ 0.01 for TEM-1 and TEM-121, respectively. Finally, the K_i of the $CAb_{TEM\text{-}1}$ (13) VHH for TEM-1 (**equation XIV**) and TEM-121 (**equation XV**) were equal to 4.7 $\pm$ 2.5 nM and 6.6 $\pm$ 0.9 nM, respectively, which were in agreement with the equilibrium constant of dissociation determined by bio-layer interferometry (**Table 4.1**).

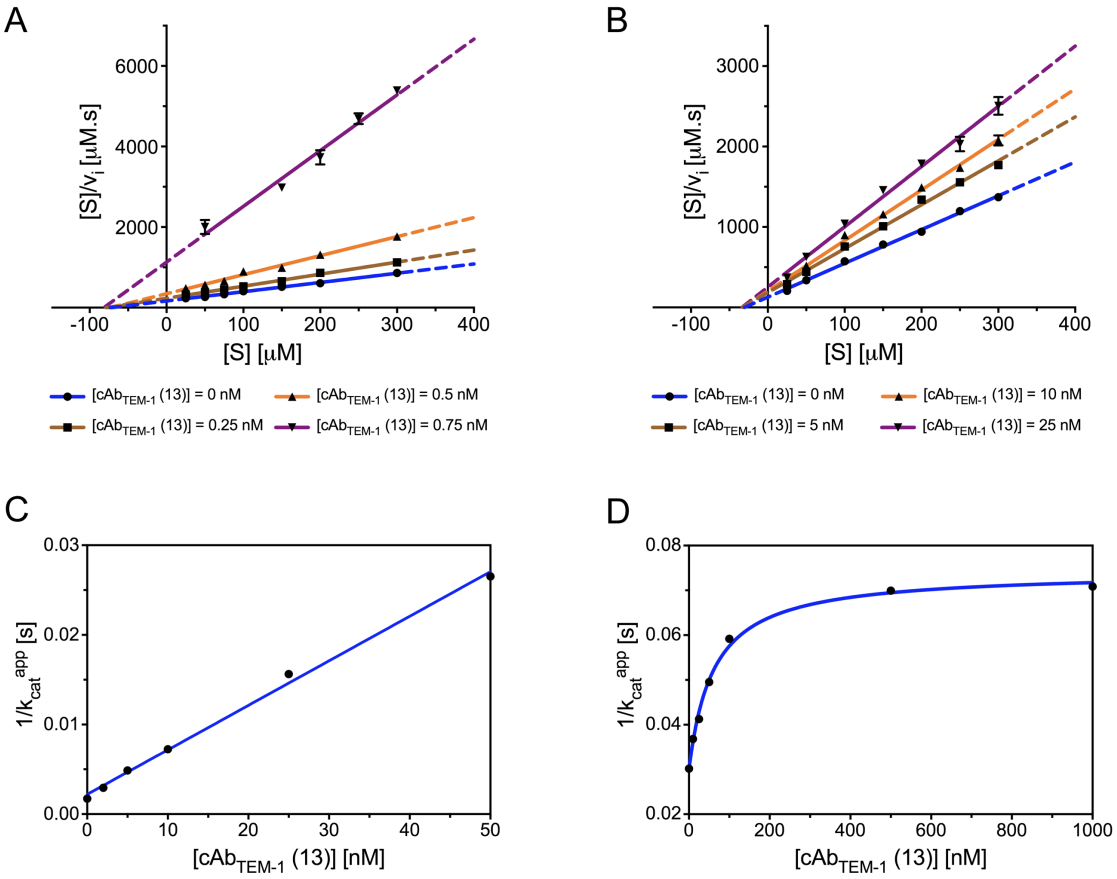

Fig 4.25. *Inhibitory model of TEM-1 and TEM-121 for the nitrocefin by the $cAb_{TEM\text{-}1}$ (13) VHH. Hanes-Woolf linearization of 0.5 nM TEM-1 (A) and 3.7 nM TEM-121 (B) activity for the nitrocefin. Linear and hyperbole trend of $1/K_{cat}^{app}$ in function of the VHH concentration for TEM-1 (C) and TEM-121 (D).*

TEM-1		
[cAb_{TEM-1} (13)] [nM]	K_m^{app} [µM]	k_{cat}^{app} [s^{-1}]
0	73 ± 1	953 ± 19
0.25	76 ± 4	710 ± 49
0.5	75 ± 2	454 ± 24
0.75	80 ± 3	154 ± 2
TEM-121		
[cAb_{TEM-1} (13)] [nM]	K_m^{app} [µM]	k_{cat}^{app} [s^{-1}]
0	26 ± 6	66 ± 8
5	27 ± 9	50 ± 7
10	25 ± 9	44 ± 6
25	27 ± 11	36 ± 6

Table 4.8. *Steady-state kinetic parameters of TEM-1 and TEM-121 in complex with the VHH determined from the Hanes-Woolf linearization. Averages and standard deviations result from two independent experiments.*

4.10.3) Cephaloridin

The hydrolysis of cephaloridin by TEM-1 and the TEM-1 R244S mutant in the presence of the VHH highlighted the crucial role of the R244 in the inhibition. The replacement of the arginine by a serine completely abolished the inhibitory activity of the cAb_{TEM-1} (13) VHH (**Table 4.9**). The cephaloridin is a zwitterion at physiological pH and owns a pyridinium cycle at position C3 which is positively charged (**section 1.3**). The presence of the VHH increased the number of conformations adopted by the lateral chain of the R244. Therefore, the diffusion of the cephaloridin in the active site is impaired by the electrostatic repulsions between the R244 positive charge and the C3 pyridinium moiety of the cephaloridin. A different pattern of inhibition was observed for TEM-121. The mutation R244S was not able to abolish the enzyme's inhibition in the presence of the VHH. In addition, the TEM-121 S244R mutant was at least twice less efficient in the presence of saturating concentrations of VHHs compared to TEM-121. Our data indicate the probable involvement of another mutation present in TEM-121 and not in the TEM-1 R244S mutant.

Cephaloridin	v_0 (μmol min^{-1} mg^{-1}) TEM	v_0 (μmol min^{-1} mg^{-1}) VHH/TEM	Residual activity [%]
TEM-1	568 ± 335	21 ± 1	4 ± 2
TEM-1 R244S	20 ± 5	25 ± 1	125 ± 26
TEM-121	45 ± 8	21 ± 1	48 ± 12
TEM-121 S244R	128 ± 7	24 ± 8	19 ± 7

Table 4.9. *Initial rates of cephaloridin hydrolysis in presence of TEM-1 (2 nM) or TEM-121 (20 nM). The concentration of the cAb_{TEM-1} (13) VHH was equal to 1 μM*

4.11) Conclusions and perspectives

The main objective of this study was to demystify the mechanism behind the cAb_{TEM-1} (13) VHH inhibition of the TEM-1 activity. X-ray structures, molecular dynamic simulations and NMR experiments highlighted two main pathways involved in the reduced activity of TEM-1.

First, the VHH disrupts "the carboxylic pocket" of TEM-1 which is required to stabilize the carboxylic function of the antibiotic during the acylation phase (**Fig 4.26A**). The residues Y52 (CDR2) and S103 (CDR3) are in interaction with D214 of TEM-1. Those interactions disrupt the H-bonds network established between the aspartate and residues K215-V216-A217 on the hinge region. This leads to the reorientation of the side chain of the V216 in the active site and does not allow the stabilization of the carboxylic function of the antibiotic via a water molecule (1). Furthermore, the H-bonds between the residues R99 and W100 (CDR3) of the VHH with the residue D273 located on the α12-helix of TEM-1 displaces the residues L220 and N276 required for the correct orientation of R244 also involved in the "carboxylic pocket" (2).

The VHH is also able to interact with residues P219, L225 and I231 belonging to a hydrophobic node constituted by α11, α12-helices and β3, β4 and β5-strands (**Fig 4.26B**). An allosteric site is present in this hydrophobic node formed by the triad P226-W229-P252. The VHH binding in this area changes the conformation of the P226 which is unable to realize stacking interactions with W229 (3). Via the cooperative coupling of loops dynamic, this may perturb the dynamic of secondary structures located near and far from the binding site as in the α/β domain, but also in crucial loops for the enzyme activity, as the protruding loop and the ω loop. As shown for the inhibitor protein BLIP, the understanding of mechanisms by

which this antibody inhibits TEM-1 activity opens a new way for the development of allosteric inhibitors (**Huang et al, 2020**).

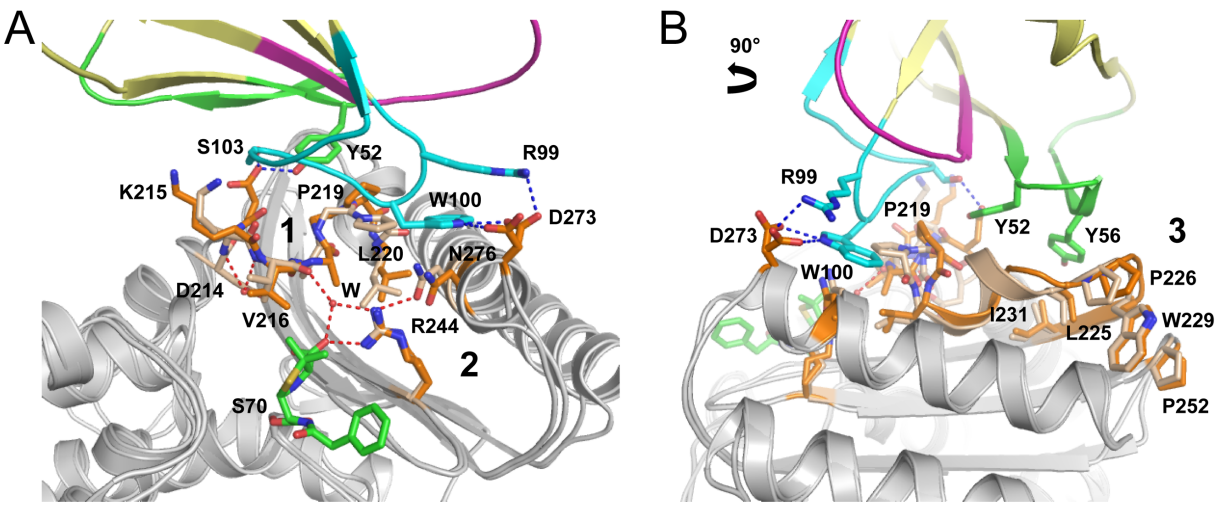

Fig 4.26. *Global impact of the VHH binding on TEM-1 activity. (A) "Carboxylic pocket" allowing the stabilization of the carboxylic function of the antibiotic. (B) Allosteric site corresponded to the triad P226-W229-P252 and belonging to a hydrophobic node formed by both α11, α12-helices and the β3, β4 and β5-strands. The acyl-enzyme correspond to the PenG-TEM-1 model (PDB code 1FQG). Residues in orange and beige belong to the VHH/TEM-1 and PenG/TEM-1, respectively. For more clarity, the rest of the both models are colored in grey (except for the VHH). Dotted red lines illustrate the H-bonds stabilizing the carboxylic function of the antibiotic, whereas the blue ones highlight the H-bonds between the enzyme and the VHH.*

The VHH presents a high specificity since it does not interact with other class A families such as SHV and CTX-M β-lactamases. But, it was able to interact with another TEM family member, TEM-121, presenting 4 ESBL and one IRT mutations. We demonstrated that its inhibition efficiency is lower for TEM-121 than TEM-1 for all tested β-lactam substrates. The R244S mutation clearly impacts the inhibitory activity of the VHH for cefalotin and cephaloridin. But for benzylpenicillin and nitrocefin, this mutation does not impede the enzyme activity resulting in a probable involvement of another mutation present in TEM-121 and/or different dynamic motions which should be verified by NMR relaxation experiments.

5. Development of VHHs as theranostic agents against the class C BLA CMY-2

5.1) Immune VHHs library, biopanning and selection of binders specific to CMY-2

An immune library of 10^{10} transformants with 75 % of clones containing a VHH gene was obtained from the blood of an immunized *V. pacos* (alpacas). We realized three rounds of panning with the immune library to decrease the diversity of the library and to enrich the library in CMY-2 specific binders. We only obtained an enrichment at round 3 with about 30 times more clones for the antigen coated well (positive experiment) compared to the negative assay (**Fig 5.1**).

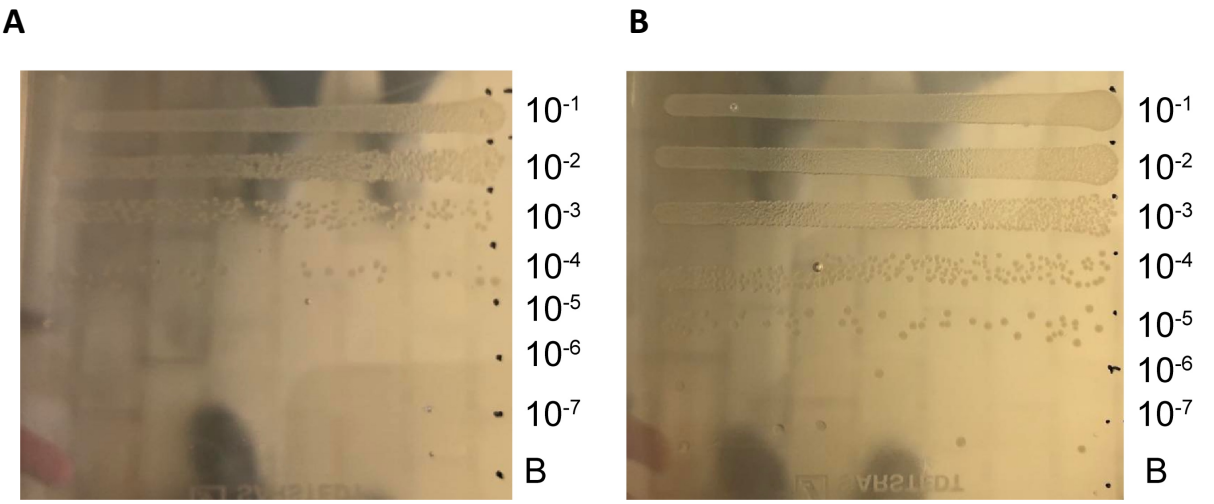

Fig 5.1. *LB Agar plates illustrating the enrichment of the VHHs immune library against CMY-2. (A) TG1 cell transformants with 10 times serial diluted phages that were eluted from the panning without the coating of CMY-2 (negative control). (B) TG1 cell transformants with 10 times serial diluted phages that were eluted from the panning with the coating of CMY-2.*

Ninety clones of each round of panning were isolated and tested for their production of VHHs. They were screened by indirect ELISA to detect the presence of binders. Only eight clones, all coming from the round 3 of panning, gave a signal 1.5 times greater in the well containing CMY-2 than the non-coated well (**Fig 5.2**).

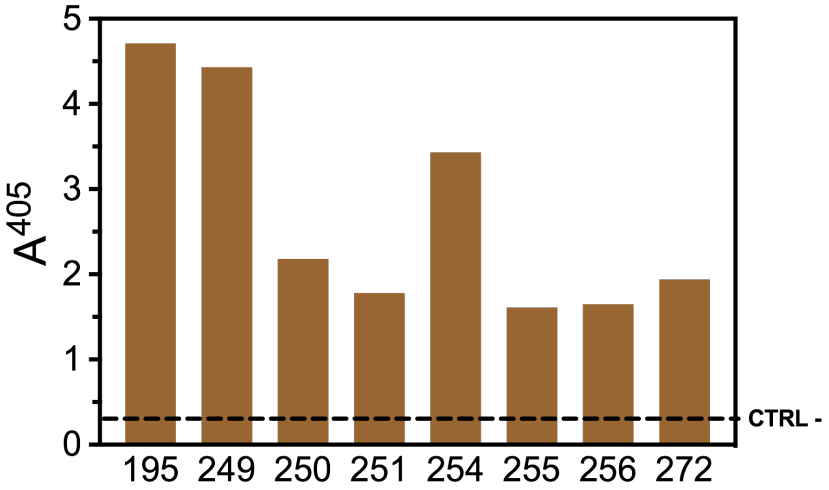

Fig 5.2. *Screening of VHHs for CMY-2 by an indirect ELISA assay. This graph illustrates only the eight clones giving a positive signal. The negative control corresponds to signal for the ELISA without VHHs.*

The clones were sequenced. Our results indicated three genetically different VHHs based on the sequence of their CDRs. The cAb_{CMY-2} (250) and cAb_{CMY-2} (272) VHHs present a deletion of 4 AA in the CDR3 and 1 AA in the CDR2 compared to the cAb_{CMY-2} (254) VHH. Moreover, the cAb_{CMY-2} (272) VHH presents a 2 AA deletion in the FR3 compared to other VHHs. We also noticed punctual mutations in the three CDRs and in both FR2 and FR3 (**Fig 5.3**).

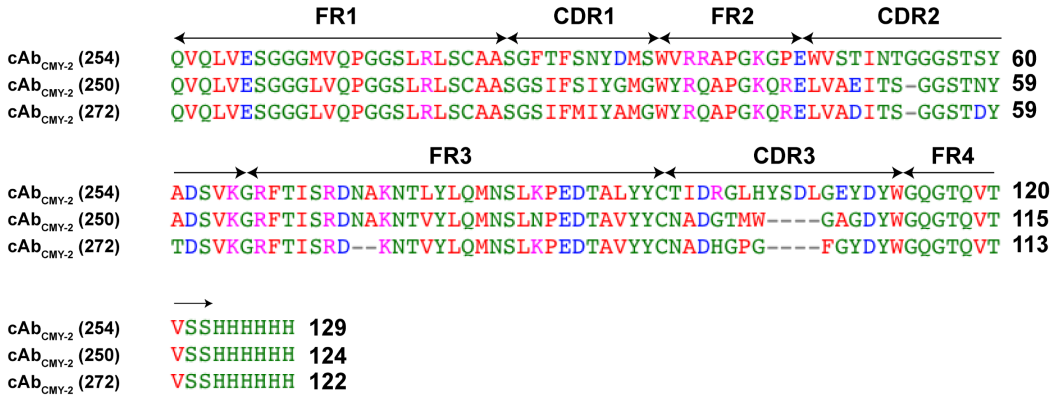

Fig 5.3. *Multiple sequence alignment of VHHs selected by phage display performed with CLUSTALW program. Polar residues are colored in green, hydrophobic residues in red, negatively charged residues in blue and finally, positively charged residues in magenta. Frameworks (conserved regions, FRs) and Complementary-Determining Region (CDRs) of the VHHs are indicated by double arrows on the alignment.*

5.2) Binding characterization of cAb_{CMY-2} (250), cAb_{CMY-2} (254) and cAb_{CMY-2} (272) VHHs for CMY-2

5.2.1) Specificity of the cAb_{CMY-2} (250), cAb_{CMY-2} (254) and cAb_{CMY-2} (272) VHHs

Qualitative binding measurements by bio-layer interferometry were performed to determine the specificity of cAb_{CMY-2} (250), cAb_{CMY-2} (254) and cAb_{CMY-2} (272) VHHs for CMY-2 via Anti-His sensors. We assessed their abilities to interact with different representatives of all molecular classes of β-lactamases: TEM-1 (class A), VIM-4 (class B), CMY-1, CMY-2 (two sub-groups of CMY family), P99 belonging to *Enterobacter cloacae* for the class C and finally, the carbapenemase OXA-48 for the class D. Interestingly, cAb_{CMY-2} (254) and cAb_{CMY-2} (272) recognized specifically CMY-2 (**Fig 5.4B&C**), while cAb_{CMY-2} (250) was also able to bind to P99 highlighting a cross reaction and, in consequence, less specificity (**Fig 5.4A**).

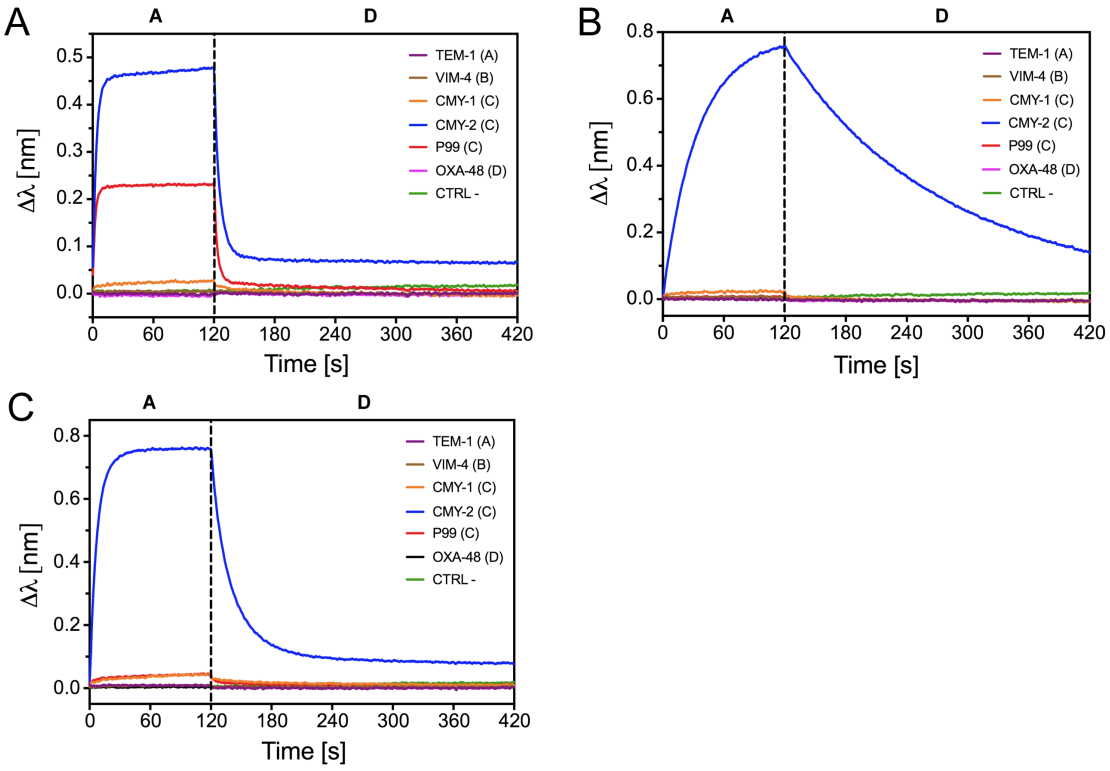

Fig 5.4. *Specificity binding assessment performed by bio-layer interferometry for cAb_{CMY2} (250) (A), cAb_{CMY-2} (254) (B) and cAb_{CMY-2} (272) (C) VHHs. Names and classes of the β-lactamases are indicated in brackets. The CTRL - corresponds to the assay performed without VHH.*

5.2.2) Kinetic (k_{on}, k_{off}) and equilibrium (K_D) constants

Quantitative binding measurements were performed by bio-layer interferometry to determine the kinetic constants of association (k_{on}) and dissociation (k_{off}), and the equilibrium constant (K_D) following the same experimental set-up as the specificity assessment (**Fig 5.5**).

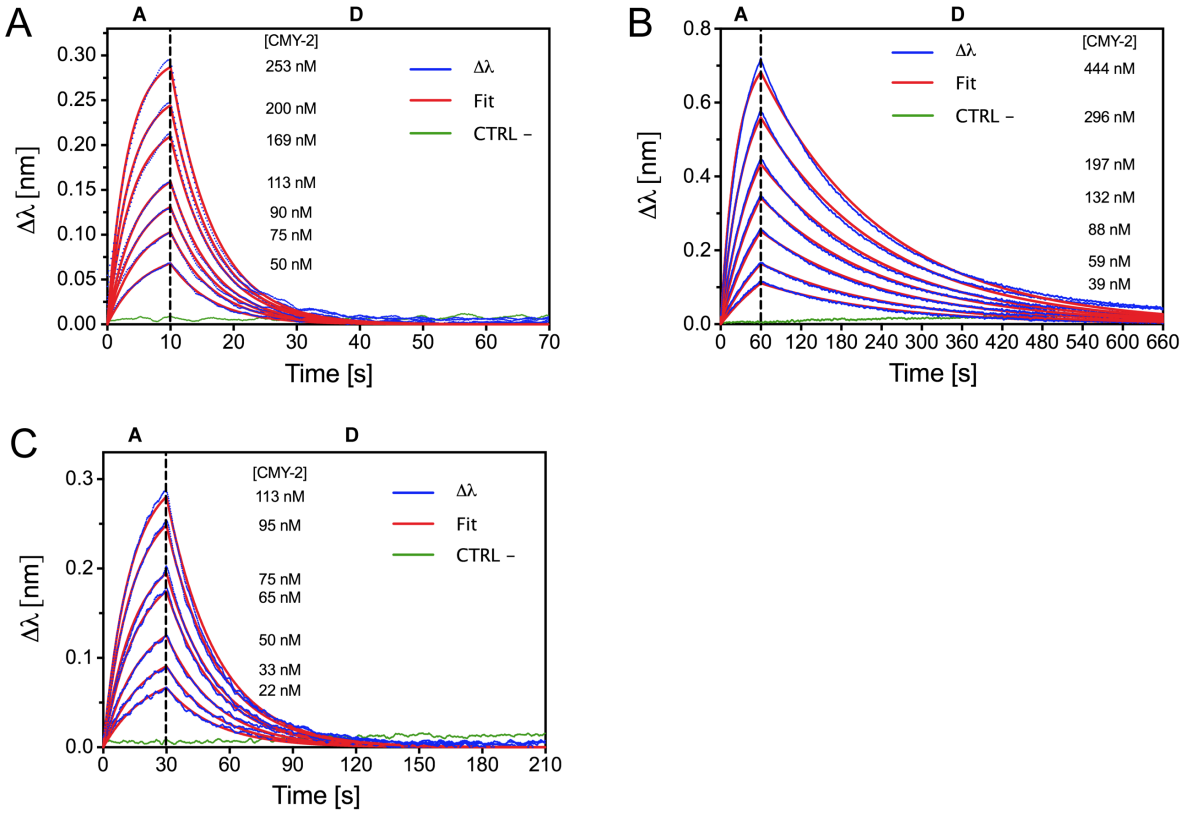

Fig 5.5. *Quantitative binding measurements of cAb_{CMY-2} (250) (A), cAb_{CMY-2} (254) (B) and cAb_{CMY-2} (272) (C) performed by bio-layer interferometry. The experimental data (Δλ, blue) recorded with seven different concentrations were fitted using a 1:1 binding model (red). The CTRL - was measured without VHH loading.*

Association kinetic constants (k_{on}) of the three VHHs for CMY-2 were comprised between 10^5 and 10^6 M^{-1} s^{-1} highlighting a rapid association of the VHHs for the antigen (**Table 5.1**). In opposition, complexes were quite unstable with dissociation constants (k_{off}) larger than 5.10^{-3} s^{-1} leading to moderate affinities (K_D > 60 nM). Nevertheless, among the three VHHs, the cAb_{CMY-2} (254) presents the best kinetic features essentially due to a dissociation 20 times lower than the two other VHHs (**Fig 5.5B**). This result indicated that the cAb_{CMY-2} (254) VHH forms the most stable complex.

	k_{on} (10^5 M^{-1} s^{-1})	k_{off} (10^{-3} s^{-1})	K_D (nM)
cAb_{CMY-2} (250)	6.6 ± 0.1	140 ± 10	220 ± 10
cAb_{CMY-2} (254)	0.9 ± 0.1	5.9 ± 0.7	66 ± 1
cAb_{CMY-2} (272)	3.7 ± 0.5	36 ± 9	100 ± 40

Table 5.1. *The kinetic (k_{on}, k_{off}) and equilibrium (K_D) constants determined by bio-layer interferometry. Values were obtained with a global fit on seven CMY-2 different concentrations with the equation of a 1:1 binding model. Values in the table above correspond to averages and standard deviations from two independent experiments.*

5.2.3) Competition binding assay by a premix method.

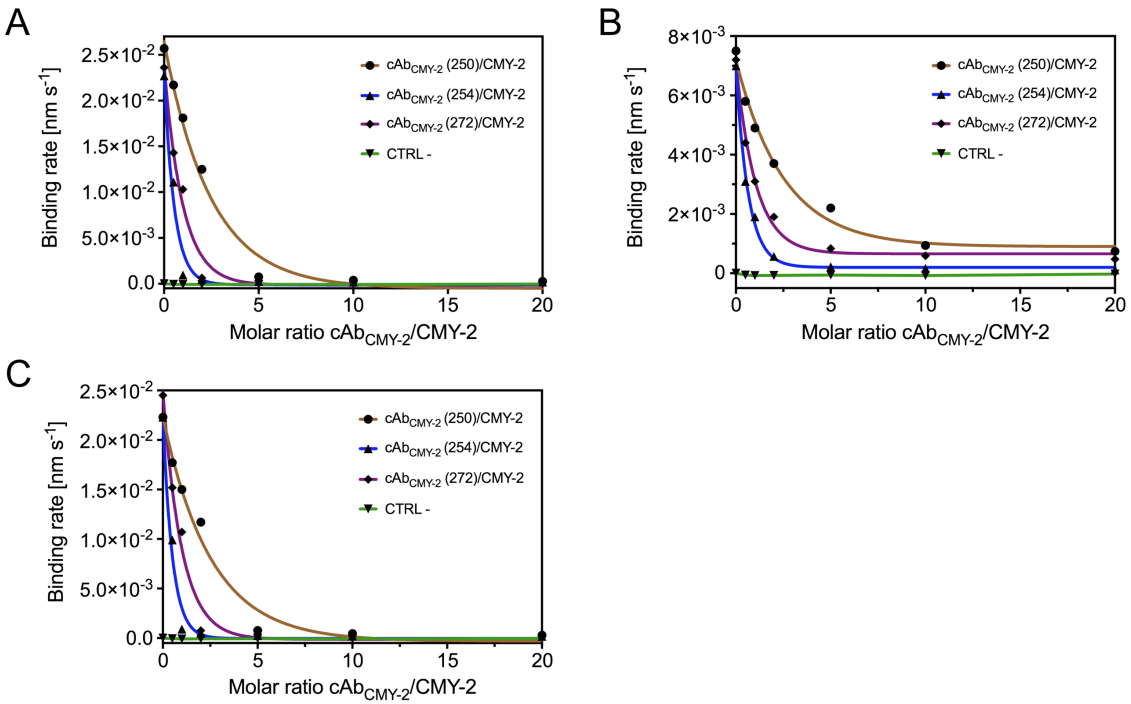

Fig 5.6. *Competition binding assays of VHHs for CMY-2 monitored by bio-layer interferometry. The biotinylated cAb_{CMY-2} (250) (A), cAb_{CMY-2} (254) (B) or cAb_{CMY-2} (C) VHHs were coated on streptavidin sensor (SA sensor) while the associations were measured with analytes corresponding to cAb_{CMY-2} (250)/CMY-2 (brown), cAb_{CMY-2} (254)/CMY-2 (blue), cAb_{CMY-2} (272)/CMY-2 (purple) complexes pre-incubated at 30°C. The binding rates were assessed by fitting the association hyperbole with an exponential mathematic model on the first 120 seconds. The CTRL - were measured by loading the different complexes directly on the SA sensor. This represents a single representation of experiments realized twice.*

We carried out competition binding assays by bio-layer interferometry with a premix method consisting in the loading of a biotinylated VHH on a streptavidine sensor (SA sensor) and to measure its association rate in presence of increasing molar ratios of soluble complexes formed by a second VHH and CMY-2 (**section 3.7.2**). In all cases, we noted a decrease in the binding rates with increasing VHH/CMY-2 molar ratios indicating, at least, a partial epitope overlapping of the three VHHs for CMY-2 (**Fig 5.6**).

The epitope overlapping of the three VHHs does not allow the development of a VHHs-based sandwich assay. Therefore, we decided to develop and characterize a second type of antibodies: polyclonal antibodies.

5.3) Binding properties of rabbit polyclonal antibodies (pAbs) directed against TEM-1 (anti-TEM-1 pAbs) and CMY-2 (anti-CMY-2 pAbs)

We produced and characterized polyclonal antibodies against CMY-2 (anti-CMY-2 pAbs) with the purpose to be used in pair with the cAb_{CMY-2} (254) VHH, the VHH forming the most stable complex with CMY-2. Comparatively, we also developed pAbs against TEM-1 (anti-TEM-1 pAbs) to design a sandwich ELISA with the cAb_{TEM-1} (13) VHH.

5.3.1) Rabbit pAbs titration against TEM-1 and CMY-2

The production of pAbs was achieved by immunizations of rabbits consisting in four injections with the antigen. The first blood sample was recovered around five weeks after the first injection and the sera were tittered by an indirect ELISA. Results indicated an important immune response against TEM-1 (**Fig 5.7A**) and CMY-2 (**Fig 5.7B**).

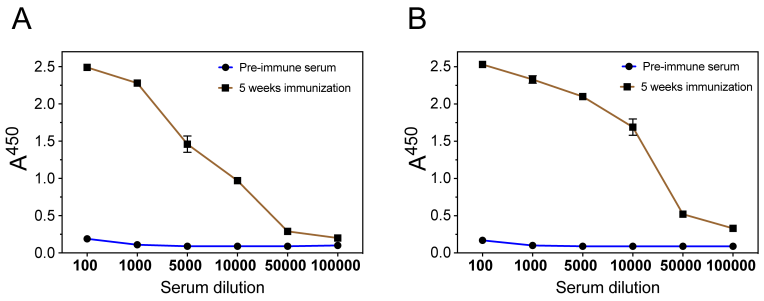

Fig 5.7. *Indirect ELISA assay to detect the presence of pAbs directed against TEM-1 (A) and CMY-2 (B).*

5.3.2) Purification of pAbs by an affinity chromatography

The pAbs were purified by an affinity chromatography using a HiTrap A HP antibody purification column (Cytiva, United-States). This chromatography allows the binding of the antibodies to the protein A on the matrix by the FC (Fragment Crystallizable) region of the antibodies. The elution of the pAbs was realized with a 20 mM glycine buffer at pH 2.0 (acid condition). The chromatogram of the purification illustrates a high absorbance at 280 nm during the loading corresponding to all contaminants not fixed on the protein A and one pic at 26-30 mL of elution buffer (**Fig 5.8A**). The Coomassie-stained SDS-PAGE demonstrated two bands in the elution pic at 25 and 50 kDa corresponding to the light and heavy chains of the pAbs, respectively (**Fig 5.8B**).

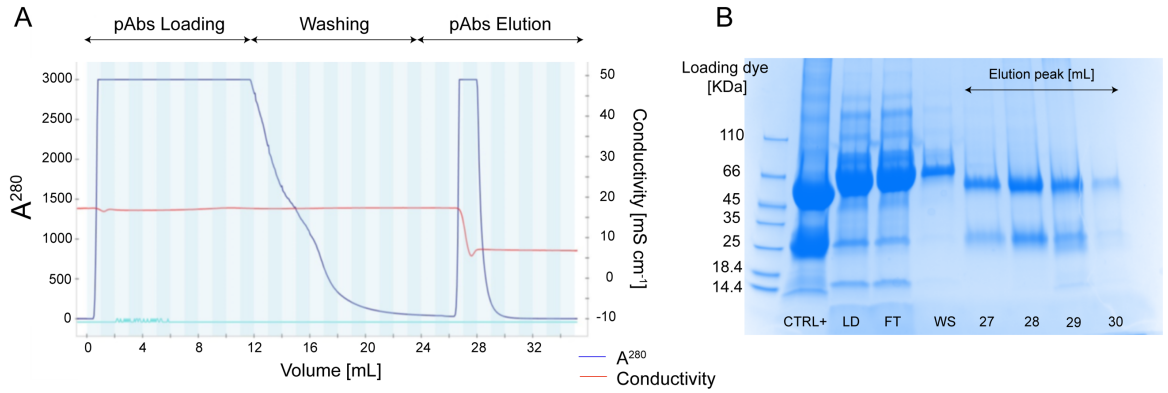

Fig 5.8. *Purification of rabbit anti-TEM-1 pAbs by a HiTrap A HP antibody purification column (Cytiva, United-States). (A) chromatogram of the different steps of purification. (B) Coomassie-stained SDS-PAGE to assess the efficiency of the affinity purification. The CTRL + corresponds to pAbs already purified, LD: loading, FT: flow-through and WS: wash. The same profile was obtained for pAbs directed against CMY-2.*

5.3.3) Binding characterization of anti-TEM-1 and anti-CMY-2 pAbs

Firstly, the specificity of the pAbs was analyzed by an indirect ELISA where a panel of β-lactamases representative of all classes were adsorbed on a 96-well plate. The data clearly indicated that the anti-TEM-1 pAbs (**Fig 5.9A**) and anti-CMY-2 pAbs (**Fig 5.9B**) were unspecific. Indeed, they cross-reacted with other members from the class A β-lactamases such as SHV-104 and BlaP (*Bacillus licheniformis*) and with other members from the class C β-lactamases as CMY-1 and P99 for anti-TEM-1 and anti-CMY-2 pAbs, respectively. A second assay via bio-layer interferometry was also conducted to further investigate the specificity of the pAbs. The biotinylated antigens were loaded on a streptavidin sensor (SA sensor) and immerged in a pAbs solution. These experiments confirmed the lack of specificity of the anti-CMY-2 pAbs since interactions were measured for CMY-2 and P99 (**Fig 5.9D**). By contrast with the indirect ELISA results, the pAbs did not bind to CMY-1. The anti-TEM-1 pAbs seemed to be more specific in this assay since no cross-reaction was observed for CTX-M-1 and only a weak signal for BlaP (**Fig 5.9C**). Finally, the dissociation constants (k_{off}) were evaluated by bio-layer interferometry and correspond to $k_{off} = 1.1 \pm 0.1 \times 10^{-4}\ s^{-1}$ and $k_{off} = 3.6 \pm 0.9 \times 10^{-5}\ s^{-1}$ for TEM-1/anti-TEM-1 pAbs (**Fig 5.9E**) and CMY-2/anti-CMY-2 pAbs (**Fig 5.9F**) complexes, respectively. These slow dissociation constants reflect a multi-avidity behavior commonly observed for the polyclonal antibodies (**Lipman et al, 2005**).

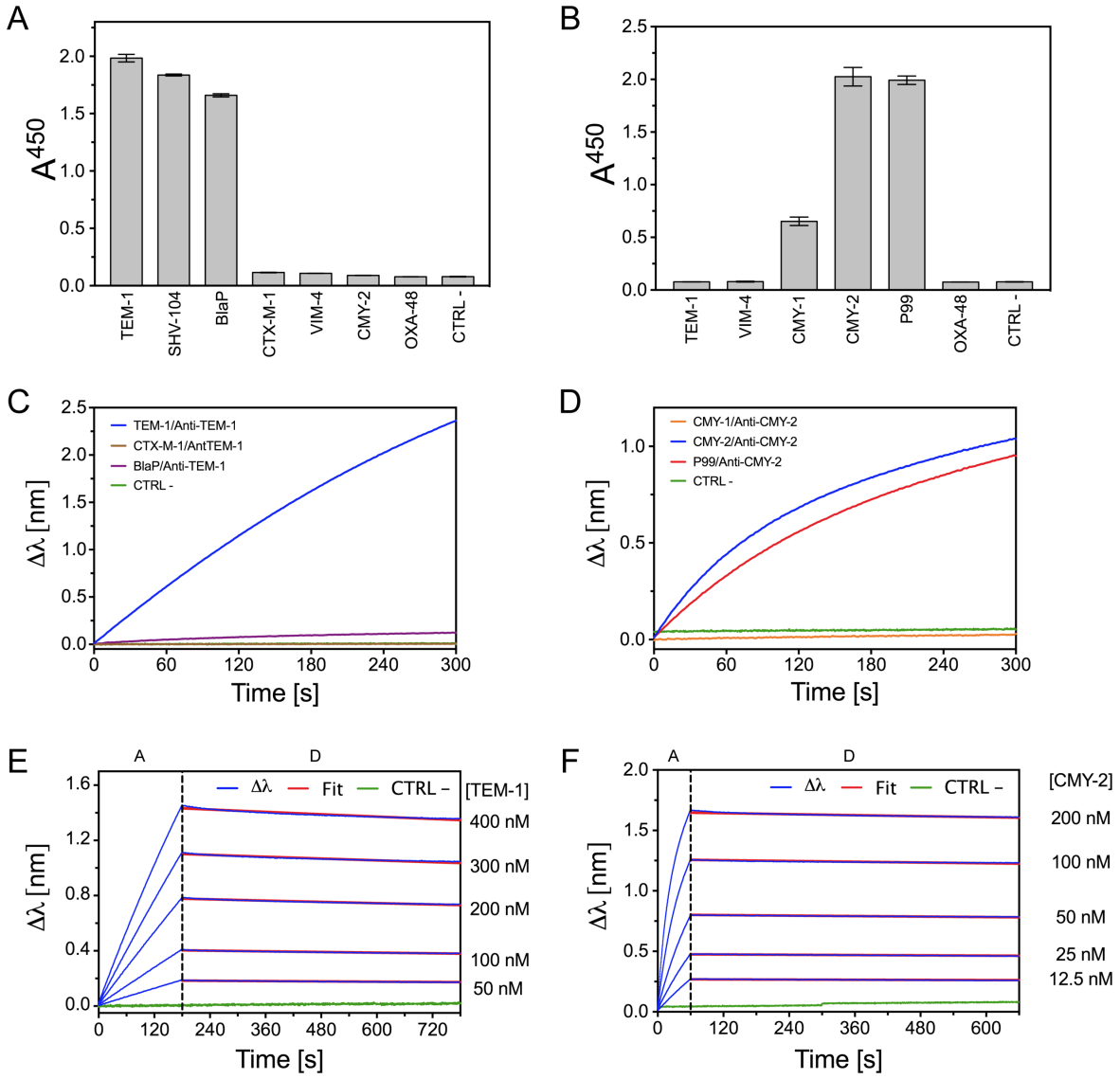

Fig 5.9. *Binding properties of rabbit polyclonal antibodies. (A-B) Indirect ELISAs where antigens were adsorbed on a maxisorp plate (except for the CTRL -) to investigate the specificity of the anti-TEM-1 pAbs (A) and the anti-CMY-2 pAbs (B). Values correspond to averages and standard deviations from at least twice experiments realized independently. (C-D) Qualitative binding specificity assays monitored with SA biosensors of anti-TEM-1 pAbs (C) and anti-CMY-2 pAbs (D) for their respective antigen. (E-F) Quantitative binding assays performed with SA biosensors to assess avidity of polyclonal antibodies directed against TEM-1 (E) and CMY-2 (F). The experimental data (Δλ, blue) recorded with five different concentrations were fitted using a 1:1 binding model only on the dissociation phase. The negative control (green) corresponds to pAbs directly loaded on the biosensor. CAP: capture, REV: revelation*

5.4) Sandwich ELISA for the detection of the β-lactamases TEM-1 and CMY-2

5.4.1) Limit of detection (LOD) and specificity of TEM-1 detection

The first step of the ELISA development consisted in defining the limit of detection (LOD) for a sandwich ELISA using the cAb_{TEM-1} (13) VHH as capture antibody and the anti-TEM-1 pAbs as detection antibodies (**Fig 5.10A**). The LOD was calculated from the average of the CTRL – (without antigen) plus three times the standard deviation and corresponded to 0.2 ng mL^{-1}. It means that our assay was able to detect 20 pg of TEM-1. Moreover, the specificity of the sandwich ELISA was also evaluated on purified enzymes (**Fig 5.10B**). The VHH is able to abolish the possible lack of specificity of the anti-TEM-1 pAbs since no cross-reaction was observed for other class A β-lactamases. However, this configuration allows the detection of different members of the TEM family including the IRTs and ESBLs.

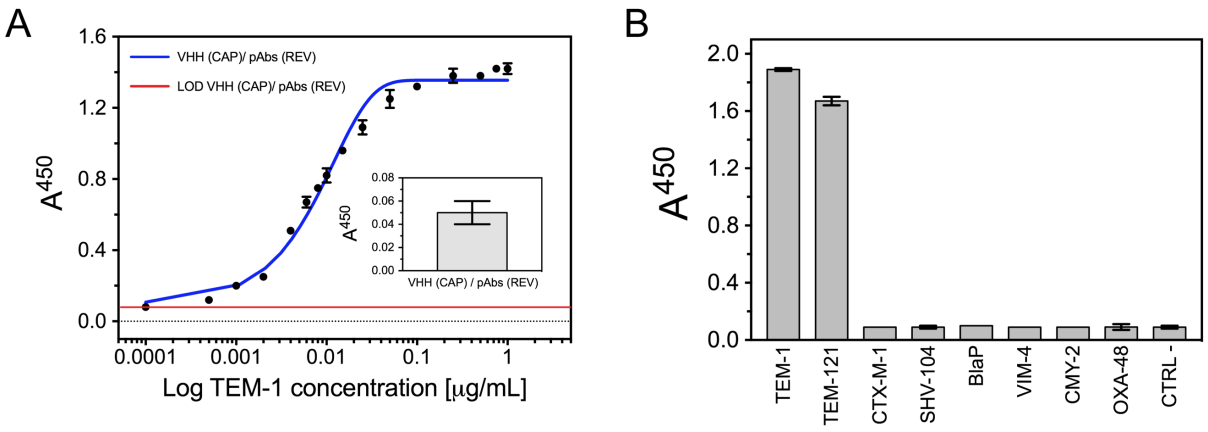

Fig 5.10. *Sandwich ELISA on purified enzymes for TEM-1 detection. (A) Limit of detection (LOD) where the cAb_{TEM-1} (13) VHH was used as antibody for the capture of the antigen and the anti-TEM-1 pAbs for the revelation of the system. The curve was fitted with the equation V. The inset includes the A^{450} for the negative control corresponding to the assay without antigen (CTRL -). The LOD (red line) was calculated from the average of the CTRL – plus three times the standard deviation. (B) Specificity assessment following the same experimental scheme than for the LOD. Averages and standard deviations of the both experiments resulted from at least twice measurements.*

5.4.2) Screening of bacterial isolates for TEM-1 detection

Based on previous results using purified enzymes, we designed the same sandwich ELISA to detect the presence of TEM-1 in bovine and human bacterial isolates (**Table 5.2**). Foremost, the ELISA permitted to detect a large number of TEM members with different activity spectra. Indeed, we detected TEM-1 but also the TEM_{IRT} (TEM-30 and TEM-78) and TEM_{ESBL} such as TEM-24 and TEM-52. Interestingly, no cross-reactions were measured for other class A β-lactamases such as SHV and CTX-M families, but also PER-7 and LEN β-lactamases. Moreover, our assay presented a high sensitivity since all the 56 bacterial isolates presenting a gene coding for a β-lactamase TEM were detected by the ELISA. We finally demonstrated our assay could be used for a large panel of *Enterobacterales* increasing the ability to use this kind of assay for a routinely application.

Table 5.2. *Detection of TEM β-lactamases in bovine and human bacterial.*

Bacterial isolates[a]	Species	Detected *bla* genes[b,c]	A^{450} VHH capture pAbs revelation
RUBLA0127	*E. coli*	**TEM-1** + DHA	0.92 ± 0.07
RUBLA0188	*E. coli*	**TEM-1**	1.89 ± 0.02
RUBLA0328	*E. coli*	**TEM-30** + MutAmpC (3)	1.89 ± 0.11
RUBLA0396	*E. coli*	**TEM-1** + MutAmpC (3) + OXA-1	0.19 ± 0.03
RUBLA0463	*E. coli*	**TEM-1** + MutAmpC (3) + OXA-1	1.91 ± 0.05
RUBLA0482	*E. coli*	**TEM-1** + MutAmpC (3) + OXA-1	1.95 ± 0.06
RUBLA0512	*E. coli*	**TEM-1** + OXA-1	1.12 ± 0.10
RUBLA0549	*E. coli*	**TEM-1** + MutAmpC (2)	1.82 ± 0.07
RUBLA0565	*E. coli*	**TEM-1** + MutAmpC (3) + OXA-1	1.60 ± 0.08
RUBLA0625	*E. coli*	**TEM-1** + MutAmpC (3) + OXA-1	1.34 ± 0.05
RUBLA0671	*E. coli*	**TEM-1** + CTX-M-1 + OXA-1	1.46 ± 0.03
RUBLA0730	*E. coli*	**TEM-1**	1.14 ± 0.03
RUBLA0765	*E. coli*	**TEM-78** + CTX-M-2 + MutAmpC (2)	1.63 ± 0.05
RUBLA0884	*E. coli*	**TEM-1** + CMY-2	1.08 ± 0.05
RUBLA0945	*E. coli*	**TEM-1** + CMY-2	1.14 ± 0.04
RUBLA0949	*E. coli*	**TEM-1** + MutAmpC (3)	1.65 ± 0.06
RUBLA0963	*E. coli*	**TEM-1**	1.53 ± 0.09
RUBLA1008	*E. coli*	**TEM-1** + CTX-M-1 + MutAmpC (2)	1.43 ± 0.12
RUBLA1013	*E. coli*	**TEM-1** + CMY-2	0.95 ± 0.06
RUBLA1151	*E. coli*	**TEM-1** + CTX-M-1	1.16 ± 0.03
RUBLA1170	*E. coli*	**TEM-1** + OXA-1	1.58 ± 0.10
RUBLA1212	*E. coli*	**TEM-1** + CTX-M-14 + MutAmpC (2)	1.48 ± 0.05
RUBLA1241	*E. coli*	**TEM-35** + CTX-M-1 (1)	1.89 ± 0.01
RUBLA1411	*E. coli*	**TEM-1** + CTX-M-156 + OXA-1	1.34 ± 0.04
RUBLA1442	*E. coli*	**TEM-1**	0.87 ± 0.04
RUBLA1448	*E. coli*	**TEM-1**	0.90 ± 0.06
RUBLA0045	*E. coli*	MutAmpC (3) + OXA-1	0.00 ± 0.00
RUBLA0195	*E. coli*	CTX-M-2	0.00 ± 0.00
RUBLA0229	*E. coli*	CTX-M-2	0.02 ± 0.00

RUBLA0315	*E. coli*	MutAmpC (3)	0.03 ± 0.01
RUBLA0319	*E. coli*	MutAmpC (3)	0.01 ± 0.01
RUBLA0677	*E. coli*	OXA-1	0.02 ± 0.01
RUBLA0686	*E. coli*	CTX-M-32	0.02 ± 0.00
RUBLA0791	*E. coli*	MutAmpC (3)	0.04 ± 0.01
RUBLA0825	*E. coli*	MutAmpC (3)	0.04 ± 0.01
RUBLA0944	*E. coli*	OXA-1 + MutAmpC (2)	0.01 ± 0.00
RUBLA0967	*E. coli*	MutAmpC (3)	0.00 ± 0.01
RUBLA0982	*E. coli*	MutAmpC (3)	0.03 ± 0.01
RUBLA1048	*E. coli*	MutAmpC (3)	0.04 ± 0.00
RUBLA1143	*E. coli*	MutAmpC (3)	0.04 ± 0.03
RUBLA1274	*E. coli*	MutAmpC (3)	0.06 ± 0.00
RUBLA1354	*E. coli*	OXA-1	0.02 ± 0.01
RUBLA1365	*E. coli*	MutAmpC (3)	0.05 ± 0.00
RUBLA1358	*E. coli*	CMY-2	0.04 ± 0.01
RUBLA1390	*E. coli*	CTX-M-1	0.02 ± 0.01
RUBLA1401	*E. coli*	OXA-1 + MutAmpC (3)	0.01 ± 0.02
A^{450} positive cut-off[d]	*E. coli* DH5α	X	**0.07**
PEP-010	*E. aerogenes*	**TEM-24**	2.37 ± 0.04
COL20140042	*E. aerogenes*	**TEM-24**	2.02 ± 0.06
COL20140125	*E. aerogenes*	**TEM-121**	1.61 ± 0.06
COL20140080	*E. cloacae*	**TEM-1** + CTX-M-15 + OXA-1 + OXA-1-like	2.25 ± 0.07
PEP-008	*E. asburiae*	**TEM-1** + SHV-12 + ACT	0.70 ± 0.03
COL20140047	*E. coli*	**TEM-52**	2.30 ± 0.07
PEP-007	*E. coli*	**TEM-1** + SHV-12 + DHA-7	1.24 ± 0.07
PEP-060	*E. coli*	**TEM-1** + CTX-M-2	1.72 ± 0.01
CP40	*E. coli*	**TEM-1** + CMY-2 + OXA-1 + OXA-1-like	1.11 ± 0.07
CP42	*E. coli*	**TEM-1** + CMY-2	1.21 ± 0.00
COL20140090	*E. coli*	**TEM-1** + CTX-M-15 + OXA-1 + OXA-1-like	0.42 ± 0.05
COL20140113	*E. coli*	**TEM-1** + CTX-M-15 + OXA-1 + OXA-1-like	2.12 ± 0.05
PEP-041	*K. pneumoniae*	**TEM-1/10** + SHV-11 + ACT-1 + OXA-2	2.05 ± 0.06
PEP-194	*K. pneumoniae*	**TEM-1/52** + SHV-1 + CMY-10 + OXA-4	2.34 ± 0.04
PEP-108	*K. pneumoniae*	**TEM-1** + CTX-M-15 + SHV-28 + OXA-1	0.64 ± 0.01
COL20140054	*K. pneumoniae*	**TEM-1** + CTX-M-19 + SHV-1	1.98 ± 0.03
COL20140070	*K. pneumoniae*	**TEM-1** + CTX-M-15 + SHV-1 + DHA-2 + OXA-1 + OXA-1-like	1.34 ± 0.03
COL20140087	*K. pneumoniae*	**TEM-1** + CTX-M-15 + CTX-M-9 + SHV-1 + CMY-2	2.22 ± 0.06
COL20140135	*K. pneumoniae*	**TEM-1** + CTX-M-9 (19) + SHV-1	1.71 ± 0.03
COL20140137	*P. aeruginosa*	**TEM-4**	0.53 ± 0.07
COL20140051	*C. freundii*	**TEM-1/3**	1.88 ± 0.08
COL20140083	*C. freundii*	**TEM-1/3**	2.04 ± 0.03
COL20140084	*C. freundii*	**TEM-1** + CTX-M-15 + CMY-2 + OXA-1/9/10	1.69 ± 0.11
COL20140129	*A. baumannii*	**TEM-1** + PER-7 + OXA-23	0.89 ± 0.08
PEP-001	*P. vulgaris*	**TEM-24**	0.37 ± 0.03
COL20140136	*P. stuartii*	**TEM-24**	1.22 ± 0.02
PEP-058	*E. cloacae*	CTX-M-9 + SHV-12	0.16 ± 0.01
COL20140062	*E. coli*	CTX-M-1	0.15 ± 0.00
COL20140064	*E. coli*	CTX-M-14 + OXA-1 + OXA-1-like	0.16 ± 0.01
COL20140069	*E. coli*	CTX-M-2	0.16 ± 0.00
PEP-013	*K. pneumoniae*	LEN	0.17 ± 0.00
PEP-121	*K. pneumoniae*	SHV-1 + DHA-1 + OXA-1	0.21 ± 0.00
PEP-205	*K. pneumoniae*	SHV-11 + CMY-2	0.15 ± 0.00
PEP-140	*K. pneumoniae*	SHV-11 + OXA-48	0.15 ± 0.01
PEP-177	*K. pneumoniae*	CTX-M-15 + SHV-28 + NDM-1 + OXA-1	0.14 ± 0.00
CNR20120135	*K. pneumoniae*	KPC-2 + SHV-4 like + SHV-1	0.15 ± 0.00
CNR20130483	*K. pneumoniae*	SHV-2 + SHV-1 + VIM	0.14 ± 0.00
COL20140067	*K. oxytoca*	X	0.14 ± 0.01
PEP-095	*P. aeruginosa*	IMP-13	0.12 ± 0.01
PEP-014	*C. koseri*	X	0.12 ± 0.01
A^{450} positive cut-off[d]	*E. coli* DH5α	X	**0.17**

[a]RUBLA isolates (bovine isolates) belong to ARSIA (Association Régionale de Santé et d'Identification Animale), Ciney, Belgium. Col, PEP and CNR isolates (human isolates) belong to the National Reference Center for Antimicrobial Resistance in Gram -, CHU UCL Namur (Mont-Godinne), Belgium. [b]Gene content of RUBLA isolates was determined by Whole Genome Sequencing (WGS) while gene content of Col, PEP and CNR isolates was determined by PCR and amplified fragment sequencing. [c]MutAmpC: chromosomal overexpressed AmpC presenting two or three mutations in the promotor at positions -1 and -18 for MutAmpC (2) and -1, -18 and -42 for MutAmpC (3). [d]The A^{450} positive cut-off values were calculated as an average A^{450} value of the strain E. coli DH5α presenting no bla genes plus three times the standard deviation.

5.4.3) LOD and specificity for CMY-2 detection

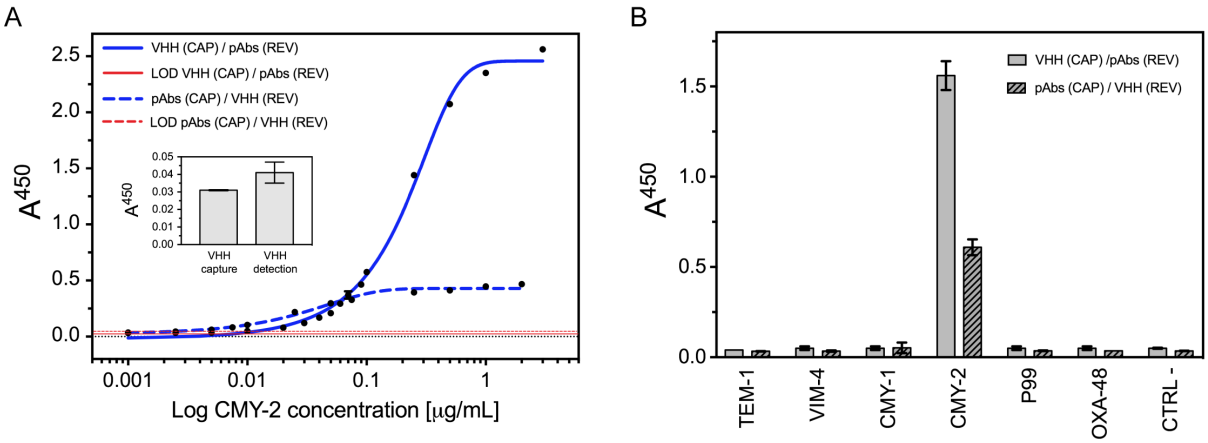

Fig 5.11. *Sandwich ELISA performed with purified CMY-2. (A) Limits of detection (LOD) when the cAb_{CMY-2} (254) VHH was used as capture antibody and the anti-CMY-2 pAbs as revelation antibody (full blue line) or inversely (blue dotted line). Curves were fitted with equation V. The inset indicates the A^{450} for the CTRL -. The LOD was assessed with the A^{450} of the CTRL - plus three times the standard deviation. This is indicated by a full red line for the assay using the VHH as capture antibody and the pAbs for the revelation and a red dotted line for the inverse. (B) Specificity assessment of CMY-2 detection using the cAb_{CMY-2} (254) VHH as capture antibody and the pAbs for the revelation (grey) or inversely (grey, pattern). For both experiments, the CTRL – represents the same assay without antigen (e.g. CMY-2). All averages and standard deviations resulted from at least two experiments.*

We determined the minimal quantity of CMY-2 detectable by an ELISA using the cAb_{CMY-2} (254) VHH and the anti-CMY-2 pAbs as capture and revelation antibodies (full blue line), or inversely (blue dotted line). The LODs were equivalent to 13.3 and 3.9 ng mL^{-1} using the cAb_{CMY-2} (254) VHH as capture and detection antibody, respectively (**Fig 5.11A**). Compared

to the LOD for TEM-1 detection, our assays were characterized by a sensitivity around 15 to 60 times lower for CMY-2 detection probably due to the rapid dissociation rate of the cAb_{CMY-2} (254)/CMY-2 complex. We showed that the use of pAbs as capture antibody and VHH for the revelation did not bring any gain since the responses were lower compared to the initial settings. The specificity of the sandwich ELISA was checked on purified enzymes (**Fig 5.11B**). Both set-ups clearly allow the specific detection of CMY-2 since no signal was measured for other families of β-lactamases.

5.4.4) Production and characterization of the bivalent cAb_{CMY-2} $(254)_{BIV}$ VHH

To improve the sensitivity of the sandwich ELISA, we decided to develop a bivalent VHH based on cAb_{CMY-2} (254) sequence. A bivalent antibody may exhibit a higher apparent affinity or avidity mainly due to a decrease in the dissociation rate. This engineered antibody (cAb_{CMY-2} $(254)_{BIV}$) consisted in the fusion of two cAb_{CMY-2} (254) VHHs repeated in tandem, joined by a peptide linker $(GGGS)_3$ (**Morales-Yanez et al, 2019**). It was produced in the same quantity as the monovalent VHH and was not more sensitive to degradation. As expected, the dissociation rate of the bivalent cAb_{CMY-2} $(254)_{BIV}$ VHH significantly decreased compared to the monovalent VHH (**Fig 5.12**). In fact, the k_{off} value was 15 times lower for the cAb_{CMY-2} $(254)_{BIV}$ VHH (k_{off} = 3.8 ± 0.4 x 10^{-4} s^{-1}) than cAb_{CMY-2} (254) (k_{off} = 6.3 ± 0.5 x 10^{-3} s^{-1}) indicating a more stable antigen/antibody complex.

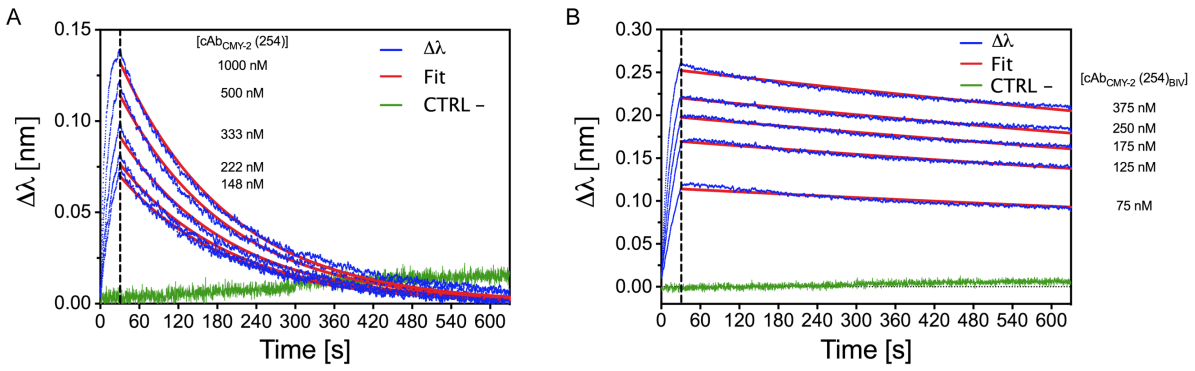

Fig 5.12. *Quantitative binding measurement of the biotinylated cAb_{CMY-2} (254) VHH (A) and bivalent cAb_{CMY-2} $(254)_{BIV}$ VHH (B) for CMY-2 using streptavidin bio-sensors. Experimental data (Δλ) were fitted on at least five CMY-2 concentrations using a 1:1 fitting model (red). The negative control (green) was obtained by loading the VHH directly on the sensor.*

5.4.5) LOD and specificity for CMY-2 detection with the cAb_{CMY-2} $(254)_{BIV}$ VHH

As for the monovalent counterpart, we determined the LODs of the ELISA using the cAb_{CMY-2} $(254)_{BIV}$ as capture antibody and pAbs for the revelation of the system (full blue line) or inversely (blue dotted line) (**Fig 5.13A**). Those sets up provided LODs values around 2.3 and 1.4 ng mL^{-1} for the first and the second configurations, respectively. Therefore, the use of the bivalent VHH clearly improved the detection of CMY-2. Moreover, the bivalent VHH didn't affect the specificity of the assay since only CMY-2 was detected in both ELISAs (**Fig 5.13B**). Indeed, higher sensitivity of the assay combined with its high specificity gave an interest to use the cAb_{CMY-2} $(254)_{BIV}$ for the detection of CMY-2 produced in bacterial isolates.

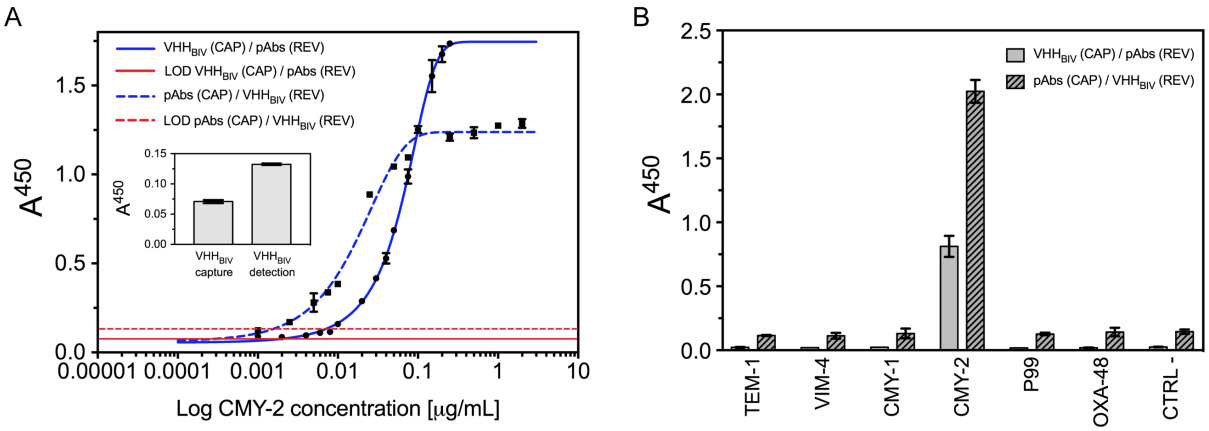

Fig 5.13. *Sandwich ELISA for the sensitivity (LODs) (A) and the specificity (B) of CMY-2 detection by the bivalent* cAb_{CMY-2} $(254)_{BIV}$ *VHH. The LOD was assessed with the* A^{450} *of the CTRL - plus three times the standard deviation. For both assays, the CTRL – represents the same assay without antigen. All averages and standard deviations result from at least twice measurements.*

5.4.6) Detection of CMY-2 in bacterial isolates via the cAb_{CMY-2} $(254)_{BIV}$ VHH

Based on previous results obtained with purified enzymes, we decided to develop three ELISAs for the detection of CMY-2 in bacterial isolates. In these experiments, the monovalent cAb_{CMY-2} (254) was only used as capture antibody and the pAbs for the revelation of the system. On the other hand, the bivalent VHH was used for the capture and the revelation of the system since both configurations improved the sensitivity of the assay (**Table 5.3**). Firstly, the three different ELISA allowed the detection of different variants of the CMY-

2 sub-group (e.g. CMY-16, CMY-60). Moreover, no cross reaction was detected for other class C β-lactamases as CMY-10 (CMY-1-like), DHA, ACT or chromosomal encoded AmpC. Interestingly, the bivalent cAb_{CMY-2} $(254)_{BIV}$ ensured a higher sensitivity of the assay. In fact, only 17 on 22 bacterial isolates presenting one CMY-2 sub-group *bla* gene were detected by the ELISA using cAb_{CMY-2} (254) VHH while 21 isolates had a positive signal with the bivalent VHH. Our data demonstrated the use of the bivalent cAb_{CMY-2} $(254)_{BIV}$ VHH favors the specific detection of CMY-2 with a better sensitivity than the monovalent VHH counterpart. However, a screening on a larger panel of bacterial isolates will be considered to be statistically significant.

Table 5.3. *Detection of CMY-2 in bovine and human bacterial isolates by a sandwich ELISA.*

Bacterial isolates[a]	Species	Detected *bla* genes[b,c]	A^{450}		A^{450}		A^{450}	
			VHH capture	pAbs revelation	VHH_{biv} capture	pAbs revelation	pAbs capture	VHH_{biv} revelation
PEP031	*E. coli*	TEM-1, CTX-M-15, NDM-1, **CMY-58**, OXA-1	**1.28 ± 0.01**		**1.60 ± 0.03**		**1.96 ± 0.03**	
PEP135	*E. coli*	TEM-1, NDM-1, **CMY-16**, OXA-10	**0.94 ± 0.05**		**1.37 ± 0.01**		**1.88 ± 0.06**	
PEP175	*K. pneumoniae*	TEM-1, SHV-1, CTX-M-15,NDM-1**, CMY-2**, DHA, OXA-9	0.06 ± 0.00		**0.12 ± 0.01**		**0.55 ± 0.05**	
PEP224	*E. coli*	TEM, NDM-5, **CMY-2-like**	0.06 ± 0.00		**0.24 ± 0.03**		**0.69 ± 0.04**	
PEP202	*E. coli*	**CMY-60**	**1.10 ± 0.04**		**1.67 ± 0.06**		**1.37 ± 0.02**	
PEP203	*E. coli*	**CMY-61**	**1.42 ± 0.01**		**1.78 ± 0.01**		**2.05 ± 0.00**	
PEP205	*K. pneumoniae*	SHV-11, **CMY-2**	**1.08 ± 0.03**		**1.62 ± 0.01**		**2.03 ± 0.06**	
PEP206	*E. coli*	OXA-1, **CMY-42**	**0.41 ± 0.02**		**1.13 ± 0.05**		**1.87 ± 0.04**	
PEP207	*P. mirabilis*	**CMY-2**	**1.37 ± 0.03**		**1.72 ± 0.00**		**1.89 ± 0.03**	
PEP218	*E. coli*	TEM-39, TEM-84, **CMY-2**	**0.27 ± 0.02**		**0.85 ± 0.01**		**1.58 ± 0.10**	
PEP234	*K. pneumoniae*	TEM, SHV, CTX-M (G1), VIM-19, **CMY-2**	**0.12 ± 0.01**		**0.41 ± 0.00**		**0.97 ± 0.01**	
PEP235	*E. coli*	VIM-19, **CMY-2**	**0.19 ± 0.00**		**0.67 ± 0.01**		**1.81 ± 0.06**	
PEP006	*C. freundii*	TEM-1, **CMY-2-like**	**1.28 ± 0.06**		**1.82 ± 0.03**		**2.01 ± 0.03**	
PEP157	*C. freundii*	TEM-1, CTX-M-9, **CMY-2-like**, OXA-9, OXA-48	0.05 ± 0.00		**0.12 ± 0.00**		**0.67 ± 0.03**	
CP40	*E. coli*	TEM-1, OXA-1 , OXA-1-like, **CMY-2**	0.04 ± 0.00	0.06 ± 0.00	0.08 ± 0.01			
CP42	*E. coli*	TEM-1, **CMY-2**	**0.18 ± 0.01**		**0.43 ± 0.01**		**1.46 ± 0.04**	
Col20140084	*C. freundii*	TEM-1, CTX-M-15, OXA-1/9/10, **CMY-2**	0.04 ± 0.01		**0.08 ± 0.01**		**1.76 ± 0.02**	
Col20140087	*K. pneumoniae*	TEM-1, CTX-M-9/15, SHV-1, **CMY-2**	**0.86 ± 0.11**		**1.39 ± 0.01**		**1.87 ± 0.07**	
RUBLA0884	*E. coli*	TEM-1, **CMY-2**	**0.45 ± 0.03**		**1.19 ± 0.00**		**1.76 ± 0.04**	
RUBLA0945	*E. coli*	TEM-1, **CMY-2**	**0.25 ± 0.02**		**0.87 ± 0.05**		**1.58 ± 0.17**	
RUBLA1013	*E. coli*	TEM-1, **CMY-2**	**0.11 ± 0.01**		**0.28 ± 0.01**		**1.02 ± 0.11**	
RUBLA1358	*E. coli*	**CMY-2**	**0.20 ± 0.01**		**0.40 ± 0.01**		**1.32 ± 0.06**	
PEP121	*K. pneumoniae*	SHV-1, OXA-1, DHA-1	0.05 ± 0.00	0.06 ± 0.00	0.09 ± 0.00			
PEP194	*K. pneumoniae*	TEM-1/52, SHV-1, OXA-4, CMY-10	0.05 ± 0.00	0.06 ± 0.01	0.08 ± 0.00			
PEP041	*K. pneumoniae*	TEM-1/10, SHV-11, OXA-2, ACT-1	0.05 ± 0.00	0.06 ± 0.00	0.07 ± 0.00			
PEP007	*E. coli*	TEM-1, SHV-12, DHA-7	0.04 ± 0.00	0.05 ± 0.00	0.07 ± 0.01			
Col20140070	*K. pneumoniae*	TEM-1, CTX-M-15, SHV-1, OXA-1, OXA-1-like, DHA-2	0.04 ± 0.00	0.05 ± 0.00	0.08 ± 0.00			
RUBLA0127	*E. coli*	TEM-1, DHA	0.05 ± 0.00	0.05 ± 0.00	0.09 ± 0.00			
RUBLA0045	*E. coli*	MutAmpC (3), OXA-1	0.08 ± 0.01	0.05 ± 0.00	0.07 ± 0.00			
RUBLA0315	*E. coli*	MutAmpC (3)	0.06 ± 0.01	0.05 ± 0.00	0.07 ± 0.00			
RUBLA1048	*E. coli*	MutAmpC (3)	0.08 ± 0.01	0.05 ± 0.00	0.08 ± 0.00			
PEP032	*M. morganii*	TEM-1, CTX-M-15, NDM-1, DHA, OXA-1	0.04 ± 0.00	0.07 ± 0.01	0.08 ± 0.00			

PEP033	*E. cloacae*	TEM-1, SHV-12, CTX-M-15, NDM-1, MIR, OXA-1	0.05 ± 0.00	0.08 ± 0.00	0.09 ± 0.00
PEP122	*M. morganii*	TEM-1, CTX-M-15, NDM-1, DHA-1, OXA-1	0.06 ± 0.00	0.07 ± 0.00	0.09 ± 0.00
PEP042	*E. coli*	TEM-1, CTX-M-9, CMY-10, OXA-4, OXA-224	0.06 ± 0.01	0.07 ± 0.01	0.08 ± 0.00
PEP176	*A. Baumannii*	NDM-1	0.05 ± 0.00	0.06 ± 0.00	0.08 ± 0.00
PEP239	*K. pneumoniae*	SHV-28, NDM-1, OXA-1	0.04 ± 0.00	0.07 ± 0.00	0.07 ± 0.00
PEP177	*K. pneumoniae*	SHV-28, CTX-M-15, NDM-1, OXA-30	0.05 ± 0.00	0.08 ± 0.00	0.08 ± 0.01
Col20140047	*E. coli*	TEM-52	0.05 ± 0.00	0.05 ± 0.00	0.08 ± 0.00
Col20140090	*E. coli*	TEM-1, CTX-M-15, OXA-1, OXA-1-like	0.05 ± 0.00	0.06 ± 0.00	0.09 ± 0.00
A^{450} positive cut-off[d]			**0.08**	**0.08**	**0.09**

[a]RUBLA isolates (bovine isolates) belong to ARSIA (Association Régionale de Santé et d'Identification Animale), Ciney, Belgium. Col, PEP and CNR isolates (human isolates) belong to the National Reference Center for Antimicrobial Resistance in Gram -, CHU UCL Namur (Mont-Godinne), Belgium. [b]Gene content of RUBLA isolates was determined by Whole Genome Sequencing (WGS) while gene content of Col, PEP and CNR isolates was determined by PCR and fragment sequencing. [c]MutAmpC: chromosomal overexpressed AmpC presenting three mutations in the promotor at positions -1, -18 and -42 for MutAmpC (3). [d]The A^{450} positive cut-off values were calculated as an average A^{450} value of the strain E. coli DH5α presenting no bla genes plus three times the standard deviation (Highlighted in red in the table).

5.5) Effects of the VHHs on the enzymatic activity of CMY-2

5.5.1) Residual activity of CMY-2 in presence of VHHs

The CMY-2 activity in complex with cAb_{CMY-2} (254) was studied for 4 β-lactam substrates (**Fig 5.14A**). They were chosen on the nature of the side chain in position C2 for the penicillin and C3 for the cephalosporins in order to evaluate the potential link between the size, the charge brought by the side chain of the antibiotics and the VHH inhibitor properties. Interestingly, the results highlighted a residual activity of CMY-2 in complex with the cAb_{CMY-2} (254) VHH at around 15-20 % compared to the free enzyme for all cephalosporins. Moreover, the residual activity of CMY-2 for the ampicillin remained equal to 40 % even at saturating concentration of the nanobody. Those data may underlie a different mechanism of inhibition than the cephalosporins. Finally, we also studied the residual activity of CMY-2 for the nitrocefin in complex with the cAb_{CMY-2} (250) and cAb_{CMY-2} (272) VHHs (**Fig 5.14B**). Results indicated a similar inhibition profile than the cAb_{CMY-2} (254) VHH and support the hypothesis that the three VHHs bind to an overlapping epitope.

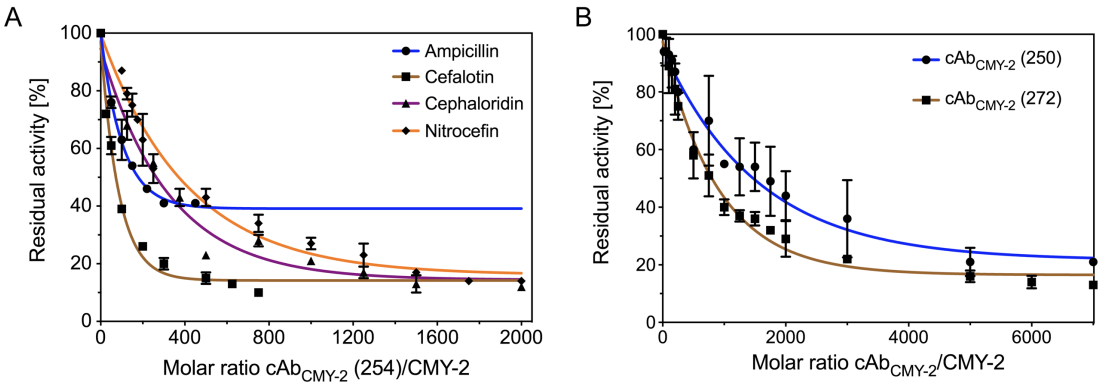

Fig 5.14. *Residual activity of CMY-2 in complex with the cAb$_{CMY-2}$ (254) VHH for four β-lactam ring substrates (A). Ampicillin, cefalotin and cephaloridin were used at a concentration of 100 µM and nitrocefin at 40 µM. The concentration of CMY-2 for each substrate described above were 5 nM, 1 nM, 0.2 nM and 0.5 nM, respectively. (B) Residual activity of CMY-2 in complex with the cAb$_{CMY-2}$ (250) (blue line) and cAb$_{CMY-2}$ (272) (brown line) VHHs. Nitrocefin was used at 40 µM and CMY-2 at 0.5 nM. Data resulted from twice experiments and were fitted with a one phase exponential decay equation from graph prism program.*

5.5.2) Inhibitory model of CMY-2 activity for the nitrocefin by cAb$_{CMY-2}$ (254)

We characterized the mechanism of inhibition of CMY-2 activity for the nitrocefin by the cAb$_{CMY-2}$ (254) VHH. Complete hydrolysis of 40 µM nitrocefin by 0.5 nM of CMY-2 in complex with the VHH was performed and the linearization of curves by the equation IX allowed to obtain the different steady-state kinetic parameters. The K_m^{app} values of CMY-2 were not affected by the presence of the VHH suggesting cAb$_{CMY-2}$ (254) does not prevent the entry of the substrate in the active site. On the contrary, the deacylation constant k_{cat}^{app} decreased in presence of increasing concentrations of VHH (**Fig 5.15A**). This highlighted a non-competitive inhibition of CMY-2 activity for the nitrocefin where the VHH is more probably able to impact the stability of the acyl-enzyme and/or to influence the dynamic of the enzyme. Moreover, the plot illustrating $1/k_{cat}^{app}$ in function of an increasing concentration of the cAb$_{CMY-2}$ (254) VHH displayed a linear trend indicating a pure non-competitive inhibition (**Fig 5.15B**). Based on the classical kinetic schema (scheme IV), it means that the complex ESI is completely inactive when the concentration of inhibitor is largely superior to the inhibition constant value (K_i). Based on this model, the theoretical parameters α and β equal to 1 and 0, respectively. The K_i value of the VHH for CMY-2 was very similar to the equilibrium constant (K_D) determined by bio-layer interferometry (**Table 5.4**).

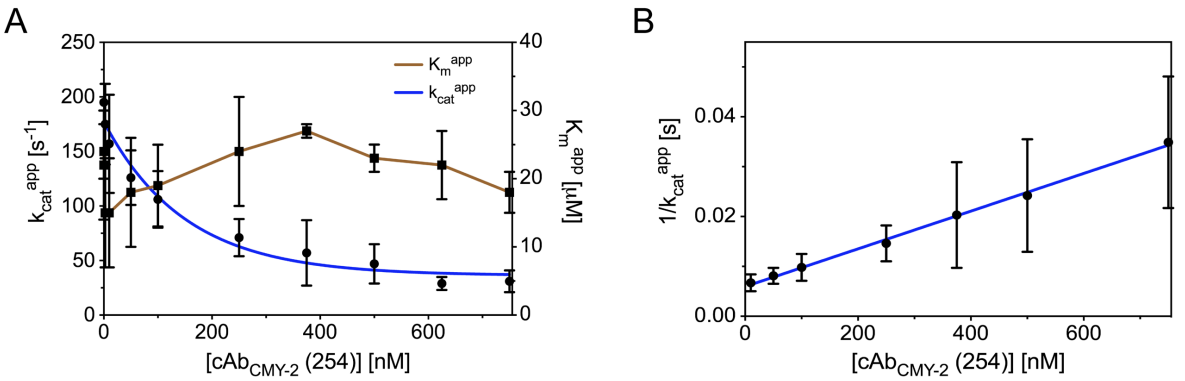

Fig 5.15. *Inhibitory model of CMY-2 activity for the hydrolysis of nitrocefin by cAb_{CMY-2}(254). (A) The K_m^{app} (blue) and the k_{cat}^{app} (brown) are derived from the linearization of the complete hydrolysis of 40 µM of nitrocefin by 0.5 nM of CMY-2 in complex with cAb_{CMY-2} (254). k_{cat}^{app} values were fitted with an exponential decay equation from graph prism. (B) Trend of $1/k_{cat}^{app}$ in function of the concentration in cAb_{CMY-2} (254). All values resulted from three independent experiments.*

5.5.3) Inhibitory model of CMY-2 activity for other β-lactams by cAb_{CMY-2} (254)

A similar inhibitory pattern of cAb_{CMY-2} (254) was observed for the activity of CMY-2 using the three cephalosporins as reporter substrates. Hence, considering K_m^{app} values unchanged for any concentrations of inhibitors, the tendency of k_{cat}^{app} and $1/k_{cat}^{app}$ in function of increasing VHH concentrations also illustrated a pure non-competitive inhibition (**Fig 5.16A&B**) (**Table 5.4**). On the contrary, for ampicillin, the hyperbole trend of $1/k_{cat}^{app}$ as a function of the VHH concentration was indicative of a mixed non-competitive inhibition (**Fig 5.16C**). In this case, the parameter β equaled to 0.41 ± 0.01 and the K_i value, calculated from the equation XV, was assessed at 352 ± 62 nM (**Table 5.4**). This observation indicated that the ESI complex presents a reduced but not abolished activity compared to the ES complex when the concentration of cAb_{CMY-2}(254) is significantly higher than the inhibition constant value (K_i).

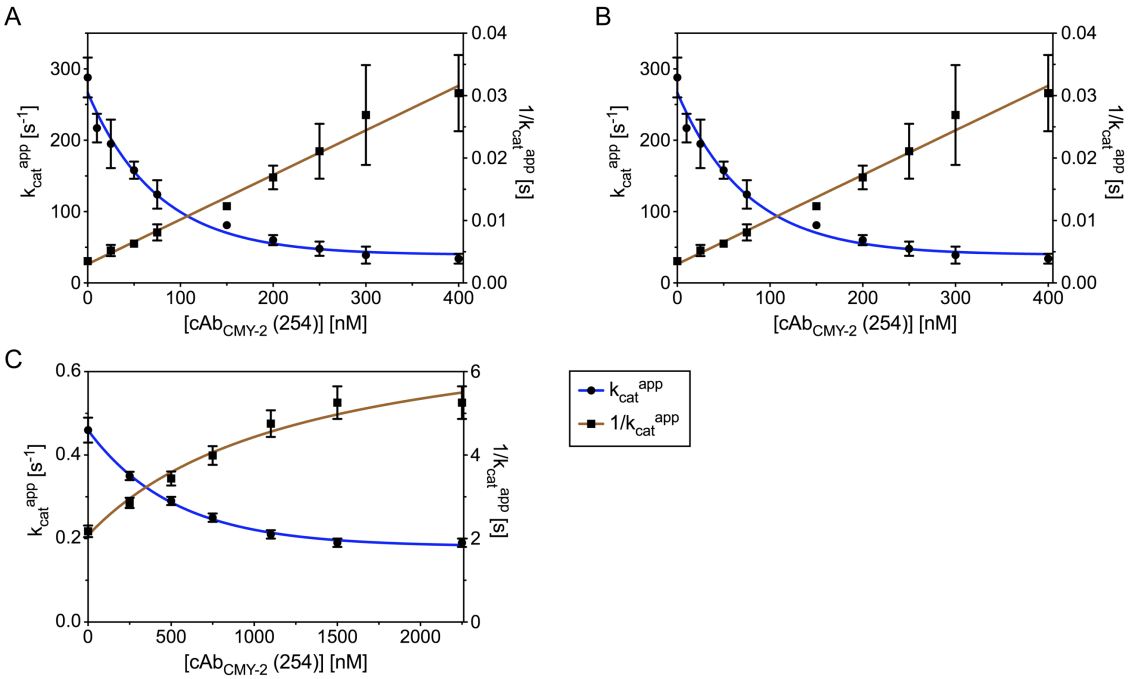

Fig 5.16. *Inhibitory model for CMY-2 activity for the cephaloridin (A), the cefalotin (B) and the ampicillin (C) by the cAb_{CMY-2} (254) VHH. The k_{cat}^{app} values were obtained from the linear phase (equation X) of hydrolysis of the corresponding substrate. All experiments were achieved twice independently.*

Table 5.4. *Resuming of α and β parameters and K_i values for the four studied β-lactam substrates.*

	α	β	K_i [nM][b]
Nitrocefin	1	0	88 ± 3
Cefalotin	1	0	107 ± 13
Cephaloridin	1	0	48 ± 10
Ampicillin	1	0,41 ± 0.01[a]	352 ± 62

[a]*This β value corresponds to the plateau obtained by residual activities experiments.*
[b]*The K_i values for the three cephalosporins were calculated from the equation XIV while the K_i value for the ampicillin is derived from the equation XV.*

5.6) Structural model of the cAb_{CMY-2} (254)/CMY-2 complex

The crystal of the cAb_{CMY-2} (254)/CMY-2 complex belonged to the $P6_222$ space group and diffracted at a final resolution of 3.2 Å. Each asymmetric unit contained one cAb_{CMY-2} (254)/CMY-2 complex. Our model included residues K3 to Q361 of the β-lactamase and residues Q1 to H124 of cAb_{CMY-2} (254) except for residues G108 and E109 in the CDR3 which were not defined in the electronic density. All data and refinement statistics are summarized in the **Table 5.5**.

Table 5.5. *Data collection and refinement statistics*

Crystal	**cAb_{CMY-2} (254)/CMY-2**
PDB code	7PA5
Data collection	
Space group	P 6_222
Cell constants	
a, b, c [Å]	95.12, 95.12, 242.94
α, β, γ [°]	90.00, 90.00, 120.00
Resolution range [Å][a]	48.88 – 3.18 (3.37-3.18)
Rmerge [%][a]	71 (342)
<I>/<σI>[a]	7.1 (1.28)
Completeness [%][a]	99.6 (97.9)
Redundancy[a]	37.8 (34.8)
CC (1/2)[a]	0.999 (42.9)
Refinement	
No. of unique reflections	11518
R work [%]	0.2067
R free [%]	0.2502
No. atoms	7475
Protein	7467
Solvent	8
RMS deviations from	
Bond lengths [Å]	0.004
Bond angles [°]	1.03
Mean B factor [$Å^2$]	78.0
Ramachandran plot:	
Favored region [%]	96
Allowed regions [%]	4

[a] *Values in parentheses are related to high resolution shell.*

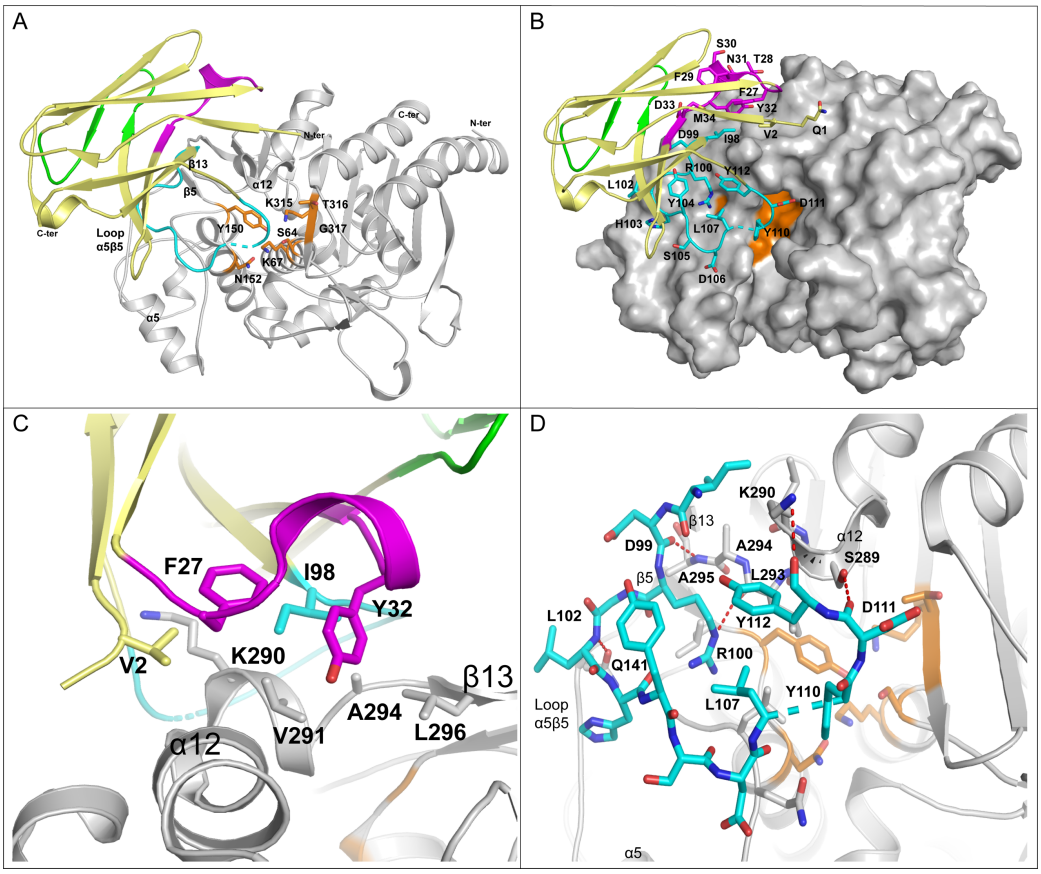

Fig 5.17. *Binding interface of the cAb$_{CMY-2}$ (254)/CMY-2 complex. (A) Cartoon representing the overall view of the complex between CMY-2 (grey with **S**64XX**K**67, **Y**150X**N**152 and **K**315T**G**317 conserved motifs as orange sticks) and cAb$_{CMY-2}$(254) (yellow with CDR1, CDR2 and CDR3 in magenta, green and cyan respectively). (B) Same illustration with CMY-2 represented as a surface. (C) Hydrophobic interactions between the CDR1 and the N-terminal extremity of the VHH and CMY-2. (D) Hydrogen bonds between the CDR3 and CMY-2. Hydrogen bonds are displayed as red dashed line. Residues G108 and D109 from the CDR3 of cAb$_{CMY-2}$(254) are not illustrated in the model due to a lack of information in the electronic density.*

The binding area between the cAb$_{CMY-2}$ (254) VHH and CMY-2 was about 950 Å^2. cAb$_{CMY-2}$ (254) interacted mainly via its CDR1 and CDR3 loops at the junction between the α and α/β domains near the active site of CMY-2 (**Fig 5.17A&B**). In more details, a first cluster of hydrophobic interactions was formed by residues V2 (N-terminal), F27 and Y32 (CDR1) and I98 (CDR3) of cAb$_{CMY-2}$ (254) and residues K290, V291, A294 and L296 located mainly on the α12-helix and a loop comprised between the α12-helix and the β13-strand from CMY-2 (**Fig 5.17C**). Furthermore, we noticed that the N-terminal residues of CDR3 (e.g. D99, R100 and L102) established H-bonds with the main chain residues L293 and A295 (α12β13 loop) and the side chain of residue Q141 of CMY-2 (α5β5 loop). Finally, the C-terminal residues D111 and

Y112 of the VHH CDR3 were involved in H-bonds with residues S289 and K290 located on the α12-helix of CMY-2 (**Fig 5.17D**). All these interactions induced a partial entry of the CDR3 VHH in the CMY-2 active site mainly by the intermediate of the residue Y110. However, the lack of information in the electronic density for residues G108 and D109 indicated an important flexibility of this CDR3 region and could explain the inability of the VHH to directly block the entrance of the substrate in the CMY-2 active site.

5.7) Discussion and perspectives

5.7.1) Overlapping epitopes of the VHHs

The immunization of alpacas allowed the selection of three VHHs. Competition binding assays highlighted that the three VHHs bind to an overlapping epitope on CMY-2. The structure of the cAb_{CMY-2} (254)/CMY-2 complex revealed the insertion of the CMY-2 K290 into a pocket located at the surface of cAb_{CMY-2} (254) (**Fig 5.17C**) and a second binding area involving most of the CDR3 (**Fig 5.17D**). The residues forming the pocket are conserved between the three VHHs except for the I98 which is mutated in an alanine (**Fig 5.3**). Despite the CDR3 constitutes the least conserved region among the VHHs, it is probable that the three VHHs share a similar binding mode with different affinities related to the ability of the CDR3 to bind to CMY-2.

5.7.2) Biochemical features of the VHHs for the CMY-2 sub-family

In vitro binding assays demonstrated that cAb_{CMY-2} (254) and cAb_{CMY-2} (272) present a higher specificity for β-lactamases belonging to the CMY-2 sub-family than cAb_{CMY-2} (250) which also binds to P99. The high affinity and specificity of the cAb_{CMY-2} (254) VHH justified its use for the screening of bovine and human bacterial isolates by a sandwich ELISA.

In vivo binding assays on bacterial isolates highlighted the ability to detect different variants from the CMY-2 sub-family as CMY-16, -42, -58, -60 and -61. In fact, the sequence involved in the interaction with the VHH is conserved for all variants from the CMY-2 sub-family reflecting the high probability to detect also other CMY-2-like β-lactamases. We

observed exactly the same ability of the cAb_{TEM-1} (13) VHH to interact with a multitude of TEM mutants resulting in the high conservation of the sequence of the binding site. Moreover, we were not able to detect other class C β-lactamases such as ACT-1, DHA-1 and CMY-10. ACT-1 and P99 present a high sequence identity with CMY-2 (77 % for ACT-1 and 76 % for P99) providing a similar conformation of the α12-helix (**Fig 5.18**). However, A295 is substituted by a proline in P99 and ACT-1 which may explain the inability to interact with the VHH. The presence of a proline may introduce a steric hindrance in the helix and displace the H-bonds network stabilizing the VHH/CMY-2 complex (**Fig 5.19A**). The steric hindrance with the glutamate E294 and the conformation change of the α12-helix due to a low sequence identity with CMY-2 could prevent the interaction of CMY-1 and CMY-10 with the VHH (**Fig 5.19B**).

	141	289	290	291	292	293	294	295	296	
CMY-2	Q	S	K	V	A	L	A	A	L	
CMY-1	V	A	K	V	I	L	E	A	N	(38%)
CMY-10	V	A	K	V	I	L	E	A	N	(44%)
DHA-1	S	N	E	V	A	L	Q	P	H	(59%)
P99	Q	S	K	V	A	L	A	P	L	(76%)
ACT-1	Q	N	K	V	A	L	A	P	L	(77%)

Fig 5.18. *Multiple sequence alignment of class C β-lactamases. Only the sequence corresponding to the binding interface between the VHH and CMY-2 is represented here. Percentages indicate the sequence identity of all the protein with CMY-2.*

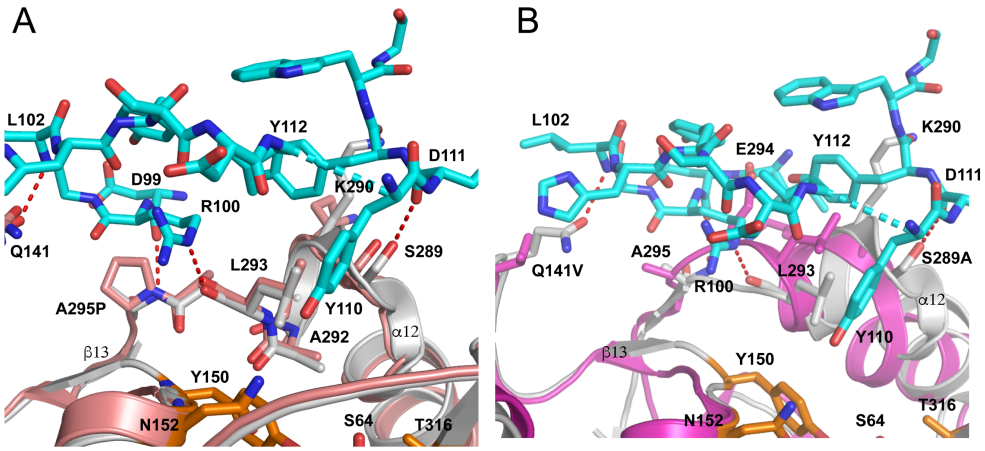

Fig 5.19. *Superposition of cAb_{CMY-2} (254)/CMY-2 complex with P99 (PDB code 1XX2) (A) and CMY-10 (PDB code 1ZKJ) (B). CMY-2, P99 and CMY-10 are colored in grey, red and magenta, respectively. Only the CDR3 of the VHH is illustrated in cyan and active site residues in orange. H-bonds are represented by red dashed lines.*

5.7.3) Biochemical features of Anti-CMY-2 pAbs

The overlapping epitope shared by the three VHHs required the development of rabbit polyclonal antibodies. These antibodies were less specific since they were able to recognize P99 and CMY-1. They correspond to a mix of antibodies able to bind epitopes shared by a large panel of AmpC β-lactamases what could explain their lack of specificity (**Lipman et al, 2005**). Fortunately, the use of the cAb_{CMY-2} (254) VHH permitted to offset the low specificity of the pAbs for the detection of CMY-2 in the sandwich ELISA. This was confirmed by the same kind of development for the detection of TEM-1.

5.7.4) Development of tandem-repeats cAb_{CMY-2} $(254)_{BIV}$ VHH

Another interesting aspect with the VHHs is the possibility to fuse them in order to decrease the dissociation rate by an avidity phenomenon leading to more stable Antigen/Antibody complexes (**Hultberg et al, 2011**). Associated with the multi-avidity ensured by the polyclonal antibodies, this allowed to detect lower quantities of CMY-2 than the monovalent counterpart despite we did not reach an identical sensitivity than for TEM-1 detection.

5.7.5) Applicability in an ELISA

One goal of the project RU-BLA-ESBL-CPE consisted to develop a sandwich ELISA for the detection of one of the most spread β-lactamase, CMY-2, in bovines and more largely in the animal world. However, our next aim is to develop an Immunochromatographic Lateral Flow Assay (LFA) that ensures a detection more rapidly and in an easier manner which could become an interesting alternative for veterinarians to phenotypic methods (**Rösner et al, 2019**).

Finally, despite this test is probably suitable for CMY-2 detection in animals, it is less applicable in human medicine where phenotypic assays constitute an unavoidable method for selection of the best antibiotic. However, we could use this kind of set up to interpret unclear phenotypic profiles generally found in MDR strains (**Conen et al, 2015**), to distinguish plasmid

to chromosomic AmpC (**Hujer et al, 2002**) and to highlight the involvement of an AmpC in a carbapenemase activity of an isolate (**Majewski et al, 2016**).

5.7.6) The cAb_{CMY-2} (254) VHH, a non-competitive inhibitor of CMY-2 activity

This work also allowed the selection of VHHs which behave as non-competitive inhibitors. The structure of the cAb_{CMY-2} (254)/CMY-2 complex highlighted an important flexibility of the CDR3 loop located in the active site that does not prevent the entry of the substrate in the active site. Nevertheless, Y110 brought by the CDR3 is situated near to Q120 which is a crucial residue in the stabilization of the acyl-enzyme by the establishment of a H-bond with the C7 amide carbonyl of the substrate (**Beadle & Shoichet, 2002**). A study of the P99 Q120E mutant demonstrated a significantly reduced activity against ampicillin and cefalotin compared to the WT proving its essential role for the β-lactamase activity (**Goldberg et al, 2003**). Therefore, despite the Y110 does not bind directly the Q120 in CMY-2, it may disrupt the stabilization of the acyl-enzyme (**Fig 5.20**). Moreover, as described for the cAb_{TEM-1}(13)/TEM-1 complex, the interaction of the VHH around the active site may perturb the dynamic of the enzyme which is known to be essential for its optimal activity.

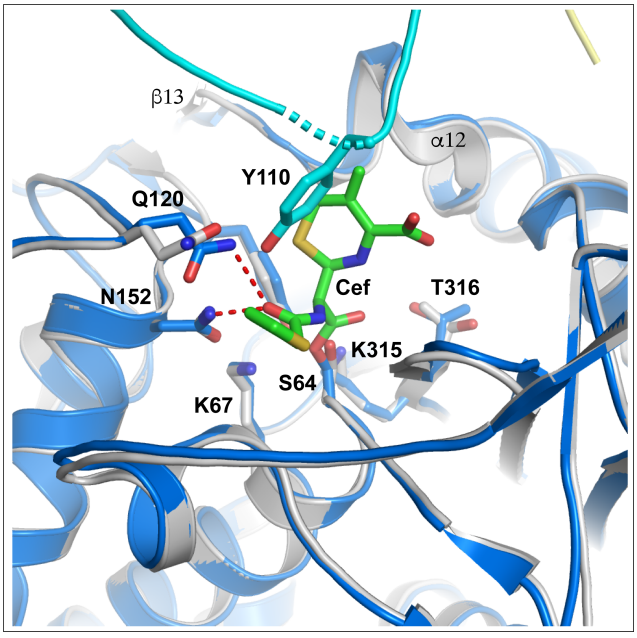

Fig 5.20. *Superposition of the cAb_{CMY-2} (254)/CMY-2 complex and an AmpC from E. coli in complex with a covalently bound cefalotin (PDB code 1KVM). CMY-2 and AmpC are colored in grey and blue, respectively.*

Our study provided evidence that the mechanism of inhibition will be different in function of the substrate. We found that the VHH behaved as a non-competitive inhibitor with its ability to completely inhibit the activity of CMY-2 for all tested cephalosporins. However, in presence of ampicillin, the complex maintained a reduced activity corresponding to a mixed non-competitive inhibition. The more plausible explanation consists in the fact that the ampicillin can easily diffuse in the active site due to its smaller size. Then, the presence of the nanobody has a minor impact on the penicillin hydrolysis.

6. Development of inhibitors against the class B β-lactamase NDM-1

6.1) Selection of binders against NDM-1

The alpaca immunization and the selection of VHHs against NDM-1 were carried out following the same general protocol as CMY-2. Three rounds of panning were performed to enrich the VHHs able to bind specifically NDM-1. Finally, ninety clones of each round of selection were randomly selected, cultured and lysed to test their periplasmic extract by an indirect ELISA. The different methods of panning to select VHHs against NDM-1 are confidential and cannot be discussed in this work.

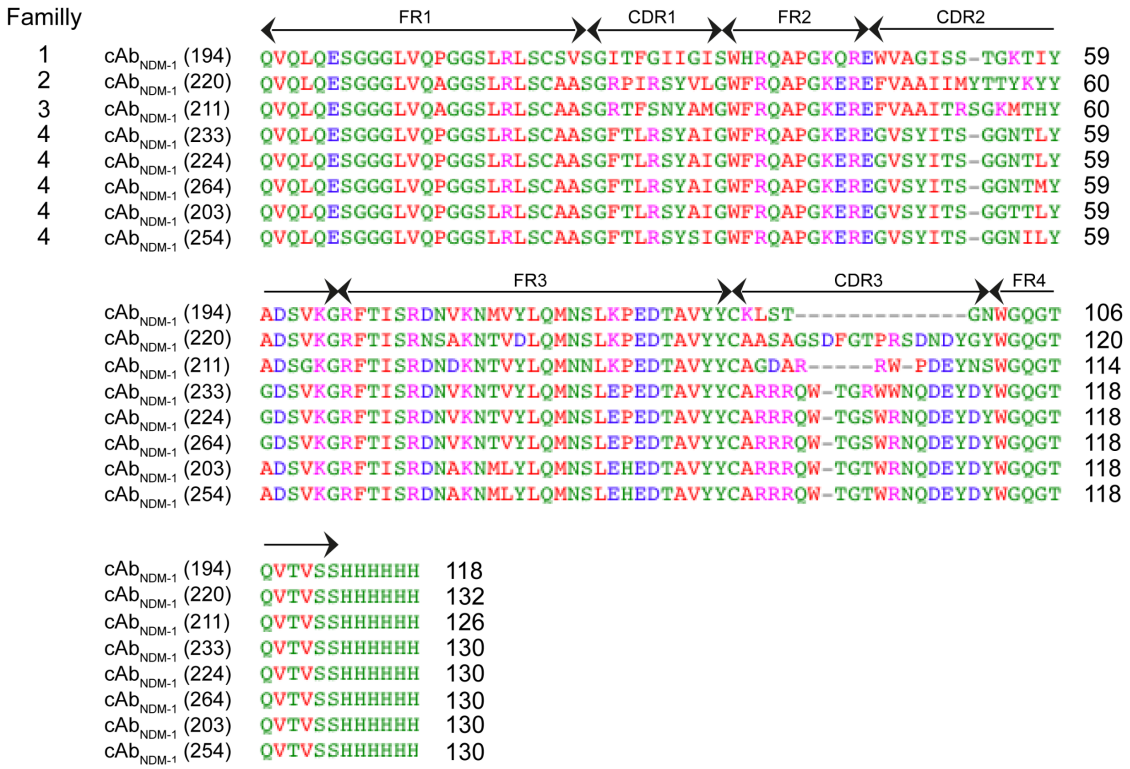

Fig 6.1. *Multiple sequences alignment of VHHs selected by phage display performed with CLUSTALW program. Residues are colored following their chemical behavior: polar feature in green, hydrophobic residues in red, negatively charged residues in blue and finally, positively charged residues in magenta. Frameworks (FRs) and Complementary-Determining Region (CDRs) of the VHHs are indicated by double arrows on the alignment.*

We obtained 8 different VHHs belonging to four families with the major diversity observed for the CDR2 and the CDR3 (**Fig 6.1**). Compared to the cAb_{NDM-1} (220) VHH presenting the longer CDR2 (20 AA) and CDR3 (19 AA), the cAb_{NDM-1} (194) VHH displays a deletion of 1 and 13 AA in its CDR2 and CDR3, respectively. The cAb_{NDM-1} (211) VHH is only depleted of 6 AA in its CDR3. Finally, the cAb_{NDM-1} (203), cAb_{NDM-1} (224), cAb_{NDM-1} (233), cAb_{NDM-1} (254) and cAb_{NDM-1} (264) VHHs belong to the same family but present some point mutations along their sequence.

6.2) Characterization of the VHHs binding for NDM-1

Based on the previous results, we decided to characterize the binding of the four VHH families for NDM-1 by bio-layer interferometry.

6.2.1) Specificity

We first carried out qualitative binding measurements to determine the specificity of the VHHs as previously described in chapters 3 and 4. In this case, we assessed their ability to distinguish the B1 sub-class metallo-β-lactamases IMP-1, VIM-1 and NDM-1. Interestingly, all VHHs specifically interacted with NDM-1. The low signal intensity for the binding to VIM-1 may indicate a low cross-reactivity (**Fig 6.2**).

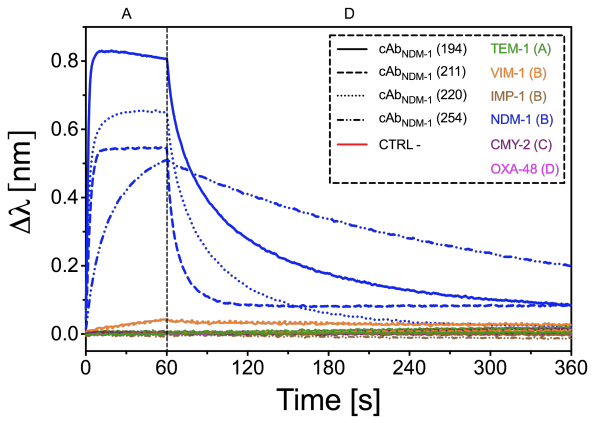

Fig 6.2. *Specificity binding of VHHs against NDM-1 by bio-layer interferometry. The CTRL – consists in the loading of NDM-1 directly on the His bio-sensor. For the VHH family 4, only the* cAb_{NDM-1} *(254) VHH is illustrated.*

6.2.2) Kinetic (k_{on}, k_{off}) and equilibrium (K_D) constants

To complete the binding characterization, we determined the kinetic constants of association (k_{on}), dissociation (k_{off}) and the equilibrium constant (K_D) of all VHHs for NDM-1 (**Table 6.1**). As for TEM-1 and CMY-2, association kinetic constants were comprised between 10^5 and 10^6 M^{-1} s^{-1} highlighting a rapid association rate. The VHHs belonging to the family 4 mainly present three ranges of affinity. cAb_{NDM-1} (254) (**Fig 6.3G**) has the highest affinity (K_D = 13 nM) due to a high stability of the complex. It is followed by the cAb_{NDM-1} (203) (**Fig 6.3B**), cAb_{NDM-1} (224) (**Fig 6.3D**) and cAb_{NDM-1} (264) (**Fig 6.3H**) VHHs which possess a K_D value around 70 nM and, cAb_{NDM-1} (233) (K_D = 320 nM) (**Fig 6.3E**) corresponding to the most unstable VHH/NDM-1 complex. In the other families, the cAb_{NDM-1} (211) (**Fig 6.3C**) and cAb_{NDM-1} (220) (**Fig 6.3D**) VHHs have a $K_D \approx 50$ nM while the cAb_{NDM-1} (194) VHH (**Fig 6.3A**) bound six times and dissociated three times more rapidly than cAb_{NDM-1} (254) resulting in a similar equilibrium constant (K_D).

VHHs	k_{on} [10^5 M^{-1} s^{-1}]	K_{off} [10^{-2} s^{-1}]	K_D [nM]
cAb_{NDM-1} (203)	2.9 ± 0.1	1.8 ± 0.1	62 ± 1
cAb_{NDM-1} (224)	2.5 ± 0.2	2.4 ± 0.1	100 ± 5
cAb_{NDM-1} (233)	1.1 ± 0.1	3.6 ± 0.3	319 ± 14
cAb_{NDM-1} (254)	2.3 ± 0.2	0.3 ± 0.0	13 ± 1
cAb_{NDM-1} (264)	1.8 ± 0.0	1.4 ± 0.0	79 ± 1
cAb_{NDM-1} (211)	8.0 ± 1.3	6.0 ± 0.8	75 ± 2
cAb_{NDM-1} (194)	12 ± 2	0.9 ± 0.1	7 ± 2
cAb_{NDM-1} (220)	5.9 ± 1.4	2.1 ± 0.2	36 ± 5

Table 6.1. The kinetic (k_{on}, k_{off}) and equilibrium (K_D) constants obtained by bio-layer interferometry. Values were calculated with a global fit on at least four NDM-1 concentrations with a 1:1 binding model. All averages and standard deviations resulted from two experiments.

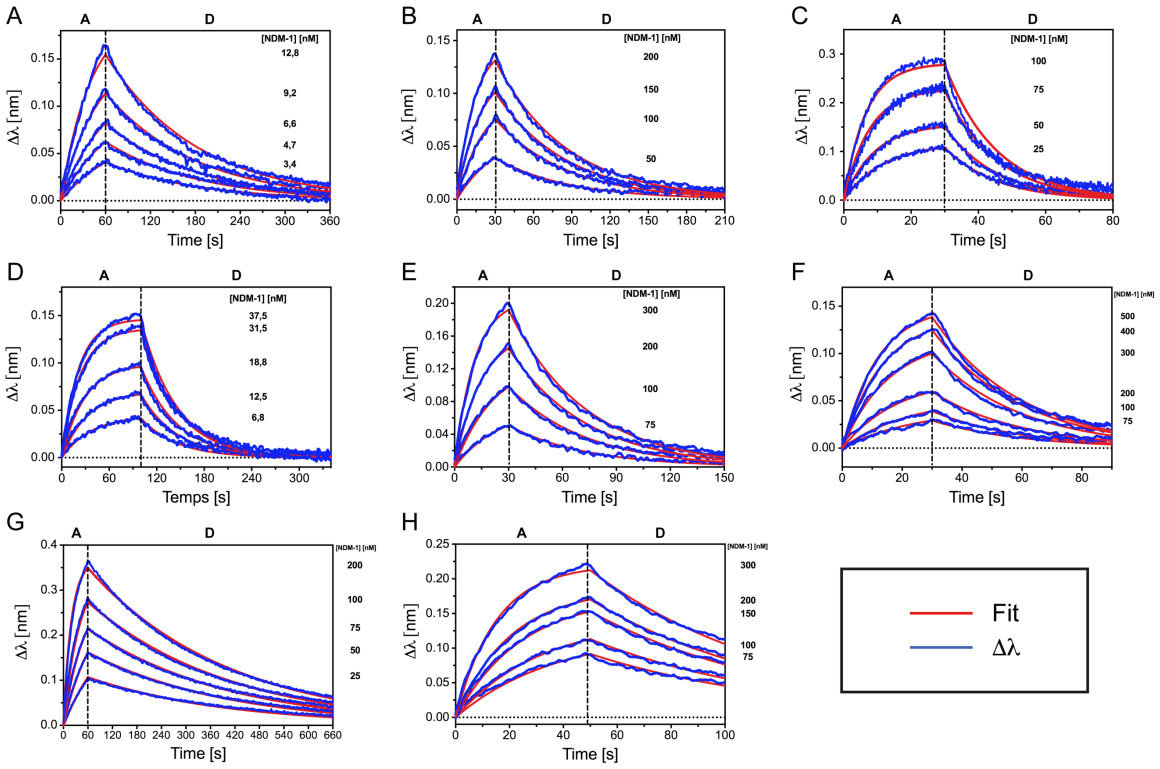

Fig 6.3. *Quantitative binding experiments carried out by bio-layer interferometry for the* cAb_{NDM-1} *(194) (A),* cAb_{NDM-1} *(203) (B),* cAb_{NDM-1} *(211) (C),* cAb_{NDM-1} *(220) (D),* cAb_{NDM-1} *(224) (E),* cAb_{NDM-1} *(233) (F),* cAb_{NDM-1} *(254) (G),* cAb_{NDM-1} *(264) (H) VHHs. The experimental data (Δλ, blue) recorded with at least four NDM-1 concentrations were fitted with a 1:1 binding model (red).*

6.2.3) Competition binding assay for NDM-1

We decided to verify the presence of an overlapping epitope at the surface of NDM-1. We carried out competition assays by bio-layer interferometry following the same protocol as for CMY-2 with only one 5:1 VHH/NDM-1 molar ratio. The sensorgrams illustrate the association between the biotinylated VHHs loaded on SA sensor and the different complexes (**Fig 6.4**). Remarkably, the cAb_{NDM-1} (194)/NDM-1 complex prevented any other VHH to bind the β-lactamase, while cAb_{NDM-1} (194) could only interact with the complex cAb_{NDM-1} (254)/NDM-1 (**Fig 6.4A**). Furthermore, the VHHs cAb_{NDM-1} (211), cAb_{NDM-1} (220) and cAb_{NDM-1} (254) seemed to recognize different epitopes on NDM-1 with an amplified association signal for all configurations (**Fig 6.4 B-D**).

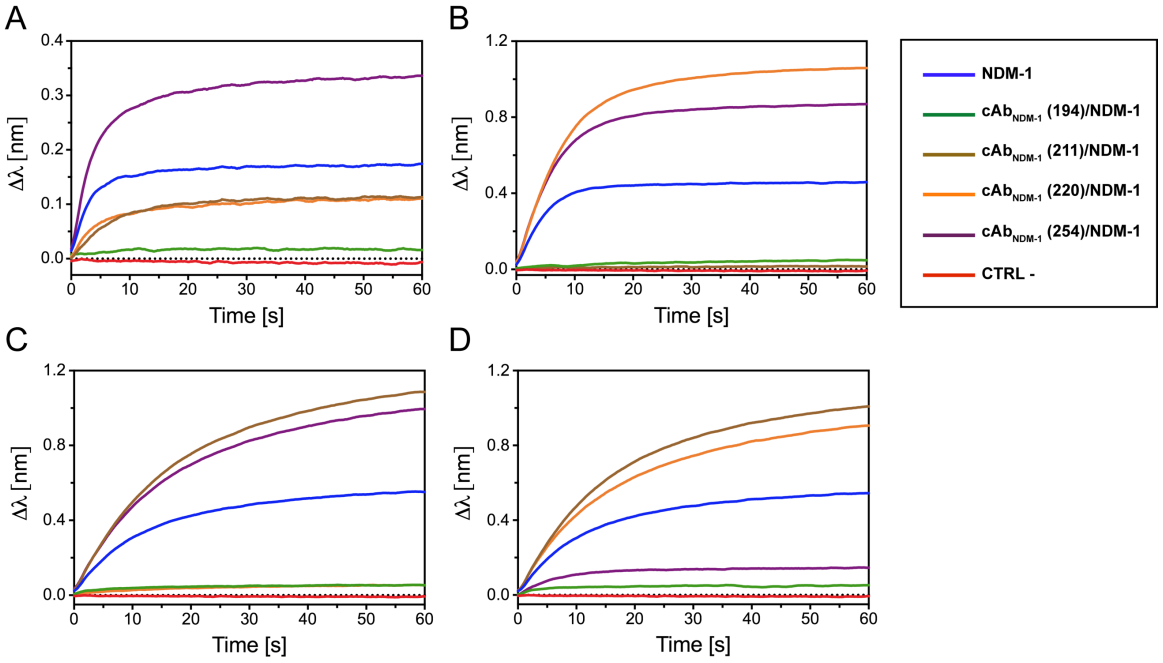

Fig 6.4. *Epitope binding assays performed by bio-layer interferometry. The biotinylated VHH cAb$_{NDM-1}$ (194) (A), cAb$_{NDM-1}$ (211) (B), cAb$_{NDM-1}$ (220) (C) and cAb$_{NDM-1}$ (254) (D) were loaded on streptavidin sensors while associations were measured on 60 seconds with cAb$_{NDM-1}$ (194)/NDM-1 (green), cAb$_{NDM-1}$ (211)/NDM-1 (brown), cAb$_{NDM-1}$ (220)/NDM-1 (orange) and cAb$_{NDM-1}$ (254)/NDM-1 (purple) complexes at a molar 5:1 ratio. The negative control (CTRL -, red) corresponded to the VHH/NDM-1 complex directly loaded on the sensor.*

6.3) Inhibitory effect of the VHHs on NDM-1 activity for carbapenems

The enzymatic activity of the different NDM-1/VHH complexes were measured for two clinically used carbapenems, the imipenem and the meropenem (**Fig 6.5**). The cAb$_{NDM-1}$ (211) and cAb$_{NDM-1}$ (254) VHHs were unable to inhibit the NDM-1 activity for imipenem. By contrast, the results highlighted a residual activity of the cAb$_{NDM-1}$ (220)/NDM-1 complex around 15 % compared to the free enzyme for both carbapenems. The cAb$_{NDM-1}$ (194) VHH inhibited similarly the NDM-1 activity for imipenem. But, the activity of the cAb$_{NDM-1}$ (194)/NDM-1 complex for meropenem displayed a residual activity of 30 % demonstrating a different mechanism of inhibition.

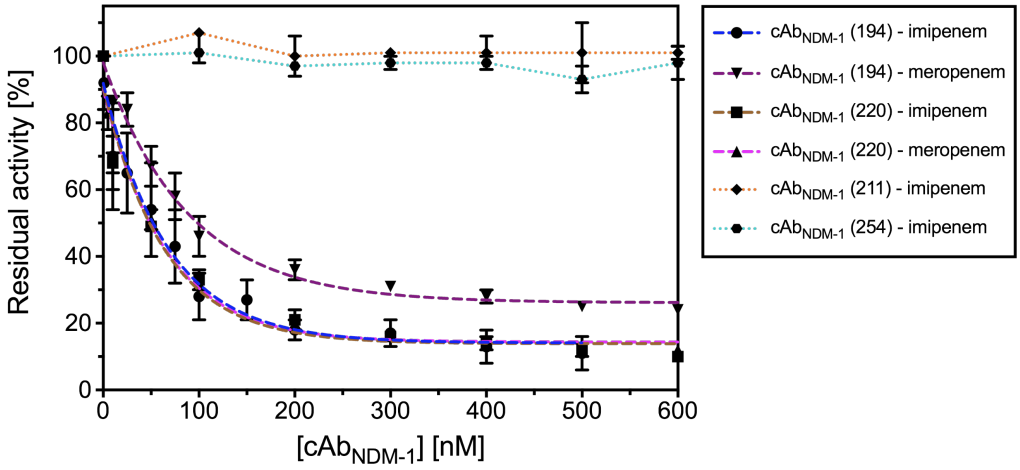

Fig 6.5. *Residual activity of 1 nM NDM-1 in complex with the cAb$_{NDM-1}$ (194), cAb$_{NDM-1}$ (211), cAb$_{NDM-1}$ (220) and cAb$_{NDM-1}$ (254) VHHs for 100 µM of imipenem and meropenem. Data were fitted with an exponential decay equation from graph prism. Averages and standard deviations resulted from two independent experiments.*

The linearization of NDM-1 residual activity by the equation XI described a competitive inhibition trend of cAb$_{NDM-1}$ (194) for imipenem and cAb$_{NDM-1}$ (220) for both tested carbapenems (**Fig 6.6**). The inhibitory constants (K_i) were in the same range as for the equilibrium constants (K_D) obtained by bio-layer interferometry (**Table 6.2**). However, the hyperbole trend of the cAb$_{NDM-1}$ (194)/NDM-1 complex activity for meropenem confirmed a different mechanism of inhibition.

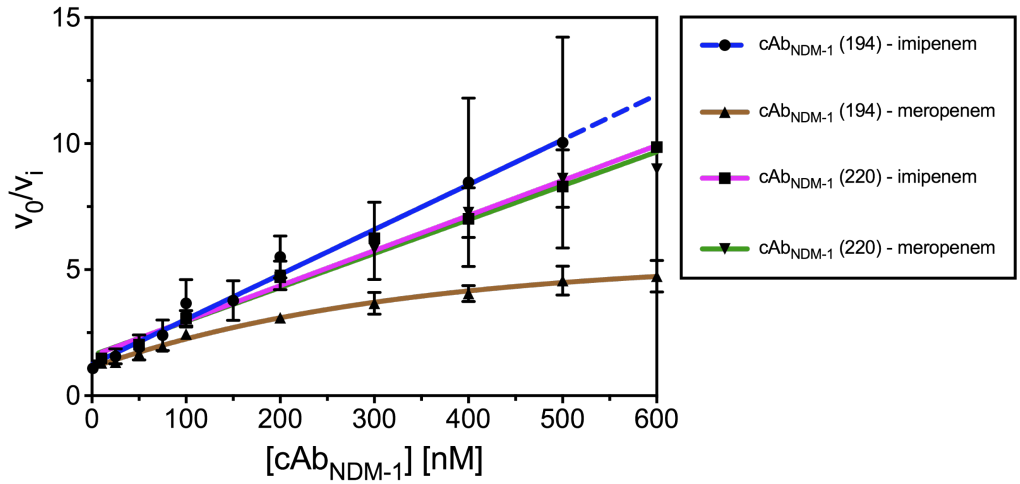

Fig 6.6. *Linear representation of cAb$_{NDM-1}$ (194)/NDM-1 and cAb$_{NDM-1}$ (220)/NDM-1 complexes activity for the imipenem and the meropenem.*

VHH	Antibiotics	K_i (nM)
cAb_{NDM-1} (194)	imipenem	16 ± 7
cAb_{NDM-1} (194)	meropenem	no linear
cAb_{NDM-1} (220)	imipenem	$19 \pm 0,4$
cAb_{NDM-1} (220)	meropenem	31 ± 5

Table 6.2. *Inhibition constants (K_i) of cAb_{NDM-1} (194) and cAb_{NDM-1} (220) VHHs for NDM-1 assessed from the equation XI. No value was provided for inhibition of NDM-1 activity for meropenem by the cAb_{NDM-1} (194) VHH given that data were fitted on a hyperbole model.*

6.4) Inhibitory effect of the VHHs on NDM variants for imipenem

In order to have a preliminary idea of the epitope for both inhibitors, we studied the impact of some mutations on VHH/NDM-1 complexes inhibition rate (**Table 6.3**). Because all mutants present similar steady-state kinetic constants, the inhibition measurements with 100 μM of imipenem were performed in similar conditions. All mutations led to a low impact of the inhibitory activity of the cAb_{NDM-1} (220) VHH with a residual activity of NDM enzymes comprised between 15 and 30 %. On the contrary, the E152K (NDM-9) and M154V (NDM-11) mutations suppressed the inhibitory effect of the cAb_{NDM-1} (194) VHH with residual activities of 93 % and 79 %, respectively. Surprisingly, the M154L mutation had no impact on the inhibitory activity of the cAb_{NDM-1} (194) VHH as observed for NDM-4, NDM-7 and NDM-15. This remains unclear considering leucine is one methylene group larger than valine.

Variants	Mutation(s)	K_m (μM)	k_{cat} (s^{-1})	cAb_{NDM-1} (194)	cAb_{NDM-1} (220)
NDM-1	WT	35 ± 1	64 ± 3	3 %	15 %
NDM-4	M154L	67 ± 4	13 ± 1	14 %	18 %
NDM-6	A233V	40 ± 3	26 ± 1	8 %	33 %
NDM-7	M154L/D130N	50 ± 3	15 ± 1	6 %	15 %
NDM-9	E152K	44 ± 3	53 ± 2	93 %	25 %
NDM-11	M154V	49 ± 3	11 ± 1	79 %	26 %
NDM-15	M154L/A233V	87 ± 6	23 ± 1	16 %	28 %
NDM-24	V88L	50 ± 4	36 ± 1	10 %	24 %

Table 6.3. *Binding effect of 500 nM cAb_{NDM-1} (194) and cAb_{NDM-1} (220) VHHs on 1 nM NDM mutants activity for 100 μM imipenem. The percentages correspond to residual activity of the VHH/NDM complex compared to the free enzyme.*

6.5) Bio-layer interferometry measurements of cAb_{NDM-1} (194) and cAb_{NDM-1} (220) VHHs for NDM variants

Steady-state kinetic measurements indicated the involvement of residues E152 and M154 in the binding interface of NDM-1 with cAb_{NDM-1} (194). This was confirmed by the absence of interaction between NDM-9 (E152K) and NDM-11 (M154V) mutants with the cAb_{NDM-1} (194) VHH (**Fig 6.7C&E**). We also hypothesized different epitopes are recognized by cAb_{NDM-1} (194) and cAb_{NDM-1} (220). Bio-layer interferometry experiments highlighted a similar affinity of cAb_{NDM-1} (220) for NDM-1 and NDM-9 (**Fig 6.7D, Table 6.4**). However, its affinity for NDM-11 was ten times lower compared to NDM-1 ($K_D \approx 400$ nM). This probably reflects a shared epitope of both VHHs for NDM-1 but with a different positioning of the nanobody (**Fig 6.7F, Table 6.4**). The binding of cAb_{NDM-1} (194) and cAb_{NDM-1} (220) with NDM-4 confirmed that the M154L mutation impacts less the interaction between the VHHs and the enzyme. This interpretation remains complex in the absence of structural models.

	Mutation	VHH	k_{on} [10^5 M^{-1} s^{-1}]	k_{off} [10^{-2} s^{-1}]	K_D [nM]
NDM-1	X	cAb_{NDM-1}(194)	12 ± 2	0.9 ± 0.1	7 ± 2
		cAb_{NDM-1}(220)	5.9 ± 1.4	2.1 ± 0.2	36 ± 5
NDM-4	M154L	cAb_{NDM-1}(194)	4 ± 0.3	2.4 ± 0.4	60 ± 6
		cAb_{NDM-1}(220)	2.3 ± 0.2	3.2 ± 0.1	145 ± 17
NDM-9	E152K	cAb_{NDM-1}(194)	ND	ND	ND
		cAb_{NDM-1}(220)	11.5 ± 0.4	7.1 ± 0.9	62 ± 10
NDM-11	M154V	cAb_{NDM-1}(194)	ND	ND	ND
		cAb_{NDM-1}(220)	1.5 ± 0.1	5.6 ± 1.0	393 ± 89

Table 6.4. *Kinetic constants obtained by bio-layer interferometry with a global fit on at least four concentrations in NDM variants with a model 1:1. All values represent averages and standard deviations from twice experiments.*

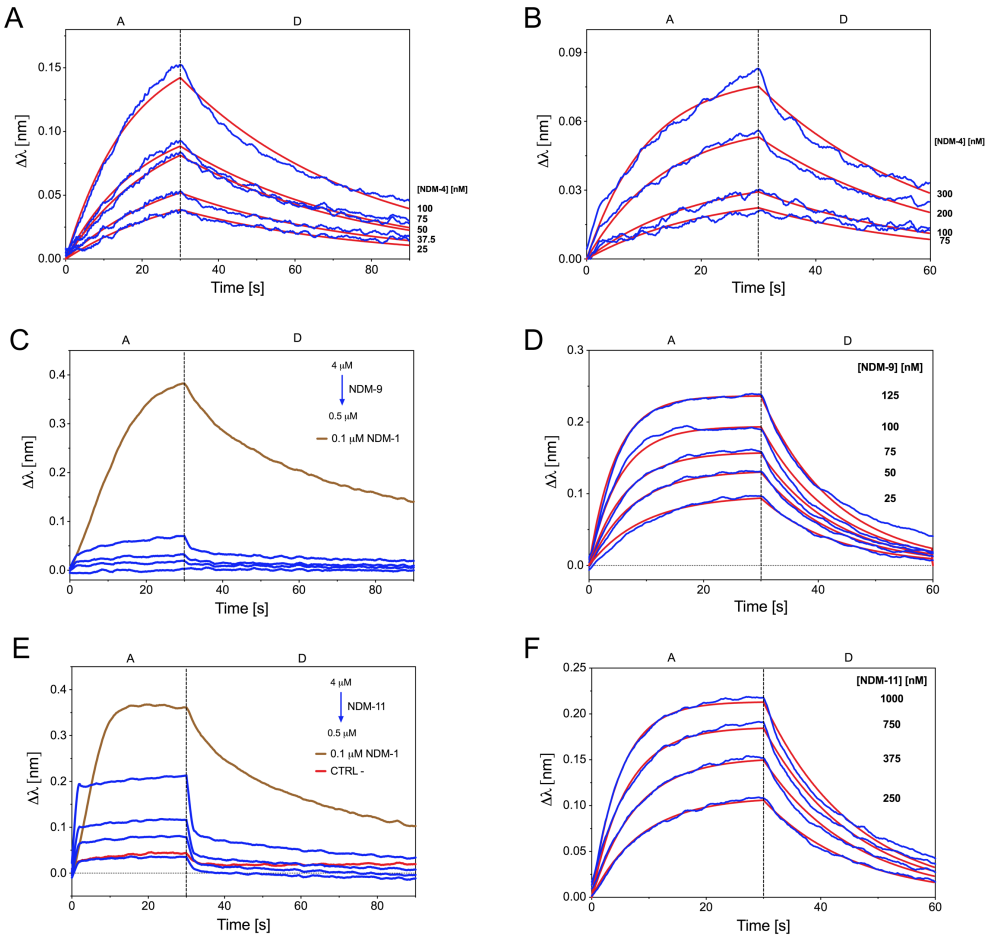

Fig 6.7. *Sensorgrams illustrating the binding of cAb_{NDM-1} (194) (left) and cAb_{NDM-1} (220) (right) VHHs coated on His1K sensor with NDM-4 (A-B) with NDM-9 (C-D) and NDM-11 (E-F). The CTRL – corresponds to the antigen loading directly on the biosensor.*

6.6) Conclusions and perspectives

This project aimed at selecting VHHs able to inhibit the NDM-1 activity for carbapenems. This β-lactamase is one of the most epidemiologically successful carbapenemases, for which therapeutic resources are limited. The bio-panning led to the selection of four genetically different families of VHHs against NDM-1. Only two families comprising the cAb_{NDM-1} (194) and cAb_{NDM-1} (220) VHHs acted as inhibitors since the VHH/NDM-1 complexes presented a reduced activity compared to the free enzyme. These VHHs probably present an overlapping epitope on NDM-1 as described by kinetic studies and competition binding assays. It revealed the involvement of both residues E152 (α3-helix) and M154 (L9 loop) from NDM-1 in the binding interface with cAb_{NDM-1} (194). These mutations impacted less the binding of the cAb_{NDM-1} (220) VHH with the enzyme. The different epitopes

recognized by both VHHs were confirmed by residual activity studies where inhibition of NDM-1 activity for meropenem was less efficient by cAb_{NDM-1} (194) than by cAb_{NDM-1} (220). The residues E152 and M154 are located close to residues H120 and H122 coordinating the zinc ion (Zn_1) essential for the activity of the enzyme (**Fig 6.8**). Combined with kinetic mutant results, it seems clear that the inhibitors probably interact near the active site, disrupting the stability of the enzyme and/or blocking directly the entry of the substrate into the active site as emphasized by the linearization of initial velocities which generally indicate a competitive inhibition. However, we cannot explain the different behavior of the cAb_{NDM-1} (194)/ NDM-1 complex for the meropenem.

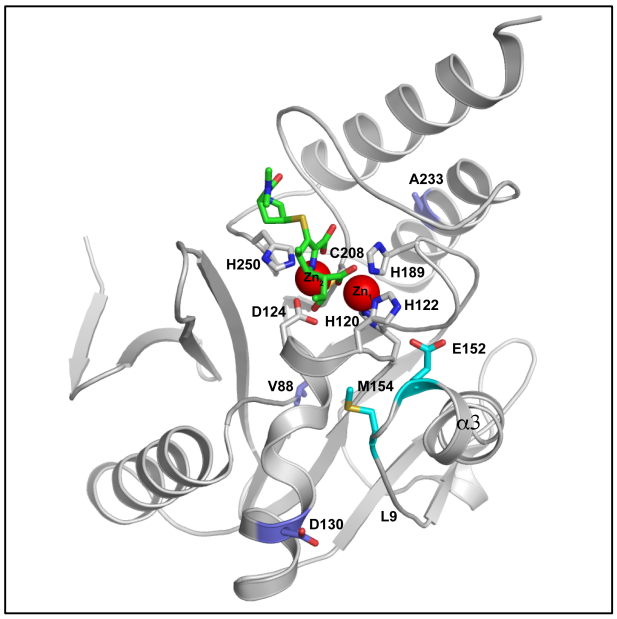

Fig 6.8. *Representation of NDM-1 in complex with the methicillin (PDB code 5NOH). Both zinc ions are represented by red dots. The both zinc are coordinated by the both consensus sequences* ***H****120-****H****122-****H****189 and* ***D****124-****C****208-****H****250. The residues E152 and M154 largely involved in the epitope recognized by* cAb_{NDM-1} *(194) and less by* cAb_{NDM-1} *(220) are colored in cyan, while other mutations are illustrated in purple.*

7. General conclusions and perpsectives

We selected and characterized VHHs recognizing specifically β-lactamases from TEM family, CMY-2 sub-group and NDM family, respectively. They bind their target with affinities generally comprised between 10 and 100 nM, which is of interest for developing detection assays and new inhibitor's scaffolds.

cAb_{TEM-1} (13) and cAb_{CMY-2} (254) VHHs behaved as non-competitive inhibitor of TEM-1 and CMY-2, respectively. The analysis of the cAb_{TEM-1} (13)/TEM-1 complex revealed that the CDR3 of the VHH binds an allosteric site brought by the hinge region close to the active site triggering conformational changes of TEM-1 that affect the β-lactamase activity. The cAb_{CMY-2} (254) VHH also interacts with the R2 loop of CMY-2 active site while the C-terminal end of its CDR3 partially entry into the CMY-2 active site.

Interestingly, the sequence of the hinge region (TEM-1) and R2 loop (CMY-2) are less impacted by naturally occurring mutations. For TEM variants, we only find mutations in the C-terminal part of the hinge region, mainly yielding the substitution of hydrophobic residues by other hydrophobic residues (e.g. A225V). No mutations are detectable in the CMY-2 sub-group variants. Ultimately, it could be more interesting to target allosteric sites or regions crucial for the activity of the enzyme, and not directly the active site which is more susceptible to mutations. As an example, no natural TEM mutants were identified for the residue D214 of TEM-1, interacting with the cAb_{TEM-1} (13) VHH, probably due to its crucial role for the stability of the hinge region and the activity of TEM-1. This hypothesis is validated by the results obtained on the non-natural D214A mutation which is characterized by decreased activity and stability. One perspective could be to focus on the analysis of non-natural mutants of TEM involved in the interactions with VHH. The same approach could be developed for CMY-2.

Unfortunately, we didn't obtain VHH/NDM-1 structures but a preliminary analysis of E152K (NDM-9) and M154V (NDM-11) variants demonstrated that the cAb_{NDM-1} (194) VHH probably interacts with the L9 loop located close to residues involved in the coordination of the zinc ion 1. We very much hope that this VHH directly blocks the entry of the substrate into

the active site, since preliminary steady-state kinetic experiments indicated that cAb_{NDM-1} (194) VHH behaved as a competitive inhibitor. In the future, it would be interesting to perform Hydrogen/Deuterium Exchange Mass Spectroscopy in order to more precisely localise the epitope of NDM-1 that is recognized by cAb_{NDM-1} (194).

Despite that VHHs are smaller than classical antibodies (15 kDa versus 150 kDa), they are still too bulky to penetrate the periplasm of bacteria. One strategy to further minimize the size of inhibitors consists in the development of small peptides based on the VHH CDRs sequence by peptidomimetics. Potent inhibitors could therefore be rationally designed by targeting allosteric site of structural features located near the enzyme's active site.

Peptides present several advantages: (I) an easier production in large scale-up with a cheaper cost, (II) the small size of peptides rendering more efficient the drug delivery and its action *in vivo* due to a better penetration through the bacterial outer-membrane (**Cho & Juliano, 1996**) and (III) peptides do not need humanization as opposed to therapeutics antibodies (**Goulet et al, 2022**). Peptides are developed based on the protein-protein interactions (PPI) which intervene mainly in the tumorigenesis and cancers. Some of them are currently in clinical trials or on the market as the ATSP-7041 which disrupts the interaction between the protein P53, implied in the DNA repair and the apoptosis, and the proteins MDMX upregulated in some cancers and blocking the activity of the protein P53 (**Chang et al, 2013**). A second category implies the development of peptides based on the therapeutic monoclonal antibodies such as the rhuMAb 4D5 (trastuzumab) utilized in the treatment of the breast cancer where a gene HER-2 is upregulated inducing the cellular proliferation (**Baselga et al, 1998 & Ramachandran et al, 2012**). More interestingly, VHHs were also used as scaffold for the development of peptides as against the VEGF factor (Vascular Endothelial Growth Factor) implied in angiogenesis in tumor development (**Karami et al, 2020**) or against the receptor β-2 adrenergic associated with chronic inflammation (**Martin et al, 2017**). The main drawback consists in generally lower affinities of the peptides (K_D > 1 µM) compared to the corresponding antibodies. However, some studies demonstrated that lower affinities resulted from a decrease in the association rate (**Geng et al, 2015 & Ding et al, 2017**).

We setup sandwich ELISAs for the specific detection of different variants of TEM β-lactamases family (TEM-1, TEM_{IRT} and TEM_{ESBL}) and members from the CMY-2 sub-group using nanobodies. They are already used in the detection of the alpha-fetoprotein (**Chen et al, 2016**), a cancer biomarker. They can be employed for the monitoring of the evolution of the multiple myeloma cancer by measuring the rate of soluble CD38 with a limit of detection which reached 10 pg/mL of antigen (**Li et al, 2018**).

Our final aim was to develop a LFA (Lateral Flow Assay) which is a one-step assay, rapid compared to classical phenotypic tests (diffusion tests) and inexpensive on contrary to methods such as MALDI-TOF or PCR (**Boutal et al, 2022**).

LFA are commercialized and currently utilized in hospital settings for the detection of CTX-M enzyme sub-groups (**Bernabeu et al, 2020**) and carbapenemases. As an example, NG CARBA-5 is a multiplex LFA triggering NDM, VIM, IMP, OXA-48 and KPC carbapenemases (**Jenkins et al, 2020**). However, the available LFAs cannot detect the presence of β-lactamases in clinical samples (e.g. saddle, urine). The bacteria need to be cultivated and isolated on an agar medium before proceeding to the identification of the resistance factors.

We demonstrated that a bivalent VHH could improve the sensitivity for the detection of CMY-2. We could imagine a multivalent VHH as well, with three or more VHHs linked together. Combined to the association of VHHs, it is easier to make affinity maturation of VHHs compared to classical antibodies. This maturation could also improve the ability of the VHH to bind stronger with its antigen and potentially improving the sensitivity of the assay.

Most of the actual LFA detect carbapenemases and ESBLs. Nevertheless, these assays miss minor ESBL and cephalosporinases which are more represented in veterinary health. As for clinical applications, we could develop very sensitive LFA able to detect β-lactamases directly in biological samples against CMY-2. It could lead to a rapid and simple detection test that can be used directly on field by veterinarians. It will also help the selection of adequate antibiotic in chemotherapy. Of course, it could be applicable for livestock, but also for the food control.

My work focused exclusively on β-lactamases. But it is clear that this kind of development could be adopted for the detection of other resistance factors such as efflux pumps or porins. Actually, several LFA allow the detection of PBP2a expressed in Methicillin-resistant *Staphylococcus aureus* (MRSA) (**Yamada et al, 2013**) or the detection of VanA ligase in *Enterococcus* spp. conferring the resistance to vancomycin (**Oueslati et al, 2021**).

To conclude, this thesis provided the evidence that the VHH acts as a powerful tool for the development of diagnostic assays and inhibitors against β-lactamases. As proof of concept, we decided to work on TEM-1, CMY-2 and NDM-1 where the accumulation of kinetics and structural data provided strategies for a future design of inhibitory peptides by peptidomimetics, while the use of a multivalent VHH presents the capability to detect β-lactamases with a better sensitivity which could be interesting for the future development of LFA applicable in clinical settings, by veterinarians or for a safest food control.

8. References

Abraham E.P., & Chain E. (1940). An Enzyme from Bacteria able to Destroy Penicillin. Nature, 146(837).

Adachi, H., Ohta, T., Matsuzawa, H. (1991). Site-directed mutants, at position 166, of RTEM-1 beta-lactamase that form a stable acyl-enzyme intermediate with penicillin. J Biol Chem, 266(5), 3186-91.

Adcock, S. A., & McCammon, J. A. (2006). Molecular Dynamics: Survey of Methods for Simulating the Activity of Proteins. Chemical Reviews, 106(5), 1589–1615.

Aktaş, Z., Kayacan, C., Oncul, O. (2012). *In vitro* activity of avibactam (NXL104) in combination with β-lactams against Gram-negative bacteria, including OXA-48 β-lactamase-producing *Klebsiella pneumoniae*. International Journal of Antimicrobial Agents, 39(1), 86–89.

Ali, A., Gupta, D., Srivastava, G., sharma, A., & Khan, A. U. (2018). Molecular and computational approaches to understand resistance of New Delhi Metallo β-lactamase variants (NDM-1, NDM-4, NDM-5, NDM-6, NDM-7)-producing strains against carbapenems. Journal of Biomolecular Structure and Dynamics, 37(8), 1–40.

Ambler, R. P. (1980). The Structure of β-Lactamases. Philosophical Transactions of the Royal Society B: Biological Sciences, 289(1036), 321–331.

Amcheslavsky, A., Wallace, A. L., Ejemel, M., Li, Q., McMahon, C. T., Stoppato, M., Giuntini, S., Schiller, Z. A., Pondish, J. R., Toomey, J. R., Schneider, R. M., Meisinger, J., Heukers, R., Kruse, A. C. Barry, E. M., Pierce, B. G., Klempner, M. S., Cavacini, L. A., & Wang, Y. (2021). Anti-CfaE nanobodies provide broad cross-protection against major pathogenic enterotoxigenic *Escherichia coli* strains, with implications for vaccine design. Sci Rep **11**, 2751.

Amstutz, P., Binz, H., Zahnd, C., & Pluckthun, A. (2006). Ribosome Display *In Vitro* Selection of Protein-Protein Interactions. Cell Biology, 497–509.

Antimicrobial Resistance Collaborators. (2022). Global burden of bacterial antimicrobial resistance in 2019: a systematic analysis. Lancet, 399, 629-55.

Avci, F. G., Altinisik, F. E., Vardar Ulu, D., Ozkirimli Olmez, E., & Sariyar Akbulut, B. (2016). An evolutionarily conserved allosteric site modulates beta-lactamase activity. Journal of Enzyme Inhibition and Medicinal Chemistry, 31(3), 33–40.

Barnes, M. D., Bethel, C. R., Alsop, J., Becka, S. A., Rutter, J. D., Papp-Wallace, K. M., & Bonomo, R. A. (2018). Inactivation of the Pseudomonas-Derived Cephalosporinase-3 (PDC-3) by Relebactam. Antimicrobial Agents and Chemotherapy, 62(5).

Baselga, J., Norton, L., Albanell, J., Kim, Y. M., & Mendelsohn, J. (1998). Recombinant humanized anti-HER2 antibody (Herceptin) enhances the antitumor activity of paclitaxel and doxorubicin against HER2/neu overexpressing human breast cancer xenografts. Cancer Res, 58(13), 2825-31.

Basuino, L., Jousselin, A., Alexander, J. A. N., Strynadka, N. C. J., Pinho, M. G., Chambers, H. F., & Chatterjee, S. S. (2018). PBP4 activity and its overexpression are necessary for PBP4-mediated high-level β-lactam resistance. Journal of Antimicrobial Chemotherapy, 73(5), 1177–1180.

Bauernfeind, A., Stemplinger, I., Jungwirth, R., & Giamarellou, H. (1996). Characterization of the plasmidic β-lactamase CMY-2, which is responsible for cephamycin resistance. Antimicrobial Agents and Chemotherapy, 40(1), 221–224.

Bauernfeind, A. C., & Yunsop, L. K. (1998). Plasmid-encoded AmpC β-lactamases: how far have we gone 10 years after the discovery? Yonsei Medical Journal, 39(6), 520–525.

Bauvois, C., Ibuka, A. S., Celso, A., Alba, J., Ishii, Y., Frere, J.-M., & Galleni, M. (2005). Kinetic Properties of Four Plasmid-Mediated AmpC β-Lactamases. Antimicrobial Agents and Chemotherapy, 49(10), 4240–4246.

Beadle, B. M., & Shoichet, B. K. (2002). Structural Bases of Stability–function Tradeoffs in Enzymes. Journal of Molecular Biology, 321(2), 285–296.

Bebrone, C., Anne, C., Kerff, F., Garau, G., De Vriendt, K., Lantin, R., Devreese, B., Van Beeumen, J., Dideberg, O., Frère, J-M., & Galleni, M. (2008). Mutational analysis of the zinc- and substrate-binding sites in the CphA metallo-β-lactamase from *Aeromonas hydrophila*. Biochemical Journal, 414(1), 151–159.

Bellais, S., Aubert, D., Naas, T., & Nordmann, P. (2000). Molecular and Biochemical Heterogeneity of Class B Carbapenem-Hydrolyzing β-Lactamases in *Chryseobacterium meningosepticum*. Antimicrobial Agents and Chemotherapy, 44(7), 1878–1886.

Bernabeu, S., Ratnam, K. C., Boutal, H., Gonzalez, C., Vogel, A., Devilliers, K., Plaisance, M., Oueslati, S., Malhotra-Kumar, S., Dortet, L., Fortineau, N., Simon, S., Volland, H., & Naas, T. (2020). A Lateral Flow Immunoassay for the Rapid Identification of CTX-M-Producing *Enterobacterales* from Culture Plates and Positive Blood Cultures. Diagnostics (Basel), 10(10): 764.

Blair, H. A., & Lyseng-Williamson, K. A. (2019). Caplacizumab in acquired thrombotic thrombocytopenic purpura: a profile of its use. Drugs & Therapy Perspectives, 35(6), 263–270.

Boder, E. T., & Wittrup, K. D. (1997). Yeast surface display for screening combinatorial polypeptide libraries. Nature Biotechnology, 15(6), 553–557.

Bonomo, R. A., Dawes, C. G., Knox, J. R., & Shlaes, D. M. (1995). β-Lactamase mutations far from the active site influence inhibitor binding. Biochimica et Biophysica Acta (BBA) - Protein Structure and Molecular Enzymology, 1247(1), 121–125.

Bottoni, C., Perilli, M., Marcoccia, F., Piccirilli, A., Pellegrini, C., Colapietro, M., Sabatini, A., Celenza, G., Kerff, F., Amicosante, G., Galleni, M., & Mercuri, P. S. (2016). Kinetic Studies on CphA Mutants Reveal the Role of the P158-P172 Loop in Activity versus Carbapenems. Antimicrobial Agents and Chemotherapy, 60(5), 3123–3126.

Bou, G., Oliver, A., & Martinez-Beltran, J. (2000). OXA-24, a Novel Class D β-Lactamase with Carbapenemase Activity in an *Acinetobacter baumannii* Clinical Strain. Antimicrobial Agents and Chemotherapy, 44(6), 1556–1561.

Boyd, S. E., Livermore, D. M., Hooper, D. C., & Hope, W. W. (2020). Metallo-β-lactamases: structure, function, epidemiology, treatment options, and the development pipeline. Antimicrobial Agents and Chemotherapy, 64(10): e00397-20.

Boyd, S.E., Holmes, A., Peck, R., Livermore, D. M., & Hope, W. (2022). OXA-48-Like β-Lactamases: Global Epidemiology, Treatment Options, and Development Pipeline. Antimicrob Agents Chemother, 66(8): e0021622.

Boolchandani, M., D'Souza, A. W., & Dantas, G. (2019). Sequencing-based methods and resources to study antimicrobial resistance. Nature Reviews Genetics, 20(6),356–370.

Boutal, H., Moguet, C., Pommiès, L., Simon, S., Naas, T., & Volland, H. (2022). The Revolution of Lateral Flow Assay in the Field of AMR Detection. Diagnostics (Basel), 12(7): 1744.

Brannigan, J., Matagne, A., Jacob, F., Damblon, C., Joris, B., Klein, D., Spratt, B. G., & Frère, J.-M. (1991). The mutation Lys234His yields a class A beta-lactamase with a novel pH-dependence. Biochem J., 278, 673-8.

Brem, J., van Berkel, S. S., Zollman, D., Lee, S. Y., Gileadi, O., McHugh, P. J., … Schofield, C. J. (2016). Structural Basis of Metallo-β-Lactamase Inhibition by Captopril Stereoisomers. Antimicrobial Agents and Chemotherapy, 60(1), 142–150.

Bugg, T. D. H., Braddick, D., Dowson, C. G., & Roper, D. I. (2011). Bacterial cell wall assembly: still an attractive antibacterial target. Trends in Biotechnology, 29(4), 167–173.

Bush, K., Macalintal, C., Rasmussen, B. A., Lee, V. J., & Yang, Y. (1993). Kinetic interactions of tazobactam with β-lactamases from all major structural classes. Antimicrobial Agents and Chemotherapy, 37(4), 851–858.

Bush, K., & Jacoby, G. A. (2009). Updated Functional Classification of β-Lactamases. Antimicrobial Agents and Chemotherapy, 54(3), 969–976.

Bush, K. (2013). The ABCD's of β-lactamase nomenclature. Journal of Infection and Chemotherapy, 19(4), 549–559.

Bush, K. & Bradford, P. A. (2016). β-lactams and β-lactamase inhibitors: an overview. Cold Spring Harb Perspect Med, 6(8), a025247.

Bush, K. (2018). Past and Present Perspectives on β-Lactamases. AAC, 62: e01076-18.

Bush, K., & Bradford, P. A. (2020). Epidemiology of β-Lactamase-Producing Pathogens. Clinical Microbiology Reviews, 33(2).

Cantu, C., & Palzkill, T. (1998). The Role of Residue 238 of TEM-1 β-Lactamase in the Hydrolysis of Extended-spectrum Antibiotics. Journal of Biological Chemistry, 273(41), 26603–26609.

Canver, M. C., Satlin, M. J., Westblade, L. F., Kreiswirth, B. N., Chen, L., Robertson, A., Fauntleroy, K., La Spina, M., Callan, K., & Jenkins, S. G. (2019). Activity of imipenem-relebactam and comparator agents against genetically characterized isolates of carbapenem-resistant *Enterobacteriaceae*. Antimicrobial Agents and Chemotherapy, 63(9): e00672-19.

Castanheira, M., Rhomberg, P. R., Flamm, R. K., & Jones, R. N. (2016a). Effect of the β-Lactamase Inhibitor Vaborbactam Combined with Meropenem against Serine Carbapenemase-Producing Enterobacteriaceae. Antimicrobial Agents and Chemotherapy, 60(9), 5454–5458.

Castanheira, M., Mendes, R. E., Jones, R. N., & Sader, H. S. (2016b). Changes in the Frequencies of β-Lactamase Genes among Enterobacteriaceae Isolates in U.S. Hospitals, 2012 to 2014: Activity of Ceftazidime-Avibactam Tested against β-Lactamase-Producing Isolates. Antimicrobial Agents and Chemotherapy, 60(8), 4770–4777.

Cawez, F., Duray, E., Hu, Y., Vandenameele, J., Romão, E., Vincke, C., Dumoulin, M., Galleni, M., Muyldermans, S., & Vandevenne, M. (2018). Combinatorial Design of a Nanobody that Specifically Targets Structured RNAs. Journal of Molecular Biology, 430(11), 1652–1670.

CDC. Antibiotic Resistance Threats in the United States, 2019. Atlanta, GA: U.S. Department of Health and Human Services, CDC, 2019.

Chain, E., Florey, H. W., Gardner, A. D., Heatley, N. G., Jennings, M. A., Orr-Ewing, J., & Sanders, A. G. (1940). PENICILLIN AS A CHEMOTHERAPEUTIC AGENT. The Lancet, 236(6104), 226–228.

Chang, Y. S., Graves, B., Guerlavais, V., Tovar, C., Packman, K., To, K.-H., Olson, K. A., Kesavan, K., Gangurde, P., Mukherjee, A., Baker, T., Darlak, K., Elkin, C., Filipovic, Z., Qureshi, F. Z., Cai, H., Berry, P., Feyfant, E., Shi, X. E., Horstick, J., Annis, D. A., Manning, A. M., Fotouhi, N., Nash, H., Vassilev, L. T., & Sawyer, T. K. (2013). Stapled α−helical peptide drug development: A potent dual inhibitor of MDM2 and MDMX for p53-dependent cancer therapy. Proceedings of the National Academy of Sciences, 110(36), E3445–E3454.

Chayen, N. E. (2004). Turning protein crystallisation from an art into a science. Current Opinion in Structural Biology, 14(5), 577–583.

Chen, J., He, Q., Xu, Y., Fu, J., Li, Y., Tu, Z., Wang, D., Shu, M., Qiu, Y-L., Yang, H-W., & Liu, Y. (2016). Nanobody medicated immunoassay for ultrasensitive detection of cancer biomarker alpha-fetoprotein. Talanta, 147, 523–530.

Chen, Y., Minasov, G., Roth, T. A., Prati, F., & Shoichet, B. K. (2006). The Deacylation Mechanism of AmpC β-Lactamase at Ultrahigh Resolution. Journal of the American Chemical Society, 128(9), 2970–2976.

Cho, M. J., & Juliano, R. (1996). Macromolecular versus small molecule therapeutics: drug discovery, development and clinical considerations. Trends in Biotechnology, 14(5), 153–158.

Coertze, R. D., & Bezuidenhout, C. C. (2020). Relating the prevalence of plasmid-mediated AmpC β-lactamase genes to aquatic environmental factors. Science of The Total Environment, 1, 763: 144119.

Concha, N. O., Janson, C. A., Rowling, P., Pearson, S., Cheever, C. A., Clarke, B. P., Lewis, C., Galleni, M., Frère, J-M., Payne, D. J., Bateson, J. H., & Abdel-Meguid, S. S. (2000). Crystal Structure of the IMP-1 Metallo β-Lactamase from *Pseudomonas aeruginosa* and Its Complex with a Mercaptocarboxylate Inhibitor: Binding Determinants of a Potent, Broad-Spectrum Inhibitor†,‡. Biochemistry, 39(15), 4288–4298.

Conen, A., Frei, R., Adler, H., Dangel, M., Fux, C. A., & Widmer, A. F. (2015). Microbiological Screening Is Necessary to Distinguish Carriers of Plasmid-Mediated AmpC β-Lactamase-Producing *Enterobacteriaceae* and Extended-Spectrum β-Lactamase (ESBL)-Producing Enterobacteriaceae because of Clinical Similarity. PLOS ONE, 10(3), e0120688.

Conrath, K. E., Lauwereys, M., Galleni, M., Matagne, A., Frere, J.-M., Kinne, J., Wyns, J., & Muyldermans, S. (2001). β-Lactamase Inhibitors Derived from Single-Domain Antibody Fragments Elicited in the Camelidae. Antimicrobial Agents and Chemotherapy, 45(10), 2807–2812.

Cornish-Bowden A., Jamin M., & Saks V. (2005). Cinétique Enzymatique. Grenoble Sciences.

Dale, J. W., Godwin, D., Mossakowska, D., Stephenson, P., & Wall, S. (1985). Sequence of the OXA2 β-lactamase: comparison with other penicillin-reactive enzymes. FEBS Letters, 191(1), 39–44.

Damblon, C., Raquet, X., Lian, L. Y., Lamotte-Brasseur, J., Fonze, E., Charlier, P., Roberts, G.C., Frère, J.-M. (1996). The catalytic mechanism of β-lactamases: NMR titration of an active-site lysine residue of the TEM-1 enzyme. Proc Natl Acad Sci U S A., 93(5), 1747-52.

Danel, F., Hall, L. M., Gur, D., & Livermore, D. M. (1995). OXA-14, another extended-spectrum variant of OXA-10 (PSE-2) β-lactamase from *Pseudomonas aeruginosa*. Antimicrobial Agents and Chemotherapy, 39(8), 1881–1884.

Davies, R. B., & Abraham, E. P. (1974). Metal cofactor requirement of β-lactamase II. Biochemical Journal, 143(1), 129–135.

Dellus-Gur, E., Elias, M., Caselli, E., Prati, F., Salverda, M. L. M., de Visser, J. A. G. M., Fraser, J. S., & Tawfik, D. S. (2015). Negative Epistasis and Evolvability in TEM-1 β-Lactamase-The Thin Line between an Enzyme's Conformational Freedom and Disorder. Journal of Molecular Biology, 427(14), 2396–2409.

Desmyter, A., Transue, T. R., Ghahroudi, M. A., Dao Thi, M.-H., Poortmans, F., Hamers, R., Muyldermans, S., & Wyns, L. (1996). Crystal structure of a camel single-domain VH antibody fragment in complex with lysozyme. Nat. Struct. Biol, 3(9), 803–811.

Ding, H., Gangalum, P. R., Galstyan, A., Fox, I., Patil, R., Hubbard, P., Murali, R., Ljubimova, J. Y., & Holler, E. (2017). HER2-positive breast cancer targeting and treatment by a peptide-conjugated mini nanodrug. Nanomedicine: Nanotechnology, Biology and Medicine, 13(2), 631–639.

Dmitriev, O. Y., Lutsenko, S., & Muyldermans, S. (2015). Nanobodies as Probes for Protein Dynamics in Vitro and in Cells. Journal of Biological Chemistry, 291(8), 3767–3775.

Doerflinger, S. Y., Tabatabai, J., Schnitzler, P., Farah, C., Rameil, S., Sander, P., Koromyslova, A., & Hansman, G. S. (2016). Development of a Nanobody-Based Lateral Flow Immunoassay for Detection of Human Norovirus. mSphere, 1(5): e00219-16.

Dong H, Li Y, Cheng J, Xia Z, Liu W, Yan T, Chen F, Wang Z, Li R, Shi J, & Qin S. (2022). Genomic Epidemiology Insights on NDM-Producing Pathogens Revealed the Pivotal Role of Plasmids on bla, Transmission. Microbiol Spectr., 27,10(2): e0215621.

Drawz, S. M., & Bonomo, R. A. (2010). Three Decades of β-Lactamase Inhibitors. Clinical Microbiology Reviews, 23(1), 160–201.

Emsley, P., Lohkamp, B., Scott, W. G., & Cowtan, K. (2010). Features and development of Coot. Acta Crystallographica Section D Biological Crystallography, 66(4), 486–501.

Endimiani, A., Doi, Y., Bethel, C. R., Taracila, M., Adams-Haduch, J. M., O'Keefe, A., Hujer, A. M., Paterson, D. L., Skalweit, M. J., Page, M. G. P., Drawz, S. M., & Bonomo, R. A. (2010). Enhancing Resistance to Cephalosporins in Class C β-Lactamases: Impact of Gly214Glu in CMY-2. Biochemistry, 49(5), 1014–1023.

Ewers, C., Bethe, A., Semmler, T., Guenther, S., & Wieler L. H. (2012). Extended-spectrum β-lactamase-producing and AmpC-producing Escherichia coli from livestock and companion animals, and their putative impact on public health: a global perspective. Clin Microbiol Infect, 18(7), 646-655.

Ewers, C., de Jong, A., Prenger-Berninghoff, E., El Garch, F., Leidner, U., Tiwari, S. K., & Semmler, T. (2021). Genomic Diversity and Virulence Potential of ESBL- and AmpC-β-Lactamase-Producing *Escherichia coli* Strains from Healthy Food Animals Across Europe. Frontiers in Microbiology, 12: 626774.

Feige, M. J., Hendershot, L. M., & Buchner, J. (2010). How antibodies fold. Trends in Biochemical Sciences, 35(4), 189–198.

Feige, M. J., Grawert, M. A., Marcinowski, M., Hennig, J., Behnke, J., Auslander, D., Herold, E. M., Pescheck, J., Castro, C. D., Flajnik, M., Hendershot, L. M., Satller, M., Groll, M., & Buchner, J. (2014). The structural analysis of shark IgNAR antibodies reveals evolutionary principles of immunoglobulins. Proceedings of the National Academy of Sciences, 111(22), 8155–8160.

Feng, H., Ding, J., Zhu, D., Liu, X., Xu, X., Zhang, Y., Zang, S., Wang, D-C., & Liu, W. (2014). Structural and Mechanistic Insights into NDM-1 Catalyzed Hydrolysis of Cephalosporins. Journal of the American Chemical Society, 136(42), 14694–14697.

Feng, H., Liu, X., Wang, S., Fleming, J., Wang, D.-C., & Liu, W. (2017). The mechanism of NDM-1-catalyzed carbapenem hydrolysis is distinct from that of penicillin or cephalosporin hydrolysis. Nature Communications, 8(1).

Feng, Y., Meshaw, R., McDougald, D., Zhou, Z., Zhao, X-G., Jannetti, S. A., Reiman, R. E., Pippen, E., Marjoram, R., Schaal, J. L., Vaidyanathan. G., & Zalutsky, M. R. (2022). Evaluation of an ^{131}I-labeled HER2-specific single domain antibody fragment for the radiopharmaceutical therapy of HER2-expressing cancers. Sci Rep, 12, 3020.

Fernandez, C. (2003). TROSY in NMR studies of the structure and function of large biological macromolecules. Current Opinion in Structural Biology, 13(5), 570–580.

Fisette, O., Morin, S., Savard, P.-Y., Lagüe, P., & Gagné, S. M. (2010). TEM-1 Backbone Dynamics-Insights from Combined Molecular Dynamics and Nuclear Magnetic Resonance. Biophysical Journal, 98(4), 637–645.

Fisette, O., Gagné, S., & Lagüe, P. (2012). Molecular Dynamics of Class A β-lactamases—Effects of Substrate Binding. Biophysical Journal, 103(8), 1790–1801.

Fisher, J., Belasco, J. G., Charnas, R. L., Khosla, S., & Knowles, J. R. (1980). β-Lactamase Inactivation by Mechanism-Based Reagents. Philosophical Transactions of the Royal Society B: Biological Sciences, 289(1036), 309–319.

Flajnik, M. F., Deschacht, N., & Muyldermans, S. (2011). A Case Of Convergence: Why Did a Simple Alternative to Canonical Antibodies Arise in Sharks and Camels? PLoS Biology, 9(8), e1001120.

Fleming, A. (1929). On the bacterial action of cultures of a penicillium with special reference to their use in the isolation of *B. influenzae*. Br. J. Exp. Pathol., 10, 226-236.

Gaibani, P., Ambretti, S., Berlingeri, A., Cordovana, M., Farruggia, P., Panico, M., Landini, M. P., Sambri, V. (2011). Outbreak of NDM-1-producing *Enterobacteriaceae* in northern Italy, July to August 2011. Euro Surveill,16(47):20027.

Galdadas, I., Qu, S., Oliveira, A. S. F., Olehnovics, E., Mack, A. R., Mojica, M. F., Agarwal, P. K., Tooke, C. L., Gervasio, F. L., Spencer, J., Bonomo, R. A., Mulholland, A. J., & Haider S. (2021). Allosteric communication in class A β-lactamases occurs via cooperative coupling of loop dynamics. Elife, 10: e66567.

Galleni, M., & Frère, J-M. (1988). A survey of the kinetic parameters of class C β-lactamases. Penicillins. Biochemical Journal, 255(1), 119–122.

Galleni, M., Lamotte-Brasseur, J., Rossolini, G. M., Spencer, J., Dideberg, O., & Frere, J.-M. (2001). Standard Numbering Scheme for Class B β-Lactamases. Antimicrobial Agents and Chemotherapy, 45(3), 660–663.

Gao, H., Liu, Y., Wang, R., Wang, Q., Jin, L., & Wang, H. (2020). The transferability and evolution of NDM-1 and KPC-2 co-producing *Klebsiella pneumoniae* from clinical settings. EBioMedicine, 51, 102599.

Garau, G., Bebrone, C., Anne, C., Galleni, M., Frère, J.-M., & Dideberg, O. (2005). A Metallo-β-lactamase Enzyme in Action: Crystal Structures of the Monozinc Carbapenemase CphA and its Complex with Biapenem. Journal of Molecular Biology, 345(4), 785–795.

García-Sáez, I., Mercuri, P. S., Papamicael, C., Kahn, R., Frère, J.-M., Galleni, M., Rossolini, G. M., & Dideberg, O. (2003). Three-dimensional Structure of FEZ-1, a Monomeric Subclass B3 Metallo-β-lactamase from *Fluoribacter gormanii*, in Native Form and in Complex with d-Captopril. Journal of Molecular Biology, 325(4), 651–660.

Geng, L., Wang, Z., Yang, X., Li, D., Lian, W., Xiang, Z., Wang, W., Bu, X., Lai, W., Hu, Z., & Fang, Q. (2015). Structure-based Design of Peptides with High Affinity and Specificity to HER2 Positive Tumors. Theranostics, 5(10), 1154–1165.

Ghuysen, J. M. (1991). Serine β-Lactamases and Penicillin-Binding Proteins. Annu. Rev. Microbiol., 45(1), 37–67.

Goldberg, S. D., Iannuccilli, W., Nguyen, T., Ju, J., & Cornish, V. W. (2003). Identification of residues critical for catalysis in a class C β-lactamase by combinatorial scanning mutagenesis. Protein Science, 12(8), 1633–1645.

Golemi, D., Maveyraud, L., Vakulenko, S., Samama, J.-P., & Mobashery, S. (2001). Critical involvement of a carbamylated lysine in catalytic function of class D β-lactamases. Proceedings of the National Academy of Sciences, 98(25), 14280–14285.

Golemi-Kotra, D., Meroueh, S. O., Kim, C., Vakulenko, S. B., Bulychev, A., Stemmler, A. J., Stemmler, T. L., & Mobashery, S. (2004). The Importance of a Critical Protonation State and the Fate of the Catalytic Steps in Class A β-Lactamases and Penicillin-binding Proteins. Journal of Biological Chemistry, 279(33), 34665–34673.

González, L. J., Bahr, G., Nakashige, T. G., Nolan, E. M., Bonomo, R. A., & Vila, A. J. (2016). Membrane anchoring stabilizes and favors secretion of New Delhi metallo-β-lactamase. Nature Chemical Biology, 12(7), 516–522.

Goulet, D.R., Chatterjee, S., Lee, W.-P., Waight, A.B., Zhu, Y., & Mak, A.N.-S. (2022). Engineering an Enhanced EGFR Engager: Humanization of Cetuximab for Improved Developability. Antibodies, 11, 6.

Guérin V., Thiry D., Lucas P., Blanchard Y., Cawez F., Mercuri P.S., Galleni M., Saulmont M., & Mainil M. (2021). Identification of β-Lactamase-Encoding (bla) Genes in Phenotypically β-Lactam-Resistant Escherichia coli Isolated from Young Calves in Belgium. Microbial Drug Resistance, 27(11), 1578-1584.

Hajjaji, H. E., Dumoulin, M., Matagne, A., Colau, D., Roos, G., Messens, J., & Collet, J.-F. (2009). The Zinc Center Influences the Redox and Thermodynamic Properties of Escherichia coli Thioredoxin 2. Journal of Molecular Biology, 386(1), 60–71.

Hamrick, J. C., Docquier, J.-D., Uehara, T., Myers, C. L., Six, D. A., Chatwin, C. L., John, K. J., Vernacchio, S. F., Cusick, S. M., Trout, R. E. L., Pozzi, C., De Luca, F., Benvenuti, M., Mangani, S., Liu, B., Jackson, R. W. Moeck, G., Xerri, L., Burns, C. J., Pevear, D. C., & Daigle, D. M. (2019). VNRX-5133 (Taniborbactam), a broad-spectrum inhibitor of serine- and metallo-β-lactamases, restores activity of cefepime in Enterobacterales and *Pseudomonas aeruginosa*. Antimicrobial Agents and Chemotherapy,64(3): e01963-19.

Harris, P. (2015). Clinical Management of Infections Caused by *Enterobacteriaceae* that Express Extended-Spectrum β-Lactamase and AmpC Enzymes. Seminars in Respiratory and Critical Care Medicine, 36(01), 056–073.

Hermann, J. C., Hensen, C., Ridder, L., Mulholland, A. J., & Höltje, H.-D. (2005). Mechanisms of Antibiotic Resistance: QM/MM Modeling of the Acylation Reaction of a Class A β-Lactamase with Benzylpenicillin. Journal of the American Chemical Society, 127(12), 4454–4465.

Hernandez Valladares, M., Felici, A., Weber, G., Adolph, H. W., Zeppezauer, M., Rossolini, G. M., Amicosante, G., Frère, J.-M., & Galleni, M. (1997). Zn(II) Dependence of the *Aeromonas hydrophila* AE036 Metallo-β-lactamase Activity and Stability†. Biochemistry, 36(38), 11534–11541.

Hobson, C. A., Pierrat, G., Tenaillon, O., Bonacorsi, S., Bercot. B., Jaouen, E., Jacquier, H., Birgy, A. (2022). *Klebsiella pneumoniae* Carbapenemase Variants Resistant to Ceftazidime-Avibactam: an Evolutionary Overview. Antimicrob Agents Chemother, 66(9): e0044722.

Horn, J. R., & Shoichet, B. K. (2004). Allosteric Inhibition Through Core Disruption. Journal of Molecular Biology, 336(5), 1283–1291.

Horsfall, L. E., Izougarhane, Y., Lassaux, P., Selevsek, N., Liénard, B. M. R., Poirel, L., Kupper, M. B., Hoffman, K. M., Frère, J.-M., Galleni, M., & Bebrone, C. (2011). Broad antibiotic resistance profile of the subclass B3 metallo-β-lactamase GOB-1, a di-zinc enzyme. FEBS Journal, 278(8), 1252–1263.

Gao, Hua., Liu, Yudong., Wang, Ruobing., Wang, Qi., Jin, Longyang., & Wang, Hui. (2020). The transferability and evolution of NDM-1 and KPC-2 co-producing *Klebsiella pneumoniae* from clinical settings. EBioMedicine, 51, 102599.

Huang, L., So, P., Chen, Y. W., leung, yun-chung, & Yao, Z.-P. (2020). Conformational Dynamics of Helix 10 Region as An Allosteric Site in Class A β-Lactamase Inhibitory Binding. Journal of the American Chemical Society, 142, 13756-13767.

Huang, L., Wu, C., Gao, H., Xu, C., Dai, M., Huang, L., Hao, H., Wang, X., & Cheng, G. (2022). Bacterial Multidrug Efflux Pumps at the Frontline of Antimicrobial Resistance: An Overview. Antibiotics, 11(4), 520.

Hujer, A. M., Page, M. G. P., Helfand, M. S., Yeiser, B., & Bonomo, R. A. (2002). Development of a Sensitive and Specific Enzyme-Linked Immunosorbent Assay for Detecting and Quantifying CMY-2 and SHV β-Lactamases. Journal of Clinical Microbiology, 40(6), 1947–1957.

Hultberg, A., Temperton, N. J., Rosseels, V., Koenders, M., Gonzalez-Pajuelo, M., Schepens, B., Ibanez, L. I., Vanlandschoot, P., Schillemans, J., Saunders, M., Weiss, R. A., Saelens, X., Melero, J. A., Verrips, C. T., Van Gucht, S., & de Haard, H. J. (2011). Llama-Derived Single Domain Antibodies to Build Multivalent, Superpotent and Broadened Neutralizing Anti-Viral Molecules. PLoS ONE, 6(4), e17665.

Huntley, J. J. A., Fast, W., Benkovic, S. J., Wright, P. E., & Dyson, H. J. (2003). Role of a solvent-exposed tryptophan in the recognition and binding of antibiotic substrates for a metallo-β-lactamase. Protein Science, 12(7), 1368–1375.

Imtiaz, U., Billings, E., Knox, J. R., Manavathu, E. K., Lerner, S. A., & Mobashery, S. (1993). Inactivation of class A β-lactamases by clavulanic acid: the role of arginine-244 in a proposed nonconcerted sequence of events. Journal of the American Chemical Society, 115(11), 4435–4442.

Imtiaz, U., Billings, E. M., Knox, J. R., & Mobashery, S. (1994). A Structure-Based Analysis of the Inhibition of Class A β-Lactamases by Sulbactam. Biochemistry, 33(19), 5728–5738.

Inoue, A., Ohmuro-Matsuyama, Y., Kitaguchi, T., & Ueda, H. (2020). Creation of a Nanobody-Based Fluorescent Immunosensor Mini Q-body for Rapid Signal-On Detection of Small Hapten Methotrexate. ACS Sensors, 5(11), 3457-3464.

Jacob, F., Joris, B., Lepage, S., Dusart, J., & Frère, J. M. (1990). Role of the conserved amino acids of the "SDN" loop (Ser130, Asp131and Asn132) in a class A β-lactamase studied by site-directed mutagenesis. Biochemical Journal, 271(2), 399–406.

Jacquin, O., Balbeur, D., Damblon, D., Marchot, P., De Pauw, E., Roberts, G. C. K., Frère, J.-M., & Matagne, A. (2009). Positively Cooperative Binding of Zinc Ions to *Bacillus cereus* 569/H/9 β-Lactamase II Suggests that the Binuclear Enzyme Is the Only Relevant Form for Catalysis. JMB, 392(5), 1278–1291.

Jaurin, B., & Grundstrom, T. (1981). ampC cephalosporinase of *Escherichia coli* K-12 has a different evolutionary origin from that of beta-lactamases of the penicillinase type. Proceedings of the National Academy of Sciences, 78(8), 4897–4901.

Jenkins, S., Ledeboer, N.A., Westblade, L.F., Burnham, C.A., Faron, M.L., Bergman, Y., Yee, R., Mesich, B., Gerstbrein, D., Wallace, M.A., Robertson, A., Fauntleroy, K.A., Klavins, A.S., Malherbe, R., Hsiung, A., Simner, P.J. (2020). Evaluation of NG-Test Carba 5 for Rapid Phenotypic Detection and Differentiation of Five Common Carbapenemase Families: Results of a Multicenter Clinical Evaluation. J Clin Microbiol, 58(7): e00344-20.

Jeon, J., Lee, J., Lee, J., Park, K., Karim, A., Lee, C.-R., Jeong, B, C., & Lee, S. (2015). Structural Basis for Carbapenem-Hydrolyzing Mechanisms of Carbapenemases Conferring Antibiotic Resistance. International Journal of Molecular Sciences, 16(12), 9654–9692.

June, C. M., Vallier, B. C., Bonomo, R. A., Leonard, D. A., & Powers, R. A. (2013). Structural Origins of Oxacillinase Specificity in Class D β-Lactamases. Antimicrobial Agents and Chemotherapy, 58(1), 333–341.

Kabsch, W. (2010). XDS. Acta Crystallographica Section D Biological Crystallography, 66(2), 125–132.

Kapoor, G., Saigal, K., & Elongavan, A. (2017). Action and resistance mechanisms of antibiotics: A guide for clinicians. Journal of Anaesthesiology Clinical Pharmacology, 33(3), 300-305.

Karami, E., Sabatier, J.-M., Behdani, M., Irani, S., & Kazemi-Lomedasht, F. (2020). A nanobody-derived mimotope against VEGF inhibits cancer angiogenesis. Journal of Enzyme Inhibition and Medicinal Chemistry, 35(1), 1233–1239.

Karlowsky, J. A., Lob, S. H., Kazmierczak, K. M., Badal, R. E., Young, K., Motyl, M. R., & Sahm, D. F. (2017). In Vitro Activity of Imipenem against Carbapenemase-Positive *Enterobacteriaceae* Isolates Collected by the SMART Global Surveillance Program from 2008 to 2014. Journal of Clinical Microbiology, 55(6), 1638–1649.

Karsisiotis, A. I., Damblon, C. F., & Roberts, G. C. K. (2013). Solution structures of the *Bacillus cereus* metallo-β-lactamase BcII and its complex with the broad spectrum inhibitor R-thiomandelic acid. Biochemical Journal, 456(3), 397–407.

Kato-Toma, Y., Iwashita, T., Masuda, K., Oyama, Y., & Ishiguro, M. (2003). pKa measurements from nuclear magnetic resonance of tyrosine-150 in class C beta-lactamase. Biochemical Journal, 371(1), 175–181.

Kay, L. E., Torchia, D. A., & Bax, A. (1989). Backbone dynamics of proteins as studied by nitrogen-15 inverse detected heteronuclear NMR spectroscopy: application to staphylococcal nuclease. Biochemistry, 28(23), 8972–8979.

Ke, W., Bethel, C. R., Thomson, J. M., Bonomo, R. A., & van den Akker, F. (2007). Crystal Structure of KPC-2: Insights into Carbapenemase Activity in Class A β-Lactamases†,‡. Biochemistry, 46(19), 5732–5740.

Keyaerts, M., Xavier, C., Heemskerk, J., Devoogdt, N., Everaert, H., Ackaert, C., Vanhoeij, M., Duhoux, F. P., Gevaert, T., Simon. P., Schallier, D., Fontaine, C., Vaneycken, I., Vanhove, C., De Greve, J., Lamote, J., Caveliers, V., & Lahoutte, T. (2016). Phase I Study of 68Ga-HER2-Nanobody for PET/CT Assessment of HER2 Expression in Breast Carcinoma. Journal of Nuclear Medicine, 57(1), 27–33.

Kim, J. Y., Jung, H. I., An, Y. J., Lee, J. H., Kim, S. J., Jeong, S. H., Lee, K. J., Suh, P-G., Lee, H-S., Lee, S. H., & Cha, S.-S. (2006). Structural basis for the extended substrate spectrum of CMY-10, a plasmid-encoded class C β-lactamase. Molecular Microbiology, 60(4), 907–916.

King, D., & Strynadka, N. (2011). Crystal structure of New Delhi metallo-β-lactamase reveals molecular basis for antibiotic resistance. Protein Science, 20(9), 1484–1491.

King, D. T., Worrall, L. J., Gruninger, R., & Strynadka, N. C. J. (2012). New Delhi Metallo-β-Lactamase: Structural Insights into β-Lactam Recognition and Inhibition. Journal of the American Chemical Society, 134(28), 11362–11365.

Kloezen, W., Melchers, R. J., Georgiou, P. C., Mouton, J. W., & Meletiadis, J. (2021). Activity of Cefepime in Combination with the Novel β-Lactamase Inhibitor Taniborbactam (VNRX-5133) against Extended-Spectrum-β-Lactamase-Producing Isolates in In Vitro Checkerboard Assays. Antimicrob Agents Chemother, 65(4): e02338-20.

Kohanski, M. A., Dwyer, D. J., & Collins, J. J. (2010). How antibiotics kill bacteria: from targets to networks. Nature Reviews Microbiology, 8(6), 423–435.

Koide, S. (2009). Engineering of recombinant crystallization chaperones. Current Opinion in Structural Biology, 19(4), 449–457.

Krishnan, N. P., Nguyen, N. Q., Papp-Wallace, K. M., Bonomo, R. A., & van den Akker, F. (2015). Inhibition of Klebsiella β-Lactamases (SHV-1 and KPC-2) by Avibactam: A Structural Study. PLOS ONE, 10(9): e0136813.

Kuga, A., Okamoto, R., & Inoue, M. (2000). ampR Gene Mutations That Greatly Increase Class C beta - Lactamase Activity in *Enterobacter cloacae*. Antimicrobial Agents and Chemotherapy, 44(3), 561–567.

Kuzmanic, A., & Zagrovic, B. (2010). Determination of Ensemble-Average Pairwise Root Mean-Square Deviation from Experimental B-Factors. Biophysical Journal, 98(5), 861–871.

Lahiri, S. D., Mangani, S., Durand-Reville, T., Benvenuti, M., De Luca, F., Sanyal, G., & Docquier, J.-D. (2013). Structural Insight into Potent Broad-Spectrum Inhibition with Reversible Recyclization Mechanism: Avibactam in Complex with CTX-M-15 and *Pseudomonas aeruginosa* AmpC β-Lactamases. Antimicrobial Agents and Chemotherapy, 57(6), 2496–2505.

Lahiri, S. D., Mangani, S., Jahić, H., Benvenuti, M., Durand-Reville, T. F., De Luca, F., Ehmann, D. E., Rossolini, G. M., Alm, R. A. & Docquier, J.-D. (2014). Molecular Basis of Selective Inhibition and Slow Reversibility of Avibactam against Class D Carbapenemases: A Structure-Guided Study of OXA-24 and OXA-48. ACS Chemical Biology, 10(2), 591–600.

Lamotte-Brasseur, J., Dive, G., Dideberg, O., Charlier, P., Frère, J. M., & Ghuysen, J. M. (1991). Mechanism of acyl transfer by the class A serine β-lactamase of *Streptomyces albus G*. Biochemical Journal, 279(1), 213–221.

Lange, F., Pfennigwerth, N., Hartl, R., Kerschner, H., Achleitner, D., Gatermann, S. G., & Kaase, M. (2018). LMB-1, a novel family of class B3 MBLs from an isolate of *Enterobacter cloacae*. Journal of Antimicrobial Chemotherapy, 73(9), 2331–2335.

Langley, G. W., Cain, R., Tyrrell, J. M., Hinchliffe, P., Calvopiña, K., Tooke, C. L., Widlake, E., Dowson, C. G., Spencer, J., Walsh, T. R., Schofield, C. J., & Brem, J. (2019). Profiling interactions of vaborbactam with metallo-β-lactamases. Bioorganic & Medicinal Chemistry Letters, 29(15), 1981–1984.

Lauretti, L., Riccio, M. L., Mazzariol, A., Cornaglia, G., Amicosante, G., Fontana, R., & Rossolini, G. M. (1999). Cloning and Characterization of blaVIM, a New Integron-Borne Metallo-β-Lactamase Gene from a *Pseudomonas aeruginosa* Clinical Isolate. Antimicrobial Agents and Chemotherapy, 43(7), 1584–1590.

Lee Y, Kim J, & Trinh S. (2019). Meropenem-Vaborbactam (Vabomere™): Another Option for Carbapenem-Resistant *Enterobacteriaceae*. P T. 44(3):110-113.

Lejeune, A., Vanhove, M., Lamotte-Brasseur, J., Pain, R. H., Frère, J.-M., & Matagne, A. (2001). Quantitative analysis of the stabilization by substrate of *Staphylococcus aureus* PC1 β-lactamase. Chemistry & Biology, 8(8), 831–842.

Leonard, D. A., Bonomo, R. A., & Powers, R. A. (2013). Class D β-Lactamases: A Reappraisal after Five Decades. Accounts of Chemical Research, 46(11), 2407–2415.

Levitt M. H. (2008). Spin dynamics, Basics of Nuclear Magnetic Resonance, John Wiley & Sons Inc. 740 Pages.

Li, T., Li, S. L., Fang, C., Hou, Y. N., Zhang, Q., Du, X., Lee, H. C., & Zhao, Y. J. (2018). Nanobody-based dual epitopes protein identification (DepID) assay for measuring soluble CD38 in plasma of multiple myeloma patients. Analytica Chimica Acta, 1029, 65–71.

Li, Z.-F., Dong, J.-X., Vasylieva, N., Cui, Y.-L., Wan, D.-B., Hua, X.-D., Huo, J.-Q., Yang, D.-C., Gee, S. J., & Hammock, B. D. (2021). Highly specific nanobody against herbicide 2,4-dichlorophenoxyacetic acid for monitoring of its contamination in environmental water. Science of The Total Environment, 753, 141950.

Liebschner, D., Afonine, P. V., Baker, M. L., Bunkóczi, G., Chen, V. B., Croll, T. I., Hintze, B., Hung, L. W., Jain, S., McCoy, A. J., Moriarty, N. W., Oeffner, R. D., Poon, B. K., Prisant, M. G., Read, R. J., Richardson, J. S., Richardson, D. C., Sammito, M. D., Sobolev, O. V., Stockwell, D. H., Terwilliger, T. C., Urzhumtsev, A. G., Videau, L. L., Williams, C. J., & Adams, P. D. (2019). Macromolecular structure determination using X-rays, neutrons and electrons: recent developments in Phenix. Acta Crystallogr D Struct Biol, 75, 861-877.

Lim, D., & Strynadka, N. C. J. (2002). Structural basis for the β lactam resistance of PBP2a from methicillin-resistant *Staphylococcus aureus*. Nature Structural Biology, 9(11), 870-76.

Lindahl, E., Hess, B., & van der Spoel, D. (2001). GROMACS 3.0: a package for molecular simulation and trajectory analysis. Journal of Molecular Modeling, 7(8), 306–317.

Lipari, G., & Szabo, A. (1982). Model-free approach to the interpretation of nuclear magnetic resonance relaxation in macromolecules. 1. Theory and range of validity. Journal of the American Chemical Society, 104(17), 4546–4559.

Lipman, N. S., Jackson, L. R., Trudel, L. J., & Weis-Garcia, F. (2005). Monoclonal Versus Polyclonal Antibodies: Distinguishing Characteristics, Applications, and Information Resources. ILAR Journal, 46(3), 258–268.

Lisa, M.-N., Palacios, A. R., Aitha, M., González, M. M., Moreno, D. M., Crowder, M. W., Bonomo, R. A., Spencer, J., Tierney, D. L., Llarrull, L. I., & Vila, A. J. (2017). A general reaction mechanism for carbapenem hydrolysis by mononuclear and binuclear metallo-β-lactamases. Nature Communications, 8(1).

Liu, B., Trout, R. E. L., Chu, G.-H., McGarry, D., Jackson, R. W., Hamrick, J., Daigle, S. M., Pozzi, C., De Luca, F., Benvenuti, M., Mangani, S., Docquier, J.-D., Weiss, W. J., Pevear, D. C., Xerri, L., & Burns, C. J. (2019). Discovery of Taniborbactam (VNRX-5133): A Broad-Spectrum Serine- and Metallo-β-Lactamase Inhibitor for Carbapenem-Resistant Bacterial Infections. Journal of Medicinal Chemistry, 63(6), 2789-2801.

Liu, M., Li, L., Jin, D., & Liu, Y. (2021). Nanobody—A versatile tool for cancer diagnosis and therapeutics. WIREs Nanomedicine and Nanobiotechnology, 13(4): e1697.

Lomovskaya, O., Sun, D., Rubio-Aparicio, D., Nelson, K., Tsivkovski, R., Griffith, D. C., & Dudley, M. N. (2017). Vaborbactam: Spectrum of Beta-Lactamase Inhibition and Impact of Resistance Mechanisms on Activity in *Enterobacteriaceae*. Antimicrobial Agents and Chemotherapy, 61(11): e01443-17.

Lu, W.-P., Kincaid, E., Sun, Y., & Bauer, M. D. (2001). Kinetics of β-Lactam Interactions with Penicillin-susceptible and -resistant Penicillin-binding Protein 2x Proteins from *Streptococcus pneumoniae*. Journal of Biological Chemistry, 276(34), 31494–31501.

Luan, Y., Li, G.-L., Duo, L.-B., Wang, W.-P., Wang, C.-Y., Zhang, H.-G., He, F., He, X., Chen, S.-J., & Luo, D.-T. (2014). DHA-1 plasmid-mediated AmpC β-lactamase expression and regulation of *Klebsiella pneumoniae* isolates. Molecular Medicine Reports, 11, 3069-3077.

Ma, G., Wang, S., Wu, K., Zhang, W., Ahmad, A., Hao, Q., Lei, X., & Zhang, H. (2021). Structure-guided optimization of D-captopril for discovery of potent NDM-1 inhibitors. Bioorganic & Medicinal Chemistry, 29, 115902.

Majewski, P., Wieczorek, P., Ojdana, D., Sieńko, A., Kowalczuk, O., Sacha, P., Niklinski, J., & Tryniszewska, E. (2016). Altered Outer Membrane Transcriptome Balance with AmpC Overexpression in Carbapenem-Resistant *Enterobacter cloacae*. Frontiers in Microbiology, 7 :2054.

Majumdar, R.D. (2015). A nuclear magnetic resonance spectroscopic investigation of the molecular structure and aggregation behavior of asphaltenes. DOI: 10.13140/RG.2.1.4929.5765.

Mandel, A. M., Akke, M., & Palmer, III, A. G. (1995). Backbone Dynamics of *Escherichia coli* Ribonuclease HI: Correlations with Structure and Function in an Active Enzyme. Journal of Molecular Biology, 246(1), 144–163.

Marciano, D. C., Brown, N. G., & Palzkill, T. (2009). Analysis of the plasticity of location of the Arg244 positive charge within the active site of the TEM-1 β-lactamase. Protein Science, 18(10), 2080–2089.

Marcoccia, F., Bottoni, C., Sabatini, A., Colapietro, M., Mercuri, P. S., Galleni, M., Kerff, F., Matagne, A., Celenza, G., Amicosante, G., & Perilli, M. (2016). Kinetic Study of Laboratory Mutants of NDM-1 Metallo-β-Lactamase and the Importance of an Isoleucine at Position 35. Antimicrobial Agents and Chemotherapy, 60(4), 2366–2372.

Martin, C., Moors, S. L. C., Danielsen, M., Betti, C., Fabris, C., Sejer Pedersen, D., Pardon, E., Peyressatre, M., Fehér, K., Martins, J. C., Mathiesen, J. M., Morris, M. C., Devoogdt, N., Caveliers, V., De Proft, F., Steyaert, J., & Ballet, S. (2017). Rational Design of Nanobody80 Loop Peptidomimetics: Towards Biased β2 Adrenergic Receptor Ligands. Chemistry - A European Journal, 23(40), 9632–9640.

Massidda, O., Rossolini, G. M., & Satta, G. (1991). The Aeromonas hydrophila cphA gene: molecular heterogeneity among class B metallo-β-lactamases. Journal of Bacteriology, 173(15), 4611–4617.

Matagne, A., Lamotte-Brasseur, J., & Frère, J.-M. (1998). Catalytic properties of class A β-lactamases: efficiency and diversity. Biochemical Journal, 330(2), 581–598.

Mauri, C., Maraolo, A.E., Di Bella, S., Luzzaro, F., & Principe, L. (2021). The Revival of Aztreonam in Combination with Avibactam against Metallo-β-Lactamase-Producing Gram-Negatives: A Systematic Review of In Vitro Studies and Clinical Cases. Antibiotics (Basel), 10(8):1012.

Maveyraud, L., Saves, I., Burlet-Schiltz, O., Swarén, P., Masson, J.-M., Delaire, M., Mourey, L., Promé, J.-C., & Samama, J.-P. (1996). Structural Basis of Extended Spectrum TEM β-Lactamases. Journal of Biological Chemistry, 271(18), 10482–10489.

Maveyraud, L., Mourey, L., Kotra, L. P., Pedelacq, J.-D., Guillet, V., Mobashery, S., & Samama, J.-P. (1998). Structural Basis for Clinical Longevity of Carbapenem Antibiotics in the Face of Challenge by the Common Class A β-Lactamases from the Antibiotic-Resistant Bacteria. Journal of the American Chemical Society, 120(38), 9748–9752.

Maveyraud, L., Golemi, D., Kotra, L. P., Tranier, S., Vakulenko, S., Mobashery, S., & Samama, J.-P. (2000). Insights into Class D β-Lactamases Are Revealed by the Crystal Structure of the OXA10 Enzyme from *Pseudomonas aeruginosa*. Structure, 8(12), 1289–1298.

McCoy, A. J., Grosse-Kunstleve, R. W., Adams, P. D., Winn, M. D., Storoni, L. C., & Read, R. J. (2007). Phaser crystallographic software. Journal of Applied Crystallography, 40(4), 658–674.

Meini, S., Tascini, C., Cei, M., Sozio, E., & Rossolini, G. M. (2019). AmpC β-lactamase-producing Enterobacterales: what a clinician should know. Infection, 47(3), 363–375.

Meneksedag, D., Dogan, A., Kanlikilicer, P., & Ozkirimli, E. (2013). Communication between the active site and the allosteric site in class A beta-lactamases. Computational Biology and Chemistry, 43, 1–10.

Meroueh, S. O., Roblin, P., Golemi, D., Maveyraud, L., Vakulenko, S. B., Zhang, Y., Samama, J.-P., & Mobashery, S. (2002). Molecular Dynamics at the Root of Expansion of Function in the M69L Inhibitor-Resistant TEM β-Lactamase from *Escherichia coli*. Journal of the American Chemical Society, 124(32), 9422–9430.

Meroueh, S. O., Fisher, J. F., Schlegel, H. B., & Mobashery, S. (2005). Ab Initio QM/MM Study of Class A β-Lactamase Acylation: Dual Participation of Glu166 and Lys73 in a Concerted Base Promotion of Ser70. Journal of the American Chemical Society, 127(44), 15397–15407.

Miltgen, G., Martak, D., Valot, B., Kamus, L., Garrigos, T., Verchere, G., Gbaguidi-Haore, H., Ben Cimon, C., Ramiandrisoa, M., Picot, S., Lignereux, A., Masson, G., Jaffar-Bandjee, MC., Belmonte, O., Cardinale, E., Hocquet, D., Mavingui, P., & Bertrand, X. (2022) One Health compartmental analysis of ESBL-producing *Escherichia coli* on Reunion Island reveals partitioning between humans and livestock. J Antimicrob Chemother, 77(5), 1254-1262.

Mollard, C., Moali, C., Papamicael, C., Damblon, C., Vessilier, S., Amicosante, G., Schofield, C. J., Galleni, M., Frère, J.-M., & Roberts, G. C. K. (2001). Thiomandelic Acid, a Broad Spectrum Inhibitor of Zinc β-Lactamases. Journal of Biological Chemistry, 276(48), 45015–45023.

Morales-Yanez, F., Trashin, S., Hermy, M. R. G., Sariego, I., Polman, K., Muyldermans, S., & De Wael, K. (2019). Fast One-Step Ultrasensitive Detection of *Toxocara canis* Antigens by a Nanobody-Based Electrochemical Magnetosensor. Analytical Chemistry, 91, 11582-88.

Mosley, J. F., Smith, L. L., Parke, C. K., Brown, J. A., Wilson, A. L., & Gibbs, L. V. (2016). Ceftazidime-Avibactam (Avycaz): For the Treatment of Complicated Intra-Abdominal and Urinary Tract Infections. P T. 41(8), 479-83.

Moutel, S., Bery, N., Bernard, V., Keller, L., Lemesre, E., de Marco, A., Ligat, L., Rain, J.-C., Favre, G., Olichon, A., & Perez, F. (2016). NaLi-H1: A universal synthetic library of humanized nanobodies providing highly functional antibodies and intrabodies. eLife, 5: e16228.

Morin, S., & Gagné, S. M. (2009). NMR Dynamics of PSE-4 β-Lactamase: An Interplay of ps-ns Order and µs-ms Motions in the Active Site. Biophysical Journal, 96(11), 4681–4691.

Muyldermans, S. (2013). Nanobodies: Natural Single-Domain Antibodies. Annual Review of Biochemistry, 82(1), 775–797.

Muyldermans, S. (2020). Applications of Nanobodies. Annual Review of Animal Biosciences, 9(1), 401-421.

Naas, T., Sougakoff, W., Casetta, A., & Nordmann, P. (1998). Molecular Characterization of OXA-20, a Novel Class D β-Lactamase, and Its Integron from *Pseudomonas aeruginosa*. Antimicrobial Agents and Chemotherapy, 42(8), 2074–2083.

Ness, S., Martin, R., Kindler, A. M., Paetzel, M., Gold, M., Jensen, S. E., Jones, J. B., & Strynadka, N. C. J. (2000). Structure-Based Design Guides the Improved Efficacy of Deacylation Transition State Analogue Inhibitors of TEM-1 β-Lactamase†,#. Biochemistry, 39(18), 5312–5321.

Nukaga, M., Bethel, C. R., Thomson, J. M., Hujer, A. M., Distler, A., Anderson, V. E., Knox, J, R., & Bonomo, R. A. (2008). Inhibition of Class A β-Lactamases by Carbapenems: Crystallographic Observation of Two Conformations of Meropenem in SHV-1. Journal of the American Chemical Society, 130(38), 12656–12662.

Oefner, C., D'Arcy, A., Daly, J. J., Gubernator, K., Charnas, R. L., Heinze, I., Hubschwerlen, F. K., & Winkler, F. K. (1990). Refined crystal structure of β-lactamase from *Citrobacter freundii* indicates a mechanism for β-lactam hydrolysis. Nature, 343(6255), 284–288.

Olehnovics, E., Yin, J., Pérez, A., De Fabritiis, G., Bonomo, R. A., Bhowmik, D., & Haider, S. (2021) The Role of Hydrophobic Nodes in the Dynamics of Class A β-Lactamases. Front. Microbiol. 12:720991.

O'Neill J. (2016). Tackling drug-resistant infections globally: final report and recommendations. London: Review on Antimicrobial Resistance.

Orencia, M. C., Yoon, J. S., Ness, J. E., Stemmer, W. P. C., & Stevens, R. C. (2001). Nature Structural Biology, 8(3), 238–242.

Oueslati, S., Volland, H., Cattoir, V., Bernabeu, S., Girlich, D., Dulac, D., Plaisance, M., Laroche, M., Dortet, L., Simon, S., & Naas, T. (2021). Development and validation of a lateral flow immunoassay for rapid detection of VanA-producing enterococci. J Antimicrob Chemother, 76(1), 146-151.

Palmeira, J. D., Cunha, M. V., Carvalho, J., Ferreira, H., Fonseca, C., & Torres, R. T. (2021). Emergence and Spread of Cephalosporinases in Wildlife: A Review. Animals, 11, 1765.

Palzkill, T. (2018). Structural and Mechanistic Basis for Extended-Spectrum Drug-Resistance Mutations in Altering the Specificity of TEM, CTX-M, and KPC β-lactamases. Frontiers in Molecular Biosciences, 5.

Pandya, A., Howard, M., Zloh, M., & Dalby, P. (2018). An Evaluation of the Potential of NMR Spectroscopy and Computational Modelling Methods to Inform Biopharmaceutical Formulations. Pharmaceutics, 10(4), 165.

Papanicolaou, G. A., Medeiros, A. A., & Jacoby, G. A. (1990). Novel plasmid-mediated β-lactamase (MIR-1) conferring resistance to oxyimino- and alpha-methoxy beta-lactams in clinical isolates of *Klebsiella pneumoniae*. Antimicrobial Agents and Chemotherapy, 34(11), 2200–2209.

Pardon, E., Laeremans, T., Triest, S., Rasmussen, S. G. F., Wohlkönig, A., Ruf, A., Muyldermans, S., Hol, W. G. J., Kobilka, B. K., & Steyaert, J. (2014). A general protocol for the generation of Nanobodies for structural biology. Nature Protocols, 9(3), 674–693.

Parker, A. C., & Smith, C J (1993). Genetic and biochemical analysis of a novel Ambler class A β-lactamase responsible for cefoxitin resistance in Bacteroides species. Antimicrobial Agents and Chemotherapy, 37(5), 1028–1036.

Patera, A., Blaszczak, L. C., & Shoichet, B. K. (2000). Crystal Structures of Substrate and Inhibitor Complexes with AmpC β-Lactamase: Possible Implications for Substrate-Assisted Catalysis. Journal of the American Chemical Society, 122(43), 10504–10512.

Pemberton, O. A., Zhang, X., & Chen, Y. (2017). Molecular Basis of Substrate Recognition and Product Release by the *Klebsiella pneumoniae* Carbapenemase (KPC-2). Journal of Medicinal Chemistry, 60(8), 3525–3530.

Pemberton, O. A., Tsivkovski, R., Totrov, M., Lomovskaya, O., & Chen, Y. (2020). Structural basis and binding kinetics of vaborbactam in class A β-lactamase inhibition. Antimicrobial Agents and Chemotherapy, 64(10): e00398-20.

Peter-Getzlaff, S., Polsfuss, S., Poledica, M., Hombach, M., Giger, J., Bottger, E. C., & Bloemberg, G. V. (2011). Detection of AmpC Beta-Lactamase in *Escherichia coli*: Comparison of Three Phenotypic Confirmation Assays and Genetic Analysis. Journal of Clinical Microbiology, 49(8), 2924–2932.

Philippon, A., Arlet, G., & Jacoby, G. A. (2002). Plasmid-Determined AmpC-Type β-Lactamases. Antimicrobial Agents and Chemotherapy, 46(1), 1–11.

Philippon, A., Jacquier, H., Ruppé, E., & Labia, R. (2019). Structure-based classification of class A β-lactamases, an update. Current Research in Translational Medicine.

Piccirilli, A., Criscuolo, E., Brisdelli, F., Mercuri, P. S., Cherubini, S., De Sciscio, M. L., Maccarrone, M., Galleni, M., Amicosante, G., & Perilli, M. (2021). Exploring the Role of L10 Loop in New Delhi Metallo-β-lactamase (NDM-1): Kinetic and Dynamic Studies. Molecules, 26(18):5489.

Pietsch, M., Irrgang, A., Roschanski, N., Brenner M. G., Hamprecht, A., Rieber, H., Käsbohrer, A., Schwarz, S., Rösler, U., Kreienbrock, L., Pfeifer, Y., Fuchs, S., & Werner, G. (2018). Whole genome analyses of CMY-2-producing *Escherichia coli* isolates from humans, animals and food in Germany. BMC Genomics, 19(1), 601–618.

Poirel, L., Heritier, C., Tolun, V., & Nordmann, P. (2003). Emergence of Oxacillinase-Mediated Resistance to Imipenem in *Klebsiella pneumoniae*. Antimicrobial Agents and Chemotherapy, 48(1), 15–22.

Poirel, L., Benouda, A., Hays, C., & Nordmann, P. (2011). Emergence of NDM-1-producing *Klebsiella pneumoniae* in Morocco. Journal of Antimicrobial Chemotherapy, 66(12), 2781–2783.

Prestinaci, F., Pezzotti, P., & Pantosti, A. (2015). Antimicrobial resistance: a global multifaceted phenomenon. Pathogens and Global Health, 109(7), 309–318.

Quale, J., Bratu, S., Gupta, J., & Landman, D. (2006). Interplay of Efflux System, ampC, and oprD Expression in Carbapenem Resistance of *Pseudomonas aeruginosa* Clinical Isolates. Antimicrobial Agents and Chemotherapy, 50(5), 1633–1641.

Ramachandran, R., Noorbakhsh, F., DeFea, K., & Hollenberg, M. D. (2012). Targeting proteinase-activated receptors: therapeutic potential and challenges. Nature Reviews Drug Discovery, 11(1), 69–86.

Raquet, X., Vanhove, M., Lamotte-Brasseur, J., Goussard, S., Courvalin, P., & Frère, J.-M. (1995). Stability of TEM β-lactamase mutants hydrolyzing third generation cephalosporins. Proteins: Structure, Function, and Genetics, 23(1), 63–72.

Reading, C., & Cole, M. (1977). Clavulanic Acid: a β-Lactamase-Inhibiting β-Lactam from *Streptomyces clavuligerus*. Antimicrobial Agents and Chemotherapy, 11(5), 852–857.

Reisbig, M. D., & Hanson, N. D. (2002). The ACT-1 plasmid-encoded AmpC β-lactamase is inducible: detection in a complex β-lactamase background. Journal of Antimicrobial Chemotherapy, 49(3), 557–560.

Roccatano, D., Sbardella, G., Aschi, M., Amicosante, G., Bossa, C., Nola, A. D., & Mazza, F. (2005). Dynamical Aspects of TEM-1 β-Lactamase Probed by Molecular Dynamics. Journal of Computer-Aided Molecular Design, 19(5), 329–340.

Rösner, S., Kamalanabhaiah, S., Küsters, U., Kolbert, M., Pfennigwerth, N., & Mack, D. (2019). Evaluation of a novel immunochromatographic lateral flow assay for rapid detection of OXA-48, NDM, KPC and VIM carbapenemases in multidrug-resistant *Enterobacteriaceae*. J Med Microbiol, 68(3), 379-381.

Sabath, L. D., & Abraham, E. P. (1966). Zinc as a Cofactor for Cephalosporinase from *Bacillus cereus569*. Biochemical Journal, 98(1), 11C–13C.

Sabir, J. S. M., Atef, A., El-Domyati, F. M., Edris, S., Hajrah, N., Alzohairy, A. M., & Bahieldin, A. (2014). Construction of naïve camelids VHH repertoire in phage display-based library. Comptes Rendus Biologies, 337(4), 244–249.

Saino, Y., Kobayashi, F., Inoue, M., & Mitsuhashi, S. (1982). Purification and properties of inducible penicillin β-lactamase isolated from *Pseudomonas maltophilia*. Antimicrobial Agents and Chemotherapy, 22(4), 564–570.

Sauvage, E., & Terrak, M. (2016). Glycosyltransferases and Transpeptidases/Penicillin-Binding Proteins: Valuable Targets for New Antibacterials. Antibiotics, 5(1), 12.

Savard, P.-Y., & Gagné, S. M. (2006). Backbone Dynamics of TEM-1 Determined by NMR: Evidence for a Highly Ordered Protein†. Biochemistry, 45(38), 11414–11424.

Saves, I., Burlet-Schiltz, O., Maveyraud, L., Samama, J.-P., Prome, J.-C., & Masson, J.-M. (1995a). Mass Spectral Kinetic Study of Acylation and Deacylation During the Hydrolysis of Penicillins and Cefotaxime by β-Lactamase TEM-1 and the G238S Mutant. Biochemistry, 34(37), 11660–11667.

Saves, I., Burlet-Schiltz, O., Swarn, P., Lefvre, F., Masson, J.-M., Prom, J.-C., & Samama, J.-P. (1995b). The Asparagine to Aspartic Acid Substitution at Position 276 of TEM-35 and TEM-36 Is Involved in the β-Lactamase Resistance to Clavulanic Acid. Journal of Biological Chemistry, 270(31), 18240–18245.

Scaife, W., Young, H.-K., Paton, R. H., & Amyes, S. G. B. (1995). Transferable imipenem-resistance in *Acinetobacter* species from a clinical source. Journal of Antimicrobial Chemotherapy, 36(3), 585–586.

Schmidtke, A. J., & Hanson, N. D. (2006). Model System To Evaluate the Effect of ampD Mutations on AmpC-Mediated β-Lactam Resistance. Antimicrobial Agents and Chemotherapy, 50(6), 2030–2037.

Schneider, K. D., Karpen, M. E., Bonomo, R. A., Leonard, D. A., & Powers, R. A. (2009). The 1.4 Å Crystal Structure of the Class D β-Lactamase OXA-1 Complexed with Doripenem. Biochemistry, 48(50), 11840–11847.

Schneider, K. D., Ortega, C. J., Renck, N. A., Bonomo, R. A., Powers, R. A., & Leonard, D. A. (2011). Structures of the Class D Carbapenemase OXA-24 from *Acinetobacter baumannii* in Complex with Doripenem. Journal of Molecular Biology, 406(4), 583–594.

Schønning, K., & Tvede, M. (2002). [Piperacillin/tazobactam--Tazocin. A penicillin-based alternative to 3rd generation cephalosporins and carbapenems]. Ugeskr Laeger, 164(20), 2606-10.

Schwechheimer, C., & Kuehn, M. J. (2015). Outer-membrane vesicles from Gram-negative bacteria: biogenesis and functions. Nature Reviews Microbiology, 13(10), 605–619.

Shcherbinin, D., Veselovsky, A., Rubtsova, M., Grigorenko, V., & Egorov, A. (2019). The impact of long-distance mutations on the Ω-loop conformation in TEM type β-lactamases. Journal of Biomolecular Structure and Dynamics, 1–13.

Simm, A. M., Higgins, C. S., Carenbauer, A. L., Crowder, M. W., Bateson, J. H., Bennett, P. M., Clarke, A. R., Halford, S. E., & Walsh, T. R. (2002). Characterization of Monomeric L1 Metallo-β-lactamase and the Role of the N-terminal Extension in Negative Cooperativity and Antibiotic Hydrolysis. Journal of Biological Chemistry, 277(27), 24744–24752.

Singh, M. K., & Dominy, B. N. (2012). The Evolution of Cefotaximase Activity in the TEM β-Lactamase. Journal of Molecular Biology, 415(1), 205–220.

Sohier, J. S., Laurent, C., Chevigné, A., Pardon, E., Srinivasan, V., Wernery, U., Lassaux, P., Steyaert, J., & Galleni, M. (2013). Allosteric inhibition of VIM metallo-β-lactamases by a camelid nanobody. Biochemical Journal, 450(3), 477–486.

Sowek, J. A., Singer, S. B., Ohringer, S., Malley, M. F., Dougherty, T. J., Gougoutas, J. Z., & Bush, K. (1991). Substitution of lysine at position 104 or 240 of TEM-1pTZ18R β-lactamase enhances the effect of serine-164 substitution on hydrolysis or affinity for cephalosporins and the monobactam aztreonam. Biochemistry, 30(13), 3179–3188.

Stewart, A. C., Bethel, C. R., VanPelt, J., Bergstrom, A., Cheng, Z., Miller, C. G., Williams, C., Poth, R., Morris, M., Lahey, O., Nix, J. C., Tierney, D. L., Page, R. C., Crowder, M. W., Bonomo, R. A., & Fast, W. (2017). Clinical Variants of New Delhi Metallo-β-Lactamase Are Evolving to Overcome Zinc Scarcity. ACS Infectious Diseases, 3(12), 927–940.

Stojanoski, V., Hu, L., Sankaran, B., Wang, F., Tao, P., Prasad, B. V. V., & Palzkill, T. (2021). Mechanistic Basis of OXA-48-like β-Lactamases' Hydrolysis of Carbapenems. ACS Infectious Diseases, 7(2), 445–460.

Strynadka, N. C. J., Adachi, H., Jensen, S. E., Johns, K., Sielecki, A., Betzel, C., Sutoh, K., & James, M. N. (1992). Molecular structure of the acyl-enzyme intermediate in β-lactam hydrolysis at 1.7 Å resolution. Nature, 359(6397), 700–705.

Sulton, D., Pagan-Rodriguez, D., Zhou, X., Liu, Y., Hujer, A. M., Bethel, C. R., Helfand, M. S., Thomson, J. M., Anderson, V. E., Buynak, J. D., Ng, L. M., & Bonomo, R. A. (2005). Clavulanic Acid Inactivation of SHV-1 and the Inhibitor-resistant S130G SHV-1 β-Lactamase. Journal of Biological Chemistry, 280(42), 35528–35536.

Swarén, P., Golemi, D., Cabantous, S., Bulychev, A., Maveyraud, L., Mobashery, S., & Samama, J.-P. (1999). X-ray Structure of the Asn276Asp Variant of the *Escherichia coli* TEM-1 β-Lactamase: Direct Observation of Electrostatic Modulation in Resistance to Inactivation by Clavulanic Acid†,‡. Biochemistry, 38(30), 9570–9576.

Takkar, R., Yadav, A., & Kumaraswamy, S. (2013). Application note 16. ForteBio

Tamma, P. D., Doi, Y., Bonomo, R. A., Johnson, J. K., & Simner, P. J. (2019). A Primer on AmpC β-Lactamases: Necessary Knowledge for an Increasingly Multidrug-resistant World. Clinical Infectious Diseases, 69(8), 1446–1455.

Theuretzbacher, U., Bush, K., Harbarth, S., Paul, M., Rex, J. H., Tacconelli, E., & Thwaites, G. E. (2020). Critical analysis of antibacterial agents in clinical development. Nature Reviews Microbiology, 18, 286–298.

Thomas, V. L., Golemi-Kotra, D., Kim, C., Vakulenko, S. B., Mobashery, S., & Shoichet, B. K. (2005). Structural Consequences of the Inhibitor-Resistant Ser130Gly Substitution in TEM β-Lactamase†,‡. Biochemistry, 44(26), 9330–9338.

Tobias Renee. (2013). Application note 14. ForteBio.

Tooke, C. L., Hinchliffe, P., Bragginton, E. C., Colenso, C. K., Hirvonen, V. H. A., Takebayashi, Y., & Spencer, J. (2019a). β-Lactamases and β-Lactamase Inhibitors in the 21st Century. Journal of Molecular Biology, 431, 3472-3500.

Tooke, C. L. Hinchliffe, P. Lang, P. A. Mulholland, A. J. Brem, J. Schofield, C. J. & Spencer, J. (2019b). Molecular Basis of Class A β-lactamase Inhibition by Relebactam. Antimicrobial Agents and Chemotherapy, 63(10): e00564-19.

Tremblay, L. W., Xu, H., & Blanchard, J. S. (2010). Structures of the Michaelis Complex (1.2 Å) and the Covalent Acyl Intermediate (2.0 Å) of Cefamandole Bound in the Active Sites of the *Mycobacterium tuberculosis* β-Lactamase K73A and E166A Mutants. Biochemistry, 49(45), 9685–9687.

Tripathi, R., & Nair, N. N. (2013). Mechanism of Acyl–Enzyme Complex Formation from the Henry–Michaelis Complex of Class C β-Lactamases with β-Lactam Antibiotics. Journal of the American Chemical Society, 135(39), 14679–14690.

Tripathi, R., & Nair, N. N. (2016). Deacylation Mechanism and Kinetics of Acyl–Enzyme Complex of Class C β-Lactamase and Cephalothin. The Journal of Physical Chemistry B, 120(10), 2681–2690.

Tsivkovski, R., & Lomovskaya, O. (2020). Biochemical Activity of Vaborbactam. Antimicrobial Agents and Chemotherapy, 64(2): e01935-19.

Uchański, T., Zögg, T., Yin, J., Yuan, D., Wohlkönig, A., Fischer, B., Rosenbaum, D. M., Kobilka, B. K., Pardon, E., & Steyaert, J. (2019). An improved yeast surface display platform for the screening of nanobody immune libraries. Scientific Reports, 9(1):382.

Ullah, J. H., Walsh, T. R., Taylor, I. A., Emery, D. C., Verma, C. S., Gamblin, S. J., & Spencer, J. (1998). The crystal structure of the L1 metallo-β-lactamase from *Stenotrophomonas maltophilia* at 1.7 Å resolution. Journal of Molecular Biology, 284(1), 125–136.

Vergalli, J., Bodrenko, I. V., Masi, M., Moynié, L., Acosta-Gutiérrez, S., Naismith, J. H., Davin-Regli, A., Ceccarelli, M., ven den Berg, B., Wintherhalter, M., & Pagès, J.-M. (2019). Porins and small-molecule translocation across the outer membrane of Gram-negative bacteria. Nature Reviews Microbiology, 18(3), 164–176.

Verlet, L. (1967). Computer “Experiments” on Classical Fluids. I. Thermodynamical Properties of Lennard-Jones Molecules. Physical Review, 159(1), 98–103.

Vincke, C., Gutiérrez, C., Wernery, U., Devoogdt, N., Hassanzadeh-Ghassabeh, G., & Muyldermans, S. (2012). Generation of Single Domain Antibody Fragments Derived from Camelids and Generation of Manifold Constructs. Methods in Molecular Biology, 907, 145–176.

Voulgari, E., Gartzonika, C., Vrioni, G., Politi, L., Priavali, E., Levidiotou-Stefanou, S., & Tsakris, A. (2014). The Balkan region: NDM-1-producing *Klebsiella pneumoniae* ST11 clonal strain causing outbreaks in Greece. Journal of Antimicrobial Chemotherapy, 69(8), 2091–2097.

Wang, X., Minasov, G., & Shoichet, B. K. (2002a). Evolution of an Antibiotic Resistance Enzyme Constrained by Stability and Activity Trade-offs. Journal of Molecular Biology, 320(1), 85–95.

Wang, X., Minasov, G., Shoichet & B. K. (2002b) The structural bases of antibiotic resistance in the clinically derived mutant β-lactamases TEM-30, TEM-32, and TEM-34. J Biol Chem, 277(35), 32149-56.

Wang, Y., Fan, Z., Shao, L., Kong, X., Hou, X., Tian, D., Sun, Y., Xiao, Y., & Yu, L. (2016). Nanobody-derived nanobiotechnology tool kits for diverse biomedical and biotechnology applications. International Journal of Nanomedicine, 11, 3287–3303.

Watanabe, M., Iyobe, S., Inoue, M., & Mitsuhashi, S. (1991). Transferable imipenem resistance in *Pseudomonas aeruginosa*. Antimicrobial Agents and Chemotherapy, 35(1), 147–151.

Woerther, P.-L., Burdet, C., Chachaty, E., Andremont, A. (2013). Trends in Human Fecal Carriage of Extended-Spectrum β-Lactamases in the Community: Toward the Globalization of CTX-M. Clinical Microbiology Reviews, 26(4), 744–758.

World Bank Group. Final report: Drug-Resistant Infections, A Threat to Our Economic Future, 2017.

Wu, W., Feng, Y., Tang, G., Qiao, F., McNally, A., & Zong, Z. (2019). NDM Metallo-β-Lactamases and Their Bacterial Producers in Health Care Settings. Clinical Microbiology Reviews, 32(2).

Xu, L., Li, Q., Myers, M., Chen, Q., Li, X. (2019). Application of nuclear magnetic resonance technology to carbon capture, utilization and storage: A review. Journal of Rock Mechanics and Geotechnical Engineering, 11(4), 892–908

Xu, M., Zhao, J., Xu, L., Yang, Q., Xu, H., Kong, H., Zhou, J., & Fu, Y. (2021). Emergence of transferable ceftazidime–avibactam resistance in KPC-producing *Klebsiella pneumoniae* due to a novel CMY AmpC β-lactamase in China. Clinical Microbiology and Infection, 28(1): 136.e1-136.e6.

Yamada, K., Wanchun, J., Ohkura, T., Murai, A., Hayakawa, R., Kinoshita, K., Mizutani, M., Okamoto, A., Namikawa, T., Ohta, M. (2013). Detection of Methicillin-Resistant *Staphylococcus aureus* Using a Specific Anti-PBP2a Chicken IgY Antibody. Japanese Journal of Infectious Diseases, 66(2), 103–108.

Yamaguchi, Y., Jin, W., Matsunaga, K., Ikemizu, S., Yamagata, Y., Wachino, J., Shibata, N., & Kurosaki, H. (2007). Crystallographic Investigation of the Inhibition Mode of a VIM-2 Metallo-β-lactamase from *Pseudomonas aeruginosa* by a Mercaptocarboxylate Inhibitor. Journal of Medicinal Chemistry, 50(26), 6647–6653.

Yong, D., Toleman, M. A., Giske, C. G., Cho, H. S., Sundman, K., Lee, K., & Walsh, T. R. (2009). Characterization of a New Metallo-β-Lactamase Gene, blaNDM-1, and a Novel Erythromycin Esterase Gene Carried on a Unique Genetic Structure in *Klebsiella pneumoniae* Sequence Type 14 from India. Antimicrobial Agents and Chemotherapy, 53(12), 5046–5054.

Zhang, H., & Hao, Q. (2011). Crystal structure of NDM-1 reveals a common β-lactam hydrolysis mechanism. The FASEB Journal, 25(8), 2574–2582.

Zhang L, Bouguet-Bonnet S, & Buck M. (2012). Combining NMR and molecular dynamics studies for insights into the allostery of small GTPase-protein interactions. Methods Mol Biol, 796, 235-59.

Zhou, H., Guo, W., Zhang, J., Li, Y., Zheng, P., & Zhang, H. (2019). Draft genome sequence of a metallo-β-lactamase (blaAIM-1)-producing *Klebsiella pneumoniae* SM32 isolated from a patient with chronic diarrhea. Journal of Global Antimicrobial Resistance, 16, 165-167.

Zou, H., Jia, X., Liu, H., Li, S., Wu, X., & Huang, S. (2020). Emergence of NDM-5-Producing *Escherichia coli* in a Teaching Hospital in Chongqing, China: IncF-Type Plasmids May Contribute to the Prevalence of blaNDM–5. Frontiers in Microbiology, 11 (334).

9. Annexes

Annexe 1

MICROBIAL DRUG RESISTANCE
Volume 00, Number 00, 2021

DOI: 10.1089/mdr.2020.0472

Identification of β-Lactamase-Encoding (*bla*) Genes in Phenotypically β-Lactam-Resistant *Escherichia coli* Isolated from Young Calves in Belgium

Virginie Guérin,[1] Damien Thiry,[1] Pierrick Lucas,[2] Yannick Blanchard,[2] Frédéric Cawez,[3] Paola Sandra Mercuri,[3] Moreno Galleni,[3] Marc Saulmont,[4] and Jacques Mainil[1]

The *bla* genes identification present in 94 phenotypically resistant *Escherichia coli* isolated from feces or intestinal contents of young calves with diarrhea or enteritis in Belgium was performed by microarrays (MA) and whole genome sequencing (WGS). According to their resistance phenotypes to 8 β-lactams at the disk diffusion assay these 94 *E. coli* produced a narrow-spectrum-β-lactamase (NSBL), an extended-spectrum-β-lactamase (ESBL) or a cephalosporinase (AmpC). All ESBL-encoding genes identified by MA and WGS belonged to the $bla_{CTX\text{-}M}$ family, with a majority to the $bla_{CTX\text{-}M\text{-}1}$ subfamily. Two different genes encoding an AmpC, $bla_{CMY\text{-}2}$, and $bla_{DHA\text{-}1}$ were detected in isolates with an AmpC phenotype. The $bla_{TEM\text{-}1}$ and the $bla_{OXA\text{-}1}$ were detected alone in isolates with a NSBL phenotype or in combination with ESBL-/AmpC-encoding *bla* genes. Furthermore, the WGS identified mutations in the *ampC* gene promoter at nucleotides -42 (C>T) and/or -18 (G>A) that could not be identified by MA, in several isolates with an AmpC-like resistance phenotype. No carbapenemase-encoding gene was detected. To our knowledge this is the first survey on the identification of *bla* genes in *E. coli* isolated from young diarrheic or septicemic calves in Belgium.

Keywords: *Escherichia coli*, calves, β-lactams resistance, microarray, whole genome sequencing, *bla* genes

Introduction

NOWADAYS, THE INCREASING spread of bacterial acquired antimicrobial resistance (AMR) in animals and humans is a major public health hazard worldwide, especially when the resistance spectrum includes hospital last resort antibiotics, such as latest generation cephalosporin and carbapenem β-lactams.[1]

Already a dozen years after the penicillin discovery,[2] Abraham and Chain[3] described the production of "an enzyme able to destroy penicillin" by *Escherichia coli*. Indeed, acquired resistance to β-lactam antibiotics in Gram-negative bacteria is most frequently mediated by the production of β-lactamase (BLA) enzymes hydrolyzing the β-lactam ring. Unfortunately the original strain of Abraham and Chain[3] has been lost and the actual identity of this enzyme remains unknown, although production of a BLA_{AmpC} is the most likely hypothesis.[4,5] The first confirmed description of a BLA_{AmpC} enzyme dates from 1973 and is produced by an *E. coli* K-12 harboring a chromosome-located bla_{ampC} gene.[6] Today, it is known that most wild-type *E. coli* possesses such a bla_{ampC} gene expressed at a low basal level, conferring no clinical resistance to β-lactams. However, when this gene is overexpressed, clinical resistance to all penicillins, cephamycins, first-/second-generation cephalosporins and sometimes low-level resistance to third-generation cephalosporins occur.[7] This BLA_{AmpC} enzyme is a member of the cephalosporinase families, also generically named AmpC rendering the nomenclature confusing.[4] Indeed, other cephalosporinase families were described during the following years (CMY, DHA, LAT, MIR, ACT, FOX) with a broad hydrolysis capacity of different β-lactams[4] that are encoded by chromosome or plasmid genes whose expression can be induced by the presence of β-lactams.[8] Cephalosporinase enzymes classically confer resistance to narrow and large spectrum penicillins, all four generation cephalosporins (although not always the fourth ones), cephamycins, BLA inhibitors or oxapenams and monobactams, but not to carbapenems.[4]

During the following decades, Gram-negative bacteria produce a large set of non AmpC-like BLAs displaying

[1]Bacteriology, Department of Infectious and Parasitic Diseases, FARAH and Faculty of Veterinary Medicine, ULiège, Belgium.
[2]Anses Sequencing Platform, ANSES, Ploufragan-Plouzané-Niort Laboratory, Ploufragan, France.
[3]Biological Macromolecules, Department of Life Sciences, Center for Protein Engineering (CIP), ULiège, Belgium.
[4]Regional Animal Health and Identification Association (ARSIA), Ciney, Belgium.

extended inactivation spectra of β-lactams. Today, thousands of BLAs have been described[9] and different classifications have been proposed based on molecular and/or functional criteria.[10,11] However, such molecular identification is not possible in routine diagnostic laboratories, especially in the veterinary field, being expensive and time consuming. The alternative is to use a phenotypic classification based on the inactivation spectra of β-lactams.

In addition to cephalosporinase families, three BLA families were described in the years 1960: BLA_{TEM}, BLA_{SHV}, and BLA_{OXA}. They confer resistance to narrow and large spectrum penicillins, to first and some second-generation cephalosporins and are encoded by acquired plasmid-located genes.[7] In this article, they will be named "narrow-spectrum-β-lactamases" or "NSBLs."

About 20 years later, BLAs conferring resistance to almost all penicillins, all four generation cephalosporins and monobactams but not to cephamycins, carbapenems, and oxapenams, were described for the first time and named "extended-spectrum-β-lactamases" (ESBLs).[12] Mutations in bla_{TEM}, bla_{SHV}, and bla_{OXA} genes,[13,14] or acquisition of genes encoding other BLA families, conferring ESBL resistance phenotypes, such as VEB,[15] GES,[16] and CTX-M[17] that are the most prevalent in human enterobacteria,[18] were progressively identified. Today, more than 240 BLA_{TEM}, 235 BLA_{SHV}, and 230 $BLA_{CTX\text{-}M}$ variants have been described,[9] as a consequence of the accumulation of mutations in the original *bla* genes.

The last resort β-lactam antibiotics against AmpC- and ESBL-producing Gram-negative bacteria are the carbapenems. However, a first carbapenemase (CP) enzyme, with serine in the active site, of enterobacteria was described in 1996 produced by a clinical isolate of *Klebsiella pneumoniae*.[19] As for ESBLs, some CP derive from existing BLAs after accumulation of mutations in the encoding genes ($bla_{GES\text{-}2}$[20] or $bla_{OXA\text{-}48}$,[21] for instance), whereas others correspond to newly acquired chromosome- or plasmid-encoded BLAs: KPC, IMI, VIM, and most recently NDM.[22] CPs can show some particularity in their β-lactam inactivation profiles (narrow and large spectrum penicillins, all cephalosporin generations, cephamycins, oxapenams, monobactams, and carbapenems), due to their action mode: serine (KPC, IMI, OXA-48) or Zn^{++} (metalloenzymes such as NDM and VIM) in their active sites.[23]

Several studies have widely demonstrated the primary importance of monitoring antibiotic resistance among farm animals (*e.g.*, cattle, small ruminants, and poultry), considered as reservoir for AMR. Yet, the direct impact on human health remains unclear.[24]

Since raising of beef cattle is most widespread in Wallonia, >90% of bacteria tested at the regional laboratory ("Association Régionale de Santé et d'Identification Animales," ARSIA) in Wallonia[25] for their antibiotic resistance profiles by the disk diffusion assay (DDA) are from bovine origin and ca. 70% of them are sampled from necropsied calves and calf feces.[26] In Belgium, since the publication of a royal decree in summer 2016, the use of carbapenems is prohibited and the use of third- and fourth-generation cephalosporins is strictly controlled in livestock.[27] Consequently, a progressive decrease of ESBL-producing pathogenic *E. coli* in cattle was observed already during the 2016–2017 calving season at ARSIA. Unfortunately, no identification of the resistance-encoding genes is routinely performed,[26] consequently the incidence of the different BLA families in these *E. coli* is unknown.

The purpose of this study was to (1) identify, by MA and whole genome sequencing (WGS), the different *bla* genes present in a set of bovine *E. coli* isolated from diarrheic and septicemic calves during the calving season 2017–2018 at ARSIA and (2) compare these *bla* genes with the β-lactam resistance phenotypes observed at the DDA. The results will help to develop PCRs targeting the identified *bla* genes to follow their evolution and to detect the emergence of other *bla* genes in pathogenic and commensal *E. coli* during the calving seasons in Belgium.

Materials and Methods

Bacterial isolates

A total of 94 bovine *E. coli* isolated at ARSIA (Ciney, Belgium) between November 2017 and February 2018 from feces, intestinal contents, or internal organs of <3-month-old calves suffering from diarrhea or septicemia were studied. The presence of β-lactam resistance was detected by DDA, following the EUCAST/CASFM guidelines with eight β-lactams: amoxicillin (AMX), amoxicillin + clavulanic acid (AMC), ceftiofur (XNL), cefquinome (CFQ), cefotaxime (CTX), cefotaxime + clavulanic acid (CTC), cefoxitin (FOX), and meropenem (MER).

A first group of 69 isolates, from feces, intestinal contents or internal organs, were chosen out of 433 bovine β-lactam-resistant *E. coli* to represent the NSBL, ESBL and AmpC spectra of resistance (Table 1). In this first set, isolates presenting a positive agglutination test (Biovac, Beaucouzé, France) after growth on Minca agar plates (Generon, San Prospero, Italy), for *fimbriae* F5 or F17 or for the CS31 antigen were, therefore, considered as pathogenic. The second group comprised 25 isolates that were randomly chosen out of 435 fecal or intestinal *E. coli* growing on MacConkey agar plates containing 1 mg/L of cefotaxime (McC-CTX) (Led Techno, Lienden, The Netherlands), selective for ESBL-, AmpC-, and CP-production, using the "RANDBETWEEN" function of Excel® (Table 1). This second set contained *E. coli* with negative agglutination test, therefore classified as nonpathogenic. To avoid as much as possible clonal relationship between the isolates, one isolate per calf and herd was chosen.

Since no bovine CP-producing *E. coli* was isolated, six CP-positive strains isolated from human were added as controls for the MA: 2 *E. coli* harboring the $bla_{NDM\text{-}1}$ or $bla_{OXA\text{-}48}$ genes, 2 *K. pneumoniae* harboring the $bla_{KPC\text{-}3}$ or $bla_{VIM\text{-}4}$ genes and 2 *Pseudomonas aeruginosa* harboring the $bla_{VIM\text{-}2}$ or $bla_{NDM\text{-}1}$ genes (kindly provided by Professor Y. Glupczynski, CHU Mont-Godinne, Catholic University of Louvain, Belgium).

Microarrays

The DNA of the 94 bovine *E. coli* and of the 6 CP-positive strains was extracted with the DNeasy Blood and Tissue kit® (Qiagen, Venlo, The Netherlands) and stored at −20°C. Tests were performed by Check-Points BV (Wageningen, The Netherlands), following the MA protocol previously described.[28] The different *bla* genes and families

TABLE 1. CLASSIFICATION OF RESISTANCE BASED ON THE PROFILE OBSERVED AT THE DISK DIFFUSION ASSAY IN *ESCHERICHIA COLI* ISOLATED FROM YOUNG DIARRHEIC OR SEPTICEMIC CALVES

	Antibiotics								*No. of isolates*		
Resistance profiles	*AMX*	*AMC*	*XNL*	*CFQ*	*CTX*	*CTC*	*FOX*	*MER*	*Set1*	*Set2*	*Total*
AmpC	R	R	R	R	R	R	R	S	8	3	11
AmpC-like	R	R	S	S	S	S	I/R	S	6	12	18
NSBL	R	S/I/R	S	S	S	S	S	S	15	1	16
ESBL	R	S/I	R	R	R	S/I	S	S	33	6	39
ESBL + NSBL	R	R	R	R	R	S/I	S	S	3	2	5
ESBL + AmpC-like	R	R	R	R	R	S/I	I/R	S	4	1	5
CP	R	R	R	R	R	R	R	R	0	0	0

R, resistant; I, intermediate; S, sensitive; AMX, amoxicillin; AMC, amoxicillin + clavulanic acid; XNL, ceftiofur; CFQ, cefquinome; CTX, cefotaxime; CTC, cefotaxime + clavulanic acid; FOX, cefoxitin; MER, meropenem; AmpC, cephalosporinase; NSBL, narrow-spectrum-β-lactamase; ESBL, extended-spectrum-β-lactamase; CP, carbapenemase; Set1, *Escherichia coli* isolates chosen for their resistance profile and their pathogenic classification; Set2, *E. coli* isolates randomly chosen for their growth on MacConkey-Cefotaxime selective agar plates and their nonpathogenic classification.

that the Check-MDR CT-103XL® microarrays kit (Check-Points BV, Wageningen, The Netherlands) can detect are listed in Table 2.

Whole genome sequencing

The genome of 29 isolates with discrepancy between the DDA and the MA results were sequenced as well as 15 isolates with matching DDA-MA results as controls. Sequencing was performed using NovaSeq 6000 Illumina technology (paired-end sequencing; Nextera XT DNA Sample Prep Kit, Illumina) by the Brain and Spine Institute (ICM Institute). Reads were cleaned and assembled with the shovill method (v1.0.4; https://github.com/tseemann/shovill), with a minimum length of 200 bp and a minimum coverage of 2. Contigs were analyzed with ResFinder-3.1[29] to detect mutations and resistance genes and annotated with the RAST tool kit in PATRIC (Pathosystems Resource Integration Center).[30]

Results

Identification of bla *genes by MA and comparison of MA and DDA results*

The following *bla* genes were detected in the 94 bovine *E. coli* isolates (Table 3): $bla_{TEM\text{-}WT}$ in 67 isolates; $bla_{CTX\text{-}M\text{-}1}$, $bla_{CTX\text{-}M\text{-}2}$, and/or $bla_{CTX\text{-}M\text{-}9}$ in 50 isolates; and $bla_{CMY\text{-}2}$ or $bla_{DHA\text{-}1}$ in 6 isolates. The $bla_{TEM\text{-}WT}$ genes were detected alone in 22 isolates and in association with $bla_{CTX\text{-}M}$ or with $bla_{CMY\text{-}2}$/$bla_{DHA\text{-}1}$ genes in 40 and 5 isolates, respectively, whereas the $bla_{CTX\text{-}M}$ genes were detected alone in 10 isolates. Four of the 5 $bla_{CMY\text{-}2}$ and the $bla_{DHA\text{-}1}$ genes were detected in association with $bla_{TEM\text{-}WT}$ genes, whereas the remaining isolate was positive for the $bla_{CMY\text{-}2}$ gene alone. No CP-encoding genes were detected in the bovine isolates, but the expected ones were detected in the six CP-positive control bacteria.

TABLE 2. TARGETED FAMILIES OF *BLA* GENES BY THE CHECK-MDR CT103XL MICROARRAY KIT

Family	*bla genes*
NSBL	TEM-WT; SHV-WT
ESBL	BEL; CTX-M (Groups 1[a], 2, 9, and 8/25); GES-ESBL; PER; SHV-ESBL; TEM-ESBL; VEB
AmpC	ACC; ACT; CMY; DHA; FOX; MIR; MOX
CP	GES-Carba; GIM; IMP; KPC; NDM; OXA (groups 23-, 24-, 48-, and 58-like); SPM; VIM

[a]Group 1 contains subgroup types 1-, 3-, 15-, and 32-like. Adapted from https://check-pointshealth.com/wp-content/uploads/2018/11/Check-MDR_CT103XL_IFU_10–0023_EN-v1.1–20170918.pdf

AmpC, cephalosporinases; CP, carbapenemases.

The comparison of the MA and DDA results yields the following conclusions (Table 3): (1) a perfect match was observed for 61 isolates, that is, the detected genes are in agreement with the phenotypes. Nevertheless, for 30 of them, presenting an ESBL phenotype, additional genes were detected; (2) a partial match was observed for 12 isolates, that is, the detected genes were not in total agreement with the phenotype; (3) no match was observed for 5 isolates, that is, the detected genes were in total disagreement with the phenotypes; and (4) no gene was detected in 16 isolates, including 13 with an AmpC-like phenotype.

Detected genes were similar between the two sets of isolates, regardless of their origins (feces, intestinal contents, or organs) (Table 1).

Identification of bla *genes by WGS and comparison with the DDA results*

All genomic data related to this study are available through the NCBI BioProject PRJNA566319.

Forty-three isolates were genome sequenced: 16 isolates with no gene detected by the MA, 5 isolates with no MA-DDA matching results, 4 isolates with partial matching results, 3 isolates with matching results and additional genes detected, and 15 isolates with matching results, as controls (Table 4).

The 16 isolates with no gene detected with the MA harbored the bla_{ampC} gene with 2 or 3 mutations in the promoter (14 isolates), the OXA-1-encoding gene (5 isolates) and/or the TEM-1B-encoding gene (1 isolate) (Table 4). The mutations in the promoter of the bla_{ampC} gene and the $bla_{OXA\text{-}1}$ gene cannot be detected by the MA (Table 2). The WGS of the remaining 27 isolates not only confirmed the presence of the genes detected by MA although the TEM-encoding genes were different from $bla_{TEM\text{-}1/2}$ in three

Table 3. Disk Diffusion Assays Phenotypes and Genes Involved in β-Lactam Resistance Detected by Microarrays in 94 Bovine *Escherichia coli* Isolates

DDA phenotype	*Detected bla genes by MA coding for*	*No. of isolates*	*MA-DDA matching*
AmpC (AMC^R)	CMY-2	1	Yes
	CMY-2 + TEM-WT	4	Yes
	CTX-M-1 + TEM-WT	1	No
	TEM-WT	4	No
AmpC-like (AMC^R)	TEM-WT	5	Partial
	DHA + TEM-WT	1	Partial
	None	13	—
NSBL ($AMC^{S/I/R}$)	TEM-WT	13	Yes
	None	3	—
ESBL ($AMC^{S/I}$)	CTX-M-1 (type 1-like)	1	Yes
	CTX-M-1 (type 32-like)	4	Yes
	CTX-M-2	3	Yes
	CTX-M-9	1	Yes
	CTX-M-1 (type 1-like) + TEM-WT	8	Yes +
	CTX-M-1 (type 15-like) + TEM-WT	6	Yes +
	CTX-M-1 (type 32-like) + TEM-WT	5	Yes +
	CTX-M-1 (type 32-like) + CTX-M-2 + TEM-WT	1	Yes +
	CTX-M-2 + TEM-WT	6	Yes +
	CTX-M-9 + TEM-WT	4	Yes +
ESBL + NSBL (AMC^R)	CTX-M-1 (type 15-like)	1	Partial
	CTX-M-1 (type 1-like) + TEM-WT	1	Yes
	CTX-M-2 + TEM-WT	1	Yes
	CTX-M-9 + TEM-WT	2	Yes
ESBL + AmpC-like (AMC^R)	CTX-M-1 (type 15-like) + TEM-WT	2	Partial
	CTX-M-1 (type 32-like) +TEM-WT	1	Partial
	CTX-M-9 + TEM-WT	2	Partial

AMC, amoxicillin + clavulanic acid; R, resistant; I, intermediate; S, sensitive; AmpC, cephalosporinase; YES, matching results between DDA and MA (the detected genes explaining the observed phenotypes); YES +, matching results with additional genes detected by MA (some of the detected genes explain the observed phenotypes); PARTIAL, partially matching results between DDA and MA (the detected genes do not fully explain the observed phenotypes); NO, no matching results between DDA and MA/WGS (the detected genes do not explain the observed phenotypes); —, no gene. DDA, disk diffusion assay; MA, microarrays; WGS, whole genome sequencing.

isolates (bla_{TEM-30}, bla_{TEM-35}, and bla_{TEM-78}), but also identified the presence of the bla_{ampC} gene with mutations in the promoter and/or of the bla_{OXA-1} gene in 14 of them.

A perfect match (yes and yes+ categories in Tables 3 and 4) was observed between the WGS and DDA results for 41 of the 43 genome-sequenced isolates versus only 18 of these 43 isolates for the MA and DDA results. In particular, 15 of the 16 AmpC-like isolates (Table 4) harbored a bla_{ampC} gene with 3 mutations in the promoter explaining this phenotype. The two isolates with partial matching between WGS and DDA results were one AmpC-like isolate harboring TEM-1B- and DHA-1-encoding genes and one ESBL+AmpC-like in which the bla_{ampC} gene carried only two mutations in the promoter (Table 4).

Of the 27 genome-sequenced isolates with genes detected by MA (Table 4), the results of the WGS matched the results of MA for 24 isolates, with additional genes detected by WGS for 13 of them and partially matched for the 3 isolates harboring the bla_{TEM-30}, bla_{TEM-35}, or bla_{TEM-78} genes and also mutations in the promoter of the bla_{ampC} gene in two of them.

As for the DDA-MA comparison, the detected genes were similar in the two sets of isolates.

Discussion

Since the existing classifications of the BLA enzymes[10,11] cannot easily be applied in veterinary routine diagnostic laboratories in Belgium, the prevalence of the different BLA families and *bla* genes in bovine *E. coli* in Belgium is unknown. The purpose of this study was, therefore, to identify the *bla* genes present in *E. coli* isolated from young calves with diarrhea, enteritis, and/or septicemia during the 2017–2018 calving season with different resistance phenotypes to eight β-lactams at the DDA (Table 1). The results will help to develop appropriate PCR assays for future studies aiming at following the incidence of the *bla* genes over the years and at comparing bovine *E. coli* with human *E. coli*, focusing more especially on those with ESBL and AmpC resistance profiles.

E. coli isolates belonging to the ESBL, ESBL+NSBL, and ESBL+AmpC-like resistance phenotypes harbor gene(s) of the bla_{CTX-M} family, mostly the $bla_{CTX-M-1}$ and less frequently the $bla_{CTX-M-2}$ or $bla_{CTX-M-9}$ genes, which explain the ESBL resistance profile (Table 3 and 4). Such results are similar to those of *E. coli* in livestock especially cattle in Europe, with the $bla_{CTX-M-1}$ and $bla_{CTX-M-9}$ genes being the most frequent ESBL-encoding gene, compared with the $bla_{CTX-M-2}$ gene.[18,31–33] In several of the same isolates, other genes are detected whose presence, either cannot be suspected according to the DDA results (ESBL phenotype) or add resistance to other β-lactams, especially to oxapenams or to cephamycins (ESBL+NSBL and ESBL+AmpC-like phenotypes; Table 1): bla_{TEM-1B}, bla_{OXA-1}, and/or bla_{ampC} with two mutations in the promoter (n-18 G>A and n-1 C>T) (Tables 3 and 4).

The results of the isolates belonging to the AmpC and AmpC-like phenotypes are more heterogeneous. At first, a

TABLE 4. DETECTED GENES INVOLVED IN β-LACTAM RESISTANCE AFTER WHOLE GENOME SEQUENCING OF 43 ISOLATES WITH DIFFERENT DISK DIFFUSION ASSAYS AND MICROARRAYS MATCHING RESULTS

MA-DDA matching	*DDA phenotype*	*Detected* bla *genes by MA coding for*	*Detected* bla *genes by WGS coding for*	*No. of isolates*	*WGS-DDA matching*
—	AmpC-like (AMC^R)	None	MutAmpC (-1, -18, -42)	10	Yes
			MutAmpC (-1, -18, -42) + OXA-1	2	
			MutAmpC (-1, -18, -42) + TEM-1B	1	
	NSBL ($AMC^{S/I/R}$)	None	OXA-1	2	Yes
			OXA-1 + MutAmpC (-1, -18)	1	
No	AmpC (AMC^R)	CTX-M-1 + TEM-WT	CTX-M-1 + TEM-35	1	Yes
		TEM-WT	MutAmpC (-1, -18, -42) + TEM-1A + OXA-1	4	
Partial	AmpC-like (AMC^R)	TEM-WT	MutAmpC (-1, -18, -42) + TEM-1A + OXA-1	1	Yes
			MutAmpC (-1, -18, -42) + TEM-30	1	
		DHA + TEM-WT	DHA + TEM-1B	1	Partial
	ESBL + AmpC-like (AMC^R)	CTX-M-9 + TEM-WT	CTX-M-14 + TEM-1B + MutAmpC (-1, -18)	1	Partial
Yes +	ESBL ($AMC^{S/I}$)	CTX-M-1 (type 1-like) + TEM-WT	CTX-M-1 + TEM-1B	1	Yes +
			CTX-M-1 + TEM-1B + OXA-1	1	
		CTX-M-1 (type 15-like) + TEM-WT	CTX-M-156[a] + TEM-1B + OXA-1	1	
Yes	AmpC (AMC^R)	CMY-2 + TEM-WT	CMY-2 + TEM-1A	2	Yes
			CMY-2 + TEM-1B	1	
	NSBL ($AMC^{S/I/R}$)	TEM-WT	TEM-1A + OXA-1	1	Yes
			TEM-1B	4	
			TEM-1B + OXA-1	1	
			TEM-1B + MutAmpC (-1, -18)	1	
	ESBL ($AMC^{S/I}$)	CTX-M-1 (type 32-like)	CTX-M-32	1	Yes
		CTX-M-2	CTX-M-2	2	
	ESBL + NSBL (AMC^R)	CTX-M-1 (type 1-like) + TEM-WT	CTX-M-1 + TEM-1B + MutAmpC (-1, -18)	1	Yes +
		CTX-M-2 + TEM-WT	CTX-M-2 + TEM-78 + MutAmpC (-1, -18)	1	

AMC, amoxicillin + clavulanic acid; R, resistant; I, intermediate; S, sensitive; AmpC, cephalosporinase; YES, matching results between DDA and MA/WGS (the detected genes explaining the observed phenotypes); YES +, matching results with additional genes detected by MA/WGS (some of the detected genes explain the observed phenotypes); PARTIAL, partially matching results between DDA and MA/WGS (the detected genes do not fully explain the observed phenotypes); NO, no matching results between DDA and MA/WGS (the detected genes do not explain the observed phenotypes); —, no gene detected by MA; MutAmpC, *ampC* gene with two or three mutations detected in the promoter, concerned position in bracket.

[a]CTX-M 156 is a member of the CTX-M-1 group in the type 15-like subgroup.

majority of AmpC and AmpC-like isolates, without DDA-MA matching, harbor a bla_{ampC} gene with 3 mutations in the promoter (n-42 C>T, n-18 G>A and n-1 C>T) (Tables 3 and 4). Chromosome-located bla_{ampC} genes are usually expressed at a very low level and do not confer clinical resistance to β-lactams.[7] However the accumulation of mutations in their promoter may increase the gene expression and confer resistance to several β-lactams, but still not to latest generation cephalosporins and carbapenems.[34–36] These resistance phenotypes can, therefore, be confused with the NSBL phenotype in routine analysis (Table 1). The level of mRNA transcription was not measured, but the production of a BLA with the Diatabs test (Rosco, via International Medical Product, Brussels, Belgium) showed the hydrolysis of the ampicillin for 16 of these 19 isolates (data not shown). The increase of the bla_{ampC} gene expression is, therefore, the most likely explanation. Nevertheless, alternative explanations of the resistance to cephamycins exist: mutation within the genes coding for the penicillin-binding proteins, production of efflux pumps and/or a modification of the membrane permeability.[37] For instance, the resistance to cephamycins of the five ESBL+ AmpC-like isolates may have similar alternative explanations,[4] since (1) the two sequenced isolates harbor only two mutations in the bla_{ampC} gene promoter (n-18 and n-1) and (2) the same two mutations in two NSBL isolates and in two ESBL+NSBL isolates have no apparent consequence on their sensitivity to cephamycins. More isolates with (ESBL+) AmpC and AmpC-like resistance profiles should be genetically studied to more precisely understand the resistance profile and the actual role of the mutated bla_{ampC} gene.

In addition, other genes of the AmpC family are present that can explain the AmpC and AmpC-like phenotypes: the bla_{CMY-2} gene in five AmpC isolates and the bla_{DHA-1} gene in one AmpC-like isolate (Tables 3 and 4).[4,8] In Europe, the bla_{CMY-2} gene is also frequent in livestock.[18,31–33] Finally the remaining AmpC isolate harbors a $bla_{CTX-M-1}$ gene and a bla_{TEM-35} gene, which is an oxapenam-resistant variant and can, therefore, also explain the resistance to oxapenams,[37] in contrast to ESBL+NSBL isolates harboring bla_{CTX-M} and bla_{TEM-WT} genes (Tables 1, 3, and 4).

As for the isolates belonging to the NSBL phenotype, either or both bla_{TEM-1B} and bla_{OXA-1} genes were detected. In addition, as discussed earlier, one bla_{ampC} gene with two

mutations in the promoter was also identified in two of the genome-sequenced NSBL isolates along with the bla_{TEM-1B} and bla_{OXA-1} genes (Tables 3 and 4), but with no consequence on the resistance phenotype. Very importantly, no bovine *E. coli* belong to the CP phenotype and no CP-encoding gene could be identified, neither by MA nor by WGS.

The comparison between the different resistance profiles observed at DDA of bovine *E. coli* isolates with their *bla* gene contents detected by MA and/or WGS was the second objective of this study. The results of the MA and DDA perfectly match (yes and yes+ categories in Table 3) for 61 of the 94 isolates studied. In addition, *bla* genes and/or mutations that could not be detected by the MA, such as the bla_{OXA-1} gene and the bla_{ampC} gene with mutations in the promoter, were detected in the genome-sequenced of 29 of the 33 isolates with no perfect match between MA and DDA. Therefore, after WGS, only 2 of these genome-sequenced 29 isolates still have partial match between genetic and phenotypic results. MA and DDA mismatch results in this study are, therefore, explained by the presence of untargeted *bla* genes such as the bla_{OXA-1} gene and of untargeted mutations in some *bla* genes, such as in the promoter of the bla_{ampC} gene. In contrast to these results on bovine *E. coli*, the MA kit Check-MDR CT103XL® correctly detected several *bla* genes (Table 2) of different *Enterobacteriaceae*, *Pseudomonaceae*, and *Acinetobacter* species.[39,40] However, the probes of the MA were chosen according to the prevalence of the *bla* genes in humans and not in animals. Moreover, in those previous studies, the targeted *bla* genes were known before the MA test.

Conclusion

As a conclusion, the detected *bla* genes are in accordance with the different resistance phenotypes of the bovine *E. coli* in Belgium (Tables 1, 3, and 4) and with the *bla* genes contents of the bovine *E. coli* in other European countries.[18,31–33] Moreover, no difference was observed between intestinal and septicemic isolates, pathogenic or not. Therefore, the PCR for the $bla_{TEM-1/2}$, bla_{OXA-1}, $bla_{CTX-M-1}$, $bla_{CTX-M-2}$, $bla_{CTX-M-9}$, and bla_{CMY-2} genes represent, currently, the most useful tools to follow the incidence of the most frequent *bla* genes identified in cattle from Belgium. Further studies are necessary to follow the evolution of the β-lactams resistance and to estimate the impact of the antibiotics use regulation, to have a better control of AmpC-/ESBL-producing *E. coli* in cattle.

Acknowledgments

The authors thank Professor Y. Glupscynski for providing the CP-positive bacterial strains isolates used as controls in this study, and the technicians from bacteriology laboratory of ARSIA for their technical help. The authors are also grateful to the ICM institute for its technical support in NovaSeq NGS sequencing. The authors thank Jean-Noël Duprez for his help in the realization of DDA and DNA extraction. The authors thank Check-Point for their excellent welcome in their laboratory, their detailed explanations, and their technical support during the MA tests. These results were presented, in part, during the 30th World Buiatrics Congress (Sapporo, Japan, August 2018) and during the 8th Symposium on Antimicrobial Resistance in Animals and the Environment (Tours, France, July 2019). The authors are grateful to two anonymous reviewers for their comments and suggestions that helped improved this article.

Authors' Contributions

V.G. performed the MA assay, analyzed the antibiotic sensitivity results and the genome sequences, and wrote the article. D.T. supervised the whole study, discussed and helped to analyze the phenotypic and genetic results, and wrote parts of the article. M.S. supervised the whole study, isolated and identified the bovine *E. coli*, performed the antibiotic sensitivity assay, and discussed the results. M.G. and J.M. supervised the whole study, discussed the results, and synthesized the different parts of the article. P.L. and Y.B. performed the genome sequencing and wrote parts of the article. F.C. and P.S.M. discussed the phenotypic and genetic results, and helped to write parts of the article.

Disclosure Statement

No competing financial interests exist.

Funding Information

This study was supported by the Belgian Federal Public Service Health, Food Chain Safety and Environment [Grant No. RF 17/6317 RU-BLA-ESBL-CPE].

References

1. Organisation for Economic Co-operation and Development (OECD). 2018. Stemming the Superbug Tide: Just A Few Dollars More, OECD Health Policy Studies. OECD Publication, Paris.
2. Fleming, A. 1929. On the antibacterial action of cultures of a Penicillium, with special reference to their use in the isolation of B. influenzae. Br. J. Exp. Pathol. 10:226–236.
3. Abraham, E.P., E. Chain. 1940. An enzyme from bacteria able to destroy penicillin. Nature 3713:837.
4. Jacoby, G.A. 2009. AmpC B-lactamases. Clin. Microbiol. Rev. 22:161–182.
5. Frère J.-M., E. Sauvage, and F. Kerff. 2016. From "An enzyme able to destroy penicillin" to carbapenemases: 70 years of beta-lactamase misbehavior. Curr. Drug Targets 17:974–982.
6. Burman, L., J. Park, B. Lindström, and H. Boman. 1973. Resistance of *Escherichia coli* to Penicillins: identification of the structural gene for the chromosomal penicillinase. J. Bacteriol. 116:123–130.
7. Livermore, D. 1995. β-Lactamases in laboratory and clinical resistance. Clin. Microbiol. Rev. 8:557–584.
8. Pham, J.N., I. Chambers, L. Poirel, P. Nordmann, and S.M. Bell. 2010. Detection of a plasmid-mediated inducible cephalosporinase DHA-1 from *Escherichia coli*. Pathology 42:196–197.
9. Naas, T., S. Oueslati, R.A. Bonnin, *et al.* 2017. Beta-lactamase database (BLDB)–structure and function. J. Enzyme Inhib. Med. Chem. 32:917–919.
10. Ambler, R.P. 1980. The structure of beta-lactamases. Philos. Trans. R. Soc. Lond. B. Biol. Sci. 289:321–331.
11. Bush, K., and G.A. Jacoby. 2010. Updated functional classification of β-lactamases. Antimicrob. Agents Chemother. 54:969–976.
12. Ghafourian, S., N. Sadeghifard, S. Soheili, and Z. Sekawi. 2015. Extended spectrum beta-lactamases: definition, classification and epidemiology. Curr. Issues Mol. Biol. 17:11–22.

13. Kliebe, C., B.A. Nies, J.F. Meyer, R.M. Tolxdorff-Neutzling, and B. Wiedemann. 1985. Evolution of plasmid-coded resistance to broad-spectrum cephalosporins. Antimicrob. Agents Chemother. 28:302–307.
14. Paul, G.C., G. Gerbraud, A. Bure, A.M. Philippon, B. Pangon, and P. Courvalin. 1989. TEM-4, a new plasmid-mediated β-lactamase that hydrolyzes broad-spectrum cephalosporins in a clinical isolate of *Escherichia coli*. Antimicrob. Agents Chemother. 33:1958–1963.
15. Poirel, L., T. Naas, M. Guibert, E.B. Chaibi, R. Labia, and P. Nordmann. 1999. Molecular and biochemical characterization of VEB-1, a novel class A extended-spectrum β-lactamase encoded by an *Escherichia coli* integron gene. Antimicrob. Agents Chemother. 43:573–581.
16. Poirel, L., I. Le Thomas., T. Naas, A. Karim, and P. Nordmann. 2000. Biochemical sequence analyses of GES-1, a novel class A extended- spectrum β-lactamase, and the class 1 integron In52 from *Klebsiella pneumoniae*. Antimicrob. Agents Chemother. 44:622–632.
17. Nordmann, P., and H. Mammeri. 2007. Extended-spectrum cephalosporinases: structure, detection and epidemiology. Future Microbiol. 2:297–307.
18. Ewers, C., A. Bethe, T. Semmler, S. Guenther, and L.H. Wieler. 2012. Extended-spectrum β-lactamase-producing and AmpC-producing *Escherichia coli* from livestock and companion animals, and their putative impact on public health: a global perspective. Clin. Microbiol. Infect. 18: 646–655.
19. Yigit, H., A.M. Queenan, G.J. Anderson, *et al.* 2001. Novel carbapenem-hydrolyzing β-lactamase, KPC-1, from a carbapenem-resistant strain of *Klebsiella pneumoniae*. Antimicrob. Agents Chemother. 45:1151–1161.
20. Poirel, L., G.F. Weldhagen, T. Naas, C. De Champs, M.G. Dove, and P. Nordmann. 2001. GES-2, a class A β-lactamase from *Pseudomonas aeruginosa* with increased hydrolysis of imipenem. Antimicrob. Agents Chemother. 45:2598–2603.
21. Poirel, L., C. Héritier, V. Tolün, and P. Nordmann. 2004. Emergence of oxacillinase-mediated resistance to imipenem in *Klebsiella pneumoniae*. Antimicrob. Agents Chemother. 48:15–22.
22. Lauretti, L., M.L. Riccio, A. Mazzariol, *et al.* 1999. Cloning and characterization of bla(VIM), a new integron-borne metallo- β-lactamase gene from a *Pseudomonas aeruginosa* clinical isolate. Antimicrob. Agents Chemother. 52:3589–3596.
23. Nordmann, P. 2014. Carbapenemase-producing Enterobacteriaceae: overview of a major public health challenge. Med. Mal. Infect. 44:51–56.
24. Madec, J.-Y., M. Haenni, P. Nordmann, *et al.* 2017. Extended-spectrum β-lactamase/AmpC- and carbapenemase-producing *Enterobacteriaceae* in animals: a threat for humans? Clin. Microbiol. Infect. 23:826–833.
25. Association Régionale de Santé et d'Identification Animales (ARSIA). 2018. Annual report (French version), 11–13. Available at https://www.arsia.be/wp-content/uploads/documents-telechargeables/RA-2018-web.pdf, (accessed February 7, 2021).
26. Association Régionale de Santé et d'Identification Animales (ARSIA). 2019. Annual report (French version), 14. Available at https://www.arsia.be/wp-content/uploads/documents-telechargeables/RA-2019-web.pdf, (accessed February 7, 2021).
27. Royal Decree of Belgium (French version). Moniteur Belge. 07-21-2016 updated 12-09-2020. Available at www.ejustice.just.fgov.be/eli/arrete/2016/07/21/2016024152/justel, (accessed February 7, 2021).
28. Cohen Stuart, J., C. Dierikx, N. Al Naiemi, *et al.* 2010. Rapid detection of TEM, SHV and CTX-M extended-spectrum β-lactamases in Enterobacteriaceae using ligation-mediated amplification with microarray analysis. J. Antimicrob. Chemother. 65:1377–1381.
29. Zankari, E., H. Hasman, S. Cosentino, *et al.* 2012. Identification of acquired antimicrobial resistance genes. J. Antimicrob. Chemother. 67:2640–2644.
30. Brettin, T., J.J. Davis, T. Disz, *et al.* 2015. RASTtk: a modular and extensible implementation of the RAST algorithm for building custom annotation pipelines and annotating batches of genomes. Sci. Rep. 5:8365
31. Gonggrijp, M.A., I.M.G.A. Santman-Berends, A.E. Heuvelink, *et al.* 2016. Prevalence and risk factors for extended-spectrum β-lactamase- and AmpC-producing *Escherichia coli* in dairy farms. J. Dairy Sci. 99:9001–9013.
32. Michael, G.B., H. Kaspar, A.K. Siqueira, *et al.* 2017. Extended-spectrum β-lactamase (ESBL)-producing *Escherichia coli* isolates collected from diseased food-producing animals in the GERM-Vet monitoring program 2008–2014. Vet. Microbiol. 200:142–150.
33. Ghosh, K.K., L.A. Lebert, S.A. McEwen, *et al.* 2019. Extended-spectrum β-lactamase and ampc β-lactamase-producing *Escherichia coli* isolates from chickens raised in small flocks in Ontario, Canada. Microb. Drug Resist. 25:1250–1256.
34. Caroff, N., E. Espaze, D. Gautreau, H. Richet, and A. Reynaud. 2000. Analysis of the effects of -42 and -32 ampC promoter mutations in clinical isolates of *Escherichia coli* hyperproducing AmpC. J. Antimicrob. Chemother. 45:783–788.
35. Mulvey, M.R., E. Bryce, D.A. Boyd, *et al.* 2005. Molecular characterization of cefoxitin-resistant *Escherichia coli* from Canadian hospitals. Antimicrob. Agents Chemother. 49: 358–365.
36. Tracz, D.M., D.A. Boyd, R. Hizon, *et al.* 2007. ampC gene expression in promoter mutants of cefoxitin-resistant *Escherichia coli* clinical isolates. FEMS Microbiol. Lett. 270: 265–271.
37. Hamed, R.B., J.R. Gomez-Castellanos, L. Henry, C. Ducho, M.A. McDonough, and C.J. Schofield. 2013. The enzymes of β-lactam biosynthesis. Nat. Prod. Rep. 30:21–107.
38. Cantón, R., M.I. Morosini, O. Martin, S. De La Maza, and E.G.G. De La Pedrosa. 2008. IRT and CMT β-lactamases and inhibitor resistance. Clin. Microbiol. Infect. 14 Suppl 1:53–62.
39. Cunningham, S.A., S. Vasoo, and R. Patel. 2016. Evaluation of the check-points check MDR CT103 and CT103 XL microarray kits by use of preparatory rapid cell lysis. J. Clin. Microbiol. 54:1368–1371.
40. Powell, E.A., D. Haslam, and J.E. Mortensen. 2017. Performance of the check-points check-MDR CT103XL assay utilizing the CDC/FDA antimicrobial resistance isolate bank. Diagn. Microbiol. Infect. Dis. 88:219–221.

Address correspondence to:
Virginie Guérin, DVM
Bacteriology
Department of Infectious and Parasitic Diseases
FARAH and Faculty of Veterinary Medicine
4000 Liège
Belgium

E-mail: vguerin@uliege.be

Annexe 2

AMERICAN SOCIETY FOR MICROBIOLOGY | Antimicrobial Agents and Chemotherapy®

MECHANISMS OF RESISTANCE

Development of Nanobodies as Theranostic Agents against CMY-2-Like Class C β-Lactamases

Frédéric Cawez,[a] Paola Sandra Mercuri,[a] Francisco Javier Morales-Yãnez,[b,c] Rita Maalouf,[b] Marylène Vandevenne,[d] Frederic Kerff,[e] Virginie Guérin,[f] Jacques Mainil,[f] Damien Thiry,[f] Marc Saulmont,[g] Alain Vanderplasschen,[c,h] Pierre Lafaye,[i] Gabriel Aymé,[i] Pierre Bogaerts,[j] Mireille Dumoulin,[b,c] Moreno Galleni[a]

[a]InBioS, Center for Protein Engineering, Biological Macromolecules, Department of Life Sciences, University of Liège, Liège, Belgium
[b]InBioS, Center for Protein Engineering, NEPTUNS, Department of Life Sciences, University of Liège, Liège, Belgium
[c]ALPANANO, Center for Protein Engineering & FARAH, University of Liège, Liège, Belgium
[d]InBios, Center for Protein Engineering, ROBOTEIN, Department of Life Sciences, University of Liège, Liège, Belgium
[e]InBioS, Center for Protein Engineering, Department of Life Sciences, University of Liège, Liège, Belgium
[f]Bacteriology, FARAH and Faculty of Veterinary Medicine, Department of Infectious and Parasitic Diseases, University of Liège, Liège, Belgium
[g]Regional Animal Health and Identification Association (ARSIA), Ciney, Belgium
[h]Immunology-Vaccinology, FARAH and Faculty of Veterinary Medicine, Department of Infectious and Parasitic Diseases, University of Liège, Liège, Belgium
[i]Institut Pasteur, Université Paris Cité, CNRS UMR 328, Paris, France
[j]National Reference Center for Antibiotic-Resistant Gram-Negative Bacilli, Department of Clinical Microbiology, CHU UCL Namur, Yvoir, Belgium

ABSTRACT Three soluble single-domain fragments derived from the unique variable region of camelid heavy-chain antibodies (VHHs) against the CMY-2 β-lactamase behaved as inhibitors. The structure of the complex VHH cAb_{CMY-2}(254)/CMY-2 showed that the epitope is close to the active site and that the CDR3 of the VHH protrudes into the catalytic site. The β-lactamase inhibition pattern followed a mixed profile with a predominant noncompetitive component. The three isolated VHHs recognized overlapping epitopes since they behaved as competitive binders. Our study identified a binding site that can be targeted by a new class of β-lactamase inhibitors designed on the sequence of the paratope. Furthermore, the use of mono- or bivalent VHH and rabbit polyclonal anti-CMY-2 antibodies enables the development of the first generation of enzyme-linked immunosorbent assay (ELISA) for the detection of CMY-2 produced by CMY-2-expressing bacteria, irrespective of resistotype.

KEYWORDS nanobodies, paratopes, antibiotic resistance, CMY-2 β-lactamase, new antibiotic scaffold, class C beta-lactamase, structural biology

Bacterial resistance to antibiotics is recognized as a major threat in human and veterinary medicine. Antimicrobial resistance accounts for 700,000 deaths per year in the world, including 30,000 deaths in Europe. This figure could exceed 10 million deaths in 2050 if no new treatments are developed (1). Among the different classes of antimicrobials, the β-lactam antibiotics are extensively used because of their wide spectrum of action and their low toxicity for eukaryotic cells (2). They are able to specifically neutralize the enzymatic activity of penicillin binding protein (PBP) involved in biosynthesis of the bacterial cell wall (3, 4). Bacteria have developed different mechanisms in order to affect the biological activity of the β-lactam antibiotics (5–9). In Gram-negative bacteria, the most common mechanism is hydrolysis of the β-lactam ring by hydrolases called β-lactamases.

The misuse and the intensive use of antibiotics lead to the selection of multidrug-resistant (MDR) bacteria, which are unaffected by the presence of antibiotics belonging to at least three different families (10). Therefore, it is essential to develop new rapid diagnostic assays in order to detect faster the presence of β-lactamases that favor the

Address correspondence to Moreno Galleni, mgalleni@uliege.be.

The authors declare no conflict of interest.

Received 9 November 2022
Returned for modification 29 November 2022
Accepted 24 January 2023
Published 9 March 2023

rapid implementation of infection control measures to circumvent nosocomial infections. In addition, it is essential to develop new inhibitor scaffolds able to block β-lactamase activity by targeting binding sites that are not tolerant to mutations.

To develop new inhibitors, one strategy is to select inhibitory antibodies that serve in the development of new β-lactamase inhibitors by peptidomimetics (11). VHH, also referred as nanobody, is the single-domain fragment corresponding to the binding domain of camelid heavy-chain antibodies (HCAbs). They constitute potential candidates for obtaining inhibitory antibodies against β-lactamases. They are exclusively found in camelids (VHH) or in cartilaginous fish (V-NAR) (12). Despite their small size (15 kDa), they are able to interact with their antigen with a high affinity and specificity (13). In addition, VHHs present unique properties, including a generally easy recombinant production in *Escherichia coli*, an ease of modification of the properties of the nanobody by protein engineering. Moreover, VHHs are able to inhibit activity of enzymes as previously described for the β-lactamases TEM-1 (14) and VIM-4 (15).

The RUBLA project, a study of the distribution of *bla* genes in bovine *E. coli* isolates in Wallonia, Belgium, highlighted that the bla_{CMY-2} gene coding for the cephalosporinase CMY-2 (16) is characterized by the broadest geographic spread (17). In addition, *Enterobacteriaceae* strains expressing this β-lactamase were isolated from animals (18) and human sources (19).

Phenotypic tests cannot distinguish between different subclasses of AmpC β-lactamases, for which molecular approaches such as PCR or DNA microarray are required (20). Nevertheless, those methods cannot identify the different subclasses of AmpC. The assays must be complemented by molecular approaches such as PCR or DNA microarray when available (21). Those methods are expensive, time-consuming, and generally used only for reference laboratories and research settings (22). Furthermore, expression of multiple β-lactamases (23) or other resistance features such as the decrease of porin expression could result in more complex susceptibility patterns (24). Altogether, those observations clearly demonstrate the real necessity to develop new diagnostic approaches for the veterinarian and the clinician in order to detect AmpC easily and with a high specificity.

On the other hand, treatments generally employed to treat infections with *Enterobacteriaceae* expressing AmpC consist of the use of carbapenems, cefepime, or recently approved β-lactam–β-lactamase inhibitor combinations (25). Newer β-lactamase inhibitors as avibactam or vaborbactam have also a high potency against AmpC activity (26). However, it is expected to favor the appearances of resistance against those antibiotics and inhibitors, specifically against carbapenems (27).

In this work, we developed nanobodies (VHHs) in order to set up a sandwich enzyme-linked immunosorbent assay (ELISA) for the detection of CMY-2 and to find inhibitors able to neutralize β-lactamase activity. We first isolated eight VHHs belonging to three families that recognized CMY-2. The results highlighted a high specificity for their antigen but rapid dissociation rates of the VHH/CMY-2 complexes. We could stabilize the complex with the development of a homobivalent VHH. Competition assays demonstrated also an overlapping epitope of the VHHs for CMY-2. With the help of an ELISA, we could detect the production of CMY-2-like enzymes in a collection of human and veterinary bacterial isolates. The second goal was to follow the effect of VHH binding on CMY-2 activity. We found that the VHHs behaved as noncompetitive inhibitors of CMY-2 and that the nature of the substrate affected the inhibition patterns of the nanobodies. The crystallographic structure of the complex formed by CMY-2 and the VHH cAb_{CMY-2}(254) allowed us to define the epitope recognized by the VHH and the nature of the paratope and to confirm the inhibitory mechanisms highlighted by the kinetic studies. Altogether, these results provide new insights for development of diagnostic and inhibitory antibodies against class C β-lactamases.

RESULTS

Construction of an immune VHH library and selection of CMY-2-targeting binders. From the blood of an alpaca (*Vicugna pacos*) immunized with CMY-2 β-lactamase, an immune library was constructed. Three rounds of panning using this library were

```
                                                                                66
cAb_CMY-2 (250) QVQLVESGGGLVQPGGSLRLSCAAS GSIFSIYGMG WYRQAPGKQRELVA EITS-GGSTNYADSVKG
cAb_CMY-2 (254) QVQLVESGGGMVQPGGSLRLSCAAS GFTFSNYDMS WVRRAPGKGPEWVS TINTGGGSTSYADSVKG
cAb_CMY-2 (272) QVQLVESGGGLVQPGGSLRLSCAAS GSIFMIYAMG WYRQAPGKQRELVA DITS-GGSTDYTDSVKG
                        FR1             CDR1        FR2             CDR2
                                                                              129
cAb_CMY-2 (250) RFTISRDNAKNTVYLQMNSLNPEDTAVYYCN ADGT----MWGAGDY WGQGTQVTVSS HHHHHH
cAb_CMY-2 (254) RFTISRDNAKNTLYLQMNSLKPEDTALYYCT IDRGLHYSDLGEYDY WGQGTQVTVSS HHHHHH
cAb_CMY-2 (272) RFTISRD--KNTVYLQMNSLKPEDTAVYYCN ADHG----PGFGYDY WGQGTQVTVSS HHHHHH
                          FR3                 CDR3          FR4
```

FIG 1 Sequence alignment of VHHs directed against CMY-2. FR, framework; CDR, complementarity-determining region.

performed to enrich the library in phage particles exposing CMY-2-specific VHHs using established protocols (28). Ninety clones of each round of panning, randomly selected, were screened by indirect ELISA to detect the presence of anti-CMY-2 VHHs. Eight clones gave a positive signal in the ELISA, and their genes were sequenced. The results of the sequencing indicated 3 genetically different VHHs [$cAb_{CMY\text{-}2}$(250), $cAb_{CMY\text{-}2}$(254), and $cAb_{CMY\text{-}2}$(272)] based on the sequence of the complementarity-determining regions (CDRs) (Fig. 1). CDR2 and CDR3 of the VHHs $cAb_{CMY\text{-}2}$(250) and $cAb_{CMY\text{-}2}$(272) present deletions of 1 and 4 amino acids, respectively, compared to the VHH $cAb_{CMY\text{-}2}$(254). The framework 4 (FR4) sequences are identical for the three VHHs, but we observed a deletion of 2 amino acids in FR3 of $cAb_{CMY\text{-}2}$(272). Finally, despite the fact that the main mutations were identified into the CDRs, $cAb_{CMY\text{-}2}$(254) is also characterized by additional mutations in the framework regions. Based on these results, $cAb_{CMY\text{-}2}$(250), $cAb_{CMY\text{-}2}$(254), and $cAb_{CMY\text{-}2}$(272) were produced and purified to complete their analysis.

Binding characterization of $cAb_{CMY\text{-}2}$(250), $cAb_{CMY\text{-}2}$(254), and $cAb_{CMY\text{-}2}$(272) by biolayer interferometry (BLI). In order to determine the specificity of the VHHs $cAb_{CMY\text{-}2}$(250), $cAb_{CMY\text{-}2}$(254), and $cAb_{CMY\text{-}2}$(272), qualitative binding measurements were performed to assess their ability to interact with different representatives of all the molecular classes of β-lactamases. The three VHHs did not recognize β-lactamases from classes A, B, and D (Fig. 2A to C). $cAb_{CMY\text{-}2}$(254) and $cAb_{CMY\text{-}2}$(272) interacted only with CMY-2-like enzymes (Fig. 2B and C) and not with other class C β-lactamases, indicating their high specificity. In contrast, $cAb_{CMY\text{-}2}$(250) displayed a cross-reaction with the AmpC P99 of *Enterobacter cloacae* but not with CMY-1 (Fig. 2A). Quantitative binding measurements were performed in order to measure the kinetic (k_{on}, k_{off}) and equilibrium (K_D) constants (Fig. 2D to F). The association kinetic constants (k_{on}) of the three VHHs against CMY-2 ranged from 10^5 to 10^6 M^{-1} s^{-1}, highlighting a rapid association of the VHHs with their target (Table 1). Nevertheless, all complexes were unstable given their relatively fast dissociation kinetic constant ($k_{off} > 5 \times 10^{-3}$ s^{-1}), which leads to overall moderate affinities of VHHs for CMY-2 (K_D > 60 nM). The comparison of binding properties of the three VHHs showed that $cAb_{CMY\text{-}2}$(254) presents a dissociation that is up to 20 times lower than those of the two other VHHs (Fig. 2B), indicating that this VHH is able to form a more stable complex than $cAb_{CMY\text{-}2}$(250) and $cAb_{CMY\text{-}2}$(272).

Competition binding assay of VHHs directed against CMY-2. We wished to determine if the three nanobodies could recognize the same or different epitopes. To this end, we carried out competition binding assays by BLI based on a premix method. This consists of (i) binding a biotinylated VHH on a streptavidin biosensor (SA sensor) and (ii) measuring its association rate in the presence of increasing molar ratios of soluble complexes formed by a second VHH and CMY-2. The three possible combinations of complexes [$cAb_{CMY\text{-}2}$(250)/CMY-2, $cAb_{CMY\text{-}2}$(254)/CMY-2, and $cAb_{CMY\text{-}2}$(272)/CMY-2] were assessed for each biotinylated VHH. A decrease in the rate of binding of the free VHH $cAb_{CMY\text{-}2}$(254) to VHH/CMY-2 complexes was observed (Fig. 3), indicating that the VHH $cAb_{CMY\text{-}2}$(254) epitope partially overlaps the epitopes of the two other VHHs. These results were confirmed when VHHs $cAb_{CMY\text{-}2}$(250) and $cAb_{CMY\text{-}2}$(272) were immobilized on the biosensor, confirming the overlap of the epitopes of the three VHHs (see Fig. S1 in the supplemental material).

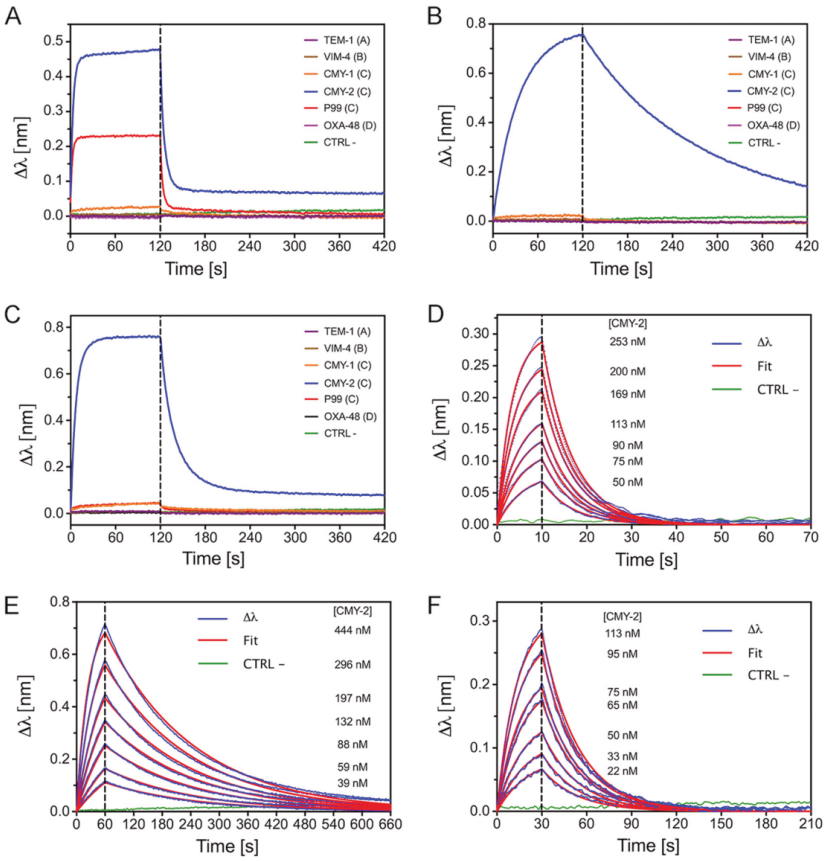

FIG 2 Binding characterization of the three selected VHHs by biolayer interferometry. (A to C) Qualitative binding specificity of $cAb_{CMY-2}(250)$ (A), $cAb_{CMY-2}(254)$ (B), and $cAb_{CMY-2}(272)$ (C). Names and classes (in parentheses) of the tested β-lactamases are indicated. (D to F) Quantitative binding measurements of $cAb_{CMY-2}(250)$ (D), $cAb_{CMY-2}(254)$ (E), and $cAb_{CMY-2}(272)$ (F). The experimental data ($\Delta\lambda$) recorded with seven different concentrations were fitted using a 1:1 binding model. The negative control (CTRL −) corresponds to CMY-2 directly loaded onto the biosensor. Each experiment was carried out twice independently.

Binding properties of rabbit pAbs directed against CMY-2. The epitope overlapping of the three VHHs does not allow the development of a VHH sandwich ELISA. To circumvent this issue, we produced and characterized rabbit polyclonal antibodies (pAbs) directed against CMY-2 with the purpose to be used in a pair with $cAb_{CMY-2}(254)$, the VHH forming the more stable complex with CMY-2. First, the specificity of anti-CMY-2 pAbs was analyzed by indirect ELISA in which a panel of β-lactamases representative of

TABLE 1 Kinetic (k_{on}, k_{off}) and equilibrium (K_D) constants determined by BLI[a]

VHH	k_{on} (10^5 M^{-1} s^{-1})	k_{off} (10^{-3} s^{-1})	K_D (nM)
$cAb_{CMY-2}(250)$	6.6 ± 0.1	140 ± 10	220 ± 10
$cAb_{CMY-2}(254)$	0.9 ± 0.1	5.9 ± 0.7	66 ± 1
$cAb_{CMY-2}(272)$	3.7 ± 0.5	36 ± 9	100 ± 40

[a]k_{on} and k_{off} values were derived from a global fit of seven analyte concentrations (i.e., illustrated on sensorgrams in Fig. 2) with the equation of a stoichiometry 1:1 binding model. All values include averages and standard deviations calculated from two independent experiments.

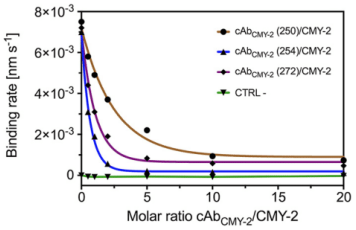

FIG 3 Competition binding assay between VHHs directed against CMY-2 monitored by BLI. The biotinylated VHH $cAb_{CMY-2}(254)$ was loaded onto a streptavidin biosensor (SA sensor), while the analyte corresponds to complexes $cAb_{CMY-2}(250)$/CMY-2, $cAb_{CMY-2}(254)$/CMY-2, and $cAb_{CMY-2}(272)$/CMY-2 in different molar ratios. The negative control corresponds to the signal recorded when the complex $cAb_{CMY-2}(254)$/CMY-2 was directly loaded onto the nonfunctionalized biosensor. All the binding rates were calculated by fitting a simple exponential mathematic model to the first 120 s of the association phase. This experiment was performed twice independently.

all classes were used to coat a 96-well plate (Fig. 4A). The data clearly indicated that pAbs directed against CMY-2 were unspecific since they recognized different members of class C β-lactamases, such as CMY-1 and P99. A second assay via BLI was also conducted to further investigate the specificity of pAbs. Biotinylated β-lactamases were immobilized on streptavidin biosensors. In a second step, the sensors were immerged into a pAb solution (Fig. 4B). This experiment confirmed the lack of specificity, since bindings were also measured for P99 and CMY-2. However, no interaction was detected for CMY-1, demonstrating that the lack of specificity can depend on the assay setting and/or the type of immobilization. Finally, the dissociation constant (k_{off}) was evaluated by BLI for pAbs (Fig. 4C) which, as commonly observed for polyvalent antibodies, presented a high avidity characterized by a slow dissociation phase ($k_{off} = 3.6 \pm 0.9\ 10^{-5}\ s^{-1}$) (29).

Sandwich ELISA for detection of the β-lactamase CMY-2. In oder to assess the robustness of the identification of CMY-2, we evaluated the detection limits of a sand-

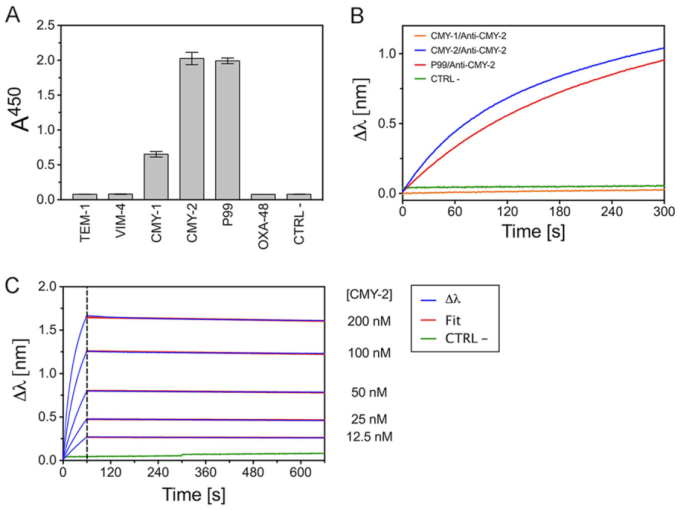

FIG 4 Binding properties of rabbit pAbs directed against the β-lactamase CMY-2. (A) Indirect ELISA where the antigens were absorbed on a Maxisorp plate (except for the CTRL −) to investigate the specificity of pAbs. (B) Qualitative binding specificity assay of pAbs for CMY-2 monitored by BLI. (C) Quantitative binding measurements of pAbs for CMY-2 by BLI. The experimental data ($\Delta\lambda$) recorded with five different concentrations were fitted using a 1:1 binding model. The negative control corresponds to anti-CMY-2 pAbs directly loaded onto the biosensor. The BLI experiments were performed twice independently.

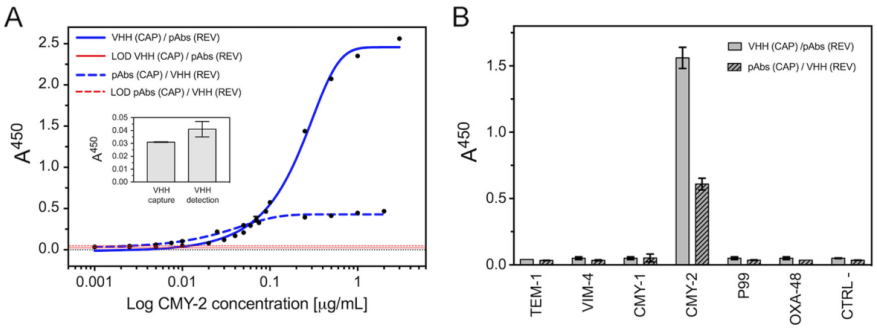

FIG 5 Sandwich ELISA on purified enzymes for CMY-2 detection. (A) LOD where $cAb_{CMY-2}(254)$ was employed as antibody for capture and pAbs for detection (blue solid line) or inversely (blue dashed line). Curves were fitted with equation I in Text S1. The inset includes the Abs_{450} for the CTRL −. The LOD was calculated from an average Abs_{450} of the CTRL − plus three times the standard deviation. They are represented in red solid and dashed lines for VHH used as capture and detection antibody, respectively. (B) Specificity assessment using $cAb_{CMY-2}(254)$ as capture agent and the pAbs for revelation (gray) or the inverse (gray, pattern). In both experiments, the CTRL − corresponds to the same ELISA without antigen. All averages and standard deviations are results from at least four measurements. CAP, capture; REV, revelation.

wich ELISA by using $cAb_{CMY-2}(254)$ as capture antibody and pAbs for the detection or, inversely, the pAbs as capture antibody and the VHH for the detection (Fig. 5A, solid blue line). The LODs were calculated considering the average value of the absorption at 450 nm (Abs_{450}) of the negative control (CTRL –) plus three times the standard deviation. They corresponded to 13.3 and 3.9 ng/mL using $cAb_{CMY-2}(254)$ as capture and detection antibodies, respectively. Compared to LOD values reported in the literature (LOD = 0.86 ng/mL) (30), our ELISA is characterized by high LOD values that are mainly due to the fast dissociation of VHH/CMY-2 complexes. This phenomenon has a negative impact on the limit of detection of our antigens. Moreover, the use of pAbs as capture antibody and VHHs for the revelation did not bring any gain, since the responses (measured as Abs_{450}) were lower than the initial settings. On the other hand, the specificity of the sandwich ELISA was checked on purified enzymes (Fig. 5B). Both assays clearly allowed the specific detection of CMY-2 since no signal was measured for other families of β-lactamases.

Production and characterization of the bivalent VHH $cAb_{CMY-2}(254)_{BIV}$. In order to increase the sensitivity of the ELISA, we designed a bivalent VHH based on the VHH $cAb_{CMY-2}(254)$. This genetically engineered bivalent antibody [$cAb_{CMY-2}(254)_{BIV}$] consists of the fusion of two $cAb_{CMY-2}(254)$ VHHs in tandem repeats, joined by a peptide linker, $(GGGS)_3$ (31). $cAb_{CMY-2}(254)_{BIV}$ was produced and purified in an amount comparable to that of monovalent VHH. In addition, no degradation of the tandem repeat was observed. Bivalent VHHs may exhibit an increased apparent affinity (or avidity) due to a significant decrease of the dissociation rate constant from the immobilized antigen (32). As expected, the dissociation rate significantly decreased for $cAb_{CMY-2}(254)_{BIV}$ ($k_{off} = 3.8 \times 10^{-4} \pm 0.4 \times 10^{-4}$ s^{-1}) compared to that of its monovalent counterpart ($k_{off} = 6.3 \times 10^{-3} \pm 0.5 \times 10^{-3}$ s^{-1}) (Fig. 6). This implies a more stable antigen/antibody complex.

Sandwich ELISA for detection of CMY-2 using the bivalent VHH $cAb_{CMY-2}(254)_{BIV}$. We also compared the LOD value for a sandwich ELISA by using the bivalent VHH $cAb_{CMY-2}(254)_{BIV}$ as capture antibody and pAbs for the detection to an ELISA in which pAb was the capture antibody and the bivalent VHH was used for detection (Fig. 7A). Indeed, the use of the bivalent VHH clearly improved the detection of CMY-2. The LOD values measured around 2.3 and 1.4 ng/mL, respectively. Moreover, the used of the pAbs as capture antibody did not affect the specificity of the ELISA system (Fig. 7B). Finally, we can conclude that the higher sensitivity of the assay combined with its high specificity allows the use of the bivalent VHH cAb_{CMY-2} $(254)_{BIV}$ for the detection of CMY-2 produced in bacterial isolates.

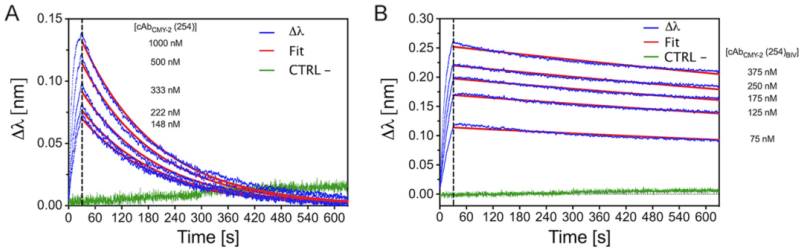

FIG 6 Quantitative binding measurements of the monovalent VHH $cAb_{CMY-2}(254)$ (A) and the bivalent VHH $cAb_{CMY-2}(254)_{BIV}$ (B) performed by BLI. The experimental data ($\Delta\lambda$) recorded with five different concentrations were fitted using a 1:1 binding model. The negative control corresponds to VHHs directly loaded onto the biosensor. Experiments were performed twice independently.

Detection of CMY-2 β-lactamase in bovine and human bacterial isolates. Three different sandwich ELISAs were designed for the direct detection of CMY-2 produced in bovine and human bacterial isolates. In those experiments, the monovalent VHH cAb_{CMY-2} (254) was only used as capture antibody and anti-CMY-2 pAbs were used for detection. In contrast, the bivalent VHH was used as antibody for capture and revelation since both configurations improved the sensitivity of the assay. As shown in Table 2, the three different ELISAs allowed the detection of a large panel of CMY-2 subgroup variants, such as CMY-16 and CMY-60. In addition, no cross-reactions were observed for other class C β-lactamases, such as CMY-10 (CMY-1-like), DHA, and ACT, or subclasses of AmpC expressed in bovine isolates. Interestingly, the use of the bivalent VHH $cAb_{CMY-2}(254)_{BIV}$ as antibody for the capture and the revelation ensured a higher sensitivity for the detection of β-lactamases belonging to the CMY-2 subgroup than did the use of monovalent VHH $cAb_{CMY-2}(254)$ as capture antibody. Indeed, only 17 of 22 bacterial isolates presenting one gene coding for CMY-2 subgroup variant were detected via the monovalent VHH, versus 21 isolates for the bivalent VHH $cAb_{CMY-2}(254)_{BIV}$ (Table 2). Our data suggest that the sandwich ELISA with VHH cAbCMY-2(254)BIV can detect β-lactamases belonging to the CMY-2 subgroup with high reliability.

Effects of the VHHs on the enzymatic activity of CMY-2: kinetic characterization. The CMY-2 activity for 4 β-lactam substrates in the presence of the VHH cAb_{CMY-2} (254) was studied (Fig. 8). The substrates were chosen based mainly on the nature of the side chain of carbon 2 (C-2) for penicillin (ampicillin) and C-3 for the cephalosporins

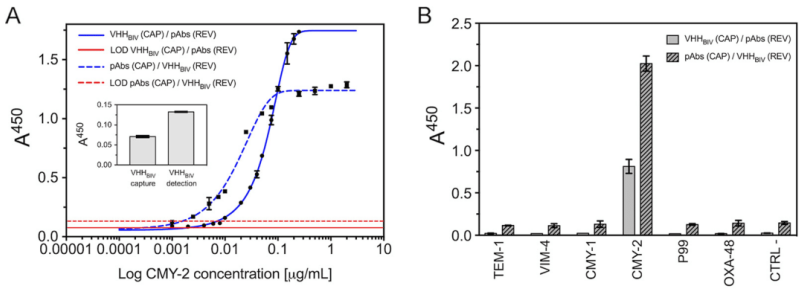

FIG 7 Sandwich ELISA for CMY-2 detection using the bivalent VHH $cAb_{CMY-2}(254)_{BIV}$. (A) Limits of detection where the VHH $cAb_{CMY-2}(254)_{BIV}$ was used as antibody for capture and pAbs for detection (blue solid line) or the inverse (blue dashed line). The inset includes the Abs_{450} for the negative control. The LOD was calculated from an average Abs_{450} of the CTRL − plus three times the standard deviation. They are represented in red full and dashed lines for VHH used as capture and detection antibody, respectively. (B) Specificity measurement by use of $cAb_{CMY-2}(254)_{BIV}$ as antibody for capture and the pAbs for the detection (gray) or inversely (gray, pattern). The negative control corresponds to the ELISA without antigen. All averages and standard deviations are results from at least four measurements.

TABLE 2 Detection of CMY-2 subgroup β-lactamases in bovine and human bacterial isolates by a sandwich ELISA[a]

Bacterial isolate[b]	Species	Detected *bla* genes[c,d]	Abs_{450}		
			VHH capture and pAb detection	VHH_{biv} capture and pAb detection	pAb capture and VHH_{biv} detection
PEP031	*E. coli*	TEM-1, CTX-M-15, NDM-1, CMY-58, OXA-1	**1.28 ± 0.01**	**1.60 ± 0.03**	**1.96 ± 0.03**
PEP135	*E. coli*	TEM-1, NDM-1, CMY-16, OXA-10	**0.94 ± 0.05**	**1.37 ± 0.01**	**1.88 ± 0.06**
PEP175	*Klebsiella pneumoniae*	TEM-1, SHV-1, CTX-M-15, NDM-1, CMY-2, DHA, OXA-9	0.06 ± 0.00	**0.12 ± 0.01**	**0.55 ± 0.05**
PEP224	*E. coli*	TEM, NDM-5, CMY-2-like	0.06 ± 0.00	**0.24 ± 0.03**	**0.69 ± 0.04**
PEP202	*E. coli*	CMY-60	**1.10 ± 0.04**	**1.67 ± 0.06**	**1.37 ± 0.02**
PEP203	*E. coli*	CMY-61	**1.42 ± 0.01**	**1.78 ± 0.01**	**2.05 ± 0.00**
PEP205	*K. pneumoniae*	SHV-11, CMY-2	**1.08 ± 0.03**	**1.62 ± 0.01**	**2.03 ± 0.06**
PEP206	*E. coli*	OXA-1, CMY-42	**0.41 ± 0.02**	**1.13 ± 0.05**	**1.87 ± 0.04**
PEP207	*Proteus mirabilis*	CMY-2	**1.37 ± 0.03**	**1.72 ± 0.00**	**1.89 ± 0.03**
PEP218	*E. coli*	TEM-39, TEM-84, CMY-2	**0.27 ± 0.02**	**0.85 ± 0.01**	**1.58 ± 0.10**
PEP234	*K. pneumoniae*	TEM, SHV, CTX-M (G1), VIM-19, CMY-2	**0.12 ± 0.01**	**0.41 ± 0.00**	**0.97 ± 0.01**
PEP235	*E. coli*	VIM-19, CMY-2	**0.19 ± 0.00**	**0.67 ± 0.01**	**1.81 ± 0.06**
PEP006	*Citrobacter freundii*	TEM-1, CMY-2-like	**1.28 ± 0.06**	**1.82 ± 0.03**	**2.01 ± 0.03**
PEP157	*C. freundii*	TEM-1, CTX-M-9, CMY-2-like, OXA-9, OXA-48	0.05 ± 0.00	**0.12 ± 0.00**	**0.67 ± 0.03**
CP40	*E. coli*	TEM-1, OXA-1, OXA-1-like, CMY-2	0.04 ± 0.00	0.06 ± 0.00	0.08 ± 0.01
CP42	*E. coli*	TEM-1, CMY-2	**0.18 ± 0.01**	**0.43 ± 0.01**	**1.46 ± 0.04**
Col20140084	*C. freundii*	TEM-1, CTX-M-15, OXA-1/9/10, CMY-2	0.04 ± 0.01	**0.08 ± 0.01**	**1.76 ± 0.02**
Col20140087	*K. pneumoniae*	TEM-1, CTX-M-9/15, SHV-1, CMY-2	**0.86 ± 0.11**	**1.39 ± 0.01**	**1.87 ± 0.07**
RUBLA0884	*E. coli*	TEM-1, CMY-2	**0.45 ± 0.03**	**1.19 ± 0.00**	**1.76 ± 0.04**
RUBLA0945	*E. coli*	TEM-1, CMY-2	**0.25 ± 0.02**	**0.87 ± 0.05**	**1.58 ± 0.17**
RUBLA1013	*E. coli*	TEM-1, CMY-2	**0.11 ± 0.01**	**0.28 ± 0.01**	**1.02 ± 0.11**
RUBLA1358	*E. coli*	CMY-2	**0.20 ± 0.01**	**0.40 ± 0.01**	**1.32 ± 0.06**
PEP121	*K. pneumoniae*	SHV-1, DHA-1, OXA-1	0.05 ± 0.00	0.06 ± 0.00	0.09 ± 0.00
PEP194	*K. pneumoniae*	TEM-1/52, SHV-1, OXA-4, CMY-10	0.05 ± 0.00	0.06 ± 0.01	0.08 ± 0.00
PEP041	*K. pneumoniae*	TEM-1/10, SHV-11, ACT-1, OXA-2	0.05 ± 0.00	0.06 ± 0.00	0.07 ± 0.00
PEP007	*E. coli*	TEM-1, DHA-7, SHV-12	0.04 ± 0.00	0.05 ± 0.00	0.07 ± 0.01
Col20140070	*K. pneumoniae*	TEM-1, CTX-M-15, SHV-1, OXA-1, OXA-1-like, DHA-2	0.04 ± 0.00	0.05 ± 0.00	0.08 ± 0.00
RUBLA0127	*E. coli*	TEM-1, DHA	0.05 ± 0.00	0.05 ± 0.00	0.09 ± 0.00
RUBLA0045	*E. coli*	MutAmpC, OXA-1	0.08 ± 0.01	0.05 ± 0.00	0.07 ± 0.00
RUBLA0315	*E. coli*	MutAmpC	0.06 ± 0.01	0.05 ± 0.00	0.07 ± 0.00
RUBLA1048	*E. coli*	MutAmpC	0.08 ± 0.01	0.05 ± 0.00	0.08 ± 0.00
PEP032	*Morganella morganii*	TEM-1, CTX-M-15, NDM-1, DHA-1, OXA-1	0.04 ± 0.00	0.07 ± 0.01	0.08 ± 0.00
PEP033	*E. cloacae*	TEM-1, SHV-12, CTX-M-15, NDM-1, MIR, OXA-1	0.05 ± 0.00	0.08 ± 0.00	0.09 ± 0.00
PEP122	*M. morganii*	TEM-1, CTX-M-15, NDM-1, DHA-1, OXA-1	0.06 ± 0.00	0.07 ± 0.00	0.09 ± 0.00
PEP042	*E. coli*	TEM-1, CTX-M-9, CMY-10, OXA-4, OXA-224	0.06 ± 0.01	0.07 ± 0.01	0.08 ± 0.00
PEP176	*Acinetobacter baumannii*	NDM-1	0.05 ± 0.00	0.06 ± 0.00	0.08 ± 0.00
PEP239	*K. pneumoniae*	SHV-28, NDM-1, OXA-1	0.04 ± 0.00	0.07 ± 0.00	0.07 ± 0.00
PEP177	*K. pneumoniae*	SHV-28, CTX-M-15, NDM-1, OXA-30	0.05 ± 0.00	0.08 ± 0.00	0.08 ± 0.01
Col20140047	*E. coli*	TEM-52	0.05 ± 0.00	0.05 ± 0.00	0.08 ± 0.00

(Continued on next page)

TABLE 2 (Continued)

Bacterial isolate[b]	Species	Detected *bla* genes[c,d]	Abs_{450}		
			VHH capture and pAb detection	VHH_{biv} capture and pAb detection	pAb capture and VHH_{biv} detection
Col20140090	*E. coli*	TEM-1, CTX-M-15, OXA-1, OXA-1-like	0.05 ± 0.00	0.06 ± 0.00	0.09 ± 0.00
Abs_{450} positive cutoff[e]			0.08	0.08	0.09

[a]Values for all positive strains in the ELISA are in bold.
[b]RUBLA isolates (21) belong to ARSIA (Association Régionale de Santé et d'Identification Animale), Ciney, Belgium. Col, PEP, and CNR isolates belong to the National Reference Center for Antimicrobial-Resistant Gram-Negative Bacilli, CHU UCL Namur (Mont-Godinne), Belgium.
[c]Gene content of RUBLA isolates was determined by whole-genome sequencing (WGS), while gene content of Col, PEP, and CNR isolates was determined by PCR and amplified fragment sequencing.
[d]MutAmpC, chromosomal overexpressed AmpC presenting three mutations in the promoter at positions −1, −18, and −42.
[e]The Abs_{450} positive cutoff values were calculated as an average Abs_{450} value of *E. coli* DH5α presenting no *bla* genes plus three times the standard deviation.

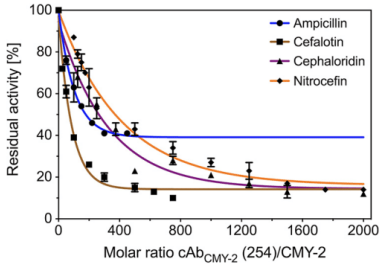

FIG 8 Residual activity of CMY-2 in complex with cAb$_{CMY-2}$(254) for β-lactam ring substrates. Reporter substrates corresponded to 100 μM ampicillin (blue line), 100 μM cephalothin, 100 μM cephaloridin, and 40 μM nitrocefin. Concentrations of CMY-2 used for each reporter substrate were 5 nM, 1 nM, 0.2 nM, and 0.5 nM, respectively. All data were fitted on a one-phase exponential decay equation from the graph prism program with values resulted from two experiments performed independently.

(cephalothin, cephaloridin, and nitrocefin) (Fig. S2). This selection aimed to provide a link between the nature of the side chains of these antibiotics and the strength of inhibition. The results highlight that the residual activity of cAb$_{CMY-2}$(254)/CMY-2 complexes, at the higher molar ratio tested, against the three cephalosporins was between 10 and 15% of the activity of the free enzyme. On the other hand, the residual activity for ampicillin hydrolysis plateaued at 40%, indicating that inhibition of CMY-2 activity for this substrate was less efficient and probably followed another mechanism of inhibition. Finally, a similar inhibitory profile was observed for CMY-2 in complex with VHHs cAb$_{CMY-2}$(250) and cAb$_{CMY-2}$(272) for the hydrolysis of nitrocefin (Fig. S3). These results are in good agreement with the hypothesis that the three VHHs bind to an overlapping epitope (Fig. 3).

The steady-state kinetic parameters of CMY-2 alone or in interaction with VHHs were computed from the linearization of the substrate hydrolysis curves (equation II in Text S1). The apparent Michaelis-Menten constant (K_m^{app}) value of CMY-2 for the nitrocefin was not affected by the presence of the VHH, while the apparent catalytic constant (k_{cat}^{app}) decreased in the presence of increasing concentrations of the VHH cAb$_{CMY-2}$(254) (Fig. 9A). These observations suggest a noncompetitive inhibition mechanism in which the VHH did not prevent the interaction between the substrate and the active site. Nevertheless, the binding of the VHH could affect the dynamic of the active site of the enzyme and reduce the efficiency of the deacylation step. Moreover, the dependence of the $1/k_{cat}^{app}$ values on the function of the inhibitor concentration (Fig. 9B) corresponded to a pure noncompetitive inhibition. Therefore, the ternary complex between the enzyme, the substrate and the inhibitor (ESI) was poorly active when the concentration of cAb$_{CMY-2}$(254) was significantly higher than the inhibition constant value (K_i). Based on this

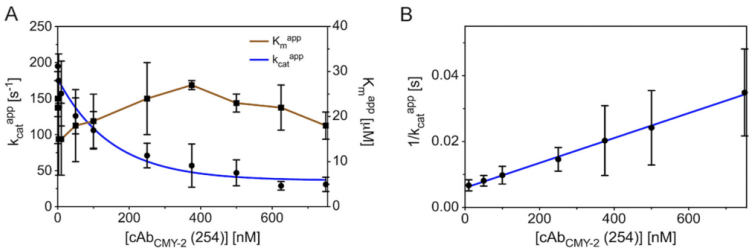

FIG 9 Inhibitory model of CMY-2 activity for nitrocefin by the VHH cAb$_{CMY-2}$(254). (A) K_m^{app} and k_{cat}^{app} (parameters derived from the complete hydrolysis of 40 μM nitrocefin by CMY-2 in complex with the VHH cAb$_{CMY-2}$(254). Experiments were performed using CMY-2 at a concentration of 0.5 nM. k_{cat}^{app} data were fitted using the one-phase exponential decay equation from graph prism. (B) Trend of $1/k_{cat}^{app}$ values as a function of VHH cAb$_{CMY-2}$ (254) concentration. All values resulted from three independent experiments.

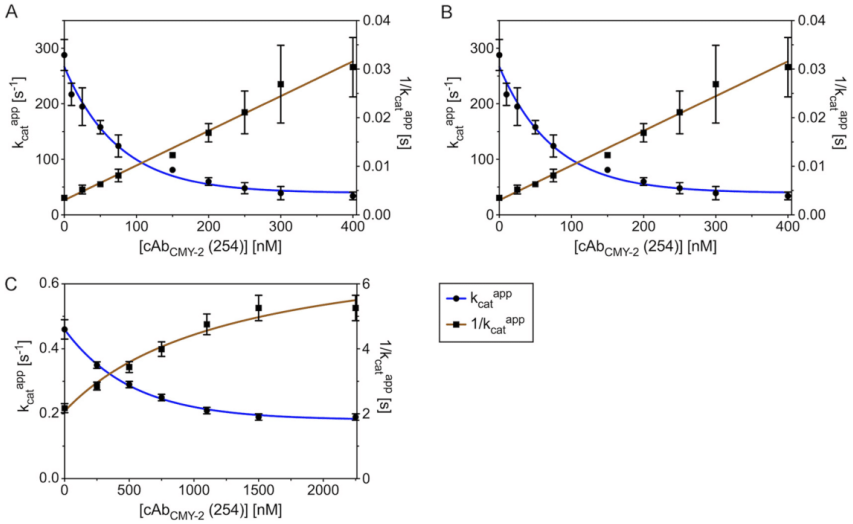

FIG 10 Inhibitory model for CMY-2 activity for cephaloridin (A), cephalothin (B), and ampicillin (C) by cAb_{CMY-2}(254). k_{cat}^{app} and $1/k_{cat}^{app}$ parameters were obtained from the linear phase (equation III in Text S1) of hydrolysis of the corresponding substrate. Concentrations of CMY-2 were at 0.2 nM, 1 nM, and 5 nM for cephaloridin, cephalothin, and ampicillin, respectively.

model, the values of the theoretical parameters α and β were estimated at 1 and 0, respectively (see description of scheme 1 in Materials and Methods). The K_i of cAb_{CMY-2}(254) for CMY-2 was determined from equation IV in Text S1 and was equal to 88 ± 3 nM, which is in good agreement with the equilibrium constant of dissociation of the complex assessed by BLI (Table 1).

Residual activity measurements suggested a similar pattern of inhibition of CMY-2 activity by the VHH cAb_{CMY-2}(254) for the hydrolysis of the three tested cephalosporins (Fig. 8). Thereby, considering K_m^{app} unchanged for any concentration of inhibitors, the VHH also behaved as a pure noncompetitive inhibitor (Fig. 10A and B) with K_i values of 48 ± 10 nM and 107 ± 13 nM for cephaloridin and cephalothin, respectively. In contrast, for ampicillin (Fig. 10C), the hyperbola tendency of $1/k_{cat}^{app}$ as function of VHH concentration was indicative of mixed noncompetitive inhibition. In this case, the parameter β was equal to 0.41 ± 0.01 and the K_i value was equal to 352 ± 62 nM (equation V in Text S1). Our data indicated that for ampicillin, the ESI complex presented a reduced but not abolished activity compared to the ES complex when the concentration of cAb_{CMY-2}(254) was significantly higher than the inhibition constant value (K_i).

Structural characterization of the cAb_{CMY-2}(254)/CMY-2 complex. The crystal of the cAb_{CMY-2}(254)/CMY-2 complex belonged to the $P6_222$ space group and diffracted at a resolution of 3.2 Å. All data and refinement statistics are summarized in Table 3. The asymmetric unit contained one CMY-2/VHH complex. The model includes residues K3 to Q361 in the β-lactamase molecules and residues Q1 to H124 in cAb_{CMY-2}(254), with the exception of residues G108 and E109 in CDR3, which were not defined in the electronic density.

The binding area between the two proteins was about 950 $Å^2$. cAb_{CMY-2}(254) interacted via the CDR1 and CDR3 loops at the junction between the α and the α/β domains of CMY-2 (Fig. 11A and B). In more detail, a first hydrophobic cluster was formed by residues V2 (N-terminal end), residues F27 and Y32 from CDR1 and I98 from CDR3 of cAb_{CMY-2}(254), and residues K290, V291, A294, and L296 located on helix α12 and β-strand β13 of CMY-2 (Fig. 11C).

Moreover, the N-terminal residues of CDR3 (i.e., D99, R100, and L102) established H-bonds with the main chain of residues L293 and A295 located, respectively, on helix

TABLE 3 Data collection and refinement statistics[a]

Crystal	cAb_{CMY-2}(254)/CMY-2
PDB code	7PA5
Data collection	
Space group	P $6_2$22
Cell constants	
a, b, c (Å)	95.12, 95.12, 242.94
α, β, γ (°)	90.00, 90.00, 120.00
Resolution range (Å)*b*	48.88–3.18 (3.37–3.18)
Rmerge (%)*b*	71 (342)
$/<\sigma I>^a$	7.1 (1.28)
Completeness (%)*b*	99.6 (97.9)
Redundancy*b*	37.8 (34.8)
CC (1/2)*b*	0.999 (42.9)
Refinement	
No. of unique reflections	11,518
R work (%)	0.2067
R free (%)	0.2502
No. of atoms	7,475
Protein	7,467
Solvent	8
RMS deviations from	
Bond lengths (Å)	0.004
Bond angles (°)	1.03
Mean B factor (Å^2)	78.0
Ramachandran plot	
Favored region (%)	96
Allowed regions (%)	4

[a]Values in parentheses are related to high-resolution shell.

α12 and β-strand β13 and with residue Q141, found on the α5β5 loop (Fig. 11D). Finally, residues D111 and Y112 from the C-terminal end of CDR3 made H-bonds with CMY-2 residues S289 and K290, respectively.

All these interactions resulted in a partial entry of CDR3 into the CMY-2 active site, mediated mainly by residue Y110 of the VHH (Fig. 11D). However, both residues G108 and E109 were not assigned in the electron density, highlighting an important flexibility of the CDR3 region and the inability of the VHH to enable the entrance of the substrate into the CMY-2 active site.

DISCUSSION

Overlapping epitopes of the VHHs. Immunization of alpacas allowed the selection of eight VHHs, belonging to three families that recognized CMY-2. One representative VHH of each of the different families was selected. Competition binding assays highlighted that the three VHHs bind to an overlapping epitope on CMY-2. The structure of the complex cAb_{CMY-2} (254)/CMY-2 revealed essentially the insertion of the CMY-2 K290 into a pocket on the surface of cAb_{CMY-2}(254) (Fig. 11C) and a second binding area involving most of CDR3 (Fig. 11D). The residues forming the pocket are conserved between the three VHHs except for I98, which is mutated into an alanine (Fig. 1). Despite the fact that CDR3 constitutes the least conserved region among the VHHs, the three VHHs may share similar binding modes with different affinities related to the ability of CDR3 to bind to CMY-2.

Biochemical features of the VHHs for the CMY-2 subfamily. *In vitro* binding assays demonstrated that cAb_{CMY-2}(254) and cAb_{CMY-2}(272) present a higher specificity for β-lactamases belonging to the CMY-2 subfamily (no recognition of CMY-1 or P99) than cAb_{CMY-2}(250), which also binds P99. The higher affinity and specificity of cAb_{CMY-2}(254)

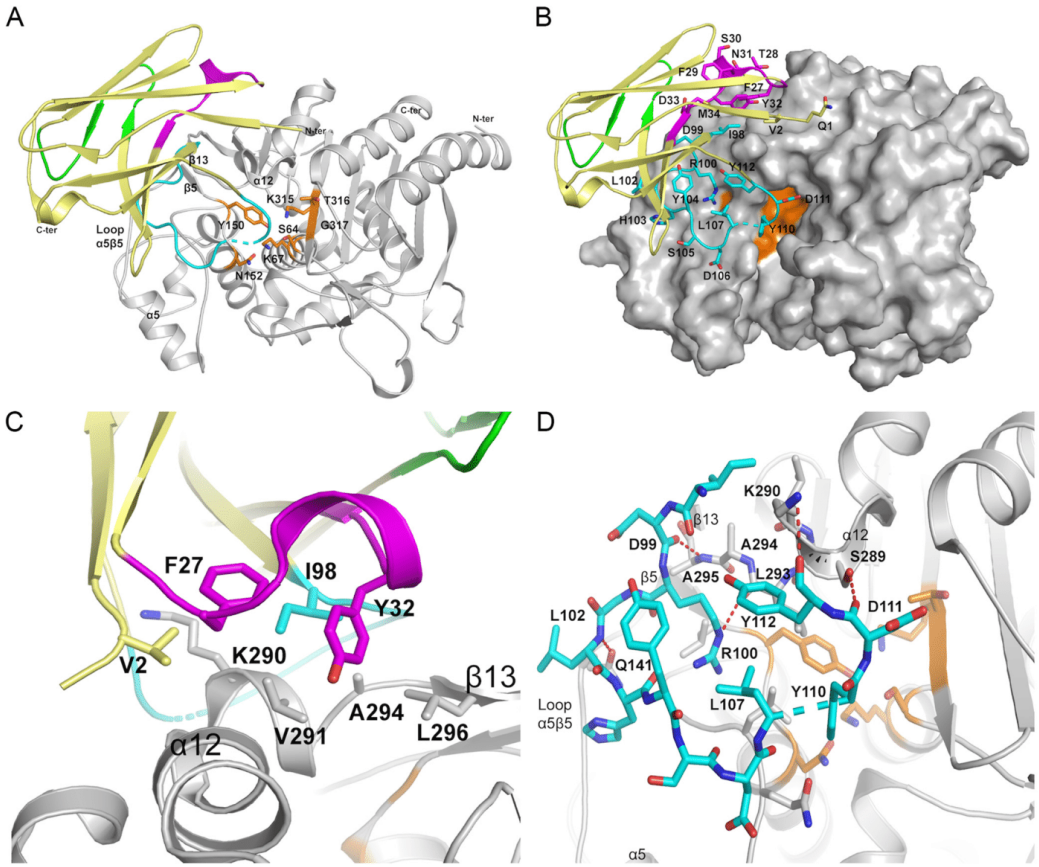

FIG 11 Binding molecular characterization of the complex cAb_{CMY-2}(254)/CMY-2. (A) Cartoon representing the overall view of the complex cAb_{CMY-2}(254)/CMY-2. (B) Surface representation of CMY-2 in the complex cAb_{CMY-2}(254)/CMY-2. (C) Hydrophobic interactions between CDR1 and the N-terminal extremity of the VHH and CMY-2. (D) Hydrogen bonds between CDR3 of the VHH and CMY-2. CDR1, CDR2, and CDR3 of the VHH are colored in purple, green, and cyan, respectively, while frameworks are represented in yellow. CMY-2 is represented in gray, while residues constituting motif 1 ($S_{64}XXK_{67}$), motif 2 ($Y_{150}XN_{152}$), and motif 3 ($K_{315}T_{316}G_{317}$) of the CMY-2 active site are colored in orange. Hydrogen bonds are highlighted by a red dotted line. Residues G108 and D109 from CDR3 of cAb_{CMY-2}(254) are not illustrated in the model due to a lack of information in the electronic density.

justified its use rather than cAb_{CMY-2}(272) for the screening of bovine and human bacterial isolates by a sandwich ELISA. *In vivo* binding assays on bacterial isolates highlighted the ability to detect different variants from the CMY-2 subfamily as CMY-16, -42, -58, -60, and -61. In fact, the sequence of the epitope recognized by cAb_{CMY-2}(254) is strictly conserved for all known variants from the CMY-2 subfamily, meaning the high probability to detect also new CMY-2-like β-lactamases. Moreover, we did not detect other class C β-lactamases, such as ACT-1, DHA-1, and CMY-10. ACT-1 and P99 present a high sequence identity with CMY-2 (Fig. S4), providing a similar conformation of helix α12 (Fig. 12A). However, A295 is replaced by a proline in P99 and ACT-1, which may explain the inability to interact with the VHH. The presence of a proline introduces a steric hindrance in the helix and may displace the H-bond network stabilizing the VHH/CMY-2 complex. The steric hindrance with E294 and the total conformation change of helix α12 due to a low sequence identity with CMY-2 could prevent the interaction of CMY-1 and CMY-10 with the VHH (Fig. 12B).

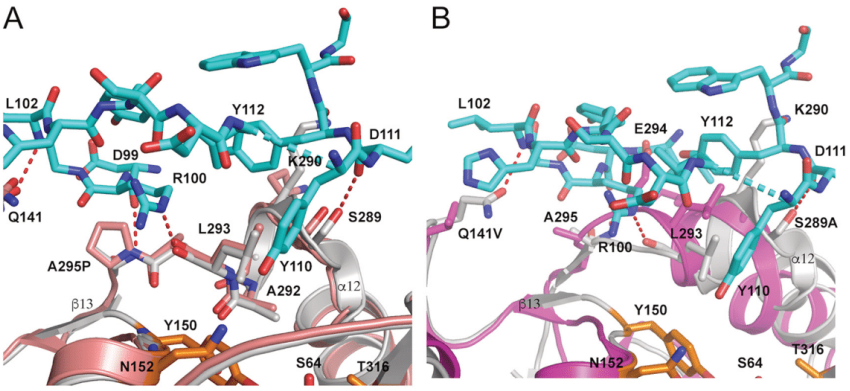

FIG 12 Superposition of complex cAb_{CMY-2}(254)/CMY-2 and P99 (PDB code 1XX2) (A) and CMY-10 (PDB code 1ZKJ) (B). CMY-2, P99, and CMY-10 are colored in gray, red, and magenta. Only CDR3 of the VHH is illustrated in cyan, and active site residues are in orange. H-bonds are represented with a red dashed line.

Biochemical features of the polyclonal antibodies against CMY-2. The overlapping epitope on CMY-2 shared by the three VHHs required the development of rabbit polyclonal antibodies. These antibodies were less specific since they were able to recognize P99 and CMY-1. They correspond to a mix of antibodies probably able to bind to epitopes shared by a large panel of AmpC β-lactamases, which could explain their lack of specificity (29). Fortunately, the use of the VHH cAb_{CMY-2}(254) permitted us to offset the low specificity of the pAbs for the detection of CMY-2 in the sandwich ELISA.

Development of tandem-repeat VHH $cAb_{CMY-2}(254)_{BIV}$. Another aspect with the VHHs is the possibility to fuse them in order to decrease the dissociation rate by an avidity phenomenon leading to more stable antigen/antibody complexes (32–34). This allowed the detection of lower quantities of CMY-2 than the monovalent counterpart.

Applicability in an ELISA. This study presented the advantages of the use of VHH as antibody for the detection of a β-lactamase. Compared to classical monoclonal antibodies, VHHs are easier to produce and purify. They also present some biochemical features allowing better stability and solubility. Moreover, they generally display a high affinity and specificity for their antigens, essential to obtain a more suitable detection assay, as already demonstrated for cancer biomarkers (35, 36). The low affinity of some VHHs can be compensated by the engineering of tandem-repeat VHHs, improving the sensitivity of a detection assay due to an avidity phenomenon.

One goal of the project RUBLA consisted of developing a sandwich ELISA "type" for the detection of one of the most widespread β-lactamases, CMY-2, in bovines and more largely in the animal world. However, our next aim is to develop an immunochromatographic lateral flow assay that ensures the detection more rapidly and in an easier manner, aiming an interesting alternative to phenotypic methods for veterinarians (37).

Finally, despite the fact that this test is probably suitable for CMY-2 detection in animals, it remains less useful in human medicine, where phenotypic assays constitute an unavoidable method for selection of the best antibiotic. However, the detection of other β-lactamases with this setup could help to interpret more easily the difficult phenotypic profiles generally found for multidrug-resistant (MDR) strains (23), to distinguish plasmid from chromosomal AmpC (38), and to highlight the involvement of an AmpC in carbapenemase activity of the strain (24).

VHH $cAb_{CMY-2}(254)$, a noncompetitive inhibitor of CMY-2 activity. This work allowed also the selection of VHHs that behave as noncompetitive inhibitors. The structure of the complex cAb_{CMY-2}(254)/CMY-2 highlighted an important flexibility of the CDR3 loop located in the active site, which does not prevent the entry of the substrate in the active site. Nevertheless, the Y100 residue brought by CDR3 is near the Q120

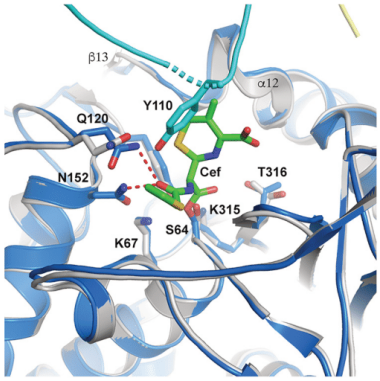

FIG 13 Superposition of the complex cAb_{CMY-2}(254)/CMY-2 and the crystal structure of AmpC WT β-lactamase from *E. coli* in complex with a covalently bound cephalothin (PDB code 1KVM). CMY-2 is in gray, AmpC in blue, cephalothin in green, and CDR3 of the VHH in cyan.

residue of CMY-2, considered a crucial residue involved in the stabilization of the acyl enzyme by the establishment of H-bonds with the C-7 amide carbonyl of the substrate (39). Therefore, despite the fact that Y110 does not directly bind Q120, it may impede the stabilization of the acyl enzyme (Fig. 13). Moreover, the interaction of the VHH around the active site may perturb the dynamic of the enzyme, which is known to be essential for the optimal activity of the enzyme (40).

Our study provided also evidence that the mechanism of inhibition can be different in function of the substrate. We found that the VHH behaved as a noncompetitive inhibitor with its ability to completely inhibit the activity of CMY-2 for all cephalosporins tested (scheme 1). However, in the presence of ampicillin, the complex maintained a reduced activity corresponding to a mixed noncompetitive inhibition. The more plausible explanation consists of the fact that the ampicillin can easily diffuse in the active site due to its smaller size, resulting in less impact by an eventual steric hindrance and/or motion perturbation.

Peptidomimetics from VHH, an alternative strategy to classical inhibitors. Despite the fact that VHH is smaller than classical antibodies (15 kDa versus 150 kDa), it stays too bulky to penetrate into the periplasmic space of the bacteria. Actually, one strategy in view to minimize the size of inhibitors consists of the development of small peptides by peptidomimetics. This strategy presents several advantages: (i) an easier production in large scale-up with low cost, (ii) a major penetration of tissues compared to large molecules and antibodies, rendering more efficient the drug delivery and its action, and (iii) the humanization of therapeutic antibodies, which can be laborious and which can lead finally to the development of human anti-mouse antibody (HAMA) (41, 42).

Peptidomimetics can lead to the development of peptides based on the therapeutics monoclonal antibodies, as from the recombinant humanized monoclonal antibody (rhuMAb) 4D5 (trastuzumab), used in the treatment of the breast cancer (43). More interestingly, VHHs were also used as scaffold for the development of peptides against vascular endothelial growth factor (VEGF), implicated in angiogenesis leading to tumor development (28), or against the receptor β-2 adrenergic associated with chronic inflammation (44).

The main drawback to consider in peptidomimetics consists of generally lower affinities of peptides than for the corresponding antibodies. In fact, we could obtain K_D values near or higher than 1 μM. However, some studies demonstrated that lower affinities resulted from a decrease of the association constant independent of the dissociation rate (45, 46).

To conclude, peptides can be an important alternative to nanobodies as therapeutic agents due to their smaller size and their interesting pharmaceutical features. We could

consider this type of development against β-lactamases such as CMY-2, which stays more interesting for the veterinarians, but also against more interesting enzymes such as metallo-β-lactamases.

MATERIALS AND METHODS

Production of the β-lactamase CMY-2. CMY-2 was produced as previously described by Bauvois et al. (16). The CMY-2 protein was stored at −20°C in 50 mM morpholinepropanesulfonic acid (MOPS) buffer at pH 7.0 containing 10% (wt/vol) glycerol. Its integrity was verified by Coomassie-stained SDS-PAGE and electrospray ionization-quadrupole time of flight (ESI-Q-TOF) mass spectrometry with a Waters Synat-G2 instrument (Waters, Milford, MA). The relevant *m/z* was equal to 910, and the exact mass was equal to 38,755. The concentration of the purified enzyme was determined by its absorbance at 280 nm. The molar extinction coefficient was calculated with the help of the Cantor and Schimmel equation (https://web.expasy.org) (ε^{280} = 93,850 M^{-1} cm^{-1}).

Selection of VHHs by phage display. One alpaca (*V. pacos*) was immunized by six weekly subcutaneous injections of 100 μL of lipopolysaccharide (LPS)-free CMY-2 (1 mg/mL) in HEPES buffer (pH 7) mixed with Gerbu adjuvant TMP. The immune library was constructed following the protocol developed by Conrath et al. (14). The screening of the anti-CMY-2 nanobodies was performed as described by Pardon et al. (47). All details concerning those experiments are described in Text S1 in the supplemental material.

Cloning of VHH genes into pHEN14, scale-up production, and purification. Genes coding for VHHs selected by phage display were subcloned into the expression vector pHEN14 between the restriction enzyme sites HindIII in the 5′ extremity and BstEII in the 3′ extremity. pHEN14 derived from the phagemid pHEN6 in which the resistance to ampicillin was replaced by the resistance to chloramphenicol and the sequence coding for the Myc tag was removed (15). Synthetic genes coding for the bivalent VHHs, corresponding to two identical VHHs in tandem repeats joined by the peptide linker $(GGGS)_3$, were purchased from GeneCust (Boynes, France) (31). Production of monovalent and bivalent VHHs started with the transformation of competent *E. coli* WK6 with plasmid constructs by thermic shock. Then, the cells were plated on LB agar containing chloramphenicol (25 μg/mL) for selection. VHHs were produced in Terrific broth medium (TB) supplemented by chloramphenicol (25 μg/mL). An overnight preculture was inoculated in fresh TB at an optical density at 600 nm (OD_{600}) of 0.2. The growth was performed at 37°C to an OD_{600} of ≈0.8 before addition of 1 mM isopropyl-β-D-thiogalactopyranoside (IPTG) to induce the production of VHHs overnight at 28°C. The cells were harvested by centrifugation at 5,000 × *g*, and a periplasmic extraction by osmotic shock was carried out with a solution containing 0.5 M sucrose. This extraction was followed by affinity chromatography with an HisTrap HP Ni-nitrilotriacetic acid column (Cytiva, Washington, DC) and purification by size exclusion chromatography (Superdex 75). Purified VHHs were conserved in 50 mM phosphate-buffered saline (PBS; pH 6.1). The purity and the integrity of the VHHs were verified by Coomassie-stained SDS-PAGE and mass spectroscopy (ESI-Q-TOF).

Immunization of rabbits and purification of pAbs. Polyclonal antibodies (pAbs) were obtained by rabbit immunization carried out by the CER Group (Marloie, Belgium). The immunization consisted of four injections of 100 μL of CMY-2 (1 mg/mL in HEPES [20 mM; pH 6.0]) over 2 weeks in a standard subcutaneous way. Then, sera recovered from blood were centrifuged and the supernatant was diluted 3-fold in 50 mM PBS (pH 7.4) buffer. pAbs were purified with a HiTrap protein A HP antibody purification column (Cytiva, Washington, DC) where the elution buffer corresponded to 20 mM glycine (pH 2.0) buffer. Fractions containing the pAbs were pooled and dialyzed against a 50 mM PBS (pH 7.4) buffer overnight at 4°C. The integrity and purity of the pAbs were assessed by Coomassie-stained SDS-PAGE, while the concentration of the pAbs was measured by bicinchoninic acid assay (BCA).

***In vitro* biotinylation of antigen and antibodies.** Some biolayer interferometry (BLI) experiments and ELISAs required biotinylated proteins. To this aim, we used the EZ-Link NHS-PEG_4 biotin kit (Thermo Scientific, USA) to covalently bind biotin molecules on lysine residues of proteins. The chemical reaction was performed at room temperature for 30 min and with a [biotin]/[protein] ratio of 3:1. The excess biotin was removed by the elution of the reaction mixture on a Sephadex G25 column. The labeled protein was conserved in 50 mM PBS at pH 7.5 at a final concentration between 100 and 500 μg/mL.

Kinetic characterization by BLI. All BLI experiments were performed on the OCTET HTX instrument (ForteBio, Sartorius, Goettingen, Germany) at 30°C using 96-well black polypropylene microplates (Greiner BioOne, Belgium). All proteins were diluted in kinetic buffer (50 mM PBS [pH 7.4], 0.1% [wt/vol] bovine serum albumin [BSA], 0.05% [vol/vol] Tween 20).

The specificity of the nanobodies was studied as follows. Purified VHHs (2 μg/mL) were immobilized on anti-His-coated sensors (His1K; Sartorius) via their His_6 tag. Then, a baseline was monitored with the kinetic buffer for 60 s. Binding to the VHHs on the sensor was monitored by incubating, for 120 s, the VHH in the presence of a solution of 500 nM antigens representing all classes of β-lactamases: TEM-1 for class A, VIM-4 for class B, CMY-1, CMY-2, and P99 for class C, and OXA-48 for class D. The dissociation kinetic constant of the complex was monitored for 300 s by incubating the sensor in the kinetic buffer. Moreover, for the quantitative binding assays, the conditions for each VHH were as follows: (i) $cAb_{CMY\text{-}2}$(250) was assessed for 10 and 60 s of association and dissociation, respectively, using a range of CMY-2 concentrations between 50 and 250 nM; (ii) $cAb_{CMY\text{-}2}$(254) was assessed for 60 and 600 s and using a range between 40 and 450 nM; and (iii) $cAb_{CMY\text{-}2}$(272) was assessed for 30 and 180 s and using a range between 20 and 110 nM.

All data were analyzed by Octet software version 12.0 (Sartorius). Kinetics constants (k_{on} and k_{off}) and equilibrium constant (K_D) were calculated using a 1:1 interaction model with a global fit based on at least seven analyte concentrations indicated on all sensorgrams.

Avidity studies were performed using streptavidin biosensors (SA sensor; Sartorius) where biotinylated CMY-2 was immobilized for 30 to 50 min at a concentration between 10 and 50 μg/mL. A quench reaction was done by incubating biocytin at 10 μM for 300 s. Then, the binding of the monovalent and the bivalent VHHs was monitored for 30 s using ranges of CMY-2 concentrations between 150 and 1,000 nM and between 75 and 375 nM, respectively. The dissociation of the complexes was measured for 600 s in the kinetic buffer. The binding of the rabbit pAbs to the antigen was monitored for 60 s (12.5 to 200 nM CMY-2), and the dissociation of the complexes was measured for 600 s. A global fit based on 5 analyte concentrations was realized only for dissociation constant (k_{off}) thanks to an exponential decay mathematic model. Specificity binding of the pAbs was undertaken following the same setup except that the association was measured for 300 s using 500 nM pAbs.

Competition binding assays were performed by a premix method with streptavidin biosensor (SA sensor; Sartorius). First, a biotinylated VHH (2 μg/mL) was immobilized on the sensor to reach a variation of the signal ($\Delta\lambda$) of around 1 nm. VHH/CMY-2 complexes were obtained by incubating CMY-2 (200 nM) and the VHH (100 nM to 4 μM) for 15 min at 30°C. Then, the solutions were loaded in order to assess the association between the immobilized VHH and the VHH/CMY-2 complexes. Binding rates were measured for the first 120 s of the association phase with an exponential mathematics model.

pAb specificity by indirect ELISA. The specificity of pAbs directed against CMY-2 was determined by an indirect ELISA. To this aim, 500 ng of antigens representing all classes of β-lactamases diluted in 50 mM morpholineethanesulfonic acid (MES; pH 5.5) buffer were immobilized by absorption on a 96-well Nunc Maxisorp plate (Thermo Scientific) overnight at 4°C. All nonspecific sites were saturated using 1% (wt/vol) BSA for 2 h. Then, 500 ng of anti-CMY-2 pAbs was added in each well. The assay was revealed by a 1/2,000 diluted goat anti-rabbit antibody conjugated to horseradish peroxidase (HRP) (Abcam, Cambridge, UK). All steps were followed by 5 washes with 50 mM (pH 7.5) buffer–0.05% Tween 20. Antibodies were diluted in the washing buffer and all incubations were performed for 1 h at 28°C. 3,3′,5,5′-Tetramethylbenzidine (TMB; Merck, Darmstadt, Germany), the HRP substrate, was used for system revelation. The reaction was quenched with 1 M H_3PO_4, and the absorbance of the different wells was read at 450 nm using an Infinite M200 Pro microplate reader (Tecan, Switzerland).

Sandwich ELISA development for CMY-2 detection. A sandwich ELISA for CMY-2 detection was designed to investigate the limit of detection (LOD) and the specificity of the different assay formats. To this aim, several combinations of capture and detection VHHs and anti-CMY-2 pAbs were tested. Briefly, 500 ng of biotinylated VHH cAb_{CMY-2}(254) (monovalent or bivalent) or 2 μg of biotinylated anti-CMY-2 pAbs was used as the capture agent on a 96-well Nunc streptavidin polysorb plate incubated overnight at 4°C. The plate was blocked by a 1% (wt/vol) BSA solution. Then, the purified CMY-2 was added in serial dilutions from 10^{-4} to 2 μg/mL to determine the LODs of the four assay combinations. The LODs were calculated with a sigmoidal model on GraphPad Prism software (equation I in Text S1).

The specificity of the assays was evaluated with 200 ng of the six chosen β-lactamases belonging to the four classes of β-lactamases. At least three wells where antigen was omitted were used as blanks. Additionally, the detection of CMY-2 produced by human and bovine bacterial isolates was performed as follows. The different strains were grown in TB medium supplemented with 100 μg/mL of ampicillin for 4 h at 37°C. Strains were lysed by sonication with a Bioruptor Plus (Diagenode, Belgium) and centrifuged at 18,000 $\times$ *g* in order to recover the bacterial content. The protein concentrations of the different samples were determined by BCA. All detection assays on bacterial isolates were performed by using 5 μg of bacterial crude extract. An *E. coli* DH5α strain was used as a negative control. Detection of CMY-2 was performed by adding 500 ng/well of pAbs themselves, followed by the addition of a 1/2,000 diluted goat anti-rabbit antibody conjugated to HRP (Abcam, UK) or by adding 200 ng/well of monovalent or bivalent cAb_{CMY-2}(254) recognized by 1/2,000 diluted rabbit anti-HCAbs antibody conjugated to HRP (Genscript, USA). All the washing steps and the detection of the HRP activity were performed as describe above.

Steady-state enzymatic kinetics. Steady-state enzymatic kinetics were determined at 30°C using a 50 mM PBS (pH 7.5) supplemented with 50 μg/mL of BSA. Absorbances were measured with a Specord 75 spectrophotometer (Analytik Jena, Germany) or a SpectraMx M2 microplate reader (Molecular Devices, USA). Initial rates and complete hydrolysis curves of the following substrates were measured: 100 μM ampicillin ($\Delta\varepsilon^{235} = -820\ M^{-1}\ cm^{-1}$), 100 μM cephalothin ($\Delta\varepsilon^{273} = -6{,}300\ M^{-1}\ cm^{-1}$), 100 μM cephaloridin ($\Delta\varepsilon^{260} = -10{,}000\ M^{-1}\ cm^{-1}$), and 40 μM nitrocefin ($\Delta\varepsilon^{482} = 15{,}000\ M^{-1}\ cm^{-1}$). The concentration of CMY-2 used to hydrolyze the various substrates was between 0.2 nM and 5 nM and was mixed with increasing amounts of the VHH cAb_{CMY-2}(254) (0 to 1,500 nM). All steady-state kinetics constants were measured by using equations described in Text S1.

The kinetic model for the inhibition events of CMY-2 activity by the VHHs is described by scheme 1 (19), where K_i corresponds to the dissociation constant of the inhibitor.

SCHEME 1. General kinetic mode. The α parameter is the degree at which the inhibitor influences the affinity of the enzyme for its substrate, while the β parameter is the activity of the tertiary complex ESI compared to the activity of the complex ES. The constant k_p corresponds to the turnover rate constant (k_{cat}).

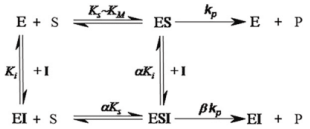

Crystallization conditions. Crystals were grown at 20°C using the sitting-drop vapor diffusion method. The drop contained 0.2 μL of CMY-2 in complex with VHH cAb_{CMY-2}(254) at a concentration of 14 mg/mL and 0.2 μL of 0.1 M Tris-HCl (pH 8.5) buffer with 1.4 M $(NH_4)_2$ tartarate. The crystal was transferred in a cryoprotectant solution containing 50% (vol/vol) polyethylene glycol 400 and 50% (vol/vol) glycerol and frozen in liquid nitrogen.

Data collection, phasing, model building and refinement. Data were collected at the Proxima 1 beamline of the Soleil synchrotron (Saint Aubin, France). Indexing, integration, and scaling of the data were performed using XDS (48). Initial phases were obtained by molecular replacement with the CMY-2 structure (PDB code 1ZC2) and a llama antibody fragment bound to galectin 10 (49) (PDB code 6GKU) as search models using Phaser (50). The structure was built with Coot (51) and refined with Phenix refine (52). Figures were prepared using PyMOL (PyMOL molecular graphics system, version 2.4.1, enhanced for Mac OS X; Schrödinger, LLC).

Data availability. The accession numbers of the nucleotide sequence of the VHHs cAb_{CMY-2}(250), cAb_{CMY-2}(254), and cAb_{CMY-2}(272) are OP700411, OP700412, and OP700413, respectively.

The PDB code for the structure of the complex is 7PA5.

SUPPLEMENTAL MATERIAL

Supplemental material is available online only.

SUPPLEMENTAL FILE 1, PDF file, 3.8 MB.

ACKNOWLEDGMENTS

We thank the Protein Factory Platform at University of Liège for providing material necessary for protein purification and for providing some purified β-lactamases necessary for the specificity binding experiments. We acknowledge the Robotein platform of the BE Instruct-ERIC Centre for providing access to the Octet HTX and the Microlab STAR liquid handling workstation.

This work was supported by the Belgian Federal Public Service Health, Food Chain Safety and Environment (grant no. RF 17/6317 RU-BLA-ESBL-CPE) and the Fonds National de la Recherche Scientifique (CDR grant no. J0081.20). The ALPANANO platform was supported by ULiège through Crédit d'Opportunité Stratégique no. OPP_CURV_20-21.

REFERENCES

1. O'Neill J. 2016. Tackling drug-resistant infections globally: report and recommendations. Wellcome Trust and UK Government, London, United Kingdom. https://amr-review.org/.
2. Bush K, Bradford P. 2016. β-Lactams and β-lactamase inhibitors: an overview. Cold Spring Harb Perspect Med 6:a025247. https://doi.org/10.1101/cshperspect.a025247.
3. Fisher J, Meroueh S, Mobashery S. 2005. Bacterial resistance to β-lactam antibiotics: compelling opportunism, compelling opportunity. Chem Rev 105:395–424. https://doi.org/10.1021/cr030102i.
4. Tipper DJ, Strominger JL. 1965. Mechanism of action of penicillins: a proposal based on their structural similarity to acyl-D-alanyl-D-alanine. Proc Natl Acad Sci U S A 54:1133–1141. https://doi.org/10.1073/pnas.54.4.1133.
5. Lim D, Strynadka NCJ. 2002. Structural basis for the β-lactam resistance of PBP2a from methicillin-resistant Staphylococcus aureus. Nat Struct Biol 9:870–876. https://doi.org/10.1038/nsb858.
6. Sauvage E, Kerff F, Fonzé E, Herman R, Schoot B, Marquette JP, Taburet Y, Prevost D, Dumas J, Leonard G, Stefanic P, Coyette J, Charlier P. 2002. The 2.4-Å crystal structure of the penicillin-resistant penicillin-binding protein PBP5fm from Enterococcus faecium in complex with benzylpenicillin. Cell Mol Life Sci 59:1223–1232. https://doi.org/10.1007/s00018-002-8500-0.
7. Jetter M, Spaniol V, Troller R, Aebi C. 2010. Down-regulation of porin M35 in Moraxella catarrhalis by aminopenicillins and environmental factors and its potential contribution to the mechanism of resistance to aminopenicillins. J Antimicrob Chemother 65:2089–2096. https://doi.org/10.1093/jac/dkq312.
8. Simonet V, Malléa M, Pagès JM. 2000. Substitutions in the eyelet region disrupt cefepime diffusion through the Escherichia coli OmpF channel. Antimicrob Agents Chemother 44:311–315. https://doi.org/10.1128/AAC.44.2.311-315.2000.
9. Hiroshi N, Pagès JM. 2012. Broad-specificity efflux pumps and their role in multidrug resistance of Gram-negative bacteria. FEMS Microbiol Rev 36:340–363. https://doi.org/10.1111/j.1574-6976.2011.00290.x.
10. Vivas R, Barbosa A, Dolabela S, Jain S. 2019. Multidrug-resistant bacteria and alternative methods to control them: an overview. Microb Drug Resist 25:890–908. https://doi.org/10.1089/mdr.2018.0319.
11. Rudgers G, Huang W, Palzkill T. 2001. Binding properties of a peptide derived from β-lactamase inhibitory protein. Antimicrob Agents Chemother 45:3279–3286. https://doi.org/10.1128/AAC.45.12.3279-3286.2001.
12. Dooley H, Flajnik M, Porter A. 2003. Selection and characterization of naturally occurring single-domain (IgNAR) antibody fragments from immunized sharks by phage display. Mol Immunol 40:25–33. https://doi.org/10.1016/s0161-5890(03)00084-1.
13. Muyldermans S. 2013. Nanobodies: natural single-domain antibodies. Annu Rev Biochem 82:775–797. https://doi.org/10.1146/annurev-biochem-063011-092449.
14. Conrath KE, Lauwereys M, Galleni M, Matagne A, Frère JM, Kinne J, Wyns L, Muyldermans S. 2001. β-Lactamase inhibitors derived from single-domain antibody fragments elicited in the Camelidae. Antimicrob Agents Chemother 45:2807–2812. https://doi.org/10.1128/AAC.45.10.2807-2812.2001.
15. Sohier JS, Laurent C, Chevigné A, Pardon E, Srinivasan V, Wernery U, Lassaux P, Steyaert J, Galleni M. 2013. Allosteric inhibition of VIM metallo-β-lactamases by a camelid nanobody. Biochem J 450:477–486. https://doi.org/10.1042/BJ20121305.
16. Bauvois C, Ibuka AS, Celso A, Alba J, Ishii Y, Frère J-M, Galleni M. 2005. Kinetic properties of four plasmid-mediated AmpC β-lactamases. Antimicrob Agents Chemother 49:4240–4246. https://doi.org/10.1128/AAC.49.10.4240-4246.2005.
17. Guérin V, Thiry D, Lucas P, Blanchard Y, Cawez F, Mercuri PS, Galleni M, Saulmont M, Mainil J. 2021. Identification of β-lactamase-encoding (bla) genes in phenotypically β-lactam-resistant Escherichia coli isolated from young calves in Belgium. Microb Drug Resist 27:1578–1584. https://doi.org/10.1089/mdr.2020.0472.
18. Ewers C, De Jong A, Prenger-Berninghoff E, El Garch F, Leidner U, Tiwari SK, Semmler T. 2021. Genomic diversity and virulence potential of ESBL- and AmpC-β-lactamase-producing Escherichia coli strains from healthy

food animals across Europe. Front Microbiol 12:626774. https://doi.org/10.3389/fmicb.2021.626774.
19. Pietsch M, Irrgang A, Roschanski N, Michael GB, Hamprecht A, Rieber H, Käsbohrer A, Schwarz S, Rösler U, Kreienbrock L, Pfeifer Y, Fuchs S, Werner G. RESET Study Group. 2018. Whole genome analyses of CMY-2-producing Escherichia coli isolates from humans, animals and food in Germany. BMC Genomics 19:601. https://doi.org/10.1186/s12864-018-4976-3.
20. Black JA, Thomson KS, Buynak JD, Pitout JDD. 2005. Evaluation of β-lactamase inhibitors in disk tests for detection of plasmid-mediated AmpC β-lactamases in well-characterized clinical strains of Klebsiella spp. J Clin Microbiol 43:4168–4171. https://doi.org/10.1128/JCM.43.8.4168-4171.2005.
21. Pérez-Pérez FJ, Hanson ND. 2002. Detection of plasmid-mediated AmpC β-lactamase genes in clinical isolates by using multiplex PCR. J Clin Microbiol 40:2153–2162. https://doi.org/10.1128/JCM.40.6.2153-2162.2002.
22. Tamma PD, Doi Y, Bonomo RA, Johnson JK, Simner PJ. Antibacterial Resistance Leadership Group. 2019. A primer on AmpC β-lactamases: necessary knowledge for an increasingly multidrug-resistant world. Clin Infect Dis 69:1446–1455. https://doi.org/10.1093/cid/ciz173.
23. Conen A, Frei R, Adler H, Dangel M, Fux CA, Widmer AF. 2015. Microbiological screening is necessary to distinguish carriers of plasmid-mediated AmpC beta-lactamase-producing Enterobacteriaceae and extended-spectrum beta-lactamase (ESBL)-producing Enterobacteriaceae because of clinical similarity. PLoS One 10:e0120688. https://doi.org/10.1371/journal.pone.0120688.
24. Majewski P, Wieczorek P, Ojdana D, Sieńko A, Kowalczuk O, Sacha P, Nikliński J, Tryniszewska E. 2016. Altered outer membrane transcriptome balance with AmpC overexpression in carbapenem-resistant Enterobacter cloacae. Front Microbiol 7:2054. https://doi.org/10.3389/fmicb.2016.02054.
25. Harris PNA, Alder L, Paterson DL. 2015. Antimicrobial susceptibility reporting and treatment selection for AmpC-producing Enterobacteriaceae: what do microbiologists and infectious disease practitioners actually practice? Pathology 47:386–388. https://doi.org/10.1097/PAT.0000000000000255.
26. Pogue JM, Bonomo RA, Kaye KS. 2019. Ceftazidime/avibactam, meropenem/vaborbactam, or both? Clinical and formulary considerations. Clin Infect Dis 68:519–524. https://doi.org/10.1093/cid/ciy576.
27. Rodríguez-Baño J, Gutiérrez-Gutiérrez B, Machuca I, Pascual A. 2018. Treatment of infections caused by extended-spectrum-beta-lactamase-, AmpC-, and carbapenemase-producing Enterobacteriaceae. Clin Microbiol Rev 31:1–42. https://doi.org/10.1128/CMR.00079-17.
28. Karami E, Sabatier JM, Behdani M, Irani S, Kazemi-Lomedasht F. 2020. A nanobody-derived mimotope against VEGF inhibits cancer angiogenesis. J Enzyme Inhib Med Chem 35:1233–1239. https://doi.org/10.1080/14756366.2020.1758690.
29. Lipman NS, Jackson LR, Trudel LJ, Weis-Garcia F. 2005. Monoclonal versus polyclonal antibodies: distinguishing characteristics, applications, and information resources. ILAR J 46:258–268. https://doi.org/10.1093/ilar.46.3.258.
30. Zhao Y, Li G. 2016. Detection of penicillinase in milk by sandwich ELISA based polyclonal and monoclonal antibody. J Immunoassay Immunochem 37:80–89. https://doi.org/10.1080/15321819.2015.1050108.
31. Morales-Yanez FJ, Idalia S, Vincke C, Hassanzadeh-Ghassabeh G, Polman K, Muyldermans S. 2019. An innovative approach in the detection of toxocara canis excretory/secretory antigens using specific nanobodies. Int J Parasitol 49:635–645. https://doi.org/10.1016/j.ijpara.2019.03.004.
32. Ibañez LI, De Filette M, Hultberg A, Verrips T, Temperton N, Weiss RA, Vandevelde W, Schepens B, Vanlandschoot P, Saelens X. 2011. Nanobodies with in vitro neutralizing activity protect mice against H5N1 influenza virus infection. J Infect Dis 203:1063–1072. https://doi.org/10.1093/infdis/jiq168.
33. Hultberg A, Temperton NJ, Rosseels V, Koenders M, Gonzalez-Pajuelo M, Schepens B, Ibañez LI, Vanlandschoot P, Schillemans J, Saunders M, Weiss RA, Saelens X, Melero JA, Verrips CT, Van Gucht S, de Haard HJ. 2011. Llama-derived single domain antibodies to build multivalent, superpotent and broadened neutralizing anti-viral molecules. PLoS One 6:e17665. https://doi.org/10.1371/journal.pone.0017665.
34. Detalle L, Stohr T, Palomo C, Piedra PA, Gilbert BE, Mas V, Millar A, Power UF, Stortelers C, Allosery K, Melero JA, Depla E. 2016. Generation and characterization of ALX-0171, a potent novel therapeutic nanobody for the treatment of respiratory syncytial virus infection. Antimicrob Agents Chemother 60:6–13. https://doi.org/10.1128/AAC.01802-15.
35. Chen J, He QH, Xu Y, Fu JH, Li YP, Tu Z, Wang D, Shu M, Qiu YL, Yang HW, Liu YY. 2016. Nanobody medicated immunoassay for ultrasensitive detection of cancer biomarker alpha-fetoprotein. Talanta 147:523–530. https://doi.org/10.1016/j.talanta.2015.10.027.
36. Li T, Li SL, Fang C, Hou YN, Zhang Q, Du X, Lee HC, Zhao YJ. 2018. Nanobody-based dual epitopes protein identification (DepID) assay for measuring soluble CD38 in plasma of multiple myeloma patients. Anal Chim Acta 1029:65–71. https://doi.org/10.1016/j.aca.2018.04.061.
37. Rösner S, Kamalanabhaiah S, Küsters U, Kolbert M, Pfennigwerth N, Mack D. 2019. Evaluation of a novel immunochromatographic lateral flow assay for rapid detection of OXA-48, NDM, KPC and VIM carbapenemases in multidrug-resistant Enterobacteriaceae. J Med Microbiol 68:379–381. https://doi.org/10.1099/jmm.0.000925.
38. Hujer AM, Page MGP, Helfand MS, Yeiser B, Bonomo RA. 2002. Development of a sensitive and specific enzyme-linked immunosorbent assay for detecting and quantifying CMY-2 and SHV β-lactamases. J Clin Microbiol 40:1947–1957. https://doi.org/10.1128/JCM.40.6.1947-1957.2002.
39. Beadle BM, Trehan I, Focia PJ, Shoichet BK. 2002. Structural milestones in the reaction pathway of an amide hydrolase. Structure 10:413–424. https://doi.org/10.1016/s0969-2126(02)00725-6.
40. Huang L, So PK, Chen YW, Leung YC, Yao ZP. 2020. Conformational dynamics of the helix 10 region as an allosteric site in class A β-lactamase inhibitory binding. J Am Chem Soc 142:13756–13767. https://doi.org/10.1021/jacs.0c04088.
41. Goulet DR, Chatterjee S, Lee WP, Waight AB, Zhu Y, Mak AN. 2022. Engineering an enhanced EGFR engager: humanization of cetuximab for improved developability. Antibodies (Basel) 11:6. https://doi.org/10.3390/antib11010006.
42. Gilliland LK, Walsh LA, Frewin MR, Wise MP, Tone M, Hale G, Kioussis D, Waldmann H. 1999. Elimination of the immunogenicity of therapeutic antibodies. J Immunol 162:3663–3671. https://doi.org/10.4049/jimmunol.162.6.3663.
43. Murali R, Greene MI. 2012. Structure based antibody-like peptidomimetics. Pharmaceuticals (Basel) 5:209–235. https://doi.org/10.3390/ph5020209.
44. Martin C, Moors SLC, Danielsen M, Betti C, Fabris C, Sejer-Pedersen D, Pardon E, Peyressatre M, Fehér K, Martins JC, Mosolff-Mathiesen J, Morris MC, Devoogdt N, Caveliers V, De Proft F, Steyaert J, Ballet S. 2017. Rational design of nanobody loop peptidomimetics: towards biased β_2 adrenergic receptor ligands. Chemistry 23:9632–9640. https://doi.org/10.1002/chem.201701321.
45. Geng L, Wang Z, Yang X, Li D, Lian W, Xiang Z, Wang W, Bu X, Lai W, Hu Z, Fang Q. 2015. Structure-based design of peptides with high affinity and specificity to HER2 positive tumors. Theranostics 5:1154–1165. https://doi.org/10.7150/thno.12398.
46. Ding H, Gangalum PR, Galstyan A, Fox I, Patil R, Hubbard P, Murali R, Ljubimova JY, Holler E. 2017. HER2-positive breast cancer targeting and treatment by a peptide-conjugated mini nanodrug. Nanomedicine 13:631–639. https://doi.org/10.1016/j.nano.2016.07.013.
47. Pardon E, Laeremans T, Triest S, Rasmussen SGF, Wohlkönig A, Ruf A, Muyldermans S, Hol WGJ, Kobilka BK, Steyaert J. 2014. A general protocol for the generation of nanobodies for structural biology. Nat Protoc 9:674–693. https://doi.org/10.1038/nprot.2014.039.
48. Kabsch W. 2010. XDS. Acta Crystallogr D Biol Crystallogr 66:125–132. https://doi.org/10.1107/S0907444909047337.
49. Persson EK, Verstraete K, Heyndrickx I, Gevaert E, Aegerter H, Percier J-M, Deswarte K, Verschueren KHG, Dansercoer A, Gras D, Chanez P, Bachert C, Gonçalves A, Van Gorp H, De Haard H, Blanchetot C, Saunders M, Hammad H, Savvides SN, Lambrecht BN. 2019. Protein crystallization promotes type 2 immunity and is reversible by antibody treatment. Science 364:eaaw4295. https://doi.org/10.1126/science.aaw4295.
50. McCoy AJ, Grosse-Kunstleve RW, Adams PD, Winn MD, Storoni LC, Read RJ. 2007. Phaser crystallographic software. J Appl Crystallogr 40:658–674. https://doi.org/10.1107/S0021889807021206.
51. Emsley P, Lohkamp B, Scott WG, Cowtan K. 2010. Features and development of Coot. Acta Crystallogr D Biol Crystallogr 66:486–501. https://doi.org/10.1107/S0907444910007493.
52. Liebschner D, Afonine PV, Baker ML, Bunkoczi G, Chen VB, Croll TI, Hintze B, Hung LW, Jain S, McCoy AJ, Moriarty NW, Oeffner RD, Poon BK, Prisant MG, Read RJ, Richardson JS, Richardson DC, Sammito MD, Sobolev OV, Stockwell DH, Terwilliger TC, Urzhumtsev AG, Videau LL, Williams CJ, Adams PD. 2019. Macromolecular structure determination using X-rays, neutrons and electrons: recent developments in Phenix. Acta Crystallogr D Struct Biol 75:861–877. https://doi.org/10.1107/S2059798319011471.

Annexe 3

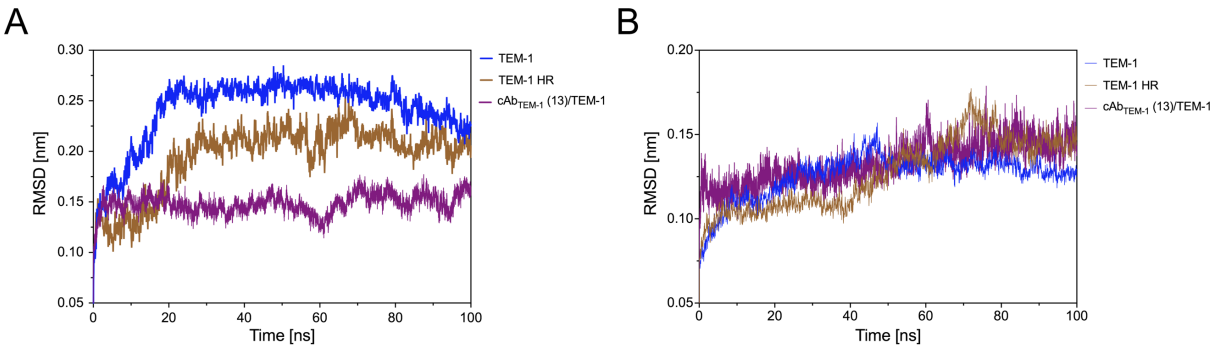

Root-mean square deviation (RMSD) of the hinge region backbone (residues 212-218) (A) and the global protein backbone (B). All data correspond to the average of 5 simulations. For clarity, the standard deviations were not represented on graphs.

Annexe 4

Full wwPDB X-ray Structure Validation Report

Nov 8, 2022 – 04:08 pm GMT

PDB ID	:	7PA5
Title	:	Complex between the beta-lactamase CMY-2 with an inhibitory nanobody
Authors	:	Frederic Cawez, F.C.; Frederic Kerff, F.K.; Moreno Galleni, M.G.; Raphael Herman, R.H.
Deposited on	:	2021-07-29
Resolution	:	3.18 Å(reported)

This is a Full wwPDB X-ray Structure Validation Report for a publicly released PDB entry.

We welcome your comments at *validation@mail.wwpdb.org*
A user guide is available at
https://www.wwpdb.org/validation/2017/XrayValidationReportHelp
with specific help available everywhere you see the ⓘ symbol.

The types of validation reports are described at
http://www.wwpdb.org/validation/2017/FAQs#types.

The following versions of software and data (see references ⓘ) were used in the production of this report:

MolProbity	:	4.02b-467
Mogul	:	1.8.4, CSD as541be (2020)
Xtriage (Phenix)	:	1.13
EDS	:	2.31.2
Percentile statistics	:	20191225.v01 (using entries in the PDB archive December 25th 2019)
Refmac	:	5.8.0267
CCP4	:	7.1.010 (Gargrove)
Ideal geometry (proteins)	:	Engh & Huber (2001)
Ideal geometry (DNA, RNA)	:	Parkinson et al. (1996)
Validation Pipeline (wwPDB-VP)	:	2.31.2

1 Overall quality at a glance (i)

The following experimental techniques were used to determine the structure:
X-RAY DIFFRACTION

The reported resolution of this entry is 3.18 Å.

Percentile scores (ranging between 0-100) for global validation metrics of the entry are shown in the following graphic. The table shows the number of entries on which the scores are based.

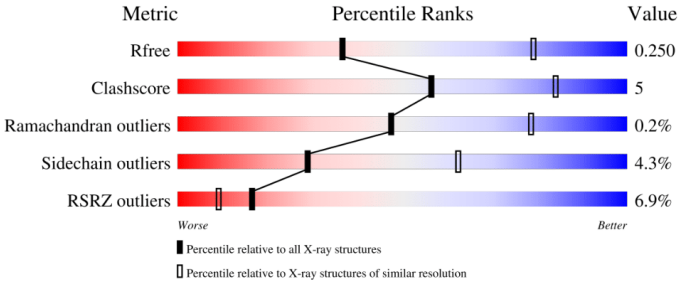

Metric	Whole archive (#Entries)	Similar resolution (#Entries, resolution range(Å))
R_{free}	130704	1467 (3.20-3.16)
Clashscore	141614	1599 (3.20-3.16)
Ramachandran outliers	138981	1574 (3.20-3.16)
Sidechain outliers	138945	1573 (3.20-3.16)
RSRZ outliers	127900	1423 (3.20-3.16)

The table below summarises the geometric issues observed across the polymeric chains and their fit to the electron density. The red, orange, yellow and green segments of the lower bar indicate the fraction of residues that contain outliers for >=3, 2, 1 and 0 types of geometric quality criteria respectively. A grey segment represents the fraction of residues that are not modelled. The numeric value for each fraction is indicated below the corresponding segment, with a dot representing fractions <=5% The upper red bar (where present) indicates the fraction of residues that have poor fit to the electron density. The numeric value is given above the bar.

Mol	Chain	Length	Quality of chain
1	A	361	2% 84% 15%
2	B	129	19% 76% 18% 5%

2 Entry composition

There are 5 unique types of molecules in this entry. The entry contains 7475 atoms, of which 3702 are hydrogens and 0 are deuteriums.

In the tables below, the ZeroOcc column contains the number of atoms modelled with zero occupancy, the AltConf column contains the number of residues with at least one atom in alternate conformation and the Trace column contains the number of residues modelled with at most 2 atoms.

- Molecule 1 is a protein called Beta-lactamase.

Mol	Chain	Residues	Atoms						ZeroOcc	AltConf	Trace
			Total	C	H	N	O	S			
1	A	359	5602	1803	2795	485	510	9	0	0	0

- Molecule 2 is a protein called nanobody.

Mol	Chain	Residues	Atoms						ZeroOcc	AltConf	Trace
			Total	C	H	N	O	S			
2	B	122	1846	589	899	166	187	5	0	1	0

- Molecule 3 is GLYCEROL (three-letter code: GOL) (formula: $C_3H_8O_3$).

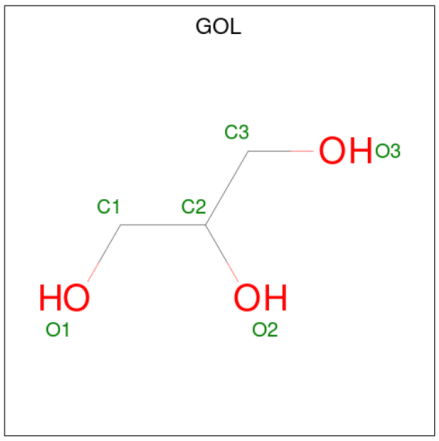

Mol	Chain	Residues	Atoms				ZeroOcc	AltConf
			Total	C	H	O		
3	A	1	14	3	8	3	0	0

- Molecule 4 is PHOSPHATE ION (three-letter code: PO4) (formula: O_4P).

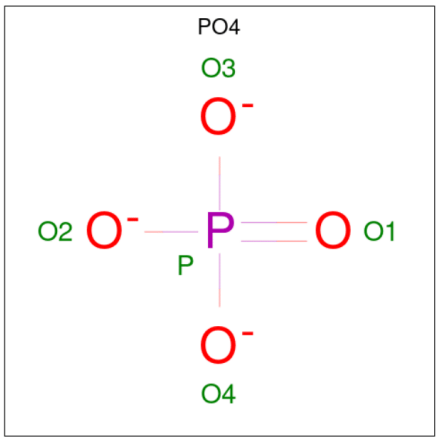

Mol	Chain	Residues	Atoms			ZeroOcc	AltConf
4	B	1	Total	O	P	0	0
			5	4	1		

- Molecule 5 is water.

Mol	Chain	Residues	Atoms		ZeroOcc	AltConf
5	A	8	Total	O	0	0
			8	8		

3 Residue-property plots (i)

These plots are drawn for all protein, RNA, DNA and oligosaccharide chains in the entry. The first graphic for a chain summarises the proportions of the various outlier classes displayed in the second graphic. The second graphic shows the sequence view annotated by issues in geometry and electron density. Residues are color-coded according to the number of geometric quality criteria for which they contain at least one outlier: green = 0, yellow = 1, orange = 2 and red = 3 or more. A red dot above a residue indicates a poor fit to the electron density (RSRZ > 2). Stretches of 2 or more consecutive residues without any outlier are shown as a green connector. Residues present in the sample, but not in the model, are shown in grey.

• Molecule 1: Beta-lactamase

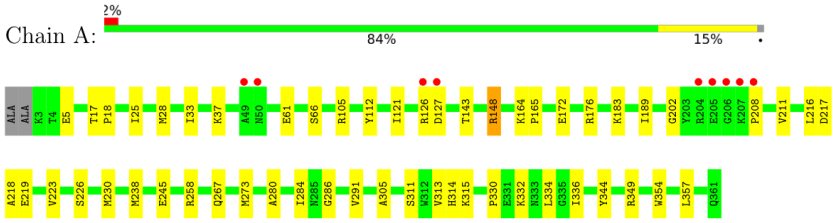

• Molecule 2: nanobody

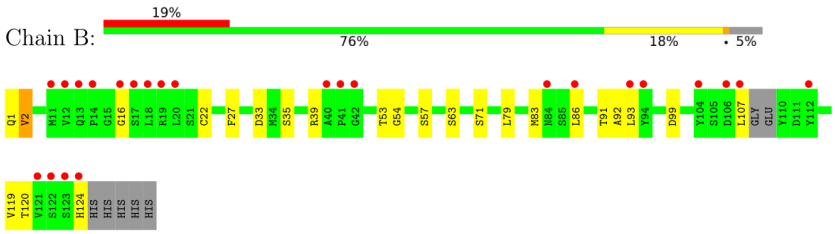

4 Data and refinement statistics (i)

Property	Value	Source
Space group	P 62 2 2	Depositor
Cell constants a, b, c, α, β, γ	95.12Å 95.12Å 242.94Å 90.00° 90.00° 120.00°	Depositor
Resolution (Å)	48.88 – 3.18 48.88 – 3.18	Depositor EDS
% Data completeness (in resolution range)	99.4 (48.88-3.18) 99.4 (48.88-3.18)	Depositor EDS
R_{merge}	0.71	Depositor
R_{sym}	(Not available)	Depositor
$< I/\sigma(I) >$ [1]	1.12 (at 3.19Å)	Xtriage
Refinement program	PHENIX 1.13_2998	Depositor
R, R_{free}	0.207 , 0.250 0.207 , 0.250	Depositor DCC
R_{free} test set	576 reflections (5.00%)	wwPDB-VP
Wilson B-factor (Å^2)	76.7	Xtriage
Anisotropy	0.483	Xtriage
Bulk solvent k_{sol}(e/Å^3), B_{sol}(Å^2)	(Not available) , (Not available)	EDS
L-test for twinning[2]	$< \|L\| > = 0.46$, $< L^2 > = 0.29$	Xtriage
Estimated twinning fraction	No twinning to report.	Xtriage
F_o,F_c correlation	0.91	EDS
Total number of atoms	7475	wwPDB-VP
Average B, all atoms (Å^2)	78.0	wwPDB-VP

Xtriage's analysis on translational NCS is as follows: *The largest off-origin peak in the Patterson function is 3.21% of the height of the origin peak. No significant pseudotranslation is detected.*

[1] Intensities estimated from amplitudes.

[2] Theoretical values of $< |L| >$, $< L^2 >$ for acentric reflections are 0.5, 0.333 respectively for untwinned datasets, and 0.375, 0.2 for perfectly twinned datasets.

5 Model quality

5.1 Standard geometry

Bond lengths and bond angles in the following residue types are not validated in this section: PO4, GOL

The Z score for a bond length (or angle) is the number of standard deviations the observed value is removed from the expected value. A bond length (or angle) with $|Z| > 5$ is considered an outlier worth inspection. RMSZ is the root-mean-square of all Z scores of the bond lengths (or angles).

Mol	Chain	Bond lengths		Bond angles	
		RMSZ	$\#\|Z\| > 5$	RMSZ	$\#\|Z\| > 5$
1	A	0.26	0/2884	0.46	0/3929
2	B	0.27	0/968	0.49	0/1310
All	All	0.27	0/3852	0.47	0/5239

There are no bond length outliers.

There are no bond angle outliers.

There are no chirality outliers.

There are no planarity outliers.

5.2 Too-close contacts

In the following table, the Non-H and H(model) columns list the number of non-hydrogen atoms and hydrogen atoms in the chain respectively. The H(added) column lists the number of hydrogen atoms added and optimized by MolProbity. The Clashes column lists the number of clashes within the asymmetric unit, whereas Symm-Clashes lists symmetry-related clashes.

Mol	Chain	Non-H	H(model)	H(added)	Clashes	Symm-Clashes
1	A	2807	2795	2795	27	1
2	B	947	899	897	10	0
3	A	6	8	8	0	0
4	B	5	0	0	0	0
5	A	8	0	0	0	1
All	All	3773	3702	3700	37	2

The all-atom clashscore is defined as the number of clashes found per 1000 atoms (including hydrogen atoms). The all-atom clashscore for this structure is 5.

All (37) close contacts within the same asymmetric unit are listed below, sorted by their clash magnitude.

Atom-1	Atom-2	Interatomic distance (Å)	Clash overlap (Å)
1:A:148:ARG:NH1	1:A:267:GLN:OE1	2.14	0.80
1:A:280:ALA:HB2	1:A:354:TRP:CE2	2.25	0.72
1:A:245:GLU:N	1:A:245:GLU:OE1	2.31	0.62
1:A:61:GLU:CD	1:A:211:VAL:HG23	2.21	0.61
2:B:35:SER:OG	2:B:99:ASP:OD1	2.19	0.60
2:B:16:GLY:O	2:B:86:LEU:HD12	2.07	0.55
1:A:5:GLU:OE2	1:A:5:GLU:N	2.35	0.55
1:A:258:ARG:NH2	1:A:311:SER:OG	2.40	0.54
1:A:121:ILE:HD11	1:A:216:LEU:HD12	1.90	0.53
1:A:189:ILE:HD13	1:A:218:ALA:HB1	1.91	0.52
1:A:25:ILE:HG21	1:A:28:MET:HG3	1.93	0.51
1:A:344:TYR:O	1:A:349:ARG:NH2	2.38	0.51
2:B:71:SER:O	2:B:79:LEU:HD12	2.13	0.49
2:B:83:MET:HE1	2:B:119:VAL:HG21	1.95	0.49
1:A:226:SER:O	1:A:230:MET:HG2	2.13	0.48
1:A:219:GLU:N	1:A:219:GLU:OE1	2.45	0.47
1:A:336:ILE:HG22	1:A:357:LEU:HD11	1.96	0.47
1:A:273:MET:HG3	1:A:313:VAL:HG22	1.96	0.47
1:A:238:MET:HG3	1:A:330:PRO:HA	1.96	0.47
2:B:1:GLN:O	2:B:2:VAL:HG23	2.14	0.47
2:B:91:THR:HG23	2:B:120:THR:HA	1.97	0.46
1:A:33:ILE:HG21	1:A:238:MET:HE1	1.97	0.45
1:A:202:GLY:O	1:A:208:PRO:HA	2.17	0.44
1:A:280:ALA:HB2	1:A:354:TRP:CZ2	2.52	0.44
1:A:334:LEU:HG	1:A:357:LEU:HD22	1.99	0.44
1:A:164:LYS:HB2	1:A:165:PRO:HD3	1.99	0.44
1:A:336:ILE:HB	1:A:357:LEU:HD21	2.00	0.44
1:A:217:ASP:OD1	1:A:218:ALA:N	2.51	0.43
2:B:39:ARG:O	2:B:92:ALA:HB1	2.18	0.43
1:A:286:GLY:HA2	1:A:291:VAL:HG11	2.00	0.43
1:A:258:ARG:HB2	1:A:305:ALA:HB3	2.00	0.43
1:A:280:ALA:HB1	1:A:284:ILE:HD12	1.99	0.43
2:B:53:THR:OG1	2:B:54:GLY:N	2.52	0.43
1:A:17:THR:HB	1:A:18:PRO:HD3	2.01	0.42
2:B:33:ASP:OD1	2:B:53:THR:HG23	2.20	0.42
1:A:66:SER:HB3	1:A:223:VAL:HG23	2.02	0.41
2:B:2:VAL:HG22	2:B:27:PHE:HB3	2.03	0.40

All (2) symmetry-related close contacts are listed below. The label for Atom-2 includes the symmetry operator and encoded unit-cell translations to be applied.

Atom-1	Atom-2	Interatomic distance (Å)	Clash overlap (Å)
1:A:172:GLU:OE2	1:A:176:ARG:NH1[4_555]	1.97	0.23
5:A:502:HOH:O	5:A:508:HOH:O[10_554]	2.00	0.20

5.3 Torsion angles (i)

5.3.1 Protein backbone (i)

In the following table, the Percentiles column shows the percent Ramachandran outliers of the chain as a percentile score with respect to all X-ray entries followed by that with respect to entries of similar resolution.

The Analysed column shows the number of residues for which the backbone conformation was analysed, and the total number of residues.

Mol	Chain	Analysed	Favoured	Allowed	Outliers	Percentiles	
1	A	357/361 (99%)	343 (96%)	14 (4%)	0	100	100
2	B	119/129 (92%)	107 (90%)	11 (9%)	1 (1%)	19	56
All	All	476/490 (97%)	450 (94%)	25 (5%)	1 (0%)	47	78

All (1) Ramachandran outliers are listed below:

Mol	Chain	Res	Type
2	B	2	VAL

5.3.2 Protein sidechains (i)

In the following table, the Percentiles column shows the percent sidechain outliers of the chain as a percentile score with respect to all X-ray entries followed by that with respect to entries of similar resolution.

The Analysed column shows the number of residues for which the sidechain conformation was analysed, and the total number of residues.

Mol	Chain	Analysed	Rotameric	Outliers	Percentiles	
1	A	291/291 (100%)	280 (96%)	11 (4%)	33	66
2	B	102/107 (95%)	96 (94%)	6 (6%)	19	52
All	All	393/398 (99%)	376 (96%)	17 (4%)	29	62

All (17) residues with a non-rotameric sidechain are listed below:

Mol	Chain	Res	Type
1	A	37	LYS
1	A	105	ARG
1	A	112	TYR
1	A	126	ARG
1	A	127	ASP
1	A	143	THR
1	A	148	ARG
1	A	183	LYS
1	A	314	HIS
1	A	315	LYS
1	A	332	LYS
2	B	22	CYS
2	B	57	SER
2	B	63	SER
2	B	93	LEU
2	B	107	LEU
2	B	124	HIS

Sometimes sidechains can be flipped to improve hydrogen bonding and reduce clashes. There are no such sidechains identified.

5.3.3 RNA (i)

There are no RNA molecules in this entry.

5.4 Non-standard residues in protein, DNA, RNA chains (i)

There are no non-standard protein/DNA/RNA residues in this entry.

5.5 Carbohydrates (i)

There are no monosaccharides in this entry.

5.6 Ligand geometry (i)

2 ligands are modelled in this entry.

In the following table, the Counts columns list the number of bonds (or angles) for which Mogul statistics could be retrieved, the number of bonds (or angles) that are observed in the model and the number of bonds (or angles) that are defined in the Chemical Component Dictionary. The Link column lists molecule types, if any, to which the group is linked. The Z score for a bond

length (or angle) is the number of standard deviations the observed value is removed from the expected value. A bond length (or angle) with $|Z| > 2$ is considered an outlier worth inspection. RMSZ is the root-mean-square of all Z scores of the bond lengths (or angles).

Mol	Type	Chain	Res	Link	Bond lengths			Bond angles		
					Counts	RMSZ	$\#\|Z\| > 2$	Counts	RMSZ	$\#\|Z\| > 2$
4	PO4	B	201	-	4,4,4	0.90	0	6,6,6	0.45	0
3	GOL	A	401	-	5,5,5	0.80	0	5,5,5	1.04	0

In the following table, the Chirals column lists the number of chiral outliers, the number of chiral centers analysed, the number of these observed in the model and the number defined in the Chemical Component Dictionary. Similar counts are reported in the Torsion and Rings columns. '-' means no outliers of that kind were identified.

Mol	Type	Chain	Res	Link	Chirals	Torsions	Rings
3	GOL	A	401	-	-	0/4/4/4	-

There are no bond length outliers.

There are no bond angle outliers.

There are no chirality outliers.

There are no torsion outliers.

There are no ring outliers.

No monomer is involved in short contacts.

5.7 Other polymers (i)

There are no such residues in this entry.

5.8 Polymer linkage issues (i)

There are no chain breaks in this entry.

6 Fit of model and data

6.1 Protein, DNA and RNA chains

In the following table, the column labelled '#RSRZ> 2' contains the number (and percentage) of RSRZ outliers, followed by percent RSRZ outliers for the chain as percentile scores relative to all X-ray entries and entries of similar resolution. The OWAB column contains the minimum, median, 95^{th} percentile and maximum values of the occupancy-weighted average B-factor per residue. The column labelled 'Q< 0.9' lists the number of (and percentage) of residues with an average occupancy less than 0.9.

Mol	Chain	Analysed	<RSRZ>	#RSRZ>2	OWAB(Å^2)	Q<0.9
1	A	359/361 (99%)	0.27	9 (2%) 57 43	51, 67, 93, 116	0
2	B	122/129 (94%)	0.80	24 (19%) 1 0	55, 71, 100, 121	0
All	All	481/490 (98%)	0.41	33 (6%) 16 9	51, 68, 96, 121	0

All (33) RSRZ outliers are listed below:

Mol	Chain	Res	Type	RSRZ
2	B	18	LEU	5.0
2	B	107	LEU	4.9
2	B	41	PRO	4.7
2	B	13	GLN	4.6
2	B	14	PRO	3.3
1	A	204	ARG	3.2
2	B	42	GLY	3.0
1	A	208	PRO	3.0
1	A	50	ASN	2.9
2	B	20	LEU	2.9
2	B	84	ASN	2.8
2	B	121	VAL	2.8
1	A	127	ASP	2.7
2	B	11	MET	2.7
2	B	17	SER	2.7
2	B	122	SER	2.6
2	B	123	SER	2.6
1	A	206	GLY	2.5
2	B	19[A]	ARG	2.5
1	A	49	ALA	2.4
1	A	126	ARG	2.4
2	B	106	ASP	2.4
1	A	207	LYS	2.3
2	B	94	TYR	2.3

Continued on next page...

Continued from previous page...

Mol	Chain	Res	Type	RSRZ
2	B	86	LEU	2.3
2	B	40	ALA	2.3
2	B	112	TYR	2.3
2	B	124	HIS	2.3
1	A	205	GLU	2.2
2	B	104	TYR	2.2
2	B	16	GLY	2.2
2	B	12	VAL	2.1
2	B	93	LEU	2.1

6.2 Non-standard residues in protein, DNA, RNA chains (i)

There are no non-standard protein/DNA/RNA residues in this entry.

6.3 Carbohydrates (i)

There are no monosaccharides in this entry.

6.4 Ligands (i)

In the following table, the Atoms column lists the number of modelled atoms in the group and the number defined in the chemical component dictionary. The B-factors column lists the minimum, median, 95^{th} percentile and maximum values of B factors of atoms in the group. The column labelled 'Q< 0.9' lists the number of atoms with occupancy less than 0.9.

Mol	Type	Chain	Res	Atoms	RSCC	RSR	B-factors(Å^2)	Q<0.9
3	GOL	A	401	6/6	0.87	0.27	63,76,105,106	0
4	PO4	B	201	5/5	0.95	0.30	61,61,65,68	5

6.5 Other polymers (i)

There are no such residues in this entry.